Durham University

Durham E-Theses

Stellar populations of X-Ray luminous clusters at z = 0.1

Kevin Alan Pimbblet

How to cite:

Pimbblet, Kevin Alan (2001) Stellar populations of X-Ray luminous clusters at z = 0.1. Doctoral thesis, Durham University.

Use policy

The full-text may be used and/or reproduced, and given to third parties in any format or medium, without prior permission or charge, for personal research or study, educational, or not-for-profit purposes provided that:

- a full bibliographic reference is made to the original source
- a https://etheses.durham.ac.uk/id/eprint/3778/ is made to the metadata record in Durham E-Theses
- the full-text is not changed in any way

The full-text must not be sold in any format or medium without the formal permission of the copyright holders.

Please consult the full Durham E-Theses policy for further details.

Academic Support Office, The Palatine Centre, Durham University, Stockton Road, Durham, DH1 3LE
e-mail: e-theses.admin@durham.ac.uk Tel: +44 0191 334 6107
https://etheses.durham.ac.uk

The copyright of this thesis rests with the author. No quotation from it should be published in any form, including Electronic and the Internet, without the author's prior written consent. All information derived from this thesis must be acknowledged appropriately.

Stellar Populations of X-Ray Luminous Clusters at $z = 0.1$

Kevin Alan Pimbblet

A dissertation submitted to the University of Durham
in accordance with the regulations for
admission to the degree of Doctor of Philosophy.

The copyright of this work rests with the author at all times.
No quotation from it should be published without his prior written
consent and information derived from it shall be acknowledged.

Department of Physics, University of Durham, 2001.

19 APR 2002

Ph.D. THESIS ABSTRACT

Stellar Populations of X-Ray Luminous Clusters at $z = 0.1$

Kevin Alan Pimbblet (2001)

This thesis presents new and unique wide-field imaging and spectroscopic observations of 21 X-ray selected rich clusters of galaxies in the redshift range $0.07 < z < 0.16$ from the Las Campanas Observatory (LCO) / Anglo-Australian Telescope (AAT) Rich Cluster Survey (LARCS). Mosaic two colour broad-band CCD imaging extending to 10 Mpc at the mean redshift of the survey have been taken at LCO; comprising over 50Gb of raw data. A reduction pipeline is developed for these data and catalogues are constructed for these clusters.

Four of these fields are compared to the APM catalogue (Maddox et al. 1990) to confirm their photometric accuracy. In making the comparison several populations of galaxies are discovered to be absent from the APM.

A statistical background correction technique is developed to examine the photometric properties of cluster members. Eleven clusters are combined together to investigate environmental trends in the stellar populations of the combined sample. It is found that the modal colours of galaxies lying on the colour-magnitude relation in the clusters become bluer by $d(B-R)/dr_p = -0.022 \pm 0.004$ with radius or $d(B-R)/d\log_{10}(\Sigma) = -0.076 \pm 0.009$ with local galaxy density.

The 2dF spectroscope at the AAT is used to make spectroscopic follow-up observations of three clusters. A reduction pipeline for these data is developed and redshifts for the galaxies are determined. The spectral catalogues are used to define cluster membership and confirm the photometric environmental trends. Spectral line strengths are used to classify the galaxy population and examine environmental trends across the clusters. The cluster cores are found to be predominantly passive compared to the field. A comparison of the two cluster membership assignment techniques underscores the need for spectroscopy to define the cluster population.

Contents

List of Figures

List of Tables

Preface and Declaration

The work presented in this thesis was undertaken whilst the Author was a graduate student working in the Department of Physics at the University of Durham under the supervision of Drs. Ian Smail, Alastair Edge and Richard Bower (Durham). The LARCS project which forms the basis of this thesis is an international collaboration between Pimbblet, Smail and Edge (Durham), Prof. Ann Zabludoff (Arizona), Prof. Warrick Couch and Dr. Eileen O'Hely (UNSW). Additionally, Dr. Tadayuki Kodama (Tokyo) assisted the collaboration whilst he was in Durham. The vast majority of the work presented in this book, however, is the Author's own except where noted explicitly below and in the main body of the text:

The observations made at Las Campanas Observatory were undertaken by O'Hely, Smail and Zabludoff prior to the commencement of Pimbblet's Ph.D. in Durham.

The first set of observations at the Anglo-Australian Telescope were prepared and made by Edge, Couch and O'Hely in 1998. The second set of observations made at the Anglo-Australian Telescope were prepared soley by Pimbblet and carried out by Pimbblet and Couch in 2000 and (in service time) by Bridges and Cannon in 2001.

Parts of this work have made use of the NASA/IPAC Extragalactic Database (NED) which is operated by the Jet Propulsion Laboratory, California Institute of Technology, under contract with the National Aeronautics and Space Administration (NASA).

Data from the APM survey (e.g. Maddox et al. 1990) and the 2dFGRS survey (e.g. Colless et al. 2001) have been used in parts this work. The Author gratefully acknowledges the kindness displayed by all of the 2dFGRS team in this respect.

This research has made use of NASA's Astrophysics Data System (ADS) Bibliographic Services.

Various results and text from this work have been (or will be) published in a number of other sources. These publications are noted below.

Material from Chapters 2 and 3 appear in the following publication:

'The Las Campanas/AAT Rich Cluster Survey: I. Precision and Reliability of the Photometric Catalogue' **Pimbblet, K. A.**, Smail, I., Edge, A. C., Couch, W. J., O'Hely, E. & Zabludoff, A. I., 2001, MNRAS, 327, 588

Material from Chapter 4 appears in the following publication:

'The Las Campanas/AAT Rich Cluster Survey: II. The Environmental Dependance of Galaxy Colours in Clusters at z$\sim$0.1' **Pimbblet, K. A.**, Smail, I., Kodama, T., Couch, W. J., Edge, A. C., Zabludoff, A. I. & O'Hely, E., 2002, MNRAS, 331, 333

Material from Chapters 4 and 7 will appear in the following publication:

'On the Merit of Observations Beyond the Cluster Core' **Pimbblet, K. A.**, 2002, ASP Conference Series 'A New Era in Cosmology', in press.

Acknowledgements

Working on the LARCS dataset for the last three and something years has been quite an experience with all of it's associated ups, downs, frustrations and struggles. I would like to thank everyone concerned: Firstly PPARC for my subsistence and the funding provided on my observational field trips to Hawai'i and Australia. I am grateful to the LCO and AAO facilities and their staff for the generous support of this survey.

I have had the pleasure (and privilege) of working closely with many people in the department without whom, this tome would not be what it is. BIG THANKS to my two totally awesome SUPERvisors: Ian (whose full name is an anagram of "Slim Aberration" and "Brainier, Almost") and Alastair (whose full name is an anagram of "Tail Graduate Coolness") - I couldn't have wished for better supervision and guidance. Also thanks to my other colleagues here in Durham and worldwide: Richard Bower (for endless encouragement and enthusiasm about my work), Warrick Couch (for unknowingly being a great inspiration to me during my research and guidance whilst I was in Australia), Eileen O'Hely (for being a kindred spirit, particularly for excessive use of exclaimation marks!), Ann Zabludoff (for her being a better referee than the actual referees and allowing me to access her template spectra) and Taddy Kodama (for allowing me to generally pick his brains and cooly discussing many heated topics). I sincerely thank Alan Lotts for his expert management of the STARLINK computing facilities in Durham, particularly for dealing with the upgrades to Athas (the Sparc Station formerly known as Hubble that I inherited from Ian). I also thank Terry Bridges for his continued persistence in making the 2dF service run a reality. Other members of the 2dFGRS team also deserve my thanks for providing some stimulating discussion and useful data: particularly Nick Cross, Simon Driver, Shaun Cole, Peder Norberg, Steve Maddox and Matthew Colless. Finally, thanks to Harald Ebeling and Bianca Poggianti for a small amounts of incidental aid and advice early and late on (respectively) during my research.

I gratefully thank those who have dedicated time to aid me in proof-reading various swathes of this tome: my academic collaborators, other members of the Durham Extra-Galactic Astronomy Group, Mary Hawkrigg, Dr.Anna Sheridan and Stephen Bell.

At last, I get to thank all of my family for believing that I could do it and for their selfless support, love and words of encouragement over the past quarter-century: Mum, Dad, Stephen, Valerie, my Grandmothers (and the rest of the Pimbblet's I discovered from my genealogical investigations). Special thanks to Mary, her siblings and her parents, Brian and Anne Hawkrigg.

More thanks to those who have endured sharing offices with me for extended periods: Henry, Luis, Katherine, Eric, Claire H., Fiona, David, Richard M., Amaya, Dajana, Richard D., Rowena, Dave and also thanks to the rest of the Young Trendy Astronomers (a.k.a. YTA) in general!

I have been lucky enough to be blessed with a large number of close friends during my time in Durham. I'm sure I've missed some people out, but in no special order I thank the following for many fond memories, their kindness, enduring friendship and a plethora of experiences together which I will remember for a very long time: Roberto, Mark, Deborah, Marion, Anna, Helen, Steve, Phil, Vivek, Lindsey, Claire C., Quintin, Mary, Joanna, Sophie, Stuart, Paul H., Paul K., Laura, Richard K., Rob, JimBob, Braddas, Mike S., Nathan, Jonti, Catherine, Carolyn, Dave, Bec, Conor, Mike L., Lucy, Dan, Michael, Kev, Sam, Colin and Shana. Further, I thank all of my ballroom dancing partners over the years: Rachel A., Lisa, Claire C. and Rachel S., my instructors Jean and Maureen and all of the Ballroom and Castle people who made Monday evenings a night to look forward to. Also thanks to Revd. John Allison and Jane and all the Elvet gang. It has also been a pleasure to serve Collingwood College in a number of capacities, particularly as the MCR President. My gratitude to Michelle, Steve and my best wishes for the future to Gerald and good luck to Jane (the outgoing and incoming Collingwood College Principals respectively).

With pleasure, I dedicate this work to my family and to my friends.

Kevin Alan Pimbblet, 5th December 2001.

eduxitque eum foras et ait illi
suspice caelum et numera stellas si
potes *et dixit ei sic erit semen tuum*

Genesis 15:5

Chapter 1 | *Introduction*

1.1 The Dawn of Extra-Galactic Cosmology

As long ago as the 18th century one is able to find authors (e.g. Wright 1750) writing that celestial nebulae may be extended systems of stars similar in nature to our own Milky Way Galaxy*. Indeed, Kant (1755) extended Wright's line of reasoning to specifically suggest that one of the best-known nebulae, Andromeda, could be similar to our own Galaxy. Wolf (1865) reported that the occurrence of such nebulae on the sky was not uniformly distributed but exhibited a tendency to be clustered. The true quantitative, scientific study of extra-galactic bodies, however, did not truly commence until the early decades of the twentieth century.

It was during the 1920s that the science of cosmology truly came into being. Hubble (1925) recognized nebulae as isolated, external (to the Galaxy) systems at great distances by resolving and identifying Cepheid variable stars contained within them. Since a Cepheid star's period is proportional to its luminosity, the distance to a galaxy in which a Cepheid resides can be evaluated. Following on from this discovery came the cataloguing and classification of these galaxies. The traditional and most widely-used morphological classification scheme is that of Hubble (1936). Figure 1.1 displays an example of the Hubble tuning fork scheme. Towards the left hand side of the diagram are elliptical galaxies; smooth, little internal structure and varying from circular (i.e. E0) to noticeably elliptical (i.e. E6). In the centre of the Hubble diagram are lenticular galaxies (i.e. S0): a centrally concentrated, smooth bulge similar to elliptical galaxies accompanied by an envelope of disc-like material. On the right hand side of the diagram are the spiral galaxies, subdivided into 'normal' spirals (having a small bulge) and barred spirals (having a bar in the

*Following convention, in this work the word 'Galaxy' refers to our own Milky Way Galaxy when capitalized and refers to any other galaxy when in lower case.

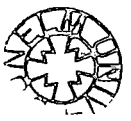

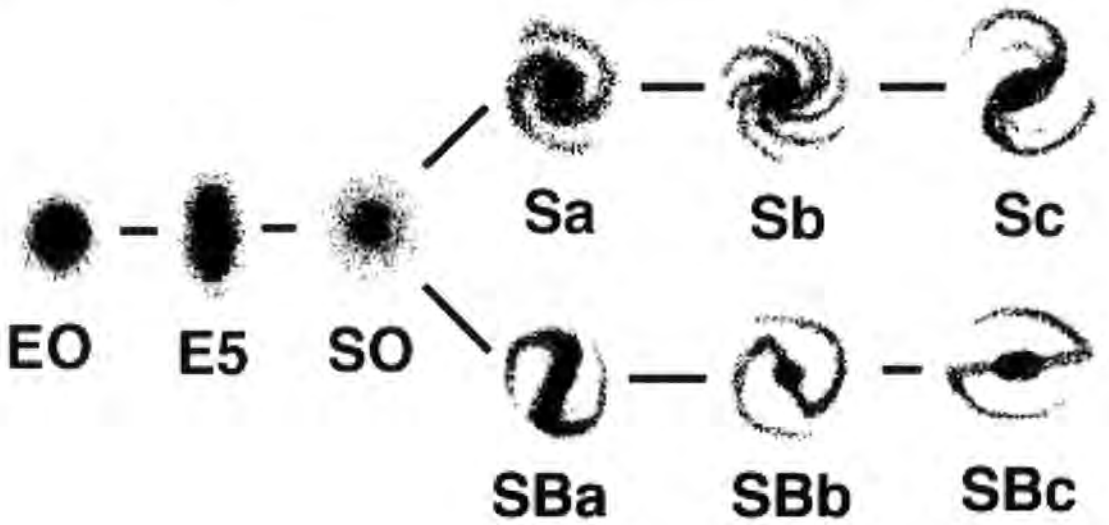

Figure 1.1: A classical Hubble 'tuning fork' diagram. Although discredited, Hubble suggested that galaxies evolved from the left hand side of this fork to the right. This suggestion still exists in convention: galaxies towards the left are referred to as 'early-type' and those to the right as 'late-type'.

central regions). Irregular galaxies are not pictured in Figure 1.1 although recent revised versions of the Hubble diagram place such galaxies at the extreme right hand side (e.g. Kormendy & Bender 1996). Further, there also exist dwarf galaxies which possess low luminosities; a discussion of these galaxies, however, is not pertinent to this work. The appearance of the constituent members of this zoo of galaxies is pictorially reviewed in detail by Sandage (1961) in the 'Hubble Atlas of Galaxies'.

1.2 Clusters of Galaxies

As noted above, galaxies appear to be spatially clustered on the sky. They are found in large conglomerates known as *clusters of galaxies*. Such clusters can be found out to high redshifts ($z > 1.0$) as they are composed of large numbers ($N > 20$) of luminous galaxies that are highly concentrated. Yet more galaxies reside in smaller *groups of galaxies* and alone in isolation within areas of very low galaxy density. As de Vaucouleurs (1961a) reviewed, there exists a second order of clustering: the clusters of galaxies themselves are not isolated but are clustered into *superclusters*. The results of the 2dF Galaxy Redshift Survey (Colless et al. 2001) clearly show

that clusters represent the corner stones of large scale structure: they are found at the intersections of chains, filaments and sheets throughout the observable Universe and are the largest gravitationally bound systems known ($M_{Cluster} \simeq 10^{15} M_{\odot}$[†]). As such, they lie on the exponential tail of the mass fluctuation spectrum. At the present epoch, clusters are growing by the accretion and infall of galaxies and small groups from the field (outside the gravitational bounds of the cluster). Therefore clusters can provide an excellent probe for the growth of gravitational structure and environmental effects.

The criteria for defining what a rich cluster of galaxies is has been fraught with ambiguity because clusters exist across a wide range of angular scales and contrasts. Much effort has gone into quantifying clusters of galaxies to permit further comparative studies. Abell (1958) defined a rich cluster using a number of criteria which are essentially a measure of the contrast. Firstly, the cluster should contain a minimum of 50 galaxies in the magnitude range m_3 to $m_3 + 2$, where m_3 is the magnitude of the third brightest galaxy. Secondly, these galaxies should be contained within a circle of radius $R_A = 1.7/z$ arcmin (or $\sim 3Mpc$[‡]) where R_A is the 'Abell radius'. These criteria give a total of ≥ 1682 ($R > 0$) clusters (out of 2712) from the Abell catalogue (1958) out to $z \leq 0.4$. Abell also gave them a richness class based upon the number of constituent galaxies and broadly defined them as regular or irregular. Authors other than Abell have also found ways to classify clusters of galaxies; Bautz & Morgan (1970) describe a scheme based upon the dominance of the brightest central galaxy whilst Rood & Sastry (1971) describe a scheme based upon the compactness and regularity of clusters.

Abell (1958) is by no means the sole cluster catalogue constructed, nor is it totally complete. Collaborating with Corwin and Olowin, Abell et al. (1984) extended his own (1958) all-sky catalogue to a total of 4073 clusters of galaxies (close to doubling the size of his previous catalogue). More recent developments include the APM catalogue (see Chapter 3 for a full discussion of the APM) from which

[†]The mass of the Sun, $M_{\odot}$, is approximately $2 \times 10^{30} kg$.

[‡]Throughout this work, values of $H_0 = 100h$ km s^{-1} Mpc^{-1} and $q_o = 0.5$ have been adopted. Throughout this work, whenever a figure is given in Mpc, one assumes that this implicitly means h^{-1}Mpc.

Dalton et al. (1994) extracts redshifts for 228 clusters, of which, 188 are previously undetected. The Edinburgh/Durham Cluster Catalogue (EDCC; Lumsden et al. 1992) uses a machine peak-finding algorithm which finds 80 per cent of Abell (1958) rich clusters, suggesting that Abell (1958) is biased towards bright magnitudes. The ROSAT satellite has also given astronomers an all-sky survey in the X-ray part of the electomagnetic spectrum. Ongoing research is still finding additional (X-ray detected) clusters of galaxies within this survey (e.g. REFLEX; Bohringer et al. 1998) that are beyond Abell's findings.

1.3 Galaxian Composition of Clusters

In addition to their clear use as probes of large scale structure, rich clusters allow the study of a large number of galaxies ($\sim 10^3$) at a common distance and visible out to a large redshift, which makes them ideal for studying galaxy evolution. The wide variety of galaxy and gas density also provides an excellent tool to probe possible environmental effects described below.

It has long been known that the cores of rich clusters of galaxies are dominated by passively evolving early-type (elliptical and lenticular) galaxies (Hubble & Humason 1931) whilst those in the field[§] are predominantly later type (spiral and irregular) galaxies. The assumption that clusters are non-evolving and in a relaxed state held firm for at least the former half of the twentieth century. Evidence to invalidate this assumption came from observations of different morphological distributions within clusters (Zwicky 1957) and inconsistent differential morphological velocity dispersions (e.g. de Vaucouleurs 1961b). Much effort in recent decades has gone into an examination of the galaxy content of clusters and the evolution of clusters. The observational techniques in optical astronomy used to trace the variation in the stellar populations of galaxies between the field and cluster and its evolution with redshift are photometry and spectroscopy.

The pioneering work in the photometric domain is considered to be that of Butcher and Oemler (1978, 1984). They identified a radial gradient within their

[§]Conventionally, the domain outside a cluster of galaxies is called *field*.

sample of 33 clusters: the fraction of blue galaxies, f_B[¶], in their clusters increased with projected radius away from the cluster core, out to the maximum extent of their data at ~ 1.5 Mpc. Further, they also uncovered evidence for an evolution in the blue fraction with redshift (Figure 1.2), increasing from ~ 0.03 at low redshifts ($z \sim 0.05$) to ~ 0.25 at larger redshifts ($z \sim 0.5$). This work has been followed up by many other authors (e.g. Couch & Newall 1984; Rakos & Schombert 1995) who have shown that the cores of $z > 0.2$ clusters contain blue galaxies; this complements the work of other authors (e.g. Terlevich, Caldwell & Bower 2001) who find uniformly red early-type galaxies populating local nearby clusters. The natural conclusion to this situation is that there has been strong, rapid evolution of clusters of galaxies with redshift.

Recently, Smail et al. (1998) examined a sample of 10 rich clusters of galaxies in the redshift range $0.22 < z < 0.28$ and found that the blue fraction (median $f_B \sim 0.05$) was lower than the values found by Butcher and Oemler (1984; see Figure 1.2). The individual measurements, however, show a large scatter. There was also found to be no significant correlation between f_B and global cluster parameters such as X-ray morphology or cluster concentration.

To test the cluster membership of these blue 'Butcher-Oemler' galaxies, a number of groups (e.g. Couch & Sharples 1987; Dressler & Gunn 1983) undertook spectroscopic surveys of distant clusters and came up with surprising results. Although some blue galaxies are found to be interloping foreground or background galaxies, the bone-fide blue cluster members are found to exhibit spectra typical of spiral galaxies. They displayed strong emission lines indicative of on-going star formation. Further, some red galaxies showed strong balmer absorption lines with a lack of emission lines; indicative of a recent decline in star formation. This latter type subsequently became known as post-starbursting galaxies (PSGs) or 'E+A'[‖]

[¶]The blue fraction, f_B, is defined to be the fraction of galaxies whose rest frame $(B - V)$ colour is at least 0.2 magnitudes bluer than the cluster's colour-magnitude relation and lie within R_{30}, the clustocentric radius that contains 30 per cent of the total galaxy population (Butcher & Oemler 1984)

[‖]The nomenclature 'E+A' derives from the dominant presence of young, luminous, blue, A-type stars (resulting from a short-lived episode of star-formation) contained within a galaxy possessing an old stellar population (E).

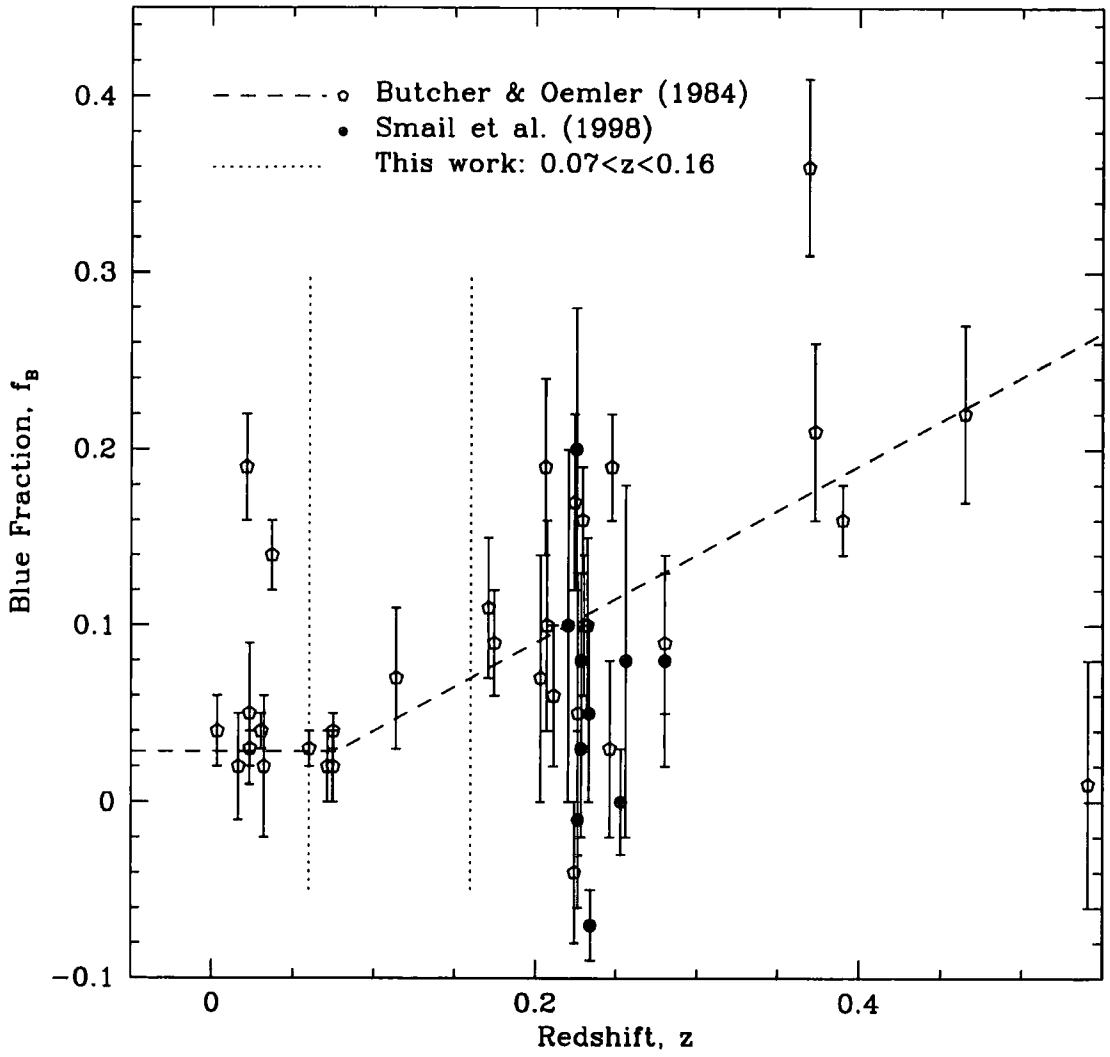

Figure 1.2: The Butcher-Oemler effect, taken from Butcher & Oemler (1984), showing an evolution in the blue fraction with redshift. Also plotted are the points from Smail et al. (1998) (filled circles). This work seeks to analyze the redshift range bounded by the dotted vertical lines.

Table 1.1: An illustration of the morphology-density relation reproduced from Oemler (1992). Because a number of sources were used in the construction of this table, the populations vary within each category and therefore these numbers should be taken as *representative* of the trend and not absolute. See also Figure 4 of Dressler (1980).

	% Type		
Environment	E	S0	Spiral
Field	10	20	70
Poor Group	10	20	70
Rich Group	10	30	60
Cluster	20	40	40

galaxies (e.g. Franx 1993). The presence of these 'E+A' galaxies in these clusters is surprising given their comparative rarity in nearby clusters (Caldwell & Rose 1997) and reaffirms the view that clusters of galaxies have been recently evolving.

A complicating issue to the Butcher-Oemler effect is the morphology-density ($T - \Sigma$) relation first discussed by Dressler (1980). Table 1.1 provides an illustration of the $T - \Sigma$ relation sufficient for this discussion: the proportion of spiral galaxies decreases strongly as a function of local galaxy density whilst S0 and E galaxies increase. Oemler (1974) demonstrates a similar result within a number of relaxed, rich clusters with the E and S0 fraction increasing towards the centre, accompanied by a decline in the fraction of spiral types. The fraction of early types is also found to be correlated with global cluster structure: more relaxed clusters have a higher early-type fraction (Oemler 1974). The question of whether local galaxy density or clustocentric radius is the more fundamental parameter driving the morphological transformation, however, is still an open question (Whitmore & Gilmore 1991; Whitmore et al. 1993)

1.3.1 Non-Galaxian Components

Necessarily, mention must also be made of some non-galaxian components of clusters of galaxies. A cluster is a gravitational potential which is not solely filled with galaxies. Rood (1965) first suggested the presence of an intra-cluster medium (ICM)

when he found that a non-negligible portion of the mass of the Coma cluster** was not contained in the galaxies. Evidence for an ICM came from X-ray observations of clusters of galaxies (see Sarazin 1988 for a detailed review). The X-ray emissions were found to source from thermal bremsstrahlung of the ICM (e.g. Sarazin 1988; Jones & Forman 1984). The typical mass of the ICM of a rich cluster is some $10^{14} M_{\odot}$ within the central few Mpc (Jones & Forman 1992); equivalent to ~ 25 per cent of the total cluster mass. As with the spatial distribution of galaxies, the X-ray emission can also be morphologically classified (Sarazin 1988; Jones & Forman 1992). Cluster that are highly relaxed, therefore, tend to have a more luminous and regular X-ray emission resulting from a hotter ICM (Edge & Stewart 1991). Rich clusters are some of the most X-ray luminous objects known.

Dark matter is the final and dominant component of clusters of galaxies. Although never actually observed at any wavelength (hence the name) its presence can be inferred from X-ray and optical observations (e.g. Jones & Forman 1992) and gravitational lensing (e.g. Smail 1993). The reader is directed to other texts for a more comprehensive evaluation of the nature of dark matter and related issues.

1.4 Current Work

Much recent effort has gone in to attempts to tie together and understand the effects outlined above. In modern times this has been facilitated with the advent of the *Hubble Space Telescope* (HST) and advances in computational power that permit more accurate simulations of clusters. The HST has provided an unrivaled tool for examination of galactic morphologies at high redshift.

1.4.1 The MORPHS Programme

Two groups attempted to analyze morphological information provided by the HST before its refurbishment (Couch et al. 1994; Dressler et al. 1994). Independently, they made preliminary connections between morphologically disturbed looking galax-

**The nearby Coma cluster of galaxies ($z \sim 0.023$; Colless & Dunn 1995), named for the constellation in which it resides, is also designated Abell 1656 (Abell 1958).

ies and blue Butcher-Oemler galaxies together with an examination of numerous elliptical galaxies possessing 'E+A' qualities (Couch et al. 1994).

Following the refurbishment of the HST, the two groups combined their efforts into what became known as the MORPHS collaboration (Smail et al. 1997). The MORPHS sample covers 11 fields in 10 clusters in the redshift range $0.37 < z < 0.56$. They demonstrated that the fraction of elliptical galaxies within the rich clusters remained near constant whilst the S0 fraction decreased with increasing redshift: a redshift evolution in the morphology-density ($T - \Sigma$) relation (Dressler et al. 1997). Meanwhile, the $T - \Sigma$ relation was generally found to be stronger in those clusters which were more relaxed and centrally concentrated. They concluded that whilst the elliptical population would have predated the gravitational collapse of a cluster, the S0 population were only generated in large numbers after this. The blue Butcher-Oemler galaxies, meanwhile, appeared morphologically disturbed and observations of their emission lines indicated that they were currently star-forming (Couch et al. 1998).

More recent work by the same collaboration concluded that recently star forming galaxies constituted ~ 20 per cent of the total population (Dressler et al. 1999). In contrast, their incidence in the field at the same redshift was found to be lower (2 per cent). Further, the frequency of recently star forming galaxies belonging to clusters at these redshifts was greater than equivalent clusters at lower redshifts and had a stronger evolution with redshift than field E+A's suggesting a strong evolution in this galaxy type. Those galaxies found to be star-forming (i.e. possessing emission lines) also exhibited a larger spatial extent and greater velocity dispersion than the passively evolving population. Correspondingly, the recently star forming galaxies exhibited qualities intermediate to the star-forming and passive populations (Dressler et al. 1999; Poggianti et al. 1999).

1.4.2 The CNOC Survey

The MORPHS collaboration is by no means the only group in this area. Another major modern study of high redshift ($z = 0.2-0.55$) clusters is that of the Canadian Network for Observational Cosmology (CNOC; e.g. Yee, Ellingson and Carlberg

1996). The primary CNOC sample is composed of 16 X-ray selected clusters of galaxies observed with the Canada-France-Hawai'i Telescope (CFHT). Over 6400 spectra have been obtained for this sample, of which over 2600 have provided a reliable redshift.

Fifteen of the CNOC clusters have been analyzed by Balogh et al. (1999). In contrast to MORPHS, they found that the fraction of star-forming galaxies only weakly increased with redshift. They further found that the recently star forming population did not increase with redshift with any significance and is not in excess to the value for the local field.

The CNOC have also examined the dependance of galaxy type with clustocentric radius: they report an absence of emission line galaxies within the cluster region correlated well with radius (Balogh et al. 1997). This correlation, however, cannot wholly be accounted for by the $T - \Sigma$ relation (Balogh et al. 1998). Several other cluster gradients have also been reported by the CNOC (Abraham et al. 1996; Morris et al. 1998) including a dependance of galaxy colour with clustocentric radius (i.e. environment). They interpreted this as an age effect whereby those galaxies at the outskirts of the cluster have younger stellar populations than those in the core region.

How is it possible to reconcile the significantly lower fraction of star-forming and post-star-forming galaxies found by the CNOC than by the MORPHS collaborations, given that their cluster samples are supposedly coeval? A number of possibilities have been explored by Ellingson et al. (2000). They attribute the discrepancies to relative differences in cluster selection technique; CNOC used X-ray selected clusters[††] whereas MORPHS used optical selection[‡‡]. The CNOC spectral data also has a lower signal-to-noise ratio than MORPHS and therefore may not be able to classify recently star forming galaxies as accurately as MORPHS.

[††]The CNOC clusters, being X-ray selected, are mostly relaxed, regular clusters, many of which contain cooling flows indicative of a lack of recent merging activity (Allen 1998).

[‡‡]The MORPHS clusters were collected over a number of years during the 1990s and are composed of both optically- and AGN-selected clusters which span a range of richness and morphology.

1.4.3 Lower Redshift

At lower redshift ($z < 0.1$) Zabludoff et al. (1996) have used the Las Campanas Redshift Survey (LCRS; Shectman et al. 1996) to find that recently star forming (E+A) galaxies in the field constitute a low fraction (0.2 per cent) of the total. This is in agreement with the CNOC team, yet is significantly smaller than that found by the MORPHS team in the field. Dressler et al. (1999) argued that the increase in recently star forming galaxies in the field is a factor of two between their two samples.

1.5 Possible Driving Mechanisms

Having outlined the case for recent cluster evolution, an obvious question presents itself: What possible mechanisms exist to drive the evolution observed and explain the resultant properties of galaxies in their given environment?

Possible mechanisms behind the evolution with redshift broadly fall into two groups. The first group contains 'hereditary' arguments, the second contains 'environmental'. As such, the debate on the mechanisms can be thought of in terms of 'nature versus nurture'. Both are briefly reviewed below.

1.5.1 Hereditary Mechanisms

In the classical hereditary scenario, the basic properties of galaxies are defined at their conception. As they grow (due to gravitational instability) out of primordial density fluctuations, aspects such as their size and their morphology manifested in proportion to the size of the initial fluctuation (e.g. Gott & Thorn 1976; Dekel & Silk 1986). Thus the ratio of collapse time to the star formation rate determines the morphology. This picture runs into difficulty when attempting to explain the preferential location of early-type galaxies at the centre of clusters. Resolution of this problem can readily be understood in terms of biased galaxy formation theory (e.g. Kaiser 1984; Silk 1985), but this still does not fully explain the observed evolution in galaxies outlined previously (Couch & Sharples 1987; Dressler et al. 1999).

1.5.2 Environmental Mechanisms

Environmental arguments provide different mechanisms to explain the observations. Assuming that initial condition considerations result in all protogalaxies being the same ($\sim$ Spiral); there are several processes that can take place which have potential to explain the observations.

One classic example is that of *ram pressure stripping* (or ram pressure ablation; Gunn & Gott 1972). On impact with the ICM, galaxies that are infalling on to the cluster have their gas removed. In the case of a spiral galaxy, the stripping of its gaseous disc would result in the creation of a lenticular cluster galaxy (Quilis, Moore & Bower 2000). Unfortunately, this mechanism does not explain the presence of S0 galaxies in low density environments.

Galaxy-galaxy interactions could also provide a mechanism for the morphological transformation of spirals into ellipticals or lenticulars (Barnes & Hernquist 1991; Toomre & Toomre 1972). Certainly there are enough strongly interacting galaxies observed to support this claim (Toomre 1978). Whilst this kind of interaction may explain some of the blue Butcher-Oemler galaxies there are certainly not enough galaxy-galaxy interactions to explain all of them (Ghigna et al. 1998; Smail et al. 1997). Moore et al. (1996) have proposed a modified form of this interaction called 'harassment' whereby just close encounters of galaxy pairs is enough to initiate morphological transmutation.

Tidal interactions may also be taking place between galaxies and the gravitational potential of the cluster itself. This process should be a more effective mechanism than ram pressure stripping in causing activity (Byrd & Valtonen 1990). Such a mechanism would, however, produce Butcher-Oemler galaxies near the cluster core (Fujita 1998) which is observationally inconsistent.

Lastly, the morphological segregation could be driven by a slow starvation of star-forming gas (Larson, Tinsley & Caldwell 1980). When a cluster ends the external gas replenishment to an infalling galaxy, that galaxy will go on using up its own internal gas until it runs out. A problem with the starvation mechanism is the inherent gentility: it does not produce enough starbursting galaxies (Oemler 1992).

Observationally, whilst the MORPHS team certainly favour an abrupt truncation of the star formation rate (Poggianti et al. 1999) to explain frequency of recently star forming galaxies, the CNOC team advocate a more steady, decline to explain the radial dependance of emission line strength (Balogh et al. 1999). Kodama & Smail (2001) report that whatever the nature of the morphological transformation mechanism, the process requires 1–3 Gyr to complete from initial infall and that clusters must necessarily have a high accretion rate. Therefore whilst the debate remains intense, the precise mechanism(s) required to drive the morphological, photometric and spectroscopic observations remains unknown.

1.6 Scope and Outline of this Thesis

Throughout this introduction attention has been paid to work investigating cluster evolution. What is clear is that in order to study galaxy evolution one requires data on all scales; from high density cluster cores out to the low density field. Although plenty of data exists separately on cluster core regions and field regions, there has been little study on the transition zone between the two. This region is crucial for understanding the evolution of the galaxy population in clusters as they grow through the accretion of field galaxies at $z \leq 1$ and hence to answer important questions regarding the origin of such basic correlations as the $T - \Sigma$ relation seen at the present day. This is the first gap in the observational dataset that this work sets out to fill.

The second noticeable gap in the current observational dataset is succinctly summed up in the words of Poggianti et al. (1999):

> '...although the existence of a strong evolution between $z \sim 0.4 - 0.5$ and $z = 0$ is well established, a dataset equivalent to the one presented in Dressler et al. (1999) does not exist for low redshift clusters and this of course limits the comparison with the present epoch.'

This work therefore seeks to map out the cluster population and chart dynamics from their cores, all the way out to where galaxies are starting to infall on to the cluster and beyond into the field at low redshifts, $z \sim 0.1$, thereby filling the

aforementioned gap. This redshift range in this work is illustrated in Figure 1.2 as the dotted vertical lines.

The outline of this thesis is as follows:

In Chapter 2 the selection of the clusters used throughout this work and the resultant optical imaging dataset from observations made at Las Campanas Observatory is described. The data reduction technique, photometric calibration and the astrometric solution is then explained in detail. The catalogue construction for the clusters is then analyzed and the star-galaxy separation technique is fully described.

To assess the accuracy of the photometric catalogues, they are directly compared to the APM catalogue in Chapter 3. Evidence for galaxies missing from the APM is presented.

Having assessed the accuracy of the survey, in Chapter 4 a statistical method is developed to define cluster membership. The environmental dependance of galaxy colours as a function of environment is then addressed by combining our homogeneous dataset into an artificial cluster.

Chapter 5 describes the spectroscopic follow-up observations made at the Anglo-Australian Telescope. The selection of spectroscopic targets is described in detail and the data reduction pipeline is examined.

In Chapter 6 analyzes the dynamics of the clusters from the spectroscopy. The velocity and spatial distributions of the clusters are mapped and mass models are used to derive cluster membership.

In Chapter 7, the spectroscopic data are analyzed in more detail. The colour-magnitude relation is re-visited and spectroscopic evidence for an environmental dependance of galaxy colours is addressed. The rest of the chapter is then devoted to an examination of the different populations of galaxies within the clusters and how they compare to the field population.

In Chapter 8 some further analysis of these data are presented; note is made of special objects within the dataset (e.g. quasi-stellar objects) and the use of the local galaxy density parameter as a tool to detect further clusters is presented.

Chapter 9 summarizes the work carried out in this thesis and provides a number of possible avenues for follow-up work.

Appendix A provides details of the method of Glazebrook et al. (1994) which is

used extensively in the data reduction pipeline (Chapter 2).

Appendix B provides details of the statistical correction technique employed in Chapter 4 and examines how this and the spectroscopic cluster membership (Chapter 6) techniques have performed. The overall success of the statistical method is assessed.

Chapter 2

Optical Imaging and Data Reduction

2.1 Abstract

Details of the mosaic observations made at optical wavelengths at the Las Campanas Observatory, Chile to fill the current gap in the observational dataset are given in this Chapter. A data reduction pipeline is developed to accurately calibrate these data and the catalogue construction is examined in depth. A robust star–galaxy separation technique is developed and the astrometric solution is obtained. The ability of these data to reliably produce morphological classifications is also examined.

2.2 A Perspective on Modern Observations

Panoramic surveys based upon systematic photographic imaging of large areas of the sky have under-pinned a large fraction of astrophysical research since the 1950s, with the three main Schmidt telescopes, at Palomar, Siding Springs and La Silla, completing at least 14 major surveys over this period. The full exploitation of these observations has been achieved through the digitization of the photographic plates on facilities such as the Automated Plate Measuring Machine (APM, Kibblewhite et al. 1984) at Cambridge, or COSMOS at Edinburgh (MacGillivray & Stobie, 1984).

While they cover impressively large areas, the photographic surveys have several drawbacks which makes them unsuitable for some applications. In particular, the low sensitivity and non-linear response of standard photographic plates means that the surveys have relatively bright surface brightness limits and require significant effort to reliably calibrate the magnitude scale over the whole range detected. In-

deed repeated scans of individual plates using the measuring machines suggests a scatter in the measured magnitudes for sources of at least ~ 0.04 mags (Maddox et al. 1990a), before other contributions are included. The relatively poor spatial resolution achieved on the Schmidt plates also limits the reliability of star–galaxy separation, placing additional restrictions on the questions which can be addressed with these data.

Panoramic imaging surveys using CCDs circumvent many of the drawbacks of photographic surveys by virtue of their high quantum efficiency and good linearity of CCD devices. Large format CCDs (and mosaic cameras) are therefore now being used to undertake wide-field surveys, whose depth, resolution and photometric precision far exceeds those achieved using photographic plates.

2.3 LARCS

The Las Campanas/AAT Rich Cluster Survey (LARCS) is one such project to take advantage of modern CCDs. The goals of LARCS are to understand the influence of environment on the characteristics of galaxies, such as star formation history and morphology. To achieve this we map the photometric, spectroscopic and dynamical properties of galaxies in rich cluster environments at $z \sim 0.1$, tracing the variation in these properties from the high-density cluster cores out into the surrounding low-density field, to a radial extent of ~ 10 Mpc at $z \sim 0.1$. This represents the era of change seen in the Butcher-Oemler plot (see figure 1.2), where a population of blue, star forming galaxies apparently disappear from the cores of rich clusters. For the most massive clusters at $z \sim 0.1$, the turn-around radius corresponds to roughly 1 degree and therefore one requires panoramic CCD imaging covering 2-degree diameter fields, as well as spectroscopic coverage of similar fields. The former is achieved by mosaicing CCD images from the 1-m Swope telescope at Las Campanas Observatory, whilst the latter comes from the subsequent spectroscopic follow-up with the 400-fibre 2dF multi-object spectrograph on the 3.9-m Anglo-Australian Telescope (AAT).

2.4 Cluster Selection

To facilitate comparisons of the observational results other groups, the cluster sample must be selected in a well defined and quantified manner with criteria which can be easily applied to theoretical simulations.

Historically, clusters of galaxies were selected from optical imaging (e.g. Abell 1958; Abell, Corwin & Olowin 1989; ACO). However, such optical selection is likely to be degraded by projection effects (superpositions of structures and surface density fluctuations) which can lead to an over-estimate of a cluster's richness. However, X-ray selection can overcome such projection effects. X-rays are emitted from the hot ($\sim 10^{7-8}$ K) intracluster medium (ICM) via thermal bremsstrahlung. The presence of these X-rays indicate that the system is gravitationally-bound in three dimensions. As the X-ray flux is proportional to the square of the electron density, X-ray selection is less prone to projection effects*: in order to be mistaken for a single more luminous object, a superposition of clusters must be well aligned along the line of sight and to reach a fixed luminosity, they need to have a stronger contamination. If there is a superposition present in optical bands, then $N_{Cl} \equiv N_1 + N_2$ where N_i is the galaxy number count for the given components. In X-rays bands, the number of X-ray photons detected, $N_{X-ray} = N^2_{Optical}$, thus $\Delta_{Cl} = N^2_{Cl} > N^2_1 + N^2_2$. Therefore quantitatively X-ray selection is an improved way to give an unbiased cluster selection which is also easy to apply to (smooth particle) hydrodynamic simulations.

The cluster sample used for LARCS is the X-ray Brightest Abell Clusters (XBACs; Ebeling et al. 1996). XBACs is an All-Sky, flux limited X-ray, sample of 242 Abell clusters of galaxies compiled from the ROSAT All-Sky Survey data set; effectively a volume-limited sample of rich clusters. As it is based upon the Abell catalogue, it is only as complete the parent catalogue: up to $z = 0.08$ (Dalton, priv. comm.). At most, XBACs misses 20 per cent of clusters in this redshift and L_X range, although this figure is realistically more like 10 per cent (Ebeling et al. 1998; Edge priv.

*There are only a small number of cases known where X-ray superposition has led to two or more clusters being misidentified as a single more luminous one; e.g. Abell 2572 (Ebeling, Mendes de Oliveira, & White 1995) and Abell 2152 (Blakeslee et al. 2001).

comm.).

LARCS selection used the following criteria to select it's clusters from XBACs :

- The clusters must be found in the parent Abell (1958) catalogue.
- $\delta \leq 10\,\mathrm{deg}$. Thus making them visible from both the Las Campanas Observatory (LCO) and the Anglo-Australian Observatory (AAO). The size is particularly suited to the 2dF spectrograph for obtaining spectra.
- $L_X \geq 3.7 \times 10^{44}\mathrm{erg\,s^{-1}}$. This represents only the most massive clusters, $M_{Cluster} \geq M_{Coma}$.
- $0.07 \leq z \leq 0.16$. This is matched to the transitory epoch of the Butcher-Oemler effect (Figure 1.2) as well as matching the median redshift of the Galaxy Redshift Survey (2dFGRS; Colless et al. 2001; see Chapter 3). This redshift range means that the sample is effectively volume-limited.

Applying the criteria listed above to XBACs gives a total of 53 clusters. Limitations of telescope time allocated to the project, the times of the year allocated and adverse weather conditions resulted in only 21 of these 53 clusters being observed (Table 2.1). These 21 clusters then define the sample used by LARCS and are considered to be representative of the 53 possible.

2.5 Observations

The LARCS project has completed panoramic (2×2 degree^2) B and R broad-band imaging of 21 clusters from the 1-m Swope telescope at Las Campanas Observatory, Chile, totaling over 70 square degrees of sky (O'Hely et al. 1998, O'Hely 2000) equivalent to $\sim$ 50 gigabytes of raw data. Of these observations, Abell 2811, 2345, 3814 and 2496 were not observed to the full 2 degrees and are only included in Table 2.1 for the sake of completeness.

Optical imaging of the clusters provided the backbone to the LARCS project. High quality broad-band B and R CCD images of all the clusters have been obtained over the course of three years: 1996-1998. The transmission of the broad-band filters used is displayed in Figure 2.1. The R-band filter's central wavelength is $\lambda = 6100$Å.

Table 2.1: Details of the 21 clusters in the LARCS sample and the multi-wavelength observations of these obtained. The column headed 'Passbands' indicates the broad band filters used to observe each cluster.

Cluster	R.A. (J2000)	Dec.	z	L_X (erg s^{-1})	Passbands	Diameter (deg.)
A22	00 20 38.64	−25 43 19	0.131	5.31	B/R	2.0
A550	05 52 51.84	−21 03 54	0.125	7.06	B/R	2.0
A644	08 17 25.20	−07 31 41	0.071	7.92	B/R	2.0
A1084	10 44 30.72	−07 05 02	0.134	7.42	B/R	2.0
A1285	11 30 20.64	−14 34 30	0.106	5.47	B/R	2.0
A1437	12 00 25.44	+03 21 04	0.133	7.72	B/R	2.0
A1650	12 58 41.76	−01 45 22	0.084	7.81	B/R	2.0
A1651	12 59 24.00	−04 11 20	0.084	8.25	B/R	2.0
A1664	13 03 44.16	−24 15 22	0.127	5.36	B/R	2.0
A2055	15 18 41.28	+06 12 40	0.102	4.78	B/R	2.0
A2104	15 40 06.48	−03 18 22	0.155	7.89	B/R	2.0
A2204	16 32 46.80	+05 34 26	0.152	20.58	B/R	2.0
A2597	23 25 16.56	−12 07 26	0.085	7.97	B/R	2.0
A3112	03 17 56.40	−44 14 17	0.070	7.70	B/R	2.0
A3378	06 05 52.80	−35 18 04	0.141	6.87	B/R	2.0
A3888	22 34 32.88	−37 43 59	0.151	14.52	B/R	2.0
A3921	22 49 59.76	−64 25 52	0.095	5.40	B/R	2.0
A2811	00 42 07.92	−28 32 10	0.108	5.43	$U/B/R/K$	0.6
A2345	21 26 58.56	−12 08 28	0.176	9.93	$U/B/R/K$	0.6
A3814	21 49 06.48	−30 41 53	0.117	3.85	$U/B/R/K$	0.6
A2496	22 50 55.92	−16 23 35	0.122	3.71	$U/B/R/K$	0.6

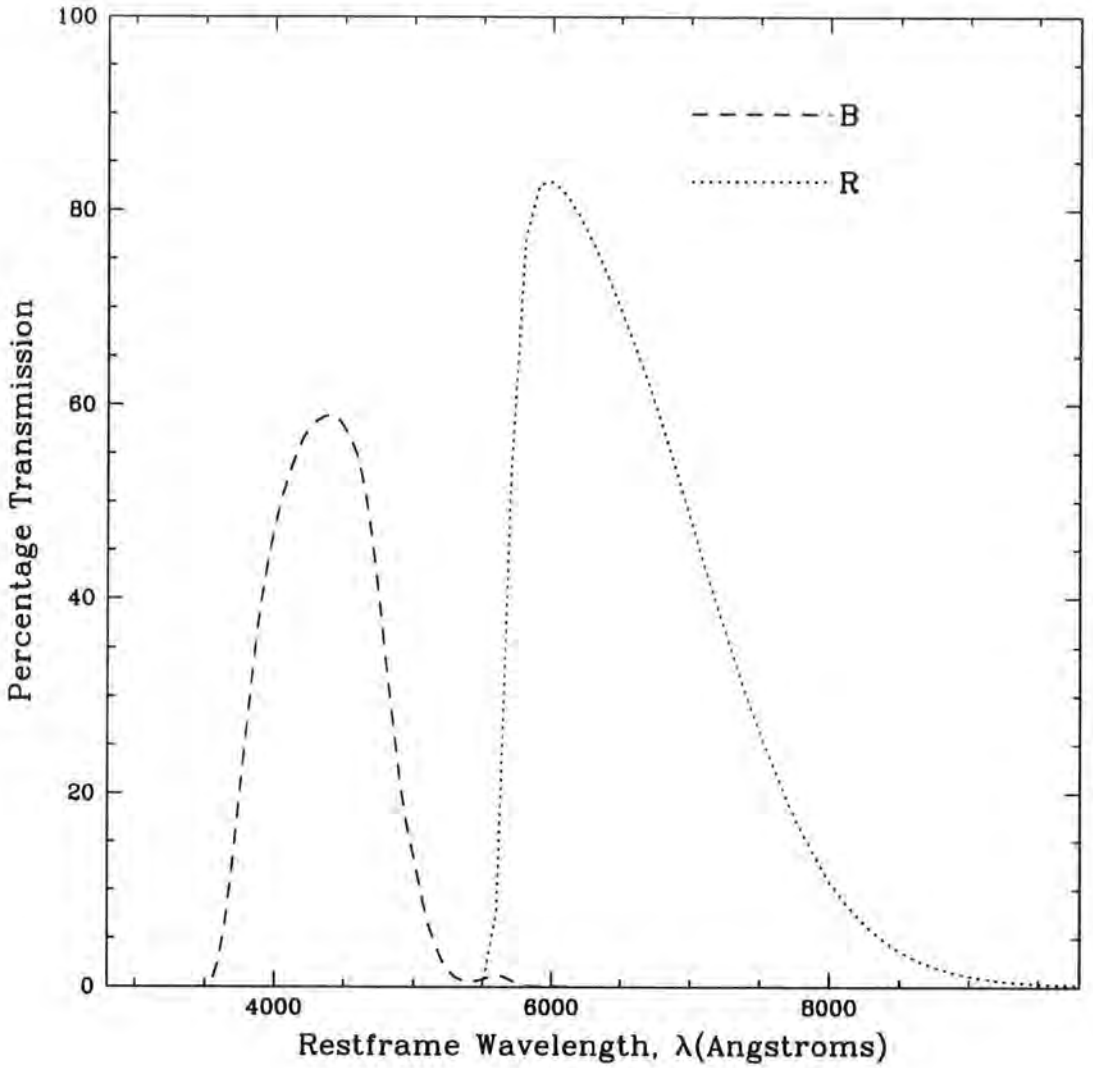

Figure 2.1: The response curves for the broad-band B (dashed line) and R (dotted line) filters used by LARCS. The data used to create this plot has been sourced from publically available data published by LCO at http://www.ociw.edu/lco/

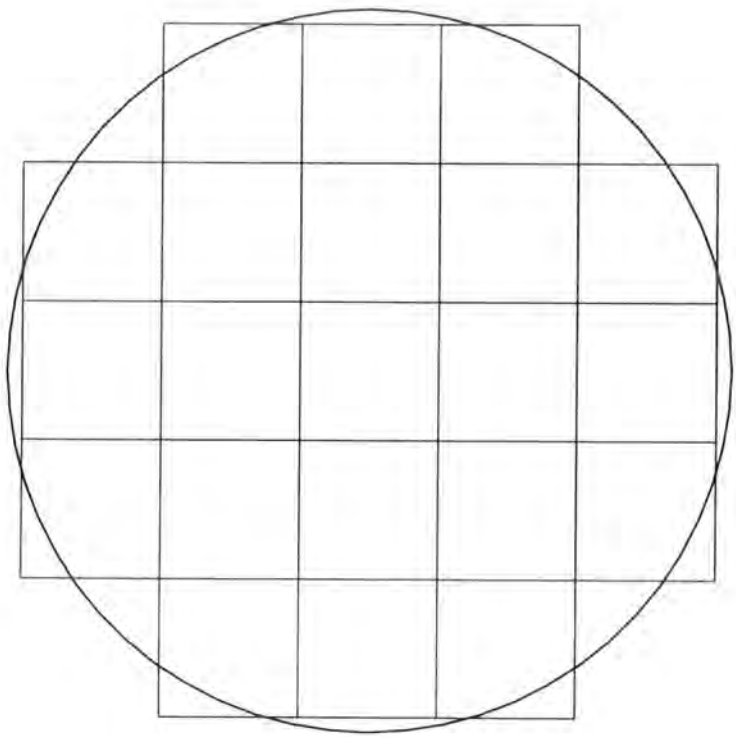

Figure 2.2: A graphical representation of the mosaic observational strategy used in LARCS. The circle represents a 2 degree diameter on the sky. Imaging a field of this size required a mosaic of 21 pointings, creating a 5×5 square grid without the corners. Each mosaic tile is 23 sq arcmin and had an overlap of 44 arcsec with each neighbouring frame in order to tie together photometry and astrometry across the entire field.

	LARCS
Tek5	2048 × 2048 pixels, 24μm
Pixel Size	0.696"/pixel
Gain	1.73 electrons / DN
Field of View	23.76 × 23.76 arcmin
Quantum Efficiency	B (75%), R (74%)
Readout time	83 seconds

Table 2.2: Instrumentational Details.

This gives sensitivity to older stars and hence early-type galaxies as most light at these wavelengths sources from old, red giant stars. The B-band filter's central wavelength is $\lambda = 4400$Å. Its sensitivity is to younger galaxies, whose light is dominated by young stars / star-formation. The observations made are summized in Table 2.1 The observations have been secured at Las Campanas Observatory (LCO) using the 1-m Swope telescope in conjunction with a thinned 2048 × 2048, 24μm pixel Tektronics CCD camera. The pixel scale used is 0.696″/pixel, giving a field of view for each exposure of 23.76′ × 23.76′. Further instrumental details are given in Table 2.2. Each cluster is constructed of a mosaic of 21 such exposures in a pattern of a 5 × 5 grid minus the corner tiles. With a built-in inter-exposure overlap of 44″ to tie together the photometry and astrometry, the total coverage of the resultant mosaic image is ∼ 2 degrees diameter. The layout of a mosaic is illustrated in Figure 2.2.

The total exposure time per pointing is typically 500s in B and 400s in R, each split into two spatially-offset (15 arcsec) sub-exposures to facilitate cosmic-ray rejection and the removal of a small number of cosmetic features. Table 2.3 gives a more detailed breakdown of the observations made at the LCO.

Table 2.3: Log of LCO imaging observations made for the clusters used in this work. The date each observation was made on is shown with the passbands used, number of pointings (out of a total of 21 required for the mosaic), seeing, exposure time and whether the observations were undertaken in photometric conditions.

Cluster	Date	Passband	N(point)	Seeing (″)	Exposure Time (s)	Phot?
Abell 22	Aug 20 1996	*R*	3	1.0–1.1	400	yes
	Aug 21 1996	*R*	6	1.1–1.3	400	yes
	Aug 22 1996	*R*	12	1.0–1.4	400	yes
	Aug 21 1996	*B*	15	1.0–1.1	500	yes
	Aug 22 1996	*B*	6	1.0–1.1	500	yes
Abell 550	Feb 14 1997	*R*	12	1.0–1.3	500	yes
	Feb 15 1997	*R*	1	1.3	500	yes
	Feb 16 1997	*R*	8	1.0–1.2	500	partial
	Feb 10 1997	*B*	3	1.1–1.3	700	yes
	Feb 11 1997	*B*	7	1.0–1.1	700	yes
	Feb 12 1997	*B*	7	1.0–1.1	700	yes
	Feb 13 1997	*B*	4	1.0–1.1	700	partial
Abell 644	Mar 19 1996	*R*	10	1.0–1.6	400	no
	Mar 20 1996	*R*	11	1.0–1.5	400	partial
	Mar 16 1996	*B*	10	1.1–1.5	600	yes
	Mar 17 1996	*B*	5	1.5–2.0	600	yes
	Mar 18 1996	*B*	6	1.1–1.2	600	yes
Abell 1084	Mar 20 1996	*R*	10	1.1–1.8	400	no
	Mar 21 1996	*R*	11	1.0–1.2	400	partial
	Mar 17 1996	*B*	10	1.4–1.9	500	yes
	Mar 18 1996	*B*	11	1.1–2.1	500	yes
Abell 1285	Feb 14 1997	*R*	10	1.1–1.2	500	yes
	Feb 15 1997	*R*	5	1.7–1.8	500	yes

...continued from previous page

Cluster	Date	Passband	N(point)	Seeing (″)	Exposure Time (s)	Phot?
	Feb 16 1997	*R*	6	1.3–1.7	500	partial
	Feb 11 1997	*B*	7	1.1–1.4	600	yes
	Feb 12 1997	*B*	10	1.4–1.8	500	yes
	Feb 13 1997	*B*	4	1.6–1.7	500	no
Abell 1437	Feb 15 1997	*R*	13	1.3–1.5	500	yes
	Feb 16 1997	*R*	8	1.5–1.7	500	no
	Feb 10 1997	*B*	8	1.3–1.7	700	yes
	Feb 11 1997	*B*	2	1.0–1.2	700	yes
	Feb 12 1997	*B*	3	1.2–1.5	700	yes
	Feb 13 1997	*B*	8	1.2–1.4	700	partial
Abell 1650	Mar 20 1996	*R*	21	1.0–1.2	400	partial
	Mar 16 1996	*B*	15	1.1–1.7	500	yes
	Mar 22 1996	*B*	6	1.2–2.3	500	yes
Abell 1651	Mar 21 1996	*R*	21	1.0–1.1	400	partial
	Mar 17 1996	*B*	21	1.1–1.4	500	yes
Abell 1664	Mar 22 1996	*R*	21	1.0–1.7	400	partial
	Mar 18 1996	*B*	21	1.0–1.6	500	yes
Abell 2055	Mar 20 1996	*R*	9	1.1–1.2	400	partial
	Mar 21 1996	*R*	12	1.0–1.2	400	partial
	Mar 16 1996	*B*	9	1.4–1.9	500	yes
	Mar 17 1996	*B*	5	1.2–1.4	500	yes
	Mar 18 1996	*B*	6	1.3–1.5	500	yes
Abell 2104	Aug 19 1996	*R*	11	1.3–2.3	400	yes
	Aug 20 1996	*R*	10	1.4–1.9	400	partial
	Aug 15 1996	*B*	6	1.3–1.6	500	yes
	Aug 16 1996	*B*	9	1.2–1.6	500	yes
	Aug 17 1996	*B*	6	1.3–1.6	500	partial
Abell 2204	Aug 20 1996	*R*	1	1.6	400	yes

...continued from previous page

Cluster	Date	Passband	N(point)	Seeing (″)	Exposure Time (s)	Phot?
	Aug 21 1996	*R*	10	1.1–1.5	400	yes
	Aug 22 1996	*R*	10	1.1–1.4	400	yes
	Aug 17 1996	*B*	3	1.4–1.6	500	yes
	Aug 18 1996	*B*	10	1.1–1.5	500	yes
Abell 2597	Aug 19 1996	*R*	11	1.7–2.1	400	yes
	Aug 20 1996	*R*	10	1.4–1.9	400	yes
	Aug 16 1996	*B*	10	1.3–1.7	500	yes
	Aug 17 1996	*B*	11	1.5–1.7	500	partial
Abell 3112	Aug 18 1996	*R*	6	1.7–2.0	400	yes
	Aug 19 1996	*R*	9	2.0–2.5	400	yes
	Aug 20 1996	*R*	6	1.5–2.1	400	partial
	Aug 15 1996	*B*	8	1.3–1.5	500	yes
	Aug 16 1996	*B*	2	1.5–1.7	500	yes
	Aug 17 1996	*B*	5	1.4–1.8	500	partial
	Aug 18 1996	*B*	6	1.6–2.0	500	yes
Abell 3378	Feb 15 1997	*R*	10	1.3–1.5	600	yes
	Feb 11 1997	*B*	4	1.3–1.8	750	yes
	Feb 12 1997	*B*	6	1.4–1.8	750	yes
Abell 3888	Aug 18 1996	*R*	19	1.4–1.8	400	yes
	Aug 15 1996	*B*	21	1.2–1.6	500	yes
Abell 3921	Aug 19 1996	*R*	10	1.5–1.8	400	yes
	Aug 20 1996	*R*	11	1.5–2.1	400	partial

2.6 Basic Reduction

The imaging data are reduced using packages within IRAF on the University of Durham's STARLINK computing facilities. Before a CCD image can be utilized for

scientific purposes, it has to be successfully corrected for flatfield and bias variations. Such variations arise naturally from the CCD hardware e.g.: variations in the CCD sensitivity across the chip. The task IMPLOT is used to read off the size of each observation and the bias section. The COLBIAS task is used to measure the bias section off each observation, subtract the bias from them and trim the observation.

Several twilight flats are taken on each night of observations. These are median averaged using IMCOMBINE to create a skyflat. The science observations are then flatfielded by dividing them by the skyflat using the IMARITH task. To check the accuracy of the flatfielding, a superflat is constructed for each night by stacking together the science observations. This superflat is utilized to remove vignetting from the observations by using the IMSURFIT task to fit a surface function to a smoothed version of the superflat. To test the accuracy of the flatfielding, the IMSTAT task is used to obtain the mean background levels at various locations on each mosaic tile. The variation in the sky background is found to be ≤ 1 percent in all cases. Bad pixels within each of the observations are then dealt with by interpolating over them using the FIXPIX command.

The science frames are finally constructed from the two spatially offset flatfielded observations. These sub-images are first aligned using the IMALIGN task, fed with information about the offset (in pixels) of the two sub-exposures and a coordinate list of ~ 10 bright stellar sources from the base sub-image. The accuracy of the alignment process is accurate to better than $\ll 0.5$ pixels in all cases.

A script originally coded by Smail and subsequently modified by Pimbblet is used to combine the two, now aligned, sub-exposures. A pair of coadded images are created: the first of these is a straight coaddition using the basic IMCOMBINE task. The second uses the same task, but with the **crreject** algorithm active. The **crreject** algorithm rejects cosmic rays by removing high pixel values that are above the saturation level of the CCD chip. The downside of this algorithm is that it not only rejects true cosmic rays but also artificially truncates the brighter objects. To rectify this, a difference image is created via subtraction of the crreject image from the straight coadded image using IMARITH. The difference image therefore contains the cosmic rays and all truncated sources.

The **crreject** image is then median smoothed and an image mask is created

from it. The image mask has blank sky (including smoothed-over cosmic rays) set to zero and the previously truncated objects set to one. Using IMARITH, the difference image is then multiplied by the mask image to create a new image in which the true cosmic rays are rejected but the erroneously truncated sources are still included. This product image is then added to the original **crreject** image so that all of the true cosmic rays are rejected and the erroneously truncated high pixel value objects are restored to the image. The new coadded images are inspected after creation. Occasionally it is found that a number of cosmic rays are still present as they have fallen onto an object in the original observations. These remaining cosmic rays total about one percent of the original number of cosmic rays present.

2.7 Seeing Matching

Seeing, caused by the Earth's atmosphere, results in the blurring of science observations. Before construction of the object catalogues, it is necessary to match the seeing of the B and R-band mosaic tiles so that reliable aperture colours can be measured. The seeing matching is achieved by degrading the mosaic tile with the superior (i.e. numerically lower) seeing to that of the inferior. Although some attempts had been made to model and predict quantitatively how much degrading would be required on a given pair of tiles, it is found that an iterative method produces the optimal results.

A first pass of SExtractor (Bertin & Arnouts 1996) is used to obtain a rough list of stellar sources on the R-band mosaic tiles by taking objects that has a CLASS_STAR (P^*) > 0.9. The seeing of the B and R-band mosaic tiles is estimated from the median value of the full-width at half-maximum (FWHM) of these stellar sources, measured with the IMEXAMINE task. An initial estimate of the value used to convolve the superior seeing mosaic tile (typically the R-band imaging) to the inferior one, σ, is then made and applied using the GAUSS task to create a new, degraded mosaic tile. The median seeing for the stars on the degraded tile is then re-measured using the IMEXAMINE task. This process is repeated iteratively to determine the correct value for σ (within the 1-σ scatter of the median FWHM) to match the seeing on the two tiles. Prior to convolution, differences of up to $1''$ are

found to be present between the median FWHM of the B and R-band mosaic tiles. After convolution, the median seeing in both bands is within $\leq 0.1''$ (less than 0.1 pixels) and colours can reliably be measured.

2.8 Cataloguing

SExtractor is used to automatically analyze the mosaic tiles, detect sources and parametrise them. The R-band mosaic tiles are catalogued by detecting sources having more than 12 contiguous pixels each 3σ of the sky above the background, equivalent to $\mu_R \sim 23.3$ mag. arcsec^{-2}. The resulting catalogues have 5σ detection limits for galaxies of $R = 21.1 - 21.3$. Spurious sources, such as satellite trails and diffraction spikes from bright stars can enhance the background flux enough to cause SExtractor to detect them as objects in their own right. Therefore these objects are cleaned manually from the resultant catalogues by visual inspection of the detections overlayed on the science observations. Only a small number of objects, $N \sim 10$, are deleted per mosaic tile in this manner.

To derive colours for these sources, the task PHOT is used to measure magnitudes in $4''$ diameter apertures (typically $\sim$ 10kpc at the cluster redshifts) from the seeing-matched B and R-band mosaic tiles. PHOT is used in preference to SExtractor's measure of the aperture magnitudes as it is more readily automated.

2.9 Photometry

Each mosaic tile is calibrated from observations of selected areas of standard stars selected from Landolt (1992), interspaced throughout each night in the observing runs at the LCO. The selected areas used are chosen for their large number of standard stars and variation in colour, e.g. SA101, SA104 and PG0231+51. Typically over 100 individual standard stars are observed and tracked for each broad-band filter used per night. Landolt (1992) uses a 14" aperture and a photomultiplier to measure magnitudes ($B_{Landolt}$) in. The LARCS project uses the same size aperture, but measures its magnitudes, B_{LARCS}, with a CCD instead of a photomultiplier. Thus, the response curves of Landolt (1992) and the LARCS project are not the

same. Calibration is made to the Landolt (1992) standards so that $B_{True} = B_{Landolt}$. In the following, the calibration for the B-band is described; the calibration for the R-band is equivalent.

A colour term (a function of the CCD chip and the filters used in the observations) is fitted for each night by taking $\sim$ 60 standard stars observed at a fixed airmass. At a fixed airmass, $B_{True} - B_{LARCS} = D + A(B - R)$, where $B_{LARCS} = B_0^{'} - 2.5log_{10}(DN/S)$ (the magnitudes are given by PHOT using an arbitrary zeropoint of $B_0^{'} = 30$). The colour term, A, is obtained by measuring the slope of the best fit line through the plot using POLYFIT within IRAF. Several weightings are applied to the fit (e.g. instrumental and uniform), outliers deleted and the best value is chosen. The colours of Landolt's standard stars are corrected to an effective colour of $(B - R) = 0$. The solution for the standard stars is of the form $B_{True} = B_0 + CsecZ + A(B - R) - 2.5log_{10}(DN/S)$, where B_0 is the zeropoint, $CsecZ$ is the extinction, $A(B - R)$ is the colour term and the logarithmic term is the flux where S is the exposure time of the image and DN is the count. An example of a fit for the colour term is shown in Figure 2.3

Atmospheric extinction (arising from light travelling through the atmosphere at different air-masses; a function of the position of the target cluster on the sky at the time of the observations) is accounted for by fitting to the variation of the standard stars photometry in one night with airmass. To obtain the correction due to extinction, a plot of the residuals of correcting the standard stars to $(B - R) = 0$ versus $secZ$ for all the standard fields is made. Because $B_{LARCS}^{B-R=0} = B_0 - 2.5log_{10}(DN/S) + A(B - R) = \Delta B_0 + CsecZ$, a plot of $B_{Landolt} - B_{LARCS}^{B-R=0} = B_{Landolt} - B_{LARCS} - A(B - R)$ yields the extinction term and the zeropoint offset, ΔB_0 (where $B_{LARCS}^{B-R=0}$ is the effective magnitude for a $B - R = 0$ standard star). An example of a fit for the extinction term and zeropoint offset is displayed in Figure 2.4.

The ultimate solution obtained is of the form :

$$B_{True} \equiv B_{Landolt} = B_0^{'} + \Delta B_0 + CsecZ + A(B - R) - 2.5log_{10}(DN/S)$$

On photometric nights, the variation in the extinction coefficient and colour term are all within 1σ of each other. The photometric solutions for the photometric nights are typically accurate to better than 0.04 mags.

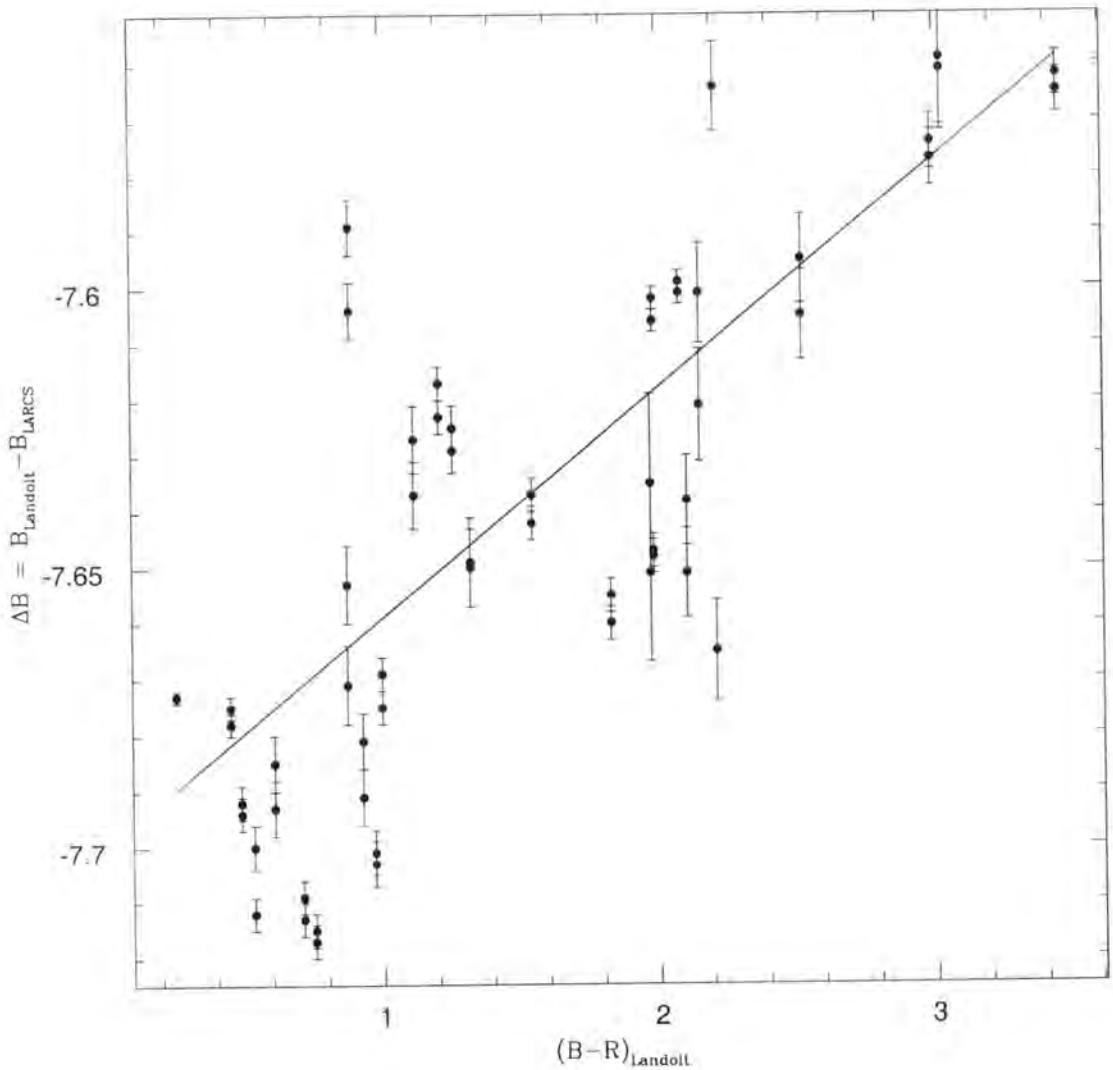

Figure 2.3: The line of fit calculated for the color term of the night of 16/March/1996. With the airmass fixed at 1.15 atmospheres, 57 standard stars are analyzed. The fitted line has the form : $\Delta B = -7.700 \pm 0.007 \times (B-R)_{Landolt} + 0.041 \pm 0.004$. This night is deemed to be photometric.

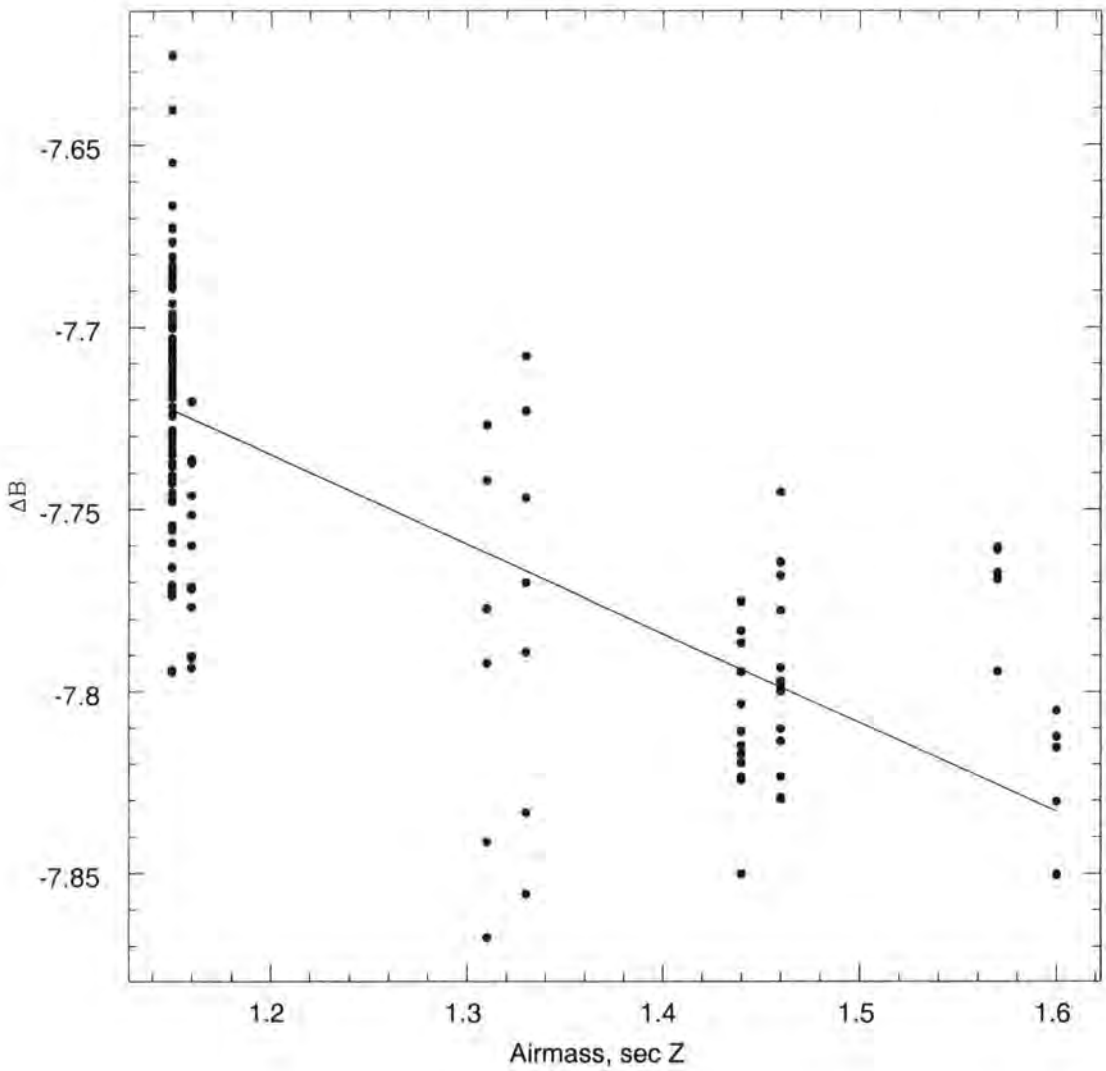

Figure 2.4: The line of fit calculated for the zeropoint and extinction term for the night of 16/March/1996. The fitted line has the form : $\Delta B = -0.245 \pm 0.002 \times secZ - 7.441 \pm 0.002$.

As some of the observations are made in non-photometric conditions it is necessary to independently calibrate such pointings. To achieve this the photometry of sources appearing in the 44″ inter-pointing overlap regions is used to determine the magnitude offset between the non-photometric and photometric pointings in each passband. Only those sources which are unsaturated, not heavily blended or close to the chip's edge are used to obtain these values. To optimally employ magnitude offset information across the whole mosaic the method of Glazebrook et al. (1994, G94) is implemented. G94 is described in detail in Appendix A, below it is briefly reviewed.

Using a single step algorithm, G94 generates appropriate magnitude offsets to be applied to the non-photometric pointings, whilst keeping the zero-points of the photometric pointings fixed. After application of G94 it is estimated that the typical tile-to-tile variation in zero-points is ≤ 0.006 mags, as estimated from the scatter in the magnitude offsets from the duplicated sources in the overlapping regions. The maximum deviations between tiles is ~ 0.015 mags.

Figures 2.5 and 2.6 show the zeropoint offsets between each pointing of an example (non-photometric) mosaic as a grey-scale before and after correction using the G94 algorithm. As can be seen, after calibration the entire mosaic is close to uniform, with a pointing-to-pointing rms of only 0.005 mags.

2.10 Star–Galaxy Separation

Accurate star–galaxy separation is essential in extragalactic surveys. Robust separation is vital for minimizing stellar contamination, while at the same time retaining compact galaxies, and optimising the efficiency of spectroscopic follow-up of the survey.

Following Reid et al. (1996) a plot is constructed of the magnitude difference between 4.0″ and 2.0″ diameter apertures ($\Delta_{2''-4''}$) on the B-band exposures, versus total B magnitude (Fig. 2.7). In such a diagram stars should trace a horizontal locus due to their fixed profile shape (the telescope PSF) and hence fixed proportion of light in the two apertures. The horizontal sequence is seen in Figure 2.7 at $\Delta_{2''-4''} \sim 0.1$. Equally, galaxies, which exhibit a range of more extended profile

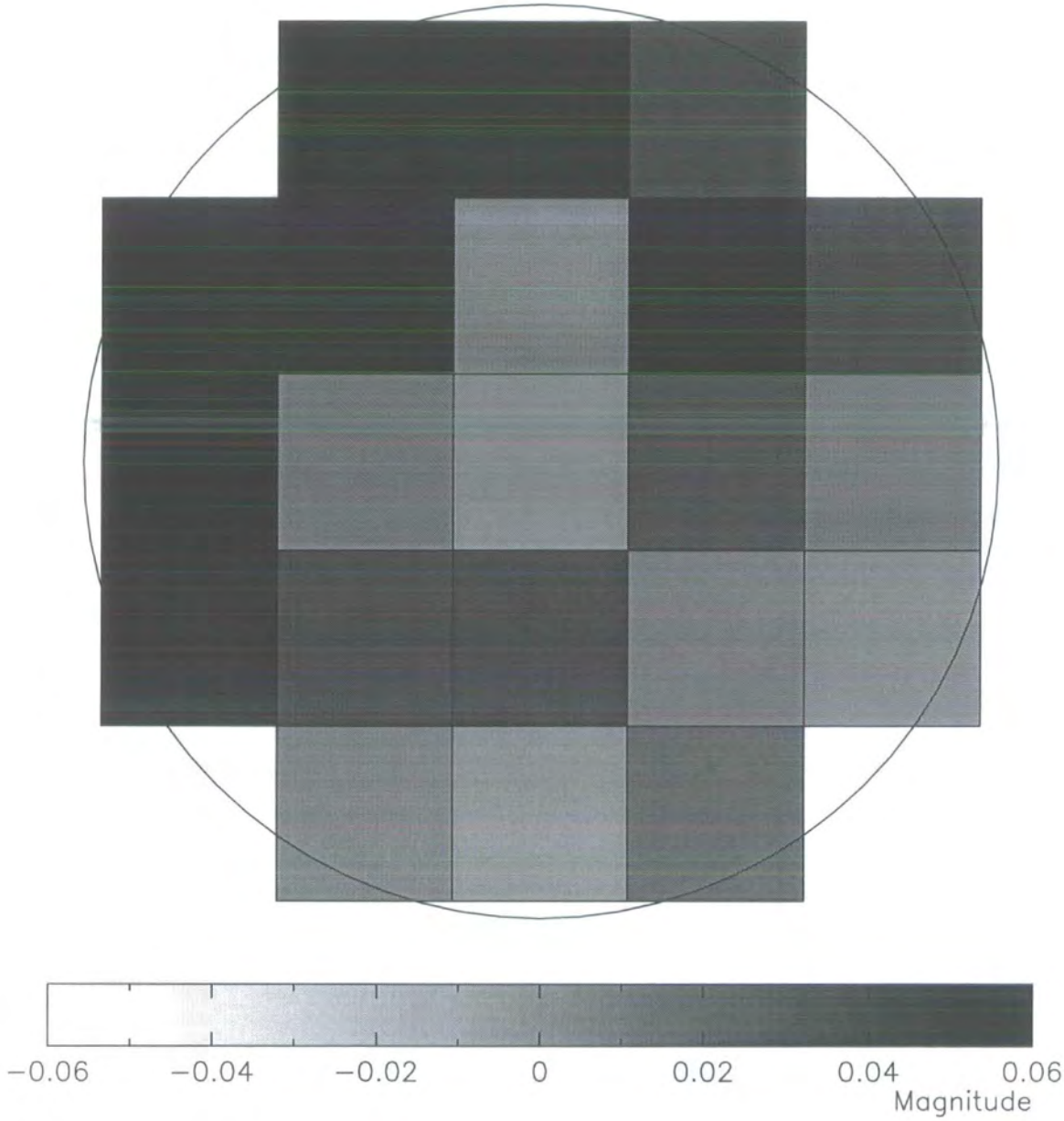

Figure 2.5: Grey-scale of the zeropoint offsets between the different pointings within the R-band mosaic of Abell 1651. The range of offsets is given by the scale at the bottom. This mosaic is non-photometric and shows a range of over 0.06 magnitudes existing across the mosaic and an rms of 0.02 mags. The circle has a diameter representing 2 degrees on the sky.

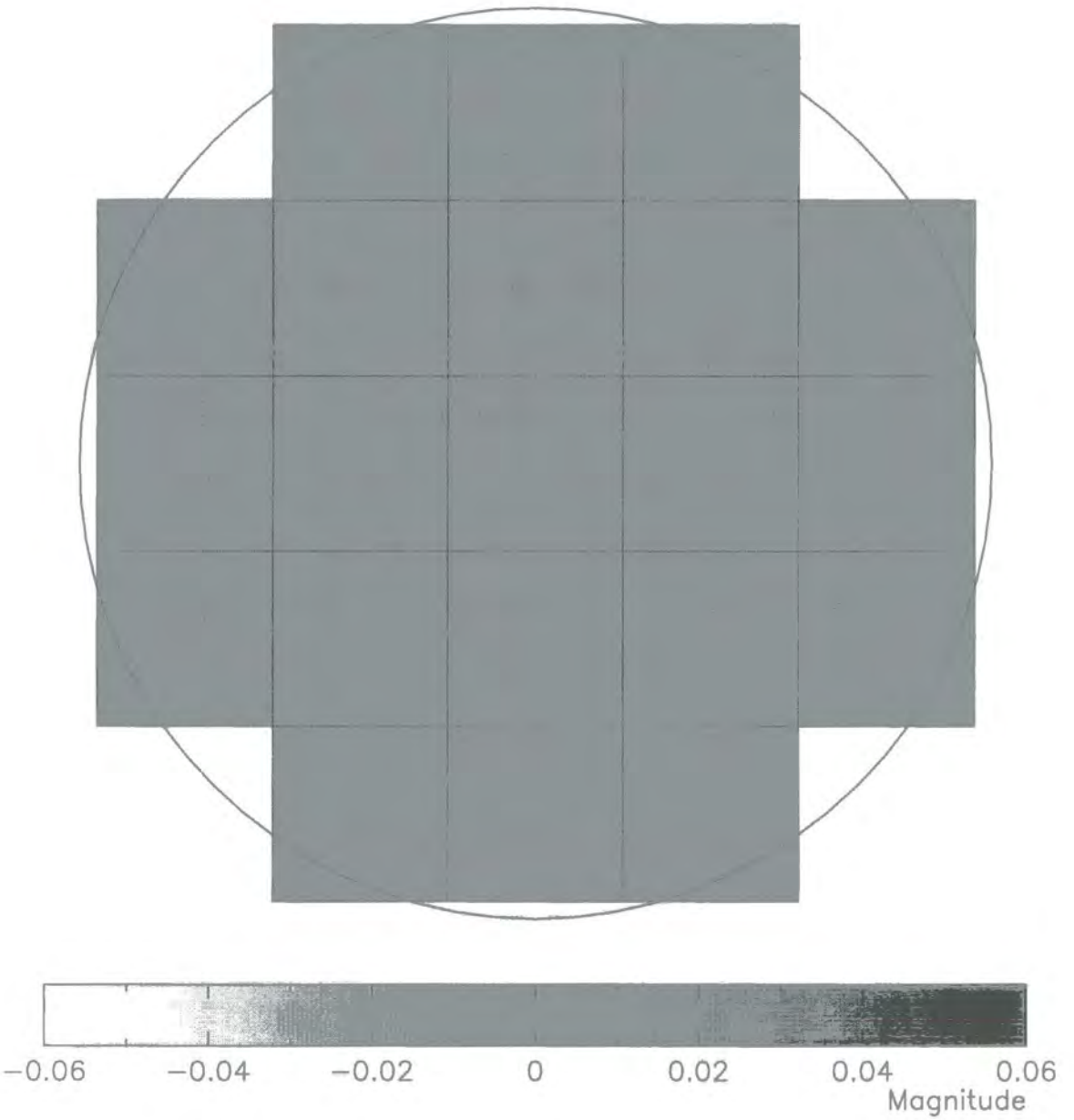

Figure 2.6: As for Figure 2.5 but after application of the iterative corrections from Glazebrook et al. (1994) – the pointing-to-pointing rms is reduced to ≤ 0.005 mag.

shapes, will show a wider range of $\Delta_{2''-4''}$ values. Close to the completeness limit of the frames the galaxy and star loci overlap due to low signal to noise. Examination of Fig. 2.7 reveals that the CCD imaging can readily differentiate stars from galaxies down to a magnitude of at least $B \sim 20.5$.

Examination of the potential of four further parameters generated from the LARCS imaging for usage in star–galaxy is now undertaken. Ellipticity is obtained from SExtractor's estimates of the semi-major and semi-minor axes for sources. The CLASS_STAR parameter (P^*) is SExtractor's[†] own estimate of stellarity and uses shape information fed into a neural-network classifier that has been trained a priori on other images. Finally, two estimates of the compactness of the image profile are used: the concentration index (Abraham et al. 1994) and FWHM. Plotted in Figure 2.8 are these critical parameters for both stars and galaxies from Abell 22. The other clusters follow the same distribution of sources on these planes. For the ellipticity and concentration index the stars and galaxies, as defined with the $\Delta_{2''-4''}$ cut, overlap somewhat, whilst the converse is true for P^* and the FWHM measurements. Therefore both the FWHM and P^* are useful in differentiating stars and galaxies.

Three criteria are used to generate robust and stringent definition of galaxies: $\Delta_{2''-4''} > 0.2$, FWHM > 2" and $P^* < 0.1$. In adopting these criteria, one must accept that a small number of stars and galaxies will be mis-classified. However, as demonstrated in Figures 2.7 and 2.8 the number of stellar sources fulfilling these rigorous criteria is small, ≤ 3 percent.

2.11 Astrometry

Accurate astrometrical solutions are essential to a project of this scope. The solutions found are a vital ingredient in constructing our own catalogues. The objects existing in the inter-tile overlaps in the mosaics need to be compared and then duplications efficiently removed. They are also vital in the subsequent followup observations using the 2dF device (see Chapter 5) and for comparison to other datasets (e.g. the APM/GRS, see Chapter 3). Indeed, the 2dF device requires as

[†]SExtractor uses a 3 pixel^2 convolution kernel for source detection.

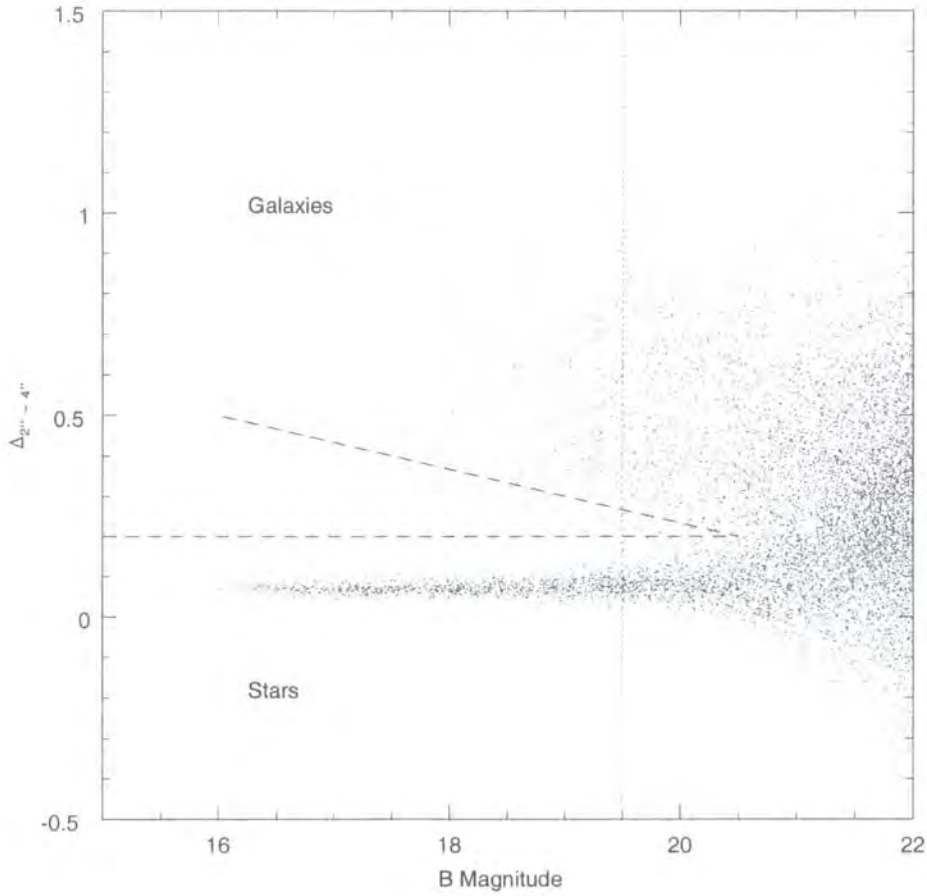

Figure 2.7: Difference between the 2.0″ and 4.0″ aperture magnitudes, ($\Delta_{2''-4''}$) versus total magnitudes for all 31,851 sources within the LARCS Abell 22 catalogue. The stellar sources are those with $\Delta_{2''-4''} \sim 0.1$–$0.2$. Galaxies typically shower larger values of $\Delta_{2''-4''}$. Our CCD imaging readily differentiates between stars and galaxies down to $B \sim 20.5$, beyond the magnitude limit of the GRS/APM catalogue. For the analysis of star-galaxy separation only those sources brighter than $B = 19.5$ are used. Those with $\Delta_{2''-4''} < 0.2$ are defined as stellar.

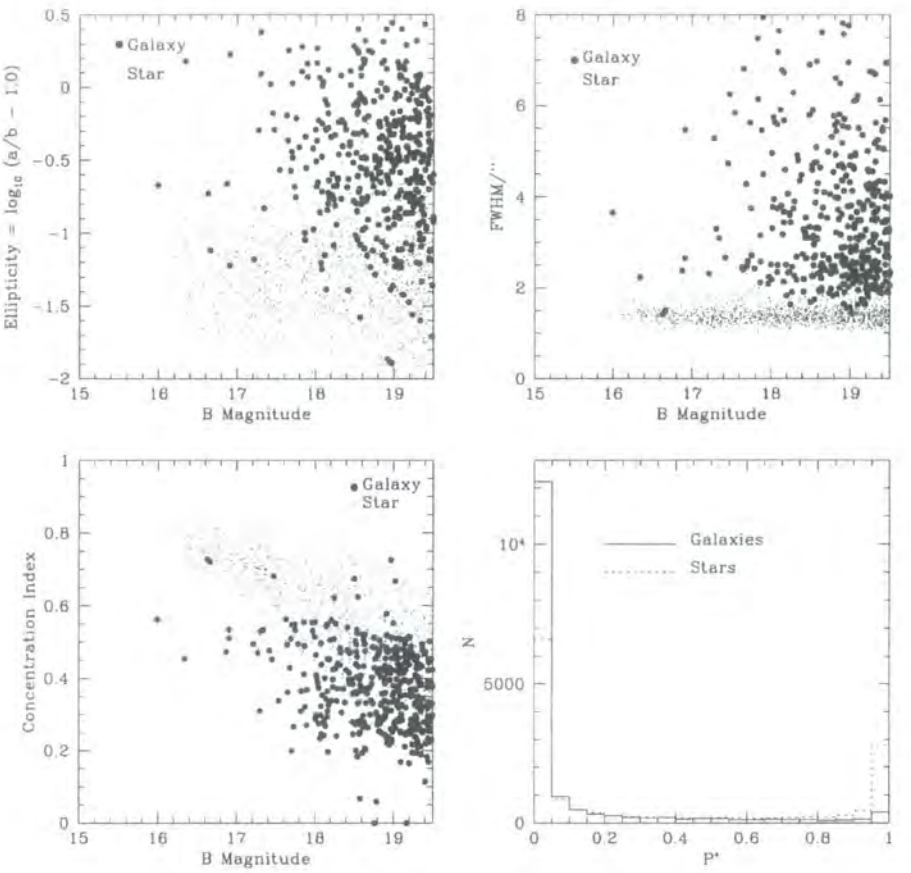

Figure 2.8: Plots of critical SExtractor parameters for stars and galaxies as defined from Figure 2.7. Upper Left: Ellipticity of the sources (defined as the ratio of semi-major to semi-minor axes) as a function of total magnitude. Upper Right: FWHM as a function of total magnitude. Lower Left: Concentration index (see Abraham et al. 1994; Bertin & Arnouts 1996) as a function of total magnitude. Lower Right: Histogram of P^*, SExtractor's own probability of a given source being a star.

a prerequisite that astrometry is accurate to within 0.3″ *rms* across the entire 2 degree mosaic.

Astrometry is performed individually on each pointing of a mosaic. Approximately 60 bright ($B < 18.0$) stars per pointing are tied to the positions from the APM (Maddox et al., 1990a; http://www.ast.cam.ac.uk/apm/) using a shell script co-written by Pimbblet, Smail and Edge.

The script enables the user to interactively tie-in the LARCS CCD positions of the bright stars to the RA and Dec of objects within the APM. Typically, a small rotation ($< 5^{o}$), a translation and a magnification are required to perform this tie-in. Once the bright star's positions are obtained, the positions of the rest of the sources (galaxies and uncatalogued stars) are computed using the ASTROM package.

As a quality test, the astrometrical solution of sources within the 44″ overlap regions of the 2 degree mosaics are compared. This method is found to produce astrometry that have a typical *rms* residual of $0.4'' - 0.8''$. The vectors of the residuals are also non-random. This level of accuracy is insufficient for the subsequent followup using the 2dF device. The reason for this poor performance is that (typicaly) a couple of the bright stars are found to have *rms* residuals which are very large ($> 1.5''$). They are pulling the overall fit off. These stars typically have poor centroiding and tend to be close to saturation on the CCD. Therefore, these bright stars are eliminated from the input list and repeat the APM tie-in procedure. On this second pass, the internal accuracy is found to be better than $\leq 0.3''$, adequate for the needs of spectroscopy on 2dF.

2.12 Catalogue Construction

Once both passbands are photometrically calibrated and the mosaic's astrometric solution found, the final catalogue is constructed by combining the catalogues from the individual 21 pointings across the entire mosaic. Typically there are over 1000 duplicated objects in this combined, catalogue arising from the thirty two 44″ overlap regions between each adjoining mosaic tile. Duplicates are defined as having a position within $< 0.3''$ (chosen as it represented an upper limit to the astrometric

accuracy) of each other.

The duplicates are removed automatically from the combined catalogue using an expedient removal program. If either version of a duplicate object has a better SExtractor FLAG than it's counterpart (e.g. one of the duplicates wholly on the CCD chip and its counterpart is not), then it is preferentially placed into the final mosaic catalogue. If they are of equal quality, then their critical SExtractor parameters (e.g. total magnitude) and position are averaged.

However, there are typically a small number of objects ($\sim$ 25 per mosaic) that are not simple duplicates. These objects fall into two broad categories. Firstly, there are objects that appeared in triplicate (or very rarely, in quadruplicate). These objects are dealt with in similar manner to the simple duplicates: if one of the objects has a SExtractor FLAG parameter lower than any of it's counterparts, then it is used preferentially, otherwise objects of equal quality have their parameters averaged. Secondly, there are objects which are matched to more than one counterpart. This arises occasionally as SExtractor deblends a detection on one mosaic tile into two (or more) detections where it is a single object on it's adjunct mosaic tile. These cases are each investigated by hand to determine which objects went into the final catalogues.

2.13 Morphology

The potential of the optical imaging to provide morphological information is examined by degrading an *HST* mosaic image of the galaxy cluster AC114 ($z = 0.31$) kindly donated by Smail & Couch to the quality typical of the ground based LCO images. The *HST* mosaic is observed through four pointings of the Wide-Field Camera using the R(F720W) filter on the *HST*. At the redshift of this cluster, only the central $\sim$ 2 Mpc of the cluster are observed.

The *HST* mosaic is degraded using standard tasks within IRAF. The degradation is made in several steps. Firstly, the *HST* mosaic is scaled to the size it would appear to be on the sky at the median redshift of the LARCS project ($z \sim 0.12$) using the MAGNIFY task. A typical seeing of 1.5″ is assumed for the LARCS imaging and the *HST* mosaic is degraded to this poorer seeing using the GAUSS task.

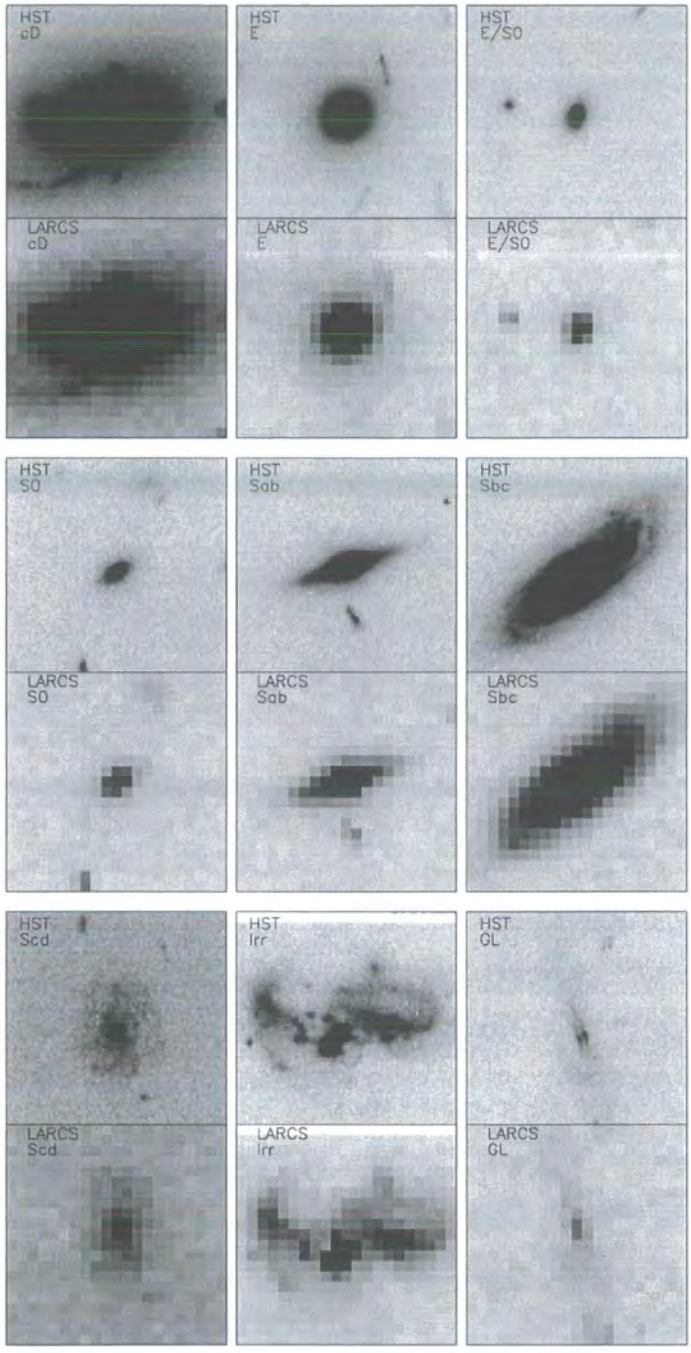

Figure 2.9: Examples of different morphological types of galaxy taken from the *HST* mosaic of AC114 and degraded to the quality of LARCS. Only broad morphological typing can be made with LARCS and even then $\sim$ 15 per cent of all galaxies suffer misclassification.

The pixel scales of the images are then matched. This is done by re-sampling the 0.1 pixel scale of AC114 to the 0.696 pixel scale used by LARCS by usage of the BLKAVG task. Finally, noise is added into the image using the MKNOISE task.

It is readily found that morphological typing within LARCS is limited to much broader types than is possible with the original *HST* mosaic. Figure 2.9 demonstrates the results of this morphological analysis succinctly. A morphological variety of galaxies ranging from cD galaxies to irregular and late spirals are shown together with their degraded counterparts. It is no longer possible to distinguish between all types of spiral galaxies and in many cases distinguish between elliptical and S0 morphologies. A broader morphological typing must be used with LARCS: E, E/S0, S0, Early Spiral, Late Spiral or Irregular / Peculiar.

SExtractor is used on both images to catalogue the objects within them. Morphological typing on the original *HST* mosaic is provided by Couch and checked by other members of the MORPHS collaboration (Couch et al. 1998) whilst both Pimbblet and Smail examined the degraded *HST* mosaic image and generated independent morphological typing for it.

Even using the broader typing after degradation, at least $\sim$ 15 per cent of galaxies typed by Smail and Pimbblet are incorrect when compared to the original *HST* designations. These cases of incorrect typings are typically one or two steps away from what they should be, i.e. many of these cases are a result of typing an early spiral (e.g. Sab) as an E/S0 or vice-versa. Such misclassification is worse for fainter galaxies. Thus whilst cD type galaxies are very obvious (due to their position and size), GL (gravitational lenses) are all but smeared out of existence. Therefore LARCS is unable to reliably differentiate between morphological types by visual inspection.

2.14 Summary

This Chapter described how 21 clusters have been selected from XBACs and observed at the LCO to fill the gap in the observational dataset at $z \sim 0.1$. A data reduction pipeline has been developed to reduce these mosaic optical imaging data. The final mosaic catalogues are demonstrated to possess internal photometric accu-

racy of < 0.005 mag and astrometric solutions to better than $0.3''$. These images, however, are only of sufficient quality to very broadly classify galaxies according to their visual morphologies.

Chapter 3

Comparison with the APM Catalogue

3.1 Abstract

Based on an overlapping area of 12.3 square degrees, the CCD-based LARCS catalogues are compared with the photographic-based galaxy catalogue used for the input to the 2dF Galaxy Redshift Survey (2dFGRS) from the Automated Plate Measuring Machine (APM) to the completeness of the GRS/APM catalogue, $b_J = 19.45$. This comparison confirms the reliability of the photometry across our mosaics and between the clusters in the LARCS survey. This comparison also provides useful information about the properties of the GRS/APM. The stellar contamination in the GRS/APM galaxy catalogue is confirmed to be around 5–10 per cent, as originally estimated. However, using the superior sensitivity and spatial resolution in the LARCS survey evidence is found for four distinct populations of galaxies that are systematically omitted from the GRS/APM catalogue. The characteristics of the 'missing' galaxy populations are described and the reasons for their absence are examined.

3.2 Comparison of the GRS/APM Galaxy Catalogue with LARCS

To test the reliability of the LARCS cataloging, photometry and star–galaxy separation, the sample* is compared to the galaxy catalogue from the APM survey

*Whenever 'the sample', 'all galaxies' and 'total population' of LARCS are referred to, this implicitly means 'all galaxies in the LARCS catalogues'. One acknowledges that the LARCS

which is used by the GRS/APM.

The APM survey (Maddox et al. 1990a, 1990b) is constructed from photographic plate materials taken at the UK Schmidt Telescope Unit in Australia. Approximately 390 photographic IIIa-J plates are scanned by the APM. The APM scans use a 16-μm pixel with a sampling rate that produces a 0.54″ pixel scale. Magnitudes are defined using the Kodak emulsion in combination with a GG395 filter and zeropointed with Johnson B-band CCD photometry. The rms random error in each galaxy magnitude is 0.1–0.2 mags to a depth of $b_J = 20.5$ (Maddox et al. 1990a). Subsequent field corrections are applied to the APM catalogues to account for non-photometric observations, vignetting and differential desensitization. Maddox et al. (1990b) argue that the rms plate zero-point error in the final matched survey catalogue is 0.04 mags. Objects in the overlapping regions between the plates are utilized for establishing the plate to plate variation and the zeropoints are iteratively corrected to remove these offsets.

Image surface brightness profiles are used in the APM to achieve star-galaxy separation. The residual differences between a given image profile and a stellar profile at the same magnitude are calculated, resulting in brighter stars being readily identified, but at fainter magnitudes, the lower signal to noise in the images make robust separation impossible. Maddox et al. (1990a) estimate that the catalogue's completeness is $\sim$ 98 per cent for $b_J < 19.5$, with a stellar contamination rate of 5–10 per cent at the same depth, depending upon proximity to the galactic plane.

The 2dFGRS is an ambitious project to collect high quality redshifts and spectra for $\sim$250,000 galaxies brighter than $b_J = 19.45$, extinction corrected (e.g. Colless et al. 2001). Galaxies are robustly selected from the extended version of the APM galaxy catalogue (Maddox et al. 1990a) covering a region of over 1700 square degrees in both the Northern and Southern Pole regions and used as the input to the 2dFGRS (Colless et al. 1998; Maddox et al. 1998; Folkes et al. 1999). Of the LARCS clusters, four overlap with the 2dFGRS parent catalogue from the APM. The details of the catalogues of these clusters (Abell 22, 1084, 1650 and 1651) are presented in Table 3.1. The 0.3″ accuracy within the LARCS astrometry is more than adequate for identifying source matches with the APM catalogues.

sample is not complete either.

Table 3.1: Parameters of the LARCS clusters that overlap with the GRS/APM, indicating the number of sources catalogued in the LARCS CCD frames, the number of galaxies (defined using the criteria presented in §2.3) and the galactic cap region of the GRS/APM with which they overlap (Southern Galactic Pole, SGP; Northern Galactic Pole, NGP).

Cluster	N(Objects)	N(Galaxies)	Overlap
Abell 22	31851	15429	SGP
Abell 1084	37801	14494	NGP
Abell 1650	34403	13480	NGP
Abell 1651	42286	15801	NGP

3.2.1 Matching LARCS to GRS/APM

Here, the GRS/APM catalogue is compared down to the 2dFGRS magnitude cut-off of $b_J = 19.45$ (extinction corrected), across the LARCS/GRS overlap area of 12.3 square degrees.

The APM catalogue is divided into two distinct (and isolated) areas: Northern and Southern Galactic Pole regions. There are 2754 GRS/APM galaxies in the overlap of the GRS/APM with the four clusters in Table 3.1. One of the clusters (Abell 22) lies in the Southern Galactic Pole Region, whilst the other three overlapping clusters are in the Northern Galactic Pole Region.

The GRS/APM galaxy catalogue is matched to the full LARCS catalogues using a search radius of 3″. Virtually all sources ($\sim$ 95 per cent) in the GRS/APM have corresponding matches within LARCS. Those sources for which matches are not found are all visually inspected - their APM positions are over-plotted upon the corresponding LARCS mosaic pointings. In most cases the unmatched sources result from differences in blending and deblending of close sources between the two surveys. Most are resolved in the LARCS CCD imaging, whereas in the APM the source appears as a blend of a number (typically 2–3) of LARCS sources (both galaxy-galaxy and galaxy-star blends). The centroiding for the astrometric solution is thus affected, resulting in the source lying outside the 3″ search radius. Only three

Table 3.2: Comparison between the input GRS/APM catalogue and the four full LARCS catalogues. N(Matched) is the number of GRS/APM sources that are matched to LARCS. N(Galaxies) is the number of sources that are defined as galaxies using the criteria presented in §3. N(Close blends) is the number of galaxies that the LARCS survey detects that are blended or in close proximity to a secondary source, which affects the astrometric matching routine. N(APM noise) is the number of sources existing within the GRS/APM survey that have no likely counterparts within LARCS – they are random detections, perhaps a moving source, plate flaw or a diffraction spike of a star.

Cluster	N(GRS/APM)	N(Matched)	N(Galaxies)	N(Close blends)	N(APM noise)
Abell 22	634	611	553	23	0
Abell 1084	473	463	371	10	0
Abell 1650	681	630	518	48	3
Abell 1651	966	932	752	34	0

sources are found within the GRS/APM catalogue that do not have any likely counterpart in the LARCS imaging. These very rare sources (< 0.1 per cent) are examples of APM mis-detections perhaps caused by plate flaws or moving/variable sources. Table 3.2 summarizes the results of the matches with the total number of sources within each catalogue.

The nature of the GRS/APM sources that are matched are further investigated using the star–galaxy separation criteria of LARCS as presented in Chapter 1. The number of matched sources which satisfy all of the 'LARCS galaxy criteria' are presented in Table 3.2. Broadly 80 per cent of matched sources defined as galaxies by the GRS/APM are also classified as galaxies by LARCS. Note that 80 per cent is the *lower* limit of the number of galaxies as the LARCS galaxy determination is very strict.

It is also possible to place a lower limit on the stellar contamination by inverting the star-galaxy selection criteria discussed previously. Conservatively, stars can be defined as having $\Delta_{2''-4''} < 0.2$, FWHM < 2.0" and $P^* > 0.9$. Of the matched GRS/APM galaxies, 3 per cent are defined as stars by LARCS. Therefore at minimum, the stellar contamination of the APM is 3 per cent, whilst at maximum it is 20 per cent. This result is close to the original estimation of 5–10 per cent stellar contamination by Maddox et al. (1990a).

3.2.2 Photometric comparison

In this section the magnitudes of sources in the LARCS and GRS/APM catalogues are examined – searching for zero-point differences between the four cluster fields, as well as between the Northern and Southern Galactic Pole regions of the GRS/APM.

To undertake such a comparison one must convert LARCS' R-selected sample to the b_J system used by the APM. Since LARCS was SExtracted using the R-band imaging, it is inconvenient. and time-consuming to repeat this on the B-band imaging, although potentially closer to the b_J system. Further, if this were to be done, one would not get back the whole of the LARCS R-band sample.

To obtain b_J magnitudes we first globally convert the R-band magnitudes from SExtractor's BEST_MAG to total magnitudes. The correction factor, $R_{tot} = mag\_best-$

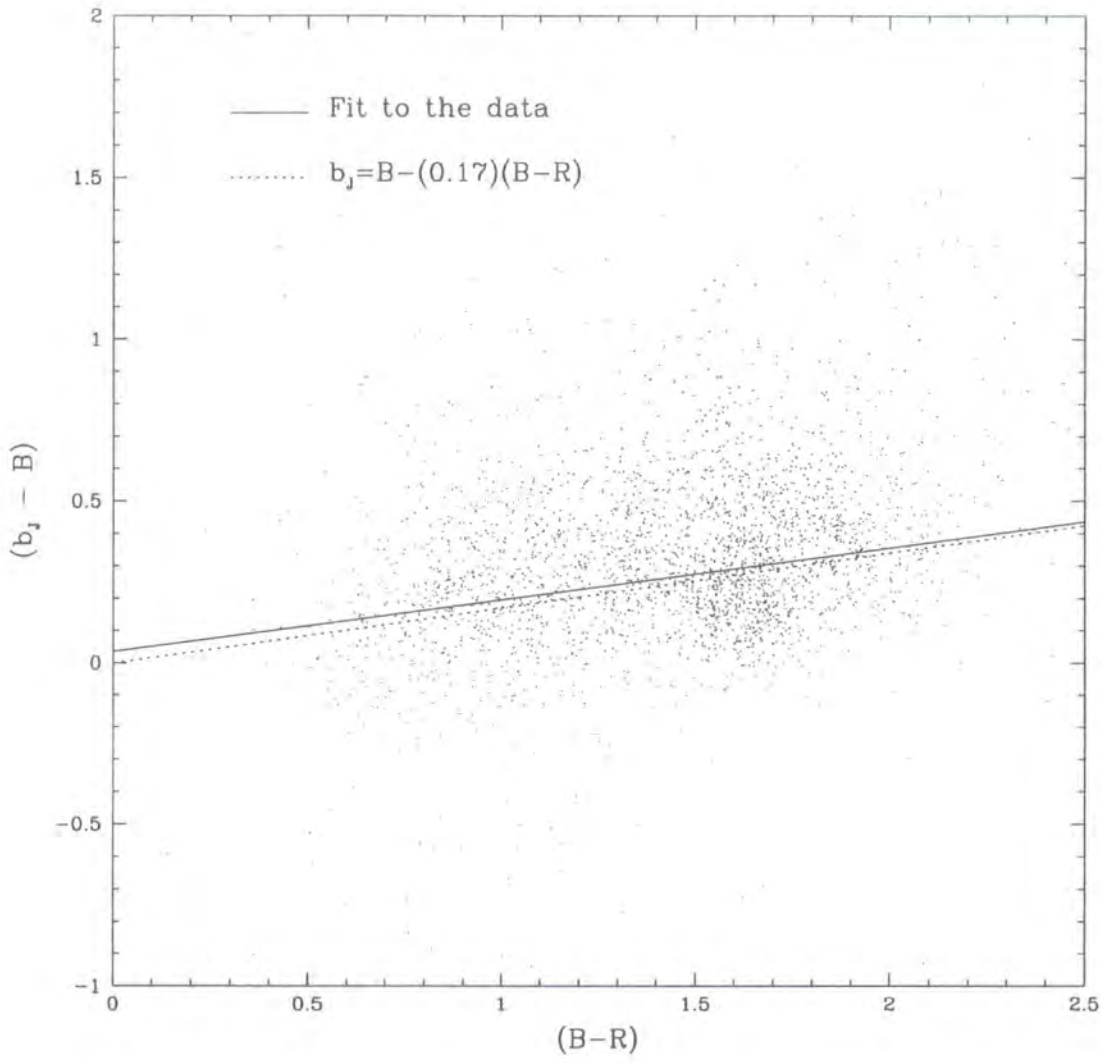

Figure 3.1: Plot of the correlation between (b_J-B) and (B-R) colour for sources from LARCS that are matched to the APM. The solid line is the best fit to the data points. The dotted line is the derived theoretical line $b_J = B - (0.17)(B - R)$. The theoretical line is consistent with the fitted line.

0.021 ± 0.010, is calculated from the median magnitude difference between SExtrator's BEST_MAG magnitude and a large (15″ diameter) aperture magnitude for isolated sources, and applied to all sources to convert their MAG_BEST magnitudes to true total magnitudes. Next, these total R-band magnitudes, R_{tot}, are globally converted to total B-band magnitudes ($B_{\rm tot}$) using: $B_{\rm tot} = R_{\rm tot} + (B - R)$ where $(B - R)$ is the colour measured from the seeing-matched tiles in a 4″-diameter aperture.

The APM uses photographic b_J magnitudes, and therefore one requires a colour transformation to convert the CCD-based Johnson B-band magnitude into b_J. Metcalfe et al. (1995), and a number of other authors including Colless (1989) and Bardelli et al. (1998), provide conversions from B to b_J: $b_J = B - (0.28 \pm 0.04)(B - V)$. From fitting the predicted colours of galaxies across the range of redshift covered by the LARCS clusters with non-evolving spectral energy distributions, the relation between $(B - V)$ and $(B - R)$ is derived to be $(B - R) = (1.66 \pm 0.03)(B - V)$. Hence to convert from the B magnitudes used in LARCS to the b_J APM magnitudes the equation $b_J = B - (0.17 \pm 0.05)(B - R)$ is utilized. This conversion is consistent with the correlation between $B - b_J$ and $(B - R)$ colour found for matched sources between APM and LARCS data (see Figure 3.1) where the calculated fit is $b_J = B - (0.16 \pm 0.03)(B - R) + (0.04 \pm 0.02)$.

In this comparison corrected (i.e. including a correction for galactic extinction, Schlegel et al. (1998)) b_J magnitudes from the APM and corrected total B-band magnitudes from LARCS, converted to b_J are used. Differences in the magnitudes of matched sources are examined as functions of LARCS mosaic pointing and magnitude.

Figure 3.2 shows the difference between LARCS b_J and the total APM b_J magnitude for each of the four clusters. The medians and the associated errors are also indicated on the panels. Based on repeat scans of the plate material, Maddox et al. (1990a) suggest an intrinsic uncertainty in the zeropoint of individual plates of 0.04 mag. Of the four clusters, Abell 1650 and Abell 1651 show very good agreement between the two photometric systems, Abell 1084 shows a larger offset – but only at the $\sim 2.5\sigma$ level, while Abell 22 has a $\sim 3\sigma$ difference ($\Delta = 0.12$ mags). Abell 22 is the only one of the four clusters which falls in the SGP area of the GRS/APM.

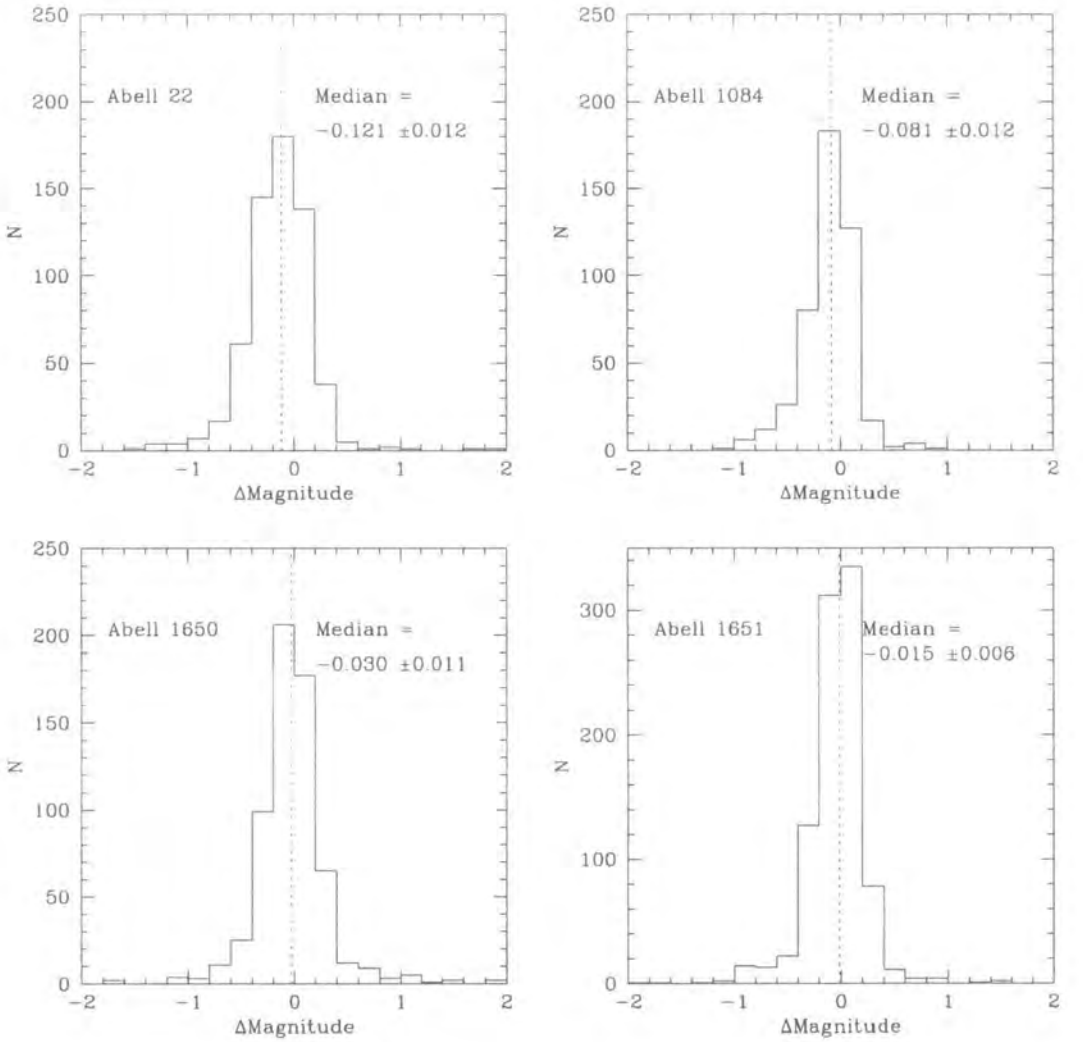

Figure 3.2: Histograms of the difference between APM magnitude and LARCS total b_J magnitude (the latter converted from R-band) for all four clusters using the full LARCS catalogues. Abell 22 lies in the SGP, the other three are in the NGP. The median magnitude offsets and associated 1σ errors are noted on the individual panels.

Attention is now turned to an investigation of the precision of individual galaxy measurements. Maddox et al. (1990a) and Folkes et al. (1999) state the random error associated with the b_J magnitudes is ± 0.2 mag for the range $17.0 \leq b_J \leq 19.45$. In Figure 3.3 the magnitude difference (in b_J) between LARCS and the APM is plotted against LARCS magnitude. Excluding regions of the plot close to the selection limits, it is found that the fit is consistent with a slope of zero, hence the APM demonstrates a linear photometric scale over at least the range $17 < b_J < 19$. The RMS scatter is also consistent with the random error previously stated by Maddox et al (1990a).

In summary, therefore, only slight evidence for systematic variations in the zero points of the GRS/APM and LARCS photometry across the four clusters is seen, but such variations are within the limit imposed by the combined errors on the GRS/APM and LARCS zero points and thus are not significant. No evidence is found for systematic variations between the photometry of the SGP and NGP regions of the GRS/APM at levels $\gg 0.1$ mag. There is no evidence for a magnitude offset between individual pointings of the mosaic tiles within LARCS at the level of > 0.02 mags (consistent with the photometric errors on the sources used in the comparison).

3.3 Comparison of the LARCS Galaxy Catalogue with the GRS/APM

The LARCS and GRS/APM catalogues are now compared in the reverse sense: that is a "complete" galaxy catalogue is constructed from LARCS and the overlap with the GRS/APM is determined.

Because the faint magnitude limit of the GRS/APM input catalogue is $b_J = 19.45$, a bright LARCS sample is generated for each of the four clusters. As confirmed in §3.2, the typical photometric errors for galaxies in the GRS/APM is 0.2 mag. To ensure the most complete comparison all sources from the LARCS catalogues which are at least 3σ (0.6 mag) away from the limit of the GRS/APM are therefore selected: $b_J = 19.45$. This imposes a magnitude limit of $b_J = 18.85$ and

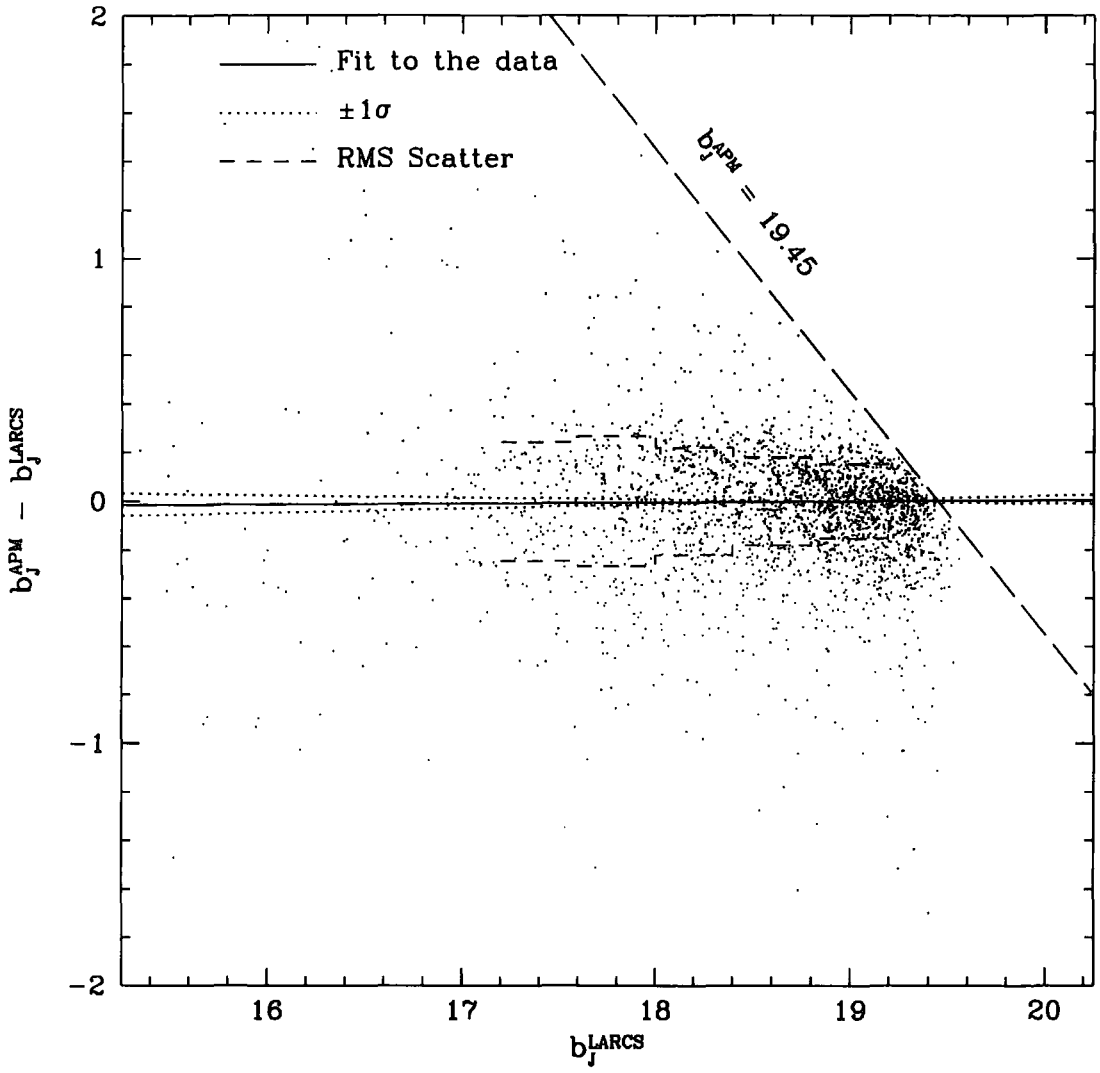

Figure 3.3: Difference in magnitude between LARCS and the APM as a function of LARCS magnitude. The solid line is a fit to those data points brighter than the median magnitude ($b_J^{LARCS} = 18.4$) so as to avoid the selection limit of the GRS/APM (long dashed line). The dotted line represents the $\pm 1\sigma$ limit of this fit. The RMS scatter (long dashed line) ranges from 0.18–0.25, confirming the original estimate of 0.2 made by Maddox et al (1990a).

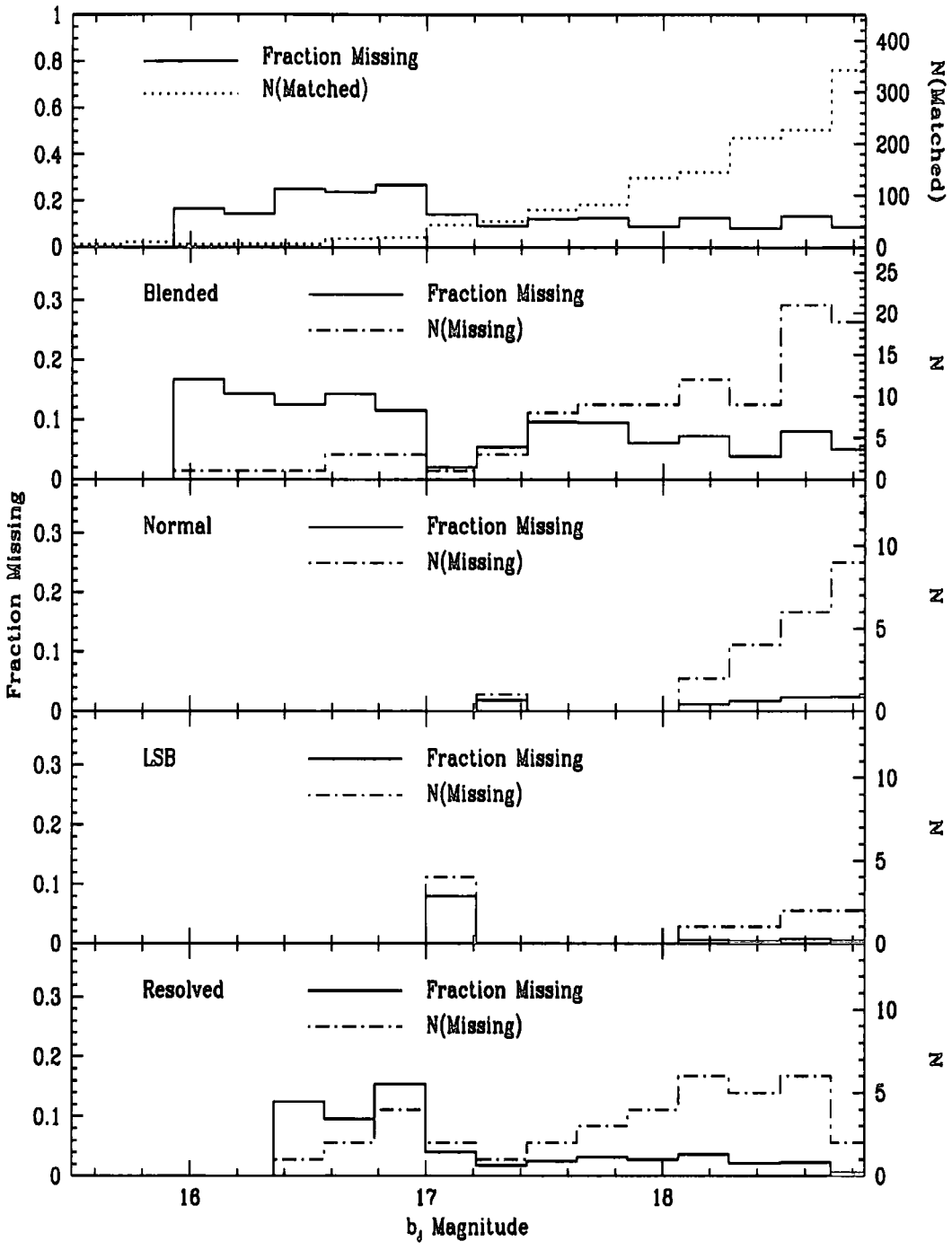

Figure 3.4: The fraction of bright LARCS galaxies missing from the GRS/APM as a function of LARCS b_J magnitude. The top panel shows the total fraction that is missing with the total number of matched galaxies. About 10–20 per cent of all galaxies are missed at all magnitudes. The four lower panels break down the missing population into the four broad constituent types. The normal and LSB populations are primarily missed at $b_J > 18.0$, but the blended population is missed across the magnitude range. See §4.2 for discussion.

Table 3.3: Comparison of the bright LARCS catalogues with the GRS/APM catalogue. N(Bright) is the number of sources within the LARCS catalogues when cut at $b_J = 18.85$. N(Matched) is the number of these LARCS sources matched to the GRS/APM catalogue. N(Galaxies, Matched) is the number of matched galaxies that fall within the stringent star-galaxy separation criteria, whilst N(Galaxies, Unmatched) is the number of unmatched galaxies. See chapter 4 for a full discussion.

Cluster	N(Bright)	N(Matched)	N(Galaxies, Matched)	N(Galaxies, Unmatched)
Abell 22	1997	249	226	35
Abell 1084	2904	177	152	29
Abell 1650	3016	328	249	35
Abell 1651	3521	471	381	70

the number of sources in each field in this "bright" sample is listed in Table 3.3. The bright comparison is thus well above the completeness limit and the random scattering of sources above/below the cut-off used for the GRS/APM catalogue. Based upon the scatter at brighter magnitudes (see Figure 3.3) selecting the sample at $b_J = 18.85$ should lose at most ~ 3 per cent of the population. The conservative galaxy selection criteria (see chapter 2) is applied to the catalogues to create bright galaxy catalogues for comparison to the GRS/APM input catalogue.

In principle, *all* of the galaxies contained within these bright LARCS galaxy catalogues should be present in the GRS/APM. Again, a search radius of 3″ is employed for the matching algorithm and a summary of the results is given in Table 3.3.

The GRS/APM identifies the majority of the galaxies contained within the bright LARCS galaxy sample. However, the GRS/APM is missing 10–20 per cent of the galaxies at all magnitudes: Figure 3.4 presents a distribution of the per centage of bright galaxies missing from the GRS/APM as a function of b_J magnitude, overlaid with the total number of matched galaxies. The missing population represents approximately a fixed fraction of the total population across the whole

Table 3.4: Breakdown of the morphologies of the bright ($b_J < 18.85$) 'missing' galaxy population from visual inspection of the LARCS CCD material. N(Missing) is the total number of missing galaxies from the GRS/APM. N(Blended) is the number of galaxies that are blended or have a close companion and thus do not appear as distinct sources in the APM. N(Resolved) is the number of apparently normal, resolved galaxies missing from the GRS/APM. N(Normal) is the number of small, often compact, normal galaxies (also see Drinkwater et al. 1999). These galaxies are mis-classified as stellar in the APM. N(LSB) is the number of low surface brightness galaxies missed by the GRS/APM. Several examples of each type of missing galaxies are presented in Figure 3.6.

Cluster	N(Missing)	N(Blended)	N(Resolved)	N(Normal)	N(LSB)
Abell 22	35	22	5	6	2
Abell 1084	29	17	10	1	1
Abell 1650	35	18	8	4	4
Abell 1651	70	42	16	7	5

magnitude range.

To investigate the properties of the missing galaxy population the characteristics of the matched and unmatched galaxies are compared in terms of their morphologies, brightnesses, spatial distributions and $(B - R)$ colours.

3.3.1 Morphologies of the Missing Populations

Figure 3.5 shows the distribution of maximum surface brightness (μ_{MAX}) versus concentration index for the matched and missing populations; late-types typically lie towards lower right and early-types populate the upper left of this plane (Abraham et al. 1994). Figure 3.5 demonstrates that, whilst the missing galaxy population broadly follows that of the matched population, there exist distinct classes of galaxies that are missed in the GRS/APM.

Figure 3.6 displays a sample of some of these bright galaxies missed from the GRS/APM. The unmatched galaxies are visually classified and four broad classes

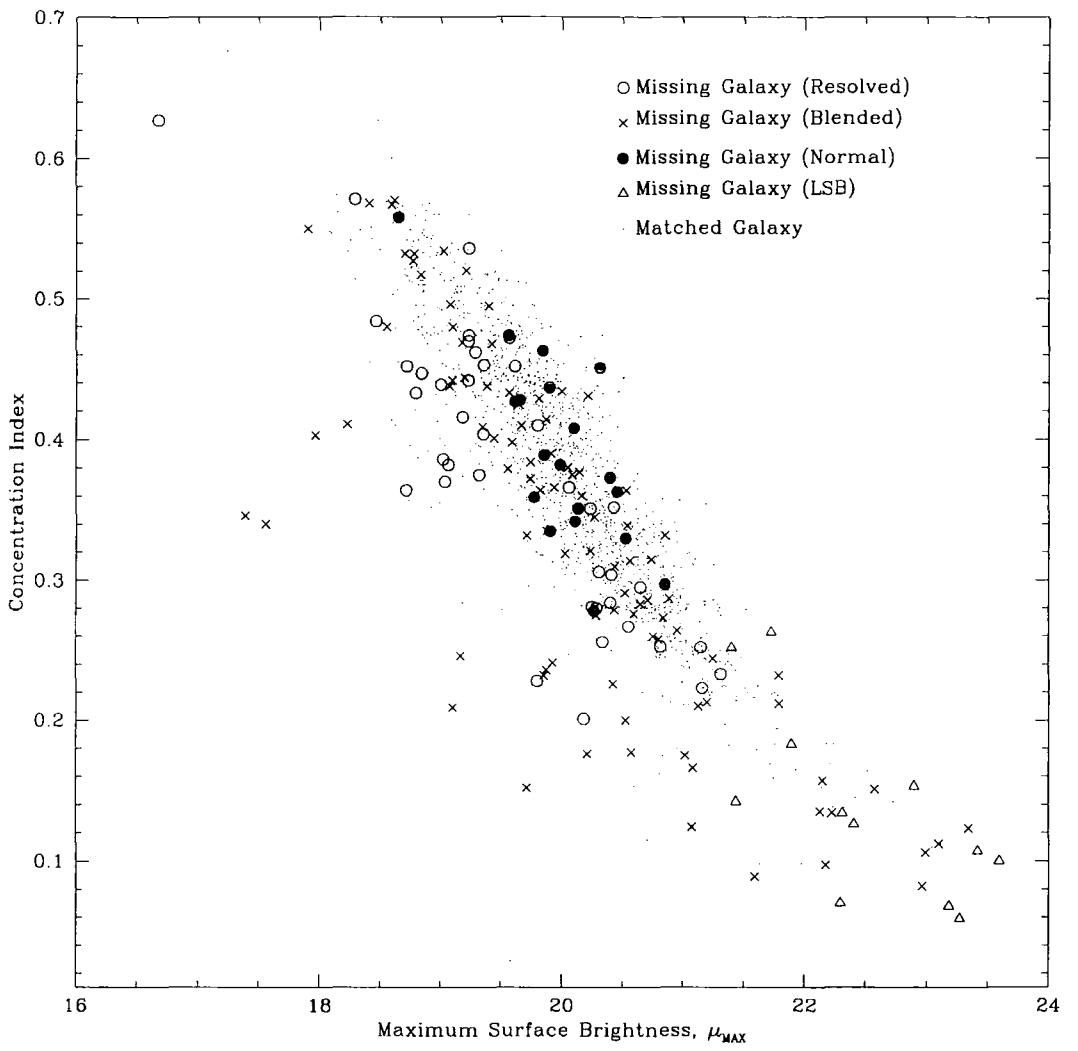

Figure 3.5: Peak surface brightness, μ_{MAX} versus concentration index (from SExtractor) for the missing galaxies and the matched sources (dots). The missing population broadly traces the matched population save for the LSBs, which preferentially lie to the lower-right.

of galaxies are now defined which are missing from the GRS/APM:

- Blends. There are many examples of blended galaxies (see the top two rows of Figure 3.6), due to the proximity of a close neighbour or neighbours (either other galaxies or stars), the galaxy is excluded from the GRS/APM catalogue.

- Resolved. There are several apparently 'normal', resolved galaxies missing from the GRS/APM. (see the third and fourth rows of Figure 3.6).

- Normal. There are also small, mostly compact, galaxies which have been missed, the bulk of these are likely to be mis-classified as stellar in the APM and missed from the galaxy survey input catalogue. (see the penultimate row of Figure 3.6).

- LSB. Finally, there are also a small number of low surface brightness galaxies. (see the bottom row of Figure 3.6).

Blends are the dominant component of the missing galaxy population, comprising 60 per cent of it, resolved galaxies 20 per cent, normal galaxies 15 per cent and low surface brightness galaxies 5 per cent (see Table 3.4).

The majority of the missing population are galaxies blended with a secondary source; both with galaxies (e.g. a1084r09_1155, in Figure 3.6) and stars (e.g. a22r13_839). In one or both of the APM passbands (http://www.ast.cam.ac.uk /~apmcat/)[†] these blends have a MERGED flag set. Moreover, as the APM data are scanned from many different plates, the plate quality varies from cluster to cluster. In principle, the plates should be of top quality, but subjective grading of plate quality and variable focus would cause the median separation between blended sources to vary and hence affect the success of deblending. Table 3.5 presents the median separation of the missing, merged galaxies. Clearly there are differences in plate to plate quality (and hence the deblending) across the APM, with one plate (containing Abell 1084) having a significantly smaller median blend offset than other plates and the fewest number of blends.

[†]The apmcat is the raw APM machine catalogue and not the processed version that went into either the APM Galaxy Survey or 2dFGRS.

Figure 3.6: Examples of galaxies missing from the GRS/APM catalogue that appear in the bright ($b_J < 18.85$) LARCS galaxy catalogues. (See §4 and Table 3.4 for details of the bright comparison). Each box is 30″ on the side with tickmarks every 5″. The contours start at a level of $\mu_B = 22$ mag. arcsec^{-2} and increase in brightness by 1 mag. The upper two rows are examples of blended galaxies near stars and other galaxies. The next two rows are normal looking, resolved galaxies incorrectly classified in the APM as not 'non-stellar' in one or both APM passbands. The penultimate row are normal galaxies, classified as stars in the APM. The last row are low surface brightness galaxies.

There are a number of apparently 'normal', resolved galaxies that the GRS/APM misses (e.g. a22r03_1196). These account for $\sim$ 20 per cent of the missing population. These resolved galaxies are further investigated by inspecting them in the online APM catalogues (see http://www.ast.cam.ac.uk/~apmcat). The Resolved galaxies have classification flags set in one or both passbands to 'noise', 'merged' or 'stellar' (e.g. a1651r05_790, has classification flags set to 'non-stellar' and 'stellar' in the B and R-scans of the APM).

Whilst issues of blending account for $\sim$ 60 per cent of the missing APM galaxies, $\sim$ 15 per cent of the remainder are bright and relatively compact in nature. With the poorer resolution of the APM these galaxies are likely to be classified as stellar and indeed most are typed as 'stellar' according to their classification flag in the APM catalogues (e.g. a1084r03_50, has classification flags in both passbands set to 'stellar'). Drinkwater et al. (1999) found evidence for a similar population of small, high surface brightness, compact galaxies within the Fornax cluster. They argue that such galaxies are readily overlooked in many surveys because they are simply misclassified as stars. This comparison confirms that the GRS/APM is systematically missing these compact galaxies from the galaxy catalogue.

The remaining $\sim$ 5 per cent of the missing galaxies are low surface brightness systems (LSB) and are also missed from the GRS/APM. The few examples of the LSB class that are found at all in the on-line APM catalogues are classified as 'noisy', but the majority are missing (e.g. a1651r18_227, has classification flags set to both 'noise-like' and 'merged' in the red and blue APM passbands respectively). Cross et al. (2000) present the bivariate brightness distribution (BBD) for the 2dFGRS survey which confirms that the majority of these LSB galaxies found in LARCS are outside 2dFGRS's detection limits in surface brightness. The LSB population likely arises as a result of the transformation from R-band to b_J-band rather than an actual incompleteness.

3.3.2 Magnitude Distribution of the Missing Populations

The missing galaxies appear to be a fixed fraction, about 10–20 per cent of the total population at all magnitudes (see Figure 3.4, upper panel), with an increase

Table 3.5: Median distance between the two closest neighbours in a merged source with bootstrap estimates of the 1σ errors.

Cluster	Median Merger Distance ($''$)
Abell 22	8.59 ± 0.85
Abell 1084	5.34 ± 0.88
Abell 1650	7.28 ± 0.65
Abell 1651	7.49 ± 0.53

(to 20 per cent) in the proportion of missing galaxies at the brightest magnitudes, $b_J < 17$.

Looking at the four separate sub-classes, because the missing Blended population dominates the total missing population number, they exhibit the same behaviour as the whole missing population across the entire magnitude range. There is no strong dependence on brightness when galaxies are lost from the GRS/APM due to blending.

The missing Resolved galaxies occur more frequently at brighter magnitudes, with few if any fainter than $b_J \sim 18.7$. Many of these brighter normal galaxies are misclassified in one or both APM passbands as blends due to slight asymmetries or irregularities in their morphology.

In contrast, the missing Normal and LSB galaxies are primarily found at fainter magnitudes, $b_J > 18$, relatively uniformly distributed between $b_J \sim 18$ and the magnitude limit of the GRS/APM. Each of these two sub-classes makes up about 1–2 per cent of the total population at $b_J > 18$ or fainter. The sensitivity limits of the plate material used in the APM survey means that it preferentially misses faint LSBs, but the dominant factor for distinguishing between faint compact galaxies and stars is the spatial resolution of the sky survey plates.

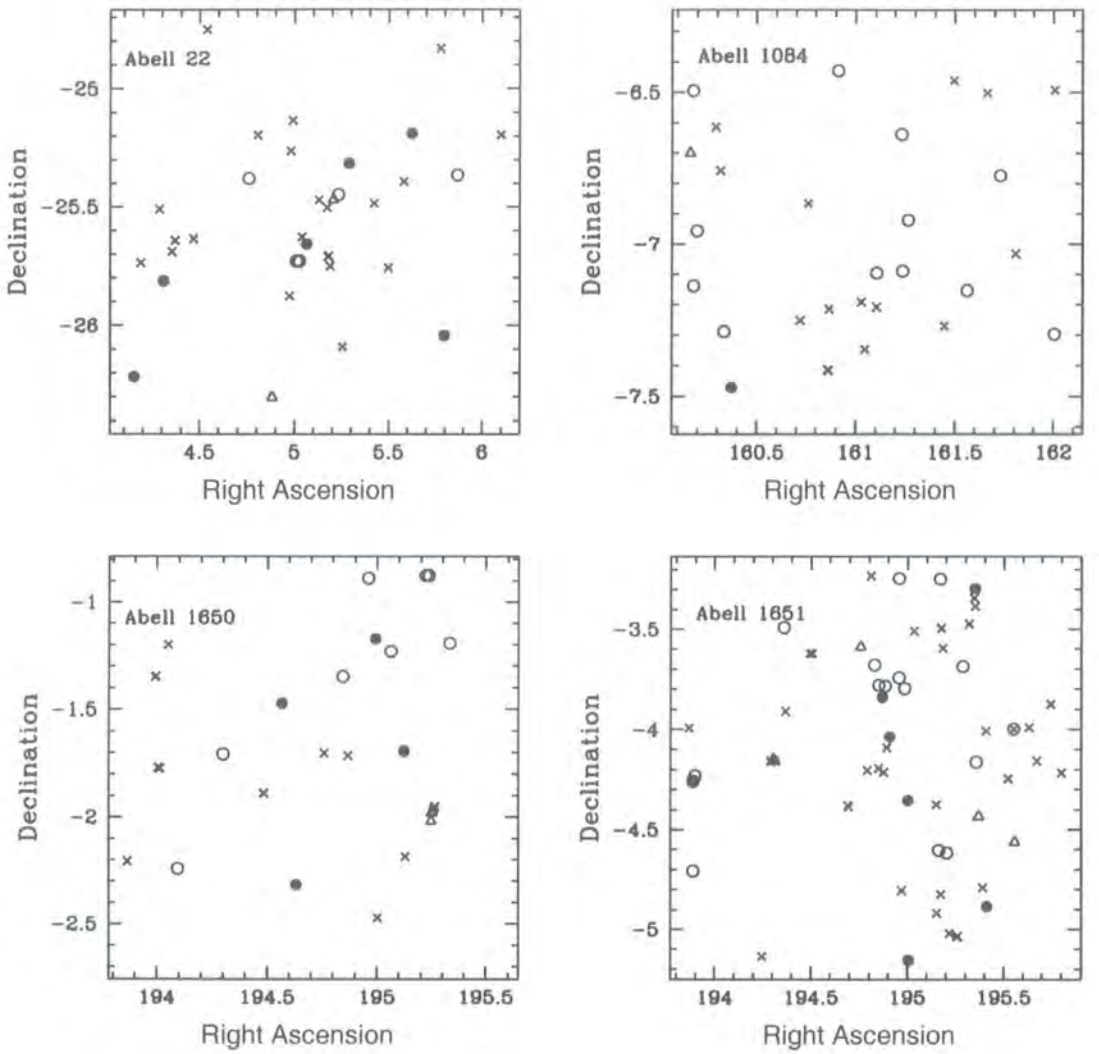

Figure 3.7: The spatial distribution of the galaxy populations missing from the GRS/APM. Each sub-population, Blends (crosses), Compact (solid circles), Normal (open circles) and LSBs (open triangles) are scattered throughout the two degree fields, with only a slight over-density towards the centre of the cluster (located in the centre of each plot). As Figure 3.8 shows, the over-density simply reflects the higher proportion of galaxies present in the cluster core.

3.3.3 Spatial Distribution of Missing Populations

The spatial distribution of the missing galaxies is presented in Figure 3.7. The galaxies are spread evenly throughout the four LARCS clusters. The radially-averaged distribution of the different missing galaxy classes for the combined sample from the four clusters are shown in Figure 3.8. The missing galaxies are seen to represent a constant fraction of the whole population at all radii. Although it might be expected that in the crowded cores of clusters the proportion of blended galaxies missing from the GRS/APM would increase there is no evidence found for this.

3.3.4 Colours of the Missing Populations

Histograms of the $(B-R)$ colours of the 'missing' population are presented in Figure 3.9 together with the colours of the 'matched' population. The excess $(B-R)=1.6$ galaxies in the matched population are the early-type cluster members; they account for only ~ 10 per cent of the galaxies matched in the bright comparison. The missing galaxies span the whole range in colours seen in the matched population, although if anything with a slight bias against galaxies with colours similar to early-type galaxies in the clusters and a slightly enhanced number of blue galaxies. The population of Blends dominates the total missing galaxy population. It broadly follows the matched population except for a slight (but not significant) enhancement in the population of very blue galaxies. The Resolved population of missing galaxies traces that of the matched fairly well. Finally, the distributions of missing Normal and LSB galaxies both show shifts to the blue compared to the matched population. This is more pronounced for the missing LSBs, but is still statistically significant for the missing Normal population: likelihood $< 10^{-4}$.

We conclude that while there are colour biases in some of the populations missing from the GRS/APM these are relatively modest, especially for the Blended population which dominates the missing sample

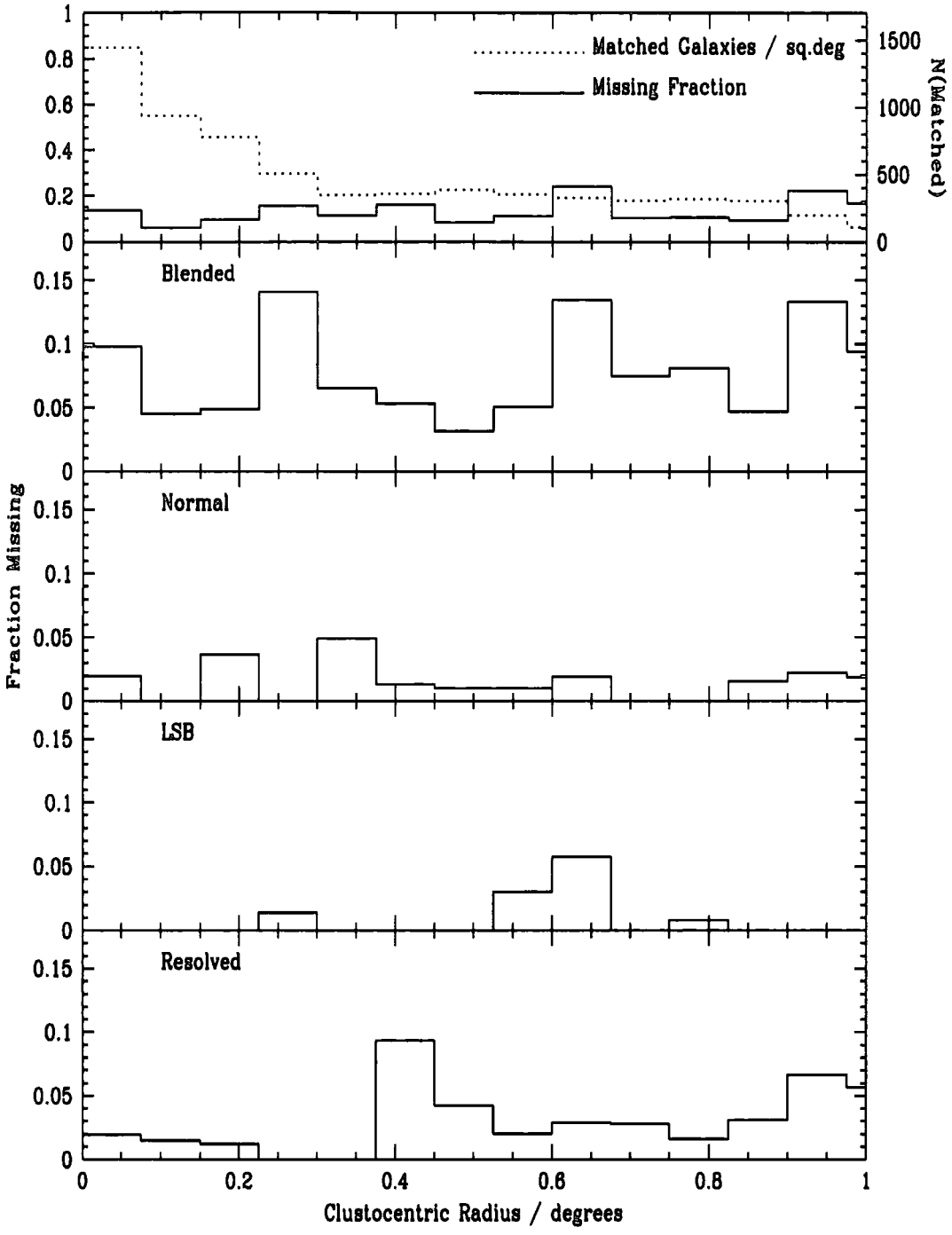

Figure 3.8: Number of galaxies matched ($b_J \leq 18.85$) per square degree as a function of clustocentric radius, over-plotted with the total fraction of missing galaxies (top panel). The missing populations are approximately a fixed fraction of the total population, which itself decreases with increasing clustocentric distance. The lower four panels illustrate the contribution to the missing fraction for each of the four sub-classes.

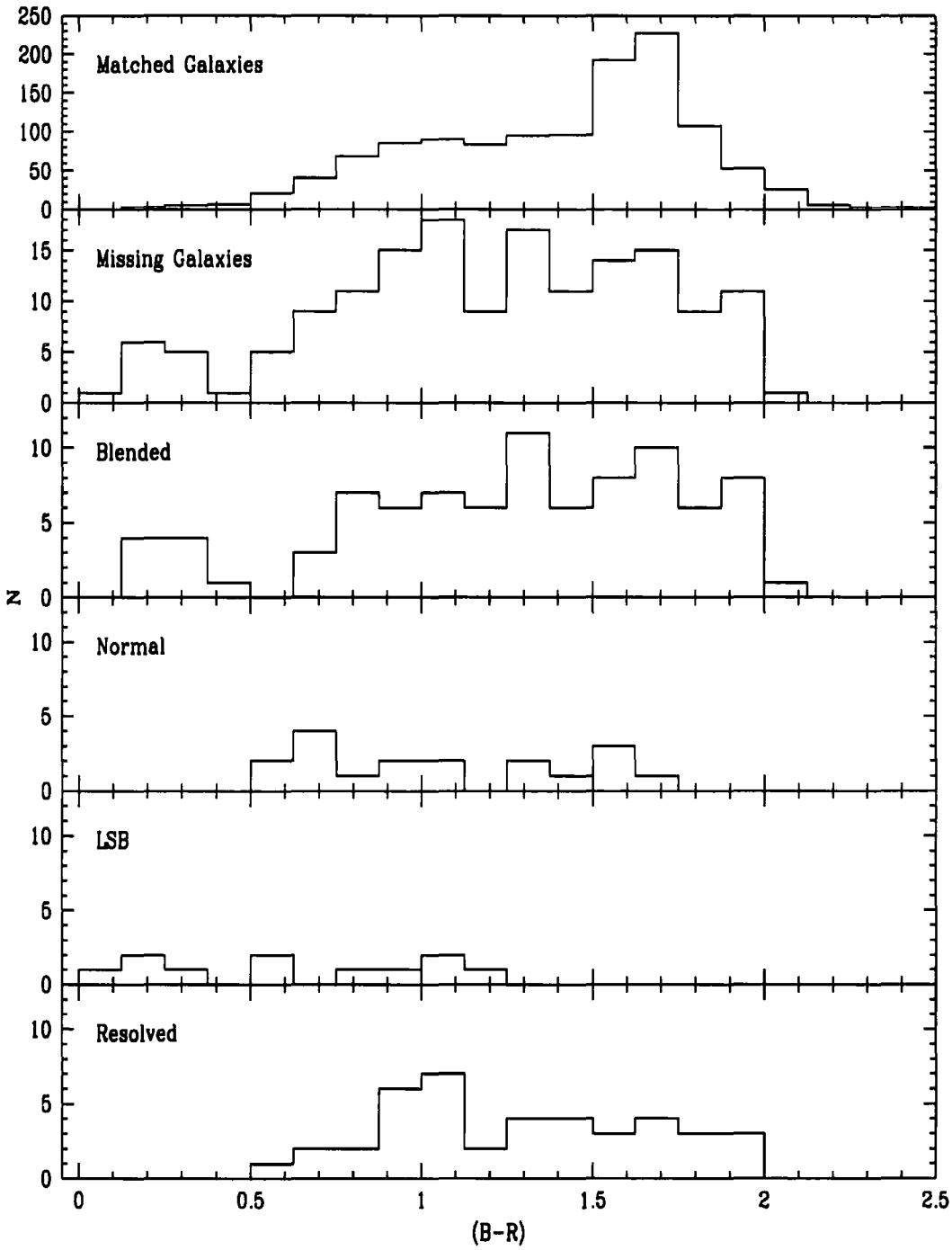

Figure 3.9: The $(B - R)$ colour histograms of the matched and missing galaxy populations, with the missing population sub-divided into its various morphological classes. Note the excess of matched galaxies with $(B - R) = 1.6$ – early-type cluster members that account for only around 10 per cent of the galaxies in the comparison.

3.4 Summary

A comparison has been made between four fields from the LARCS survey to the overlapping region of the 2dFGRS survey, based upon photographic plates scans from the APM. The comparison covers an area $\sim$ 12.3 square degrees on the sky and includes roughly 2500 galaxies brighter than $b_J = 19.45$.

The photometric accuracy of LARCS is shown to be accurate to better than 0.03 mag. There is found to be no evidence for a significant offset ($\gg$ 0.1mag) between fields in the LARCS survey or between the disconnected regions of the Northern and Southern APM catalogues.

The APM magnitudes are linear across at least two magnitudes in b_J and the random photometrical errors are found to be consistent with the value of 0.2 mag estimated by Maddox et al (1990a).

The stellar contamination within the GRS/APM is found to be about 3–20 per cent, close to the range of 5–10 per cent originally estimated by Maddox et al. (1990a).

The number of false detections within the APM is very small, at the $\sim$ 0.1 per cent level.

There are several populations of galaxies that are not present within the APM input catalogue: these comprise roughly 10–20 per cent of the total galaxy population at all magnitudes. The missing galaxies can be divided in to four broad categories: Blends (60 per cent), Resolved galaxies (20 per cent), Normal galaxies (15 per cent) and Low Surface Brightness galaxies (5 per cent).

- The Blends can readily be explained. Due to the resolution of the photographic plates, the APM has not been able to cleanly deblend two sources. As a result these sources are flagged as 'Merged' and removed from the GRS/APM input catalogue. The higher spatial resolution and dynamic range available in the CCD-based LARCS survey allows us to reliably deblend these systems and to investigate the properties of the missing galaxies.

- The missing population of Resolved galaxies has classification flags set in one or both of the APM passbands as stellar, merged or noise. Therefore they are

not included in the input catalogue of the 2dFGRS.

- The relatively compact Normal galaxies missing from the GRS/APM input catalogue are classified as stars due to the modest spatial resolution of the plates.

- The Low Surface Brightness galaxies are not present as the APM mostly classifies them as 'noisy' if they are detected. Indeed, the work of Cross et al. (2000) suggests that the majority of them will lie beyond the surface brightness detection limit of the 2dFGRS. These galaxies only represent 5 per cent of a magnitude-limited sample and so their absence is less of a concern than the other classes of missing galaxies.

To summarise, the APM input catalogue to the 2dFGRS survey has a stellar contamination of about 5–10 per cent as originally estimated, but misses 10-20 per cent of all galaxies at all magnitudes. In terms of their magnitudes, surface brightnesses, colours and compactness, the majority (80 per cent of the missing fraction, or $\sim$ 10 per cent of the total galaxy population) of these missing galaxies are similar to those included in the GRS/APM and so their absence could be corrected for by simply assuming they represent a random selection of the matched population. However, the remaining 5 per cent of the galaxy population which are missed consists of either LSB or Normal galaxies – these have significantly different properties than the matched population and so their absence cannot be easily corrected for in the 2dFGRS catalogue.

Chapter 4

Environmental Dependance

4.1 Abstract

The environmental dependance of galaxy colours in a subsample of LARCS clusters is investigated in this chapter. The properties of the galaxy populations in individual clusters are studied and advantage is taken of the homogeneity of LARCS to combine the clusters together to investigate weaker trends in the combined sample. It is found that the modal colours of galaxies lying on the colour-magnitude relation in the clusters become bluer by $d(B-R)/dr_p = -0.022 \pm 0.004$ from the cluster core out to a projected radius of $r_p = 6\,\mathrm{Mpc}$. The variation in modal galaxy colour with local density, Σ, is also examined for galaxies lying close to the colour-magnitude relation and it is found that the median colour shifts bluewards by $d(B-R)/d\log_{10}(\Sigma) = -0.076 \pm 0.009$ with decreasing local density across three orders of magnitude. The position of the red envelope of galaxies in the colour-magnitude relation is found not vary as a function of radius or density within the clusters, suggesting that the change in the modal colour results from an increasing fraction of bluer galaxies within the colour-magnitude relation, rather than a change in the colours of the *whole* population. This shift in the colour-magnitude relations with radius and local-density is found to be greater than expected from the changing morphological mix based on the local morphology–density relation. This effect is interpreted as an increasing fraction of galaxies in the lower density regions at large radii that exhibit signatures of recent star formation. Such signatures are not seen in the evolved galaxies in the highest density regions.

4.2 Introduction

Visvanathan and Sandage (1977) first noted that the more luminous early-type galaxies (ellipticals and S0s) within the Coma cluster and eight other local clusters exhibit systematically redder integrated colours than the late-types. These galaxies also demonstrate a tight correlation between their colours and magnitudes: colour-magnitude relationship (CMR; e.g. Bower, Lucey and Ellis 1992). Kodama & Arimoto (1997) show that the colour-magnitude relation is primarily due to the mean stellar metallicity (as suggested by Dressler 1984), while the scatter around the relation may be due to age effects (Kodama et al. 1999).

As one moves from clusters into the surrounding field the morphological mix in the galaxy population shifts from almost completely passive, early-types to one dominated by star-forming spiral galaxies. This is the origin of the Morphology-Density relation (T–Σ; Dressler 1980). The environmental "transition" region between clusters and the field is an important region to study if one is to learn what impact environment has on galaxy properties such as star formation rate, luminosity and morphology. Recent numerical simulations of clusters of galaxies show that the history of galaxy accretion is retained in the cluster's radial profile. The first galaxies to be accreted still reside nearer the centre while more recent additions are located preferentially on the outskirts of clusters (Diaferio et al. 2001). If the star formation in galaxies is suppressed when they enter the cluster environment (Balogh, Navarro & Morris 2000), then the variation in the typical accretion age of cluster galaxies with radius may be visible in the ages of the stellar populations of the passive cluster members which inhabit the colour-magnitude relation. Studies of galaxies in the outskirts of clusters and the variation in their properties with redshift can therefore inform us about how environment has altered the characteristics of cluster galaxies as the clusters have been assembled over the age of the Universe.

There are two main observational techniques to trace the variation in the stellar populations of galaxies between the field and cluster and its evolution with redshift: photometry and spectroscopy.

Wide-field photometric studies of clusters have uncovered evidence of changes in the colours of the galaxy populations with radius: Butcher & Oemler (1978, 1984)

first identified a photometric radial gradient; the fraction of blue galaxies increases with projected distance, out to $\sim 1.5\,\mathrm{Mpc}$ (as well as increasing dramatically with redshift). Kodama & Bower (2000) confirm this strong trend in their recent photometric study of the intermediate redshift clusters from the CNOC survey (Yee et al. 1996). Such trends with environment (i.e. radius or local density) could be due to (i) the systematic, intrinsic cluster colour gradient in one or both of the elliptical and S0 populations of the CMR with environment; or (ii) be primarily driven by the morphology-density relation (Dressler 1980), where the late-type to early-type galaxies ratio is a strongly decreasing function of local galaxy density, or equivalently an increasing function of clustocentric distance (Whitmore & Gilmore 1991). Thus the observed trend may simply reflect gross differences in the morphological mix, rather than representing evolution in the colours of the galaxies lying on the CMR with environment (as discussed below, variations in the morphological mix within the CMR may produce more subtle changes in colour with environment).

To reliably address this issue one needs to compare the properties of morphologically-selected (or failing that colour-selected) early-type galaxies in the outskirts of clusters with similar galaxies in the high density cores. Unfortunately, very few of the existing studies have the field of view, photometric precision (the expected colour shifts are < 0.10 mags) or morphological information necessary to investigate the possible variation with environment of the colour of the galaxies on the CMR. One of the few relevant studies is the recent investigation by Terlevich et al. (2001) of the $(U-V)$ colours of ~ 100 morphologically-classified early-type galaxies across a 1.5deg field within the Coma cluster ($z = 0.023$). They identify a trend for the colours of early-type galaxies to have systematically bluer colours at a fixed luminosity outside the core of the cluster. They interpret this as a result of age differences and suggest that there is a 2 Gyr difference between the mean luminosity-weighted ages of the stellar populations of galaxies in the core and those outside 0.5 Mpc.

At higher redshifts, deep multi-colour imaging with *Hubble Space Telescope* (*HST*) of distant clusters has sufficient sensitivity to uncover the signs of the variation in the CMR with environment, as well as providing morphological information which can be used to remove the effects of changes in the morphological mix from

the analysis (Ellis et al. 1997). However, the limited field of view of the *WFPC2* camera means that these *HST*-based surveys are restricted to the inner regions of clusters. For example, van Dokkum et al. (1998) discuss the radial dependence of the CMR for the distant cluster MS 1358+62 at $z = 0.33$ within a ~ 1.6 Mpc region. They find no radial dependence of the zero-point of the CMR, or the scatter around it, for bulge-dominated galaxies at any radius. They do find, however, an increasing scatter around the CMR for early-type disk galaxies in the outer parts of their survey region (van Dokkum et al. 2000). They propose that this trend is caused by infalling galaxies at the fringe of the cluster, but the absence of detailed morphological classifications for the early-type disk galaxies still leaves open the possibility that their result may again be due to the morphology-density relation.

Spectroscopy provides a much more sensitive tool to investigate the variation in the ages of the stellar populations of galaxies with environment, as well as providing unambiguous membership information for galaxies at large projected distances from the cluster. Spectral signatures of past activity can remain measurable for 3–5 Gyrs after the star formation has ceased, by which time the photometric signatures of recent star-bursts (i.e. blue colours) have become undetectable (e.g. Terlevich et al. 1999). Spectroscopic surveys of both local and distant clusters have uncovered precisely these signatures: identifying a class of galaxies with spectral features (enhanced Balmer absorption lines) indicative of recently terminated star formation (Couch & Sharples 1987; Caldwell et al. 1993). The galaxies are classified as a+k or k+a based on the strength of the Balmer absorption lines (Dressler et al. 1999), equivalent terms are E+A, PSG and HDS (Couch & Sharples 1987). Global gradients in these spectral indices have been identified in galaxies from a sample of X-ray selected distant clusters (Balogh et al. 1999). However, the samples available from most spectroscopic studies are relatively modest and for the most part lack detailed morphological classifications. Thus there is a similar ambiguity as in the analysis of the photometric gradient, due to the morphology-density relation, and it is difficult to interpret the origin of the radial gradients observed in key spectroscopic emission line indicators (Poggianti et al. 1999).

One survey which combines the photometric and spectroscopic techniques is the study of A 2390 ($z = 0.23$) by Abraham et al. (1996). They combine a large

spectroscopic survey covering a wide field (to provide spectral line indices and membership) and precise photometry and demonstrate that the colours of the reddest spectroscopically-confirmed cluster members on the colour-magnitude relation become progressively bluer as a function of clustocentric distance out to 5 Mpc, a trend which was also seen in Balmer line indices. They interpret these radial gradients as arising from a decrease in the mean luminosity-weighted age of the stellar populations in galaxies at larger projected distances from the cluster's centre. They suggest that this results from the truncation of star formation as galaxies and groups are accreted from the field onto the cluster outskirts, building up the cluster in an "onion-ring" fashion reminiscent of the hierarchical picture of cluster evolution (Lacey & Cole, 1993; Cole et al. 2000).

The impressive studies of the Coma cluster by Terlevich et al. (2001) and A 2390 by Abraham et al. (1996) illustrate the power of photometric comparisons of galaxies across a range of environments to address the questions posed earlier. Both studies, however, only cover a single cluster and so it is not clear how general their conclusions are, especially given the cluster-to-cluster differences which could arise from different evolutionary histories.

4.3 Sample

A subsample of 10 of the LARCS clusters are used in this study. These clusters are listed in Table 4.1 (an additional cluster, A 1079, $z = 0.132$, $L_X = 0.45 \times 10^{44} ergs^{-1}$ is present in the observations of A 1084 and it is included in this analysis). These ten clusters possess the highest quality and most complete photometric observations from the full survey. They are selected by taking those clusters that have complete imaging and more than 28 inter-tile overlapping regions (out of a potential of 32) to ensure high photometric accuracy. The subset covers a representative range of the complete LARCS sample, including clusters which both appear relaxed in their X-ray and galaxy distributions (e.g. A 1650), as well as more dynamically young, disturbed looking systems (e.g. A 1664 – which appears to have undergone a recent cluster–cluster merger; Edge, priv. comm.).

In this section the construction of colour-magnitude diagrams from the LARCS

catalogues is described, the use of the biweight method to fit the CMR and the distribution of the cluster galaxies (i.e. cluster morphology).

4.3.1 Statistical field correction

To examine the galaxy population of the clusters in the absence of spectroscopy it is necessary to correct for the "field" contamination in a given cluster catalogue. The statistical subtraction method utilized here is described in detail in Appendix B. The use of spectroscopy to define cluster membership will be examined in Chaper 6.

Briefly, the field population is determined from the outer regions of the LARCS cluster mosaics at a radius well beyond 6 Mpc (at a redshift of $z = 0.12$). Using such an arbitrary radius is a compromise between the desire to minimize the potential number of cluster galaxies in the field sample whilst maximizing the area of field covered. The field regions from each cluster are all examined by eye prior to being stacked to give the average field distribution. A field region is rejected if it contains an obvious (visual) over-density of galaxies in it. For example, part of the field of A 1084 is excluded from the final stacked field sample as it contains A 1079. This field is the only part that is rejected in this manner and it is not considered that the resultant field sample is biased towards a lower mean density because of its removal. Once generated, the final stacked field population* is then appropriately area-scaled to that of the cluster sample that is to be corrected.

The colour-magnitude diagrams for galaxies from the cluster sample and the final, scaled, stacked field sample are then compared. By direct comparison of corresponding regions on the colour-magnitude diagrams each galaxy in the cluster sample is assigned a probability of being a field galaxy. Then, using a Monte Carlo method, the field population is subtracted off based upon these probabilities. As described in Appendix B, however, problems can arise if the calculated probability exceeds 1.0. The solution utilized here is to expand the interval in colour and magnitude until the calculated probability lies in the range $0.0 < \mathrm{P(Field)} < 1.0$ (see Appendix B for a full discussion).

*The final effective area of the field sample used is $\sim$ 13.1 square degrees. Each individual mosaic covers $\sim$ 3.1 square degree on the sky.

Table 4.1: Details of the clusters from the LARCS subsample used in this chapter. The parameters of the biweight fit to the CMR within 2 Mpc of the centre of each of the clusters as plotted in Figure 4.1 are listed. The slope, colour at the fiducial magnitude and associated errors are taken from the median of 100 realizations of the background subtraction. The apparent R-band magnitude corresponding to the fiducial absolute magnitude of $M_V = -21.8$ is also given for each cluster. The colour of each CMR at a fiducial magnitude equivalent to $M_V = -21.8$ and the slope of the relationship are examined as a function of redshift in Figure 4.2.

Cluster	Slope	Redshift	$(B-R)_{M_V=-21.8}$	$R_{M_V=-21.8}$
A 22	0.131	-0.054 ± 0.008	1.85 ± 0.06	17.12
A 550	0.125	-0.056 ± 0.006	2.05 ± 0.07	17.01
A 1079 ‡	0.132	-0.053 ± 0.002	1.80 ± 0.03	17.14
A 1084	0.134	-0.051 ± 0.007	1.83 ± 0.05	17.17
A 1285	0.106	-0.066 ± 0.014	1.87 ± 0.12	16.61
A 1437	0.133	-0.072 ± 0.001	1.94 ± 0.11	17.15
A 1650	0.084	-0.047 ± 0.003	1.69 ± 0.06	16.06
A 1651	0.084	-0.034 ± 0.002	1.63 ± 0.07	16.06
A 1664	0.127	-0.087 ± 0.005	1.73 ± 0.12	17.05
A 2055	0.102	-0.065 ± 0.003	1.70 ± 0.07	16.53
A 3888	0.151	-0.096 ± 0.015	2.12 ± 0.15	17.47

(‡) Although not originally fulfilling the LARCS selection criteria, A 1079 resides in the field of A 1084 at a similar redshift to the latter and is thus considered here.

The statistical Monte Carlo background subtractions are realized 100 times and the colour-magnitude diagrams presented represent the median of those background subtractions.

4.3.2 Fitting the CMR

The background subtraction algorithm (see Appendix B) is run on each cluster to produce 100 realizations of the cluster's colour-magnitude diagram. In fitting the CMR only those galaxies whose absolute rest frame magnitude is brighter than $M_V = -20$ are used. This magnitude is chosen to correspond to the equivalent limit in Butcher & Oemler (1984) and is calculated using relations presented by Kodama & Arimoto (1997). Each of the CMRs are fitted using a robust biweight method (Beers et al. 1990) identical to that employed by de Propris et al. (1998). The biweight method is a statistically robust estimator that weighs outlying points (such as the blue population) low in order to find the best fit line to the CMR.

In Figure 4.1 the distribution of galaxies on colour-magnitude diagrams for one such realization of each of the clusters within a radial extent of $r_p < 2$ Mpc is shown. Details of the median values of the fits to the 100 realisations for each cluster and their associated errors are presented in Table 4.1.

All of the clusters show colour-magnitude relations for the redder, early-type galaxy members. Strong CMRs are seen in A 550, A 1285, A 1437, A 1650, A 1651 and A 3888; whilst A 1079, A 1084 and A 1664 exhibit much weaker relations. All the CMR's exhibit a negative slope as expected from the colour-luminosity relation of early-type galaxies (Table 4.1, Figure 4.2, Figure 4.3).

The colour at a fiducial magnitude of $M_V = -21.8$ (equivalent to an $L^\star$ galaxy) is also calculated from the result of the biweight fit; $(B-R)_{M_V=-21.8}$. These colours are presented in Figure 4.2 and tabulated along with the values of $M_V = -21.8$ in Table 4.1. The $(B-R)_{M_V=-21.8}$ colours of galaxies on the CMRs in the clusters form a tight relation, median deviation of 0.08 mags, which steadily reddens with redshift: the K-effect. Also shown is the expected variation with redshift in the colour of a galaxy which formed all its stars at very high redshift, $z \gg 2$. The observed reddening in colour at the fiducial magnitude is broadly in line with that expected

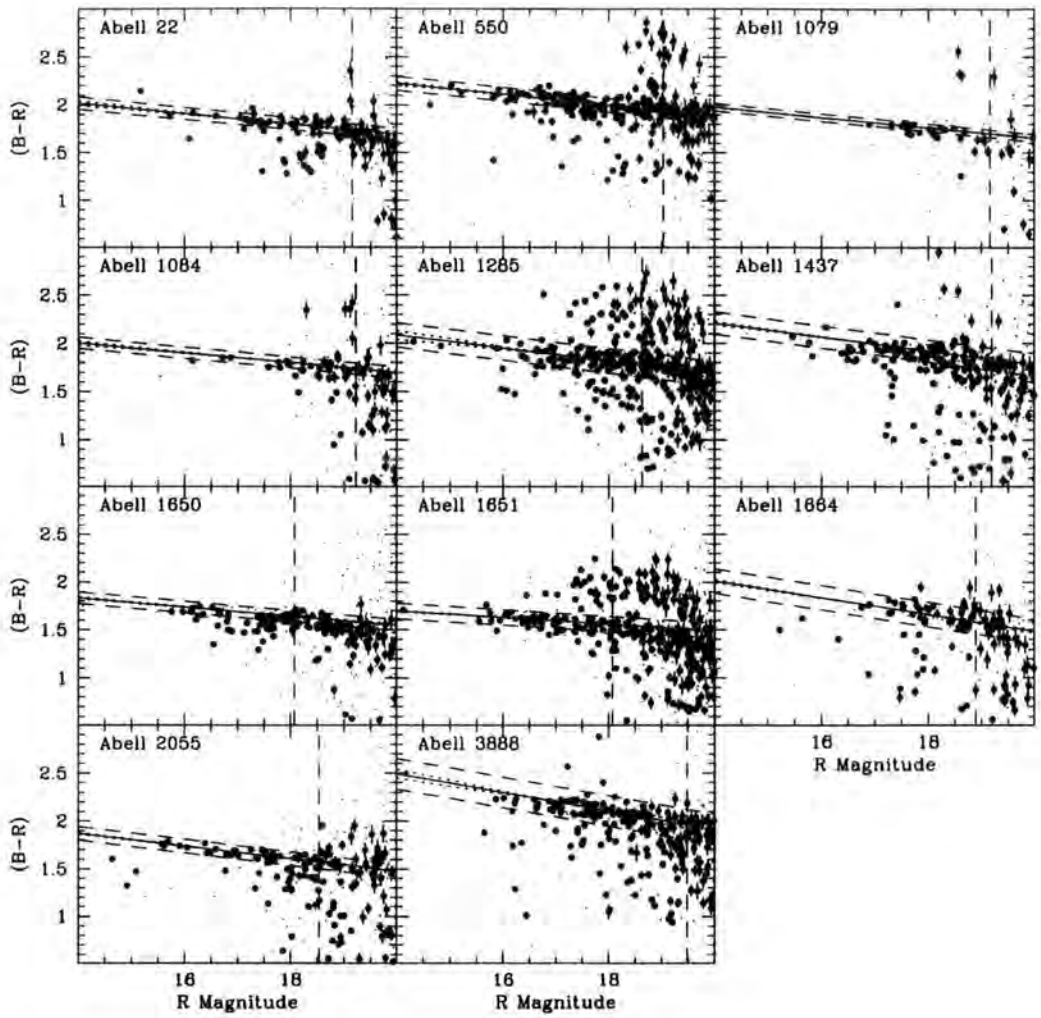

Figure 4.1: The colour-magnitude diagrams for the 11 cluster subsample. All galaxies within a 2 Mpc radius of the cluster centre from one realization of the field subtraction are plotted as heavy dots. The smaller dots are the galaxies which are rejected as field by the statistical subtraction method. The biweighted fit to the CMR is shown as a solid line. The scatter of the fit is represented by the flanking parallel lines to this fit, whilst the uncertainty in the gradient is shown as the dotted line (centred at $R = 17$). The vertical line denotes the absolute magnitude limit of $M_V = -20$ used to define the galaxy sample used for the fit.

for a population which formed the bulk of its stars at high redshift (Metcalfe et al. 1991). Similarly, in Figure 4.3, the evolution in the gradient of the CMR is shown. This broadly traces what one might expect purely from the differential K-corrections.

The statistical field correction applied is designed to detect overdensities above the level of the "average" field on the colour-magnitude plane. Therefore, if there are other over-dense regions in the fields of the clusters one expects to see some secondary CMRs in the colour-magnitude diagrams. Such CMRs are clearly seen in the colour-magnitude diagrams of A 550, A 1285 and A 1651. As expected from the available volume, these CMRs are higher redshift clusters in the background of the observed clusters, for example, the background cluster in A 1651 ($z = 0.084$) is identified as A 1658. Using the photometric redshift estimator method of Yee et al. (1999) its redshift is estimated to be $z \sim 0.145$. To reduce the influence of these systems on the biweight estimator used to fit the CMR of the LARCS cluster, an appropriate red limit is employed to ensure that the fit converges on the desired CMR.

4.3.3 The spatial distribution of cluster galaxies

The CMRs are now used to map out the two dimensional galaxy distribution within the clusters. Assuming that the galaxies on the CMR are associated with the cluster, a cluster galaxy is defined to be within the 1σ scatter of its fitted colour-magnitude relation (listed in Table 4.1). This criteria is applied to the whole sample of galaxies in each field. Having obtained their positions on the sky, a 500 kpc smoothing length is used to generate smoothed galaxy distribution maps for each cluster. The resultant distributions for the central $25'$ of each cluster are presented in Figure 4.4.

The brightest galaxy in these X-ray luminous clusters is, morphologically, typically a giant elliptical (or cD) and these are identified using the CMR and the morphology of their extended low surface brightness halo in the imaging data. For the more regular clusters, the position of this galaxy is generally in agreement with the peak of the distribution of colour-selected cluster members (Beers & Tonry 1986; Figure 4.4) and therefore the position of this galaxy is always used to define the

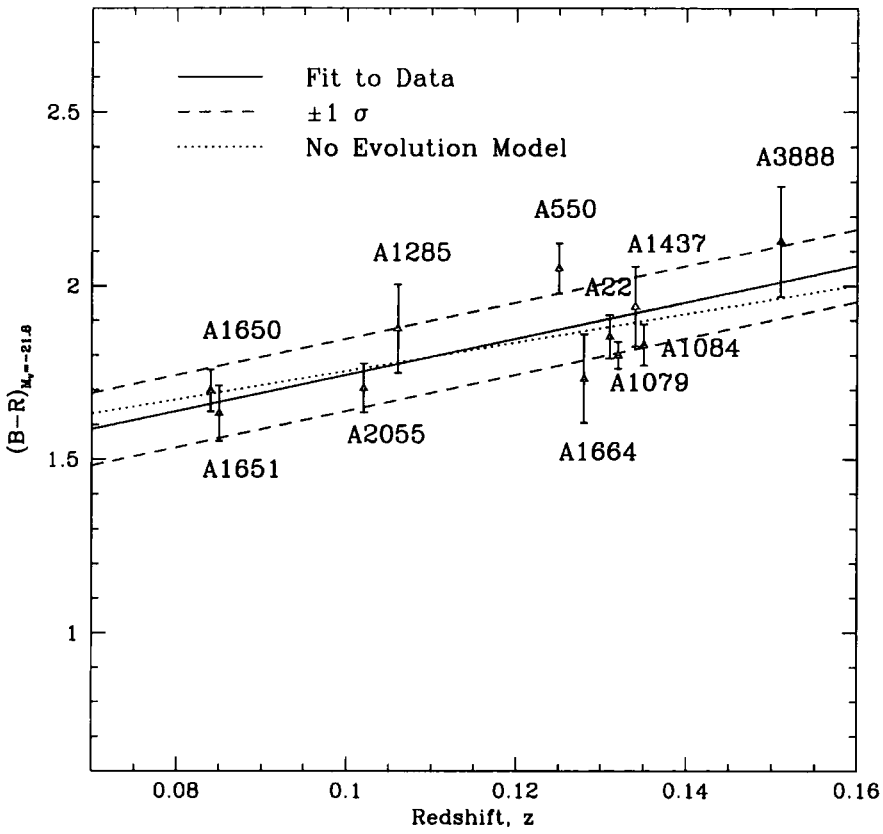

Figure 4.2: Median observed $(B-R)$ colour at $M_V = -21.8$ calculated from 100 realizations of the background subtraction plotted versus cluster redshift (with no K-correction applied). The solid line is the best fit to the data, with the parallel dashed lines being $\pm 1\sigma$. The dotted line illustrates the expected evolution in the galaxy colours of galaxies which formed all their stars at high redshift, $z \gg 2$. The clusters form a tight relation evolving redward with increasing redshift.

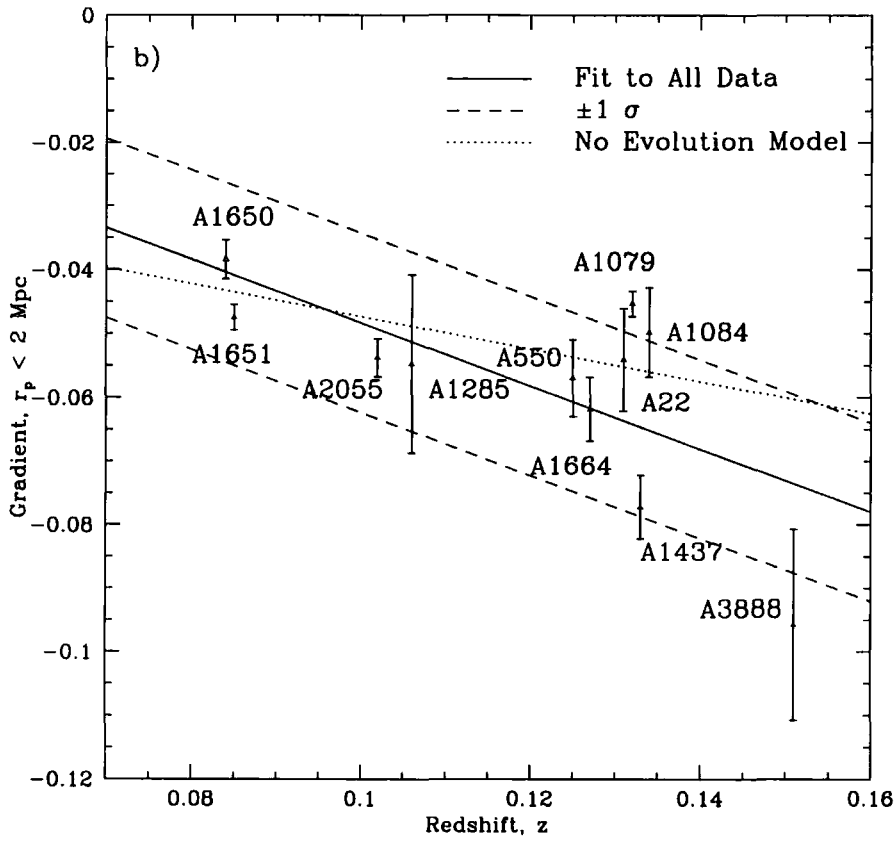

Figure 4.3: The variation in slope of the CMR with redshift. There is a trend for steeper CMR's at higher redshifts, as expected from the effects of shifting K-corrections on the observed $(B - R)$ colours of the galaxies along the CMR. A "no evolution" model is plotted which shows the behaviour expected just from the differential K-corrections.

cluster centre. The clusters demonstrate a broad range of morphological types ranging from very regular, highly-concentrated examples (e.g. A 550), through to very diffuse systems (e.g. A 1664) whose central galaxy position does not coincide with any of the main spatial overdensities seen in the colour-selected cluster members.

4.4 Analysis and Results

In this section the analysis of the properties of the cluster's CMRs as a function of radius and local galaxy density is analyzed.

4.4.1 Radial variation of the CMR

A search for any radial variations in the CMR within the clusters is undertaken by dividing the central 6 Mpc diameter region of clusters into three anulii. Note, the virial radii for these X-ray luminous clusters should lie in the range 2–4 Mpc (Carlberg et al. 1996). For each radial bin, a biweighted fit is calculated to the CMR and the colour at a fiducial magnitude (equivalent to $M_V = -21.8$) is obtained. Further, the colour based on a fixed slope (using the fit to the CMR in the central 2 Mpc diameter annulus) is calculated for the field-subtracted cluster realizations and it is found that this method produces the same results as an unconstrained gradient fit, within 1 standard deviation (see Table 4.2). The result of these fits are presented in Table 4.2, whilst the colour-magnitude relations for the first three radial intervals in each cluster can be seen in Figures 3.4.

Table 4.2: Parameters of the biweight fit to the CMRs of the clusters, split into three equal radial bins as plotted in Figures 4.5 and 4.4. The slope and colours are those found using the biweight estimator fit to each radial bin. The values reported in the final column (fixed slope) uses the slope of the central bin in the particular cluster.

Cluster	Radius (Mpc)	Slope	$(B-R)_{M_V=-21.8}$	$(B-R)_{M_V=-21.8}$ Fixed Slope
A 22	0–1	-0.054 ± 0.008	1.85 ± 0.07	1.85 ± 0.07

...continued from previous page

Cluster	Radius (Mpc)	Slope	$(B-R)_{M_V=-21.8}$	$(B-R)_{M_V=-21.8}$ Fixed Slope
	1–2	-0.110 ± 0.010	1.87 ± 0.12	1.73 ± 0.21
	2–3	-0.052 ± 0.007	1.75 ± 0.17	1.73 ± 0.22
A 550	0–1	-0.057 ± 0.001	2.05 ± 0.07	2.05 ± 0.07
	1–2	-0.060 ± 0.003	2.02 ± 0.15	2.02 ± 0.14
	2–3	-0.061 ± 0.014	1.94 ± 0.35	1.92 ± 0.38
A 1079	0–1	-0.045 ± 0.003	1.80 ± 0.05	1.80 ± 0.05
	1–2	-0.101 ± 0.004	1.82 ± 0.07	1.76 ± 0.09
	2–3	-0.081 ± 0.009	1.82 ± 0.20	1.85 ± 0.33
A 1084	0–1	-0.050 ± 0.009	1.83 ± 0.06	1.83 ± 0.06
	1–2	-0.052 ± 0.014	1.78 ± 0.42	1.79 ± 0.31
	2–3	-0.057 ± 0.027	1.55 ± 0.54	1.66 ± 0.56
A 1285	0–1	-0.055 ± 0.007	1.87 ± 0.10	1.87 ± 0.14
	1–2	-0.060 ± 0.013	1.86 ± 0.33	1.86 ± 0.34
	2–3	...	...	...
A 1437	0–1	-0.077 ± 0.005	1.94 ± 0.12	1.94 ± 0.12
	1–2	-0.065 ± 0.003	1.87 ± 0.21	1.87 ± 0.21
	2–3	...	...	...
A 1650	0–1	-0.038 ± 0.001	1.70 ± 0.06	1.70 ± 0.06
	1–2	-0.050 ± 0.005	1.65 ± 0.08	1.65 ± 0.08
	2–3	-0.041 ± 0.011	1.63 ± 0.07	1.65 ± 0.06
A 1651	0–1	-0.047 ± 0.002	1.63 ± 0.07	1.63 ± 0.08
	1–2	-0.060 ± 0.011	1.63 ± 0.16	1.64 ± 0.24
	2–3	-0.048 ± 0.008	1.59 ± 0.15	1.60 ± 0.14
A 1664	0–1	-0.062 ± 0.012	1.73 ± 0.07	1.73 ± 0.07
	1–2	-0.058 ± 0.039	1.76 ± 0.07	1.76 ± 0.08
	2–3	-0.076 ± 0.024	1.76 ± 0.08	1.76 ± 0.08
A 2055	0–1	-0.054 ± 0.007	1.71 ± 0.08	1.71 ± 0.08
	1–2	-0.050 ± 0.021	1.67 ± 0.15	1.62 ± 0.18

...continued from previous page

Cluster	Radius (Mpc)	Slope	$(B-R)_{M_V=-21.8}$	$(B-R)_{M_V=-21.8}$ Fixed Slope
	2–3	-0.054 ± 0.024	1.67 ± 0.26	1.60 ± 0.28
A 3888	0–1	-0.096 ± 0.015	2.13 ± 0.13	2.12 ± 0.13
	1–2	-0.103 ± 0.043	2.08 ± 0.22	2.04 ± 0.25
	2–3	-0.193 ± 0.013	1.88 ± 0.35	1.90 ± 0.36

In most of the clusters a trend in colour at the fiducial magnitude of $\Delta(B-R) \sim -0.09 \pm 0.11$ blueward out to 3 Mpc (Table 4.2) is observed. No significant change in this trend is observed with cluster redshift. Discrepant results arise in three clusters. In A 1084, the change in $(B-R)$ colour from the central radial bin to the third is much more than $\Delta(B-R) \sim -0.10$. This is attributed to the poor fit in the third radial bin (see Figure 4.5). The third radial bin of A 3888 is similarly poorly fitted. In A 1664, no radial trend is apparent.

There are, however, two shortcomings of this analysis. Firstly, the formal errors on the biweighted fits for individual clusters are large enough that the colour gradient trend in the individual CMRs is insignificant. Secondly, the biases in the statistical correction of the colour-magnitude diagram makes it increasingly unreliable at large radii (Appendix B). A different approach must therefore be adopted.

To trace the variation in the colour of the CMR out to larger radii and better quantify its strength, the homogeneity of the cluster sample and observations can be exploited by combining all of the clusters together into a composite cluster. This will improve the statistics for cluster members at large radii and provide a more robust measurement of the trends in the CMR.

The production of a composite cluster necessitates the transformation of the magnitudes, colours and positions of the galaxies in the individual clusters onto a common scale. The transformation of the magnitudes uses the relative magnitudes of non-evolving early-type L^* galaxies from Table 4.1, an assumption which is supported by the agreement between the no evolution predictions for colour evolution and the observations across the limited redshift range spanned by the sample. The

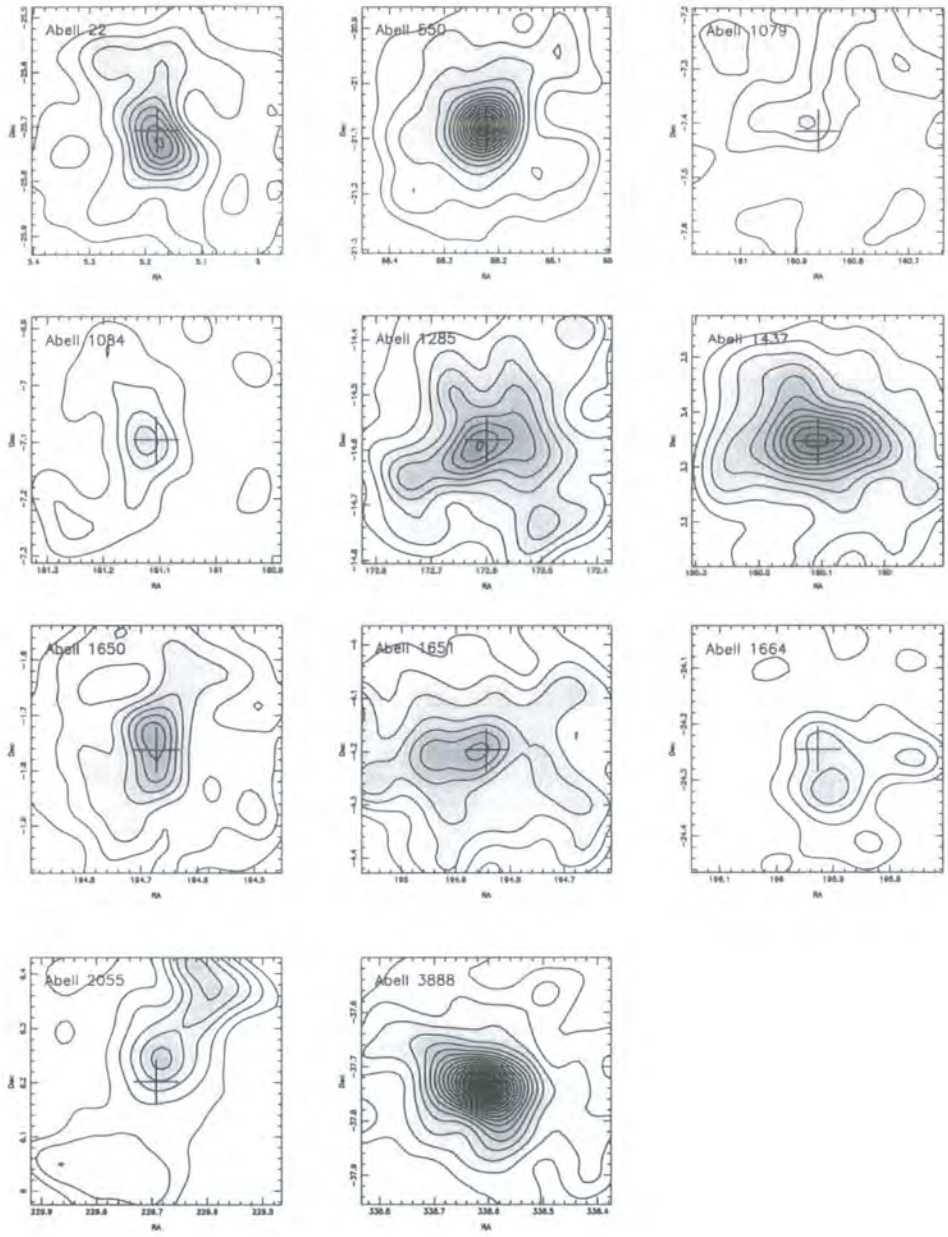

Figure 4.4: The two dimensional smoothed spatial distributions of the cluster galaxies lying within the scatter of the biweight fit to the CMR. A 500 kpc smoothing length scale is used on the positions of galaxies to generate these maps. The lowest contour represents a surface density of cluster galaxies of $6.0\,\mathrm{Mpc}^{-2}$, with each subsequent inward contour denoting an increase of $2.0\,\mathrm{Mpc}^{-2}$. The crosses indicate the adopted centre of the clusters based on the position of the apparent brightest cluster member from the CMR. Although the areas of A1079 and A1084 overlap, the contour plots are different as the clusters possess different CMRs.

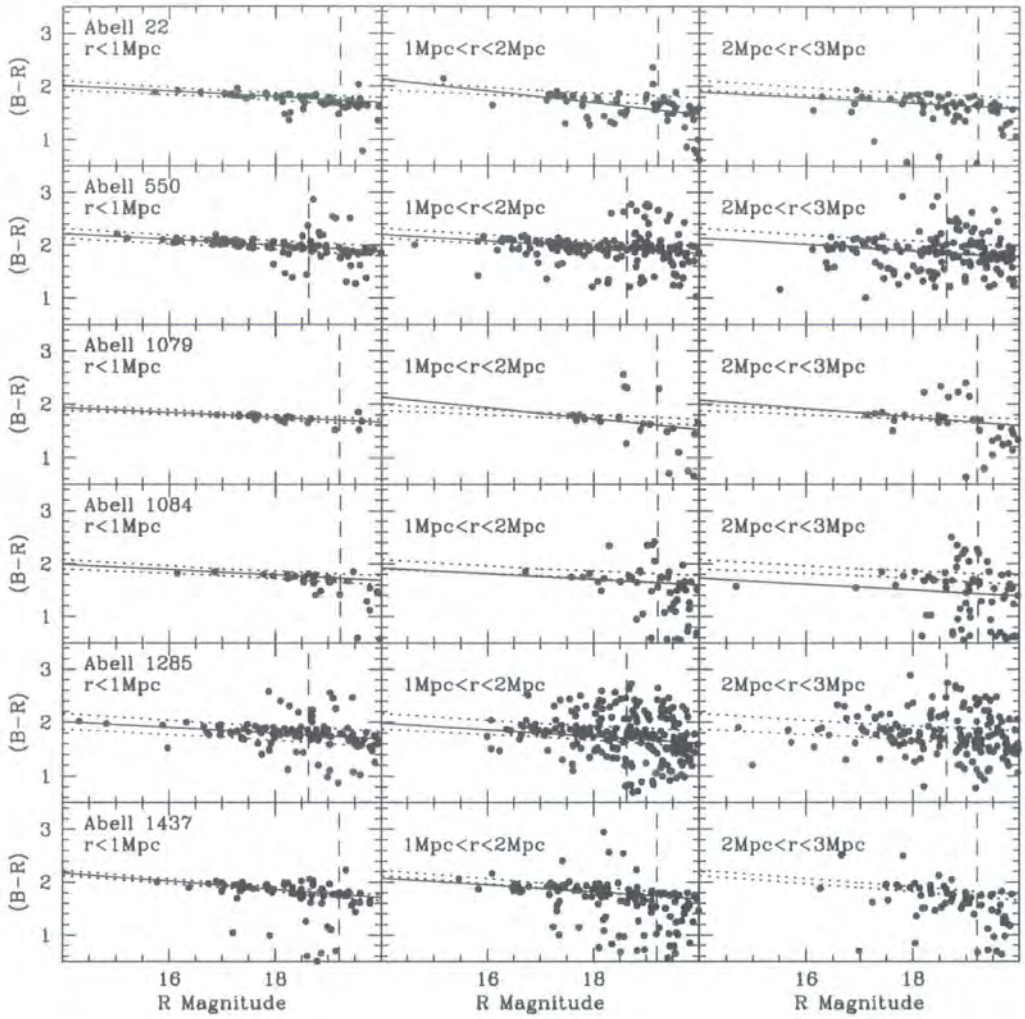

Figure 4.5: (a) Colour-magnitude diagrams for Abell 22, 550, 1079, 1084, 1285 and 1437 in 1-Mpc wide radial bins. Each diagram is one of the 100 realizations made with the background subtraction algorithm. The solid line, where present, is the biweighted fit to the CMR. The short dashed lines denote the errors associated with the $r < 1$ Mpc fit of each cluster. The longer dashed, vertical lines denote the $M_V = -20$ fiducial magnitude limit; only objects brighter than this are considered in the biweighted fit. For most of the clusters, there is a trend for the CMR to evolve bluewards by $\Delta(B-R) \sim -0.09 \pm 0.11$ over 3 Mpc.

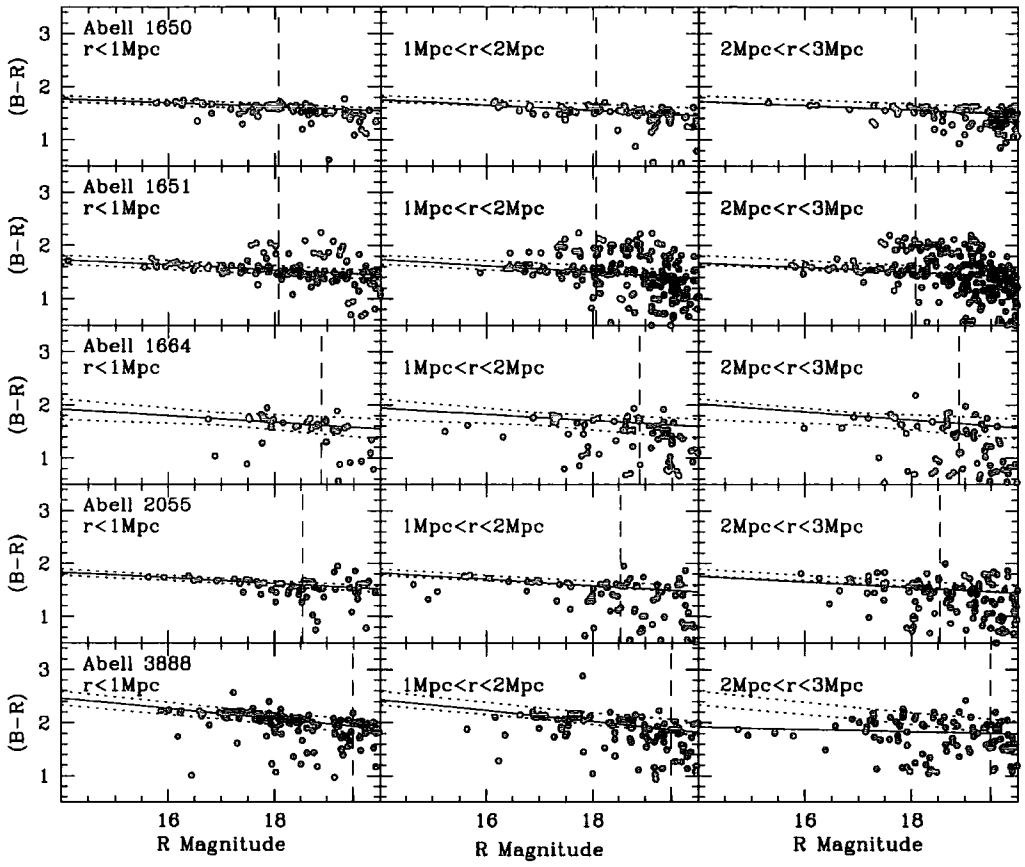

Figure 4.4: (b) As for Figure 4.5a, but with Abell 1650, 1651, 1664, 2055 and 3888.

apparent magnitudes of the galaxies can therefore be transformed to a median redshift of $z = 0.12$. To transform the colours of the galaxies on the CMR onto a uniform scale the observed CMR's are simply reduced to provide colours relative to the fitted relation. These can then be easily transformed to $z = 0.12$. The slope adopted for this transformation is assumed to be constant with radius, and equivalent to the observed values presented in Table 4.1. The most meaningful method to compare the radial positions of galaxies in the various clusters is to use their radius normalised to the virial radius of the clusters, $R_{\rm vir}$. However, the narrow X-ray luminosity range for the sample, combined with weak dependence of the virial radius on the X-ray luminosity, $R_{\rm vir} \propto L^{1/6}$ (Babul et al. 2001), means that $R_{\rm vir}$ is only expected to vary by 20 percent across the whole sample. Hence, for simplicity, the clusters are all scaled to a fixed metric size.

The final step in the analysis of the composite cluster is to construct colour histograms down to the fiducial magnitude limit, $M_V = -20$. These histograms are statistically corrected using the binned colour distribution from the field. This approach is valid because parameter of merit is the colour of the CMR, rather than its slope; information on the magnitudes of the galaxies no longer need to be retained. The advantage of using colour histograms is that it circumvents some of the concerns about the field correction techniques used on the colour-magnitude plane (Appendix B).

A colour histogram of the field sample is generated in an identical manner to the cluster sample. An appropriately area-scaled region of the field is subtracted off the composite cluster histogram in each radial bin. The result of this analysis is illustrated in Figure 4.5.

Figure 4.5 shows that the red cluster members in the CMR are still visible as a peak in the colour histogram as far out as ~ 6 Mpc from the cluster core. Beyond this, the red galaxies become swamped by an increasingly blue cluster population and the noise from the statistical field correction. To identify the peak in the CMR and quantify how it changes with radius the colour histograms are fitted with a Gaussian using a χ^2 minimization method. In making the fit the colour range is restricted to $(B - R) = 1.6$–2.2. An initial guess of the modal colour, its amplitude and the width of the distribution, σ_{PEAK}, is made and fed in as

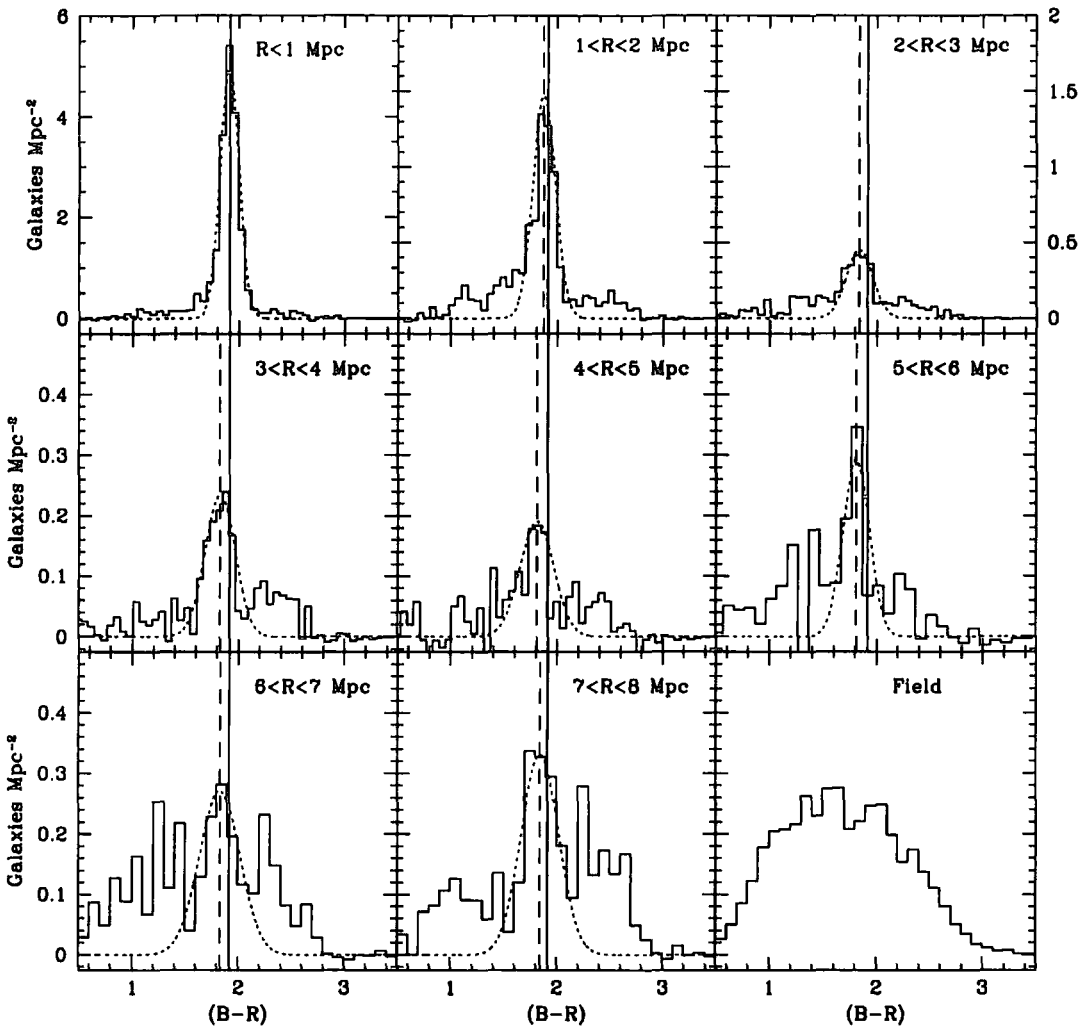

Figure 4.5: Colour histograms of the composite cluster from the center to a maximum radial extent of 8 Mpc. The field colour distribution is also pictured in the lower-right for reference (arbitrarily scaled). The best fit Gaussians are shown for the CMR peaks in each radial bin. The solid vertical line is the colour of the CMR peak in the central bin. The dashed vertical line is the peak of each individual radial bin. A blueward shift in the peak of the CMR can be seen clearly even by the second radial interval, although the position of the CMR peak becomes more uncertain at large radii. The CMR evolves blueward at a rate of $d(B-R)/dr_p = -0.022 \pm 0.004$ from the centre to the outer regions. Also note that the CMR appears to the broaden at larger radius.

Table 4.3: Peak colour and full width of the CMR's variation with radius as estimated from the fitting Gaussians to the colour distributions (Figure 5).

Radius (Mpc)	Peak $(B-R)_{M_V=-21.8}$	$\sigma_{\rm Peak}$
0–1	1.92 ± 0.01	0.13 ± 0.01
1–2	1.88 ± 0.02	0.15 ± 0.02
2–3	1.84 ± 0.03	0.18 ± 0.03
3–4	1.83 ± 0.04	0.20 ± 0.03
4–5	1.81 ± 0.05	0.23 ± 0.04
5–6	1.81 ± 0.05	0.19 ± 0.04
6–7	1.83 ± 0.05	0.23 ± 0.05
7–8	1.84 ± 0.06	0.25 ± 0.06

the input to the Gaussian fitting routine. The routine outputs new estimates of these values which are iteratively fed into the fitting routine until convergence is achieved. The resultant values are checked by visually inspecting the fit. The Gaussian fits generate the colour of the CMR at the fiducial magnitude and a measure of the width of the CMR together with associated errors in each radial interval and are presented in Table 4.3 and illustrated in Figure 4.5. The peak of the CMR in the combined cluster evolves bluewards with radius at a rate of $d(B-R)/dr_p = -0.022 \pm 0.004$ (where r_p is the projected radius from the cluster core), equivalent to $\Delta(B-R) \sim -0.11 \pm 0.05$ from the central radial bin out to 6 Mpc. Beyond 6 Mpc the constraints on the colour gradient trend of the CMR become much less reliable and so the discussion is limited to the region within 6 Mpc.

4.4.2 The colour–local density relation

As the clusters in the survey exhibit a wide range in their morphologies (see Figure 4.4), a more general method of combining the galaxy samples from the different clusters is sought, rather than simple radial-averaging, to investigate the environmental differences within the composite sample. Local galaxy density provides such

Table 4.4: Peak colour and full width of the CMR's variation with local galaxy density as estimated from the fitting Gaussians to the colour distributions (Figure 6).

Log Density (Mpc^{-2})	Peak $(B-R)_{M_V=-21.8}$	σ_{Peak}
> 2.5	1.96 ± 0.01	0.15 ± 0.02
2.0–2.5	1.88 ± 0.02	0.15 ± 0.02
1.5–2.0	1.87 ± 0.03	0.17 ± 0.03
1.0–1.5	1.85 ± 0.04	0.15 ± 0.04
0.5–1.0	1.76 ± 0.04	0.19 ± 0.04
0.0–0.5	1.77 ± 0.05	0.22 ± 0.05
-0.5–0.0	1.79 ± 0.05	0.22 ± 0.06
-1.0– -0.5	1.76 ± 0.06	0.23 ± 0.08
< -1.0	1.78 ± 0.07	0.23 ± 0.11

a comparable measure of environment across the sample and so this is employed instead.

The local density for each galaxy in the clusters are calculated and these are used to assign the galaxy to its relevant environmental bin. The local galaxy density, Σ, is estimated by finding the surface area on the sky occupied by that galaxy and its ten closest neighbours down to the fiducial magnitude limit of $M_V = -20$. Due to field galaxy contamination, this local density will clearly be over-estimated. This overestimation is corrected for by subtracting off a constant density estimated from the median local density of the combined field sample. The sample is then divided up into eight logarithmically-spaced bins covering three orders of magnitude in local galaxy density (Table 4.4).

For each local density bin a colour histogram is created. As before, the clusters are transformed to a median redshift of $z = 0.12$ and the slope of the CMR is corrected for. Since these colour histograms are not corrected for field contamination, it is necessary to subtract off an appropriately area-scaled colour distribution for the field sample (see the lower-right panel in Figure 4.5). Finding the area from which a restricted range of densities are drawn is non-trivial; a region of high density will

have a much smaller field correction than a region of low density. An adaptive map of the field region is generated by binning up the positions of the field galaxies and taking the median density of each bin. The map is thresholded using density cuts equal to the eight logarithmically-spaced bins in local galaxy density to generate the area occupied by field galaxies of that local galaxy density. This measure of the area is used to scale the colour distribution of the field sample and subtract it from each local density bin's colour histogram.

The results of this analysis are presented in Figure 4.6. The combined cluster evolves bluewards with decreasing local density at a rate of $d(B-R)/d\log_{10}(\Sigma) = -0.076 \pm 0.009$, equivalent to $\Delta(B-R) \sim -0.20 \pm 0.06$ from the highest local density regime covered by the sample ($\log_{10}(\Sigma) > 2.5$) to three orders of magnitude lower. The results from this analysis provide a comparable estimate of the shift in the CMR colour to that identified using radial considerations (for the typical cluster in the sample a local galaxy density of $\log_{10}(\Sigma) \sim 0.5$ is found at a radius of $\sim 2\,\mathrm{Mpc}$).

4.4.3 Width of the CMR

From the histograms presented in Figures 4.5 and 4.6, the behaviour of width of the CMR is examined as a function of environment. The Gaussians fitted to the data in these Figures are used to obtain σ_{Peak} -an estimate of the CMR's width. These values are plotted in the upper panels of Figure 4.7, with tabulated values presented in Tables 4.3 & 4.4. It is found that the CMR peak does appear to broaden with increasing radius and local galaxy density by $\Delta\sigma_{\mathrm{Peak}}(B-R) \sim 0.15$ across the ranges studied, although there is considerable uncertainty on the individual measurements.

To further investigate how the colour distribution of galaxies in the CMR varies with environment the colours of the 30^{th} and 70^{th} percentiles from the red side of the colour histogram distributions (Figures 4.5 & 4.6) are calculated. The 30^{th} percentile represents the reddest members of the CMR peak, the typical colour of this population appears to remain nearly constant in colour (Figure 4.7) out to $\sim 6\,\mathrm{Mpc}$ of the sample (i.e. to where the CMR peak is still visible in Figure 4.5).

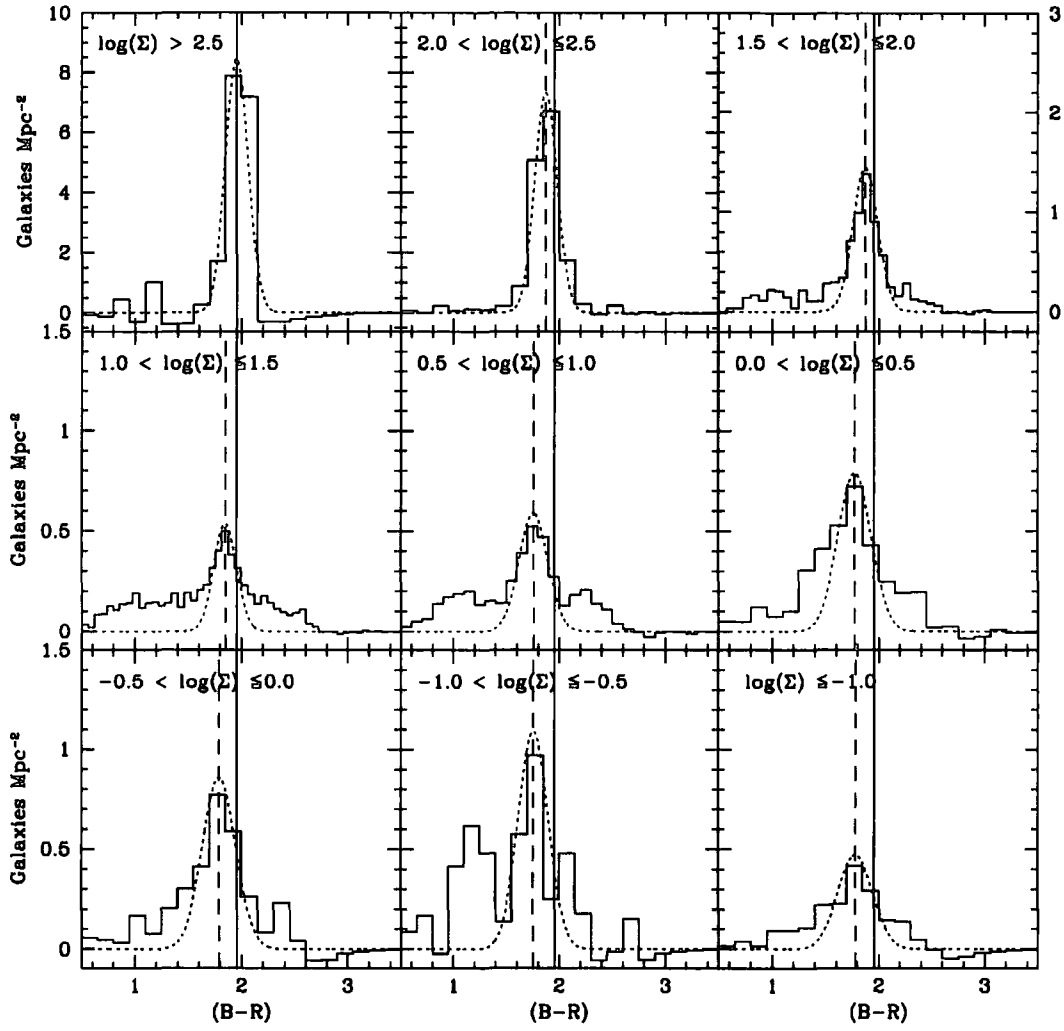

Figure 4.6: Colour histograms of the composite cluster colour magnitude relations after correcting for the slope in the CMR and field contamination in logarithmic density intervals. The best-fit Gaussians are shown for the CMR peaks in each density bin. The solid vertical line shows the colour of the peak of the CMR in the high density bin. The dashed vertical line is the peak in the particular density interval. The CMR peak evolves steadily blueward at a rate of $d(B-R)/d\log_{10}(\Sigma) = -0.076 \pm 0.009$ across three orders of magnitude in local galaxy density (Σ).

A similarly selected sample exhibits the same near constant trend in colour with local galaxy density (Σ). In contrast, the trend of the 70^{th} percentile, representing the bluer members of the CMR, shows a strong shift to the blue with both radius and local galaxy density.

Thus whilst the colour of the reddest members of the CMR appears to be relatively constant in different environments, the width of the CMR peak broadens at larger radii and lower local galaxy density, reflecting an increasing tail of blue galaxies on the outskirts of the clusters (see Figures 4.5, 4.6 & 4.7).

4.4.4 Blue cluster galaxies

The non-CMR population is now quantified by deriving the Butcher-Oemler blue fraction (Butcher & Oemler, 1984), f_B. The blue fraction is calculated for the clusters using the method described in Butcher & Oemler's (1984) landmark study. Briefly, to calculate f_B only those galaxies whose magnitude is brighter than $M_V = -20$ and lie within a radius of R_{30} are used. The parameter, R_{30}, denotes the radius of a circle containing 30 per cent of the cluster's projected galaxy distribution. After background subtraction, the net number of galaxies in these populations are a measure of cluster richness, denoted N_{30}. The blue fraction is the fraction of this population whose rest frame colour is $\Delta(B-V) = -0.2$ bluer than the fitted CMR. The concentration of the cluster is defined as $\log_{10}(R_{60}/R_{20})$ and is considered to be a measure of the cluster's central concentration (Butcher & Oemler 1978, 1984).

In Table 4.5 the median value of f_B for the clusters and the associated values of R_{30}, N_{30} and the concentration are presented. Also noted are the morphologies of the clusters from Figure 4.4.

It must be stressed that these values of f_B are likely to be slightly low due to the biases in the statistical background correction technique employed. See Appendix B for discussion on this point. There may also be biases arising from the field sample that is used. Since they are taken at the very edge of the cluster they may be marginally more dense than the 'average' field thus making f_B further underestimated. This effect is assumed to be small and the statistical background correction to be the dominant source of any bias.

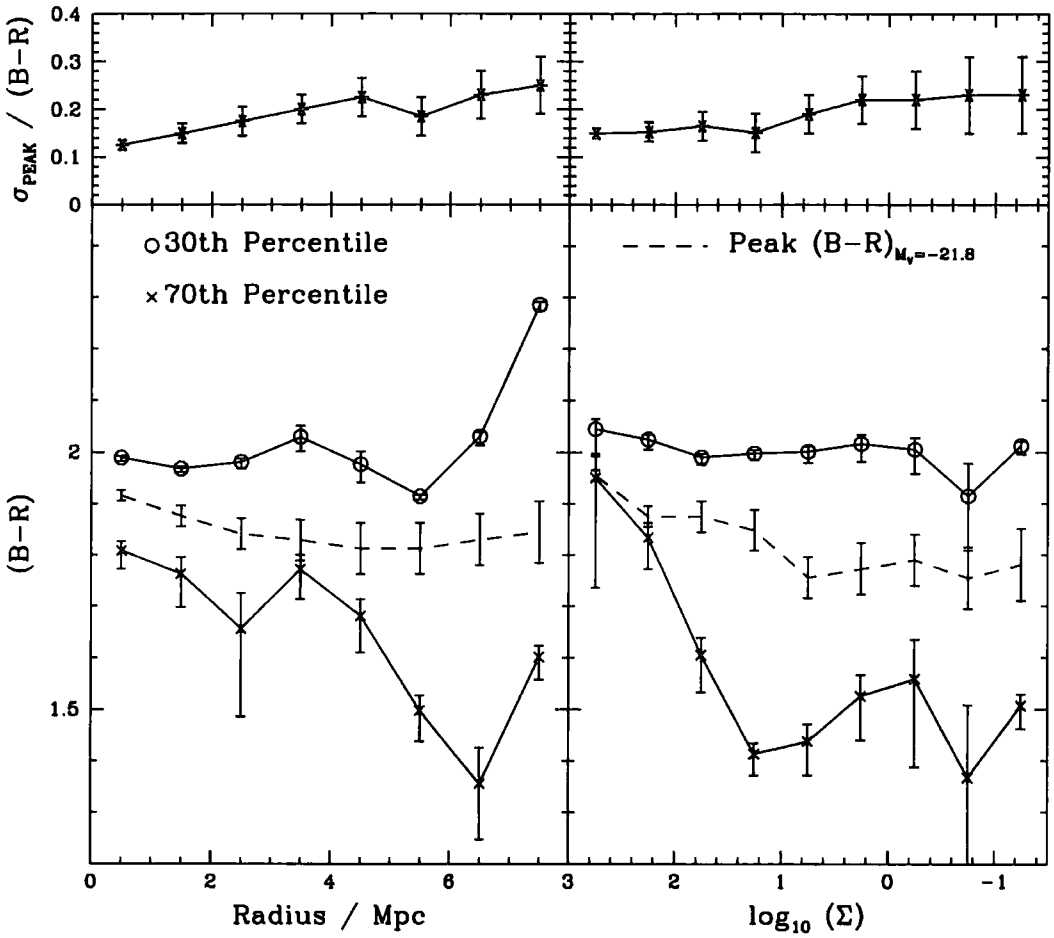

Figure 4.7: The 30th and 70th percentiles of the colour histograms presented in Figures 4.5 & 4.6, measured relative to the red end of the distribution. These are plotted as a function of radius (solid lines) together with the peak CMR colour (dashed line), taken from Figure 4.5. The 30th percentile of the distributions is near constant over at least the inner 6 Mpc of our combined cluster whilst the peak shifts to the blue by -0.11 ± 0.05 mag. The upper panel displays the width of the Gaussian, $\sigma_{\rm Peak}$, fit to the colour histograms against radius. The width steadily increases by $\sim$ 0.15 mag across the radial range. Similar behaviour is seen in the distributions when sorted in terms of local galaxy density.

Table 4.5: Median values for the Butcher-Oemler blue fraction, f_B, taken from 100 realizations of the statistical background subtraction. The errors on f_B are one standard deviation from the median. Values of R_{30}, N_{30} and the concentration, Conc, (Butcher & Oemler 1979) derived from the calculation of f_B are also tabulated. The cluster's two-dimensional distribution of CMR members is also broadly qualitatively described: Regular, R; Irregular, I.

Cluster	f_B	R_{30} (Mpc)	N_{30}	Conc	Morph.
A 22	0.02±0.02	1.06	44	0.29	R
A 550	0.04±0.01	1.35	96	0.32	R
A 1079	0.00±0.05	1.32	20	0.24	I
A 1084	0.05±0.03	1.78	37	0.27	I
A 1285	0.03±0.01	1.40	92	0.30	R
A 1437	0.19±0.02	1.11	47	0.33	R
A 1650	0.00±0.04	0.52	27	0.31	R
A 1651	0.00±0.02	1.19	50	0.29	R
A 1664	0.07±0.03	1.20	29	0.28	I
A 2055	0.06±0.03	1.26	36	0.29	R
A 3888	0.21±0.02	1.01	63	0.36	R

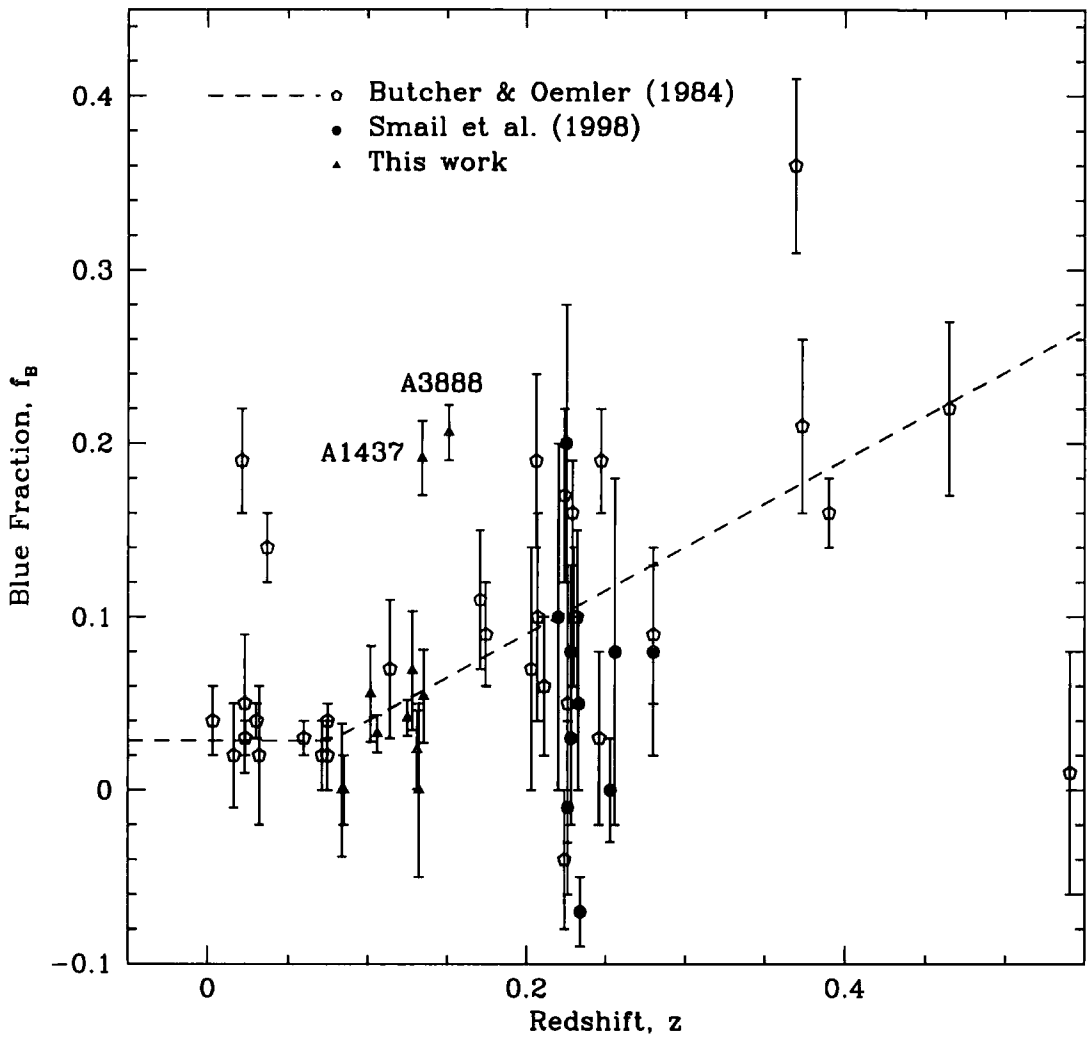

Figure 4.8: The Butcher-Oemler blue fraction, f_B, as a function of redshift. The dashed line is taken from Butcher & Oemler (1984). The LARCS clusters scatter about this line save A 1437 and A 3888 which exhibit a significantly larger blue fraction. Also plotted are Butcher & Oemler's measurements of f_B from their original 1984 work and Smail et al. (1998)

These values of f_B are presented in Figure 4.8 as a function of redshift together with measurements of f_B from other works. In the majority of the clusters the blue fraction is negligible and combined with the small range in X-ray luminosity and redshift covered in the sample it is therefore difficult to distinguish any trends with these parameters in the sample. There are two clusters, however, which do have significant blue populations: A 1437 and A 3888. Both of these clusters show evidence for recent merger events (Edge, priv. comm.) and both appear highly concentrated. It is interesting to note that these clusters also possess the largest measured gradients out of the LARCS subsample. It is probable that the excessive blue fraction in these clusters is pulling the biweighted fit steeper. The large scatter in f_B for the clusters in the homogeneous sample is surprising and suggests that this parameter is sensitive to short term events which effect the galaxy mix within the clusters.

4.5 Discussion

The variation of the CMR with environment has been examined; both with radius and with local galaxy density. It is found that the CMR peak evolves bluewards and broadens with both radius and local galaxy density (Figures 4.5, 4.6 & 4.7). Yet the colour of the reddest members of the CMR remains constant (Figure 4.7). Possible causes for these effects are now examined.

4.5.1 The effects of morphology on the CMR

The trends which should exist in the sample due to the existance of a morphology-radius relation (T–R, Whitmore & Gilmore 1991; Whitmore et al. 1993) or a morphology-density relation (T–Σ, Dressler 1980) need to be examined. A null hypothesis is adopted such that the colour gradient that is observed in the CMR with environment is due to an increasing fraction of mid-type galaxies in the cluster sample, while the colours of the early-type galaxies (ellipticals and S0s) are unaffected by their environment. This hypothesis is suggested by the fact that a broadening of the colour-magnitude relation with radius, but a fixed red envelope

Table 4.6: The median values of μ_{MAX} and CI for galaxies lying on the CMR. The K-S test statictics are the result of comparing a particular sample to the $r_p < 1$ Mpc sample (first row of the table). The morphology of galaxies lying on the CMR become significantly different from the central region from beyond ~ 4 Mpc as indicated by the low values of the *Prob* statistic and the higher values of the *D* statistic (see Fasano & Franceschini, 1987).

Sample (Mpc)	Median μ_{MAX}	Median CI	K-S *D*	K-S *Prob*
0–1	20.10 ± 0.06	0.360 ± 0.008		
1–2	20.22 ± 0.05	0.359 ± 0.007	0.103	0.192
2–4	20.14 ± 0.06	0.359 ± 0.007	0.104	0.112
4–6	20.25 ± 0.05	0.342 ± 0.008	0.131	0.025

(Figure 4.7) is seen.

The distribution of galaxies in terms of concentration index (CI) and peak surface brightness ($\mu_{\rm MAX}$) can be used to look for changes in the morphological mix in different environments within the clusters. On the CI–$\mu_{\rm MAX}$ plane, early-type galaxies populate the high-concentration and high surface brightness region, with later-types typically having lower concentrations and fainter peak surface brightnesses (Abraham et al. 1994; see Chapter 2).

Comparing the distribution in CI–$\mu_{\rm MAX}$ of galaxies lying on the CMR in the cluster core ($r_p < 1$ Mpc) and outskirts ($r_p > 4$–6 Mpc) there is also evidence found for a shift in the typical morphology – with the outer regions having a larger proportion of lower-concentration, lower-surface brightness galaxies than the cores. To quantify this difference, a two dimensional Kolmogorov-Smirnov (K-S) test (Fasano & Franceschini, 1987) is used to show that the CI–$\mu_{\rm MAX}$ distribution for the $r_p < 1$ Mpc and $r_p > 4$–6 Mpc samples are unlikely to be drawn from the same parent population at 97.5 per cent confidence (see Table 4.6). Unfortunately, it is non-trivial to transform the observed shift in the CI–$\mu_{\rm MAX}$ distribution between these environments into expected colour differences.

There is another approach that can be used to test this hypothesis: the typical $(B-R)$ colour of the galaxy distribution in the clusters can be evaluated based on Whitmore & Gilmore's (1991) radial morphological mix and Dressler's (1980) local-density morphological mix. The morphological mix in local rich clusters is adopted as it is unlikely to change dramatically from $z = 0$ to $z = 0.12$ (Fasano et al. 2001; Dressler et al. 1997). The limiting magnitude of $M_V = -20$ is also in broad agreement with Dressler's (1980) limit of $M_V \sim -20.4$.

The $(B-V)$ colours of the different morphological types from the Third Reference Catalogue (RC3, de Vaucouleurs et al. 1991) are used as illustrated in Roberts & Haynes (1994) and a no-evolution K-correction based on the SEDs in King & Ellis (1985) is assumed. The sample is split into broad morphological types corresponding to those employed by Dressler (1980) and Whitmore & Gilmore (1991): E, S0 and S+Irr. The $(B-V)$ colours of E and S0 galaxies from the RC3 are $(B-V) = 0.90$ and 0.89 respectively. These correspond to observed $(B-R)$ colours at $z = 0.12$ of $(B-R) = 1.94$ for E's and $(B-R) = 1.91$ for S0s. The third morphological class is "S+Irr": comprising spiral and irregular galaxies. The usage of this class in the analysis, however, is problematic due to its broadness. The CMR will not contain many of the later-type spirals (e.g. Sc and Sd) as their mean colours lie significantly bluewards of the CMR defined by elliptical and S0 galaxies.

To examine which morphological types from the "S+Irr" class are likely to inhabit the CMR it is neccessary to estimate how blue a galaxy has to be before it falls outside of the CMR peak and hence does not effect the Gaussian fit to the colour histogram distributions (Figures 4.5 & 4.6). It is estimated that galaxies as blue as $(B-R) \sim 1.5$–1.6 will effect the fitting of the CMR in the outskirts of the clusters, this corresponds to $(B-V) \sim 0.7$ at $z = 0$ or the colour of an Sab galaxy from RC3.

At $z = 0.12$, an Sa galaxy will have a mean colour of $(B-R) = 1.55$ while Sab's have $(B-R) = 1.49$. Hence, it can be expected that it is only the Sa/Sab class from the spiral population which is likely to influence the colour of the CMR based on the fitting procedure. Therefore the third morphological class is assigned to be Sa/Sab, instead of the broader "S+Irr" class. Before calculation of the expected colour of the CMR peak, the T–R and T–Σ morphological mixtures are re-normalized

Table 4.7: Relative changes in the colours of the cluster population at $z = 0.12$, compared to the galaxy population in the cluster core, assuming the morphological mixes from Whitmore & Gilmore (1991) and Dressler (1980). A blueward shift of -0.07 mags in $(B - R)$ is predicted from the centre out to 4 Mpc and -0.08 mags over a two orders of magnitude change in local density from the core.

Sample	E	S0	Sa/Sab	$\Delta(B-R)_{M_V=-21.8}$
Radius (Mpc)				
0–1	0.27	0.67	0.06	0.00
1–2	0.25	0.60	0.15	−0.04
2–3	0.23	0.59	0.18	−0.05
3–4	0.21	0.56	0.23	−0.07
Log Density (Mpc^{-2})				
>2.5	0.45	0.55	0.00	0.00
2.0–2.5	0.43	0.53	0.04	−0.02
1.5–2.0	0.36	0.55	0.09	−0.04
1.0–1.5	0.29	0.56	0.15	−0.07
0.5–1.0	0.21	0.59	0.20	−0.09
0.0–0.5	0.20	0.57	0.23	−0.10

to account for using only Sa/Sab galaxies. This, again, is done using RC3, from which the fraction of Sa/Sab galaxies within the "S+Irr" class is estimated. The populations are then re-scaled to the relative proportions of the three morphological classes (Table 4.7).

The gradient in mean $(B-R)$ colour predicted from the variation in morphological mix seen in the T–R relation (Table 4.7) is $d(B - R)/dr_p = -0.017$ equivalent to a change of $\Delta(B - R) = -0.07$ out to 4 Mpc, this is roughly 75 percent of that observed in the combined LARCS clusters ($d(B - R)/dr_p = -0.022 \pm 0.004$). The gradient in the CMR colour resulting from the variation in the morphological mix seen in the T–Σ relation is $d(B - R)/d\log_{10}(\Sigma) = 0.033$ or a change from $\log_{10}(\Sigma) > 2.5$ to $\log_{10}(\Sigma) = 0.0$ of $\Delta(B - R) = -0.10$, which is around 50 percent of that seen over this density range in the composite of the LARCS clusters

$(d(B-R)/d\log_{10}(\Sigma) = -0.076 \pm 0.009)$. This result is the same (99% confidence) as one that uses the high L_X sample from Dressler (1980).

4.5.2 Interpretation

Based on the results from the previous section the conclusion is that the morphology-radius and morphology-density relations seen in local clusters can account for only around half of the apparent change in galaxy colour with radius and local galaxy density seen in the sample.

It is estimated that there is an intrinsic gradient corrected for morphological differences in the colours of early-type galaxies at a fixed luminosity of $d(B-R)/d\log_{10}(\Sigma) = -0.011$ from the cores of typical rich clusters at $z \sim 0.12$ out to environments with galaxy densities of $\log_{10}(\Sigma) \sim 0$ (equivalent to a radius of 2 Mpc). The intrinsic variation with clustocentric radius give a somewhat weaker trend (Table 4.7): $d(B-R)/dr_p = -0.005 \pm 0.004$.

Radial gradients in the colours of cluster galaxies have been previously reported by Abraham et al. (1996) and Terlevich et al. (2001) for two rich clusters straddling the redshift range studied here. These two measurements are not exactly comparable as the Terlevich et al. analysis focuses on the morphologically classified E and S0 galaxies, whereas Abraham et al. investigate a colour-selected sample around the CMR, similar to the approach used here. Nevertheless, as Terlevich et al. stress, their sample in the Coma cluster is completely dominated by E and S0 galaxies and so their results would not change significantly if they considered the whole population.

Abraham et al. (1996) find a non T-Σ corrected radial gradient in $(g-r)$ colour of $d(g-r)/d\log_{10}(r_p) = -0.079$ out to 5 Mpc in A 2390 ($z = 0.23$). It is estimated there is $\sim$ 20 percent uncertainty in this gradient. Terlevich et al. (2001) report $d(g-r)/d\log_{10}(r_p) = -0.024 \pm 0.005$ for the Coma cluster, transformed to the same restframe wavebands as the observations of A 2390. To compare the LARCS result with these it is necessary to similarly transform the $(B-R)$ colours of galaxies in the composite $z = 0.12$ cluster to the wavelengths equivalent to observing a cluster in $(g-r)$ at $z = 0.23$. The result of this transformation is a radial gradient of

$d(g-r)/d\log_{10}(r_p) = -0.061 \pm 0.011$ (uncorrected for the T–Σ relation). Hence, the radial gradient of the colour of the CMR at $z = 0.12$ (a look-back time of 2 Gyrs) is intermediate between those found by Abraham et al. (1996) for A 2390 and Terlevich et al. (2001) for the Coma cluster at look-back times of 0.5 Gyr and 3.5 Gyrs respectively. Correcting the higher redshift measurements for the effects of the morphology-radius relation still results in steeper gradients at higher redshifts.

Both Abraham et al. (1996) and Terlevich et al. (2001) attribute the colour gradients they observe in the clusters to age trends (Terlevich et al. 2001 use detailed arguments to show that the variation in colour cannot be due to dust spread through the core of the cluster). Using the models for a single burst stellar population at an age of 7 Gyr (equivalent to time elapsed between a formation epoch at $z \geq 2$ and $z = 0.12$) presented in Bower et al. (1998), it is found $d(B-R)/dt \sim 0.03$ mag Gyr^{-1} (Kodama & Arimoto, 1997). This implies that the galaxies on the CMR in the outer regions of the clusters have luminosity-weighted stellar populations which are approximately 3 Gyrs younger than those in the cores ($r_p < 1$ Mpc). This age difference is comparable to that found by Terlevich et al. (2001) who predict that early-type galaxies in the outskirts of Coma have stellar populations which are ~ 2 Gyr younger than those in galaxies in the central regions.

The interpretation of the colour gradients observed in the LARCS sample is that they represent variations in the ages of the stellar populations in the cluster galaxies arising from diffences in their star formation histories (Abraham et al. 1996; Smail et al. 1998, 2001; Kodama & Bower 2000). The bulk of galaxies on the CMR are expected to be S0's (Table 4.7; Dressler 1980; Fasano et al. 2001) and thus changes in the colours of this morphological class must play a major role in causing the observed colour gradient (Abraham et al. 1996). However, evidence for a proportion of old, evolved galaxies is also seen whose colours are constant with environment and define the red wing of the CMR (Figure 4.7). This presents the suggestion that the majority of these galaxies are probably ellipticals, which show modest environmental variation in their properties (Treu et al. 1999). Thus a mix of ellipticals with constant colours and a dominant population of S0 galaxies, whose colours vary with environment, can reconcile the main results from the LARCS survey.

Why should galaxies which have S0 morphologies, or at least the colours of S0's at the present-day, vary with environment? Although still controversial, there is increasing evidence that the S0 population in rich clusters has come into being relatively recently. The proportion of S0 galaxies in rich clusters appears to increase rapidly to the present-day (Dressler et al. 1997; Fasano et al. 2001), possibly as the result of the transformation of star-forming disk galaxies which are accreted by the clusters from the surrounding field (Poggianti et al. 1999; Kodama & Smail 2001). The fact that one can see differences in the properties of cluster galaxies out at least as far as 6 Mpc from the cluster core suggests that the process which may suppress the star formation of infalling galaxies can operate in low density environments (Fasano et al. 2000; Bekki et al. 2001; Carlberg et al. 2001; Couch et al. 2001). One mechanism for causing this transformation is the suppresion of star formation due to the removal of the gas reservoirs as galaxies enter the cluster (Poggianti et al. 1999; Balogh, Navarro & Morris 2000). This mechanism may lead directly to the formation of an S0, or other processes may be involved (Balogh et al. 2001).

If this scenario is correct then the accretion and transformation of spiral galaxies from the surrounding field will lead to a gradual build-up of the S0 population within the cluster. Some morphological studies of the early-type galaxies in cluster cores at $z \sim 0.5$ imply that the majority of the S0 population in these regions today are transformed in the 6 Gyrs between $z = 0.5$ and the present-day (e.g. Poggianti et al. 1999). On the outskirts of the clusters one expects a higher proportion of recently accreted cluster members, reflecting the accretion history of the cluster (Abraham et al. 1996). Thus the S0 galaxies in these regions will show the strongest signatures of their past star formation activity, exhibiting the youngest luminosity-weighted ages for their stellar populations and hence the bluest colours. These two effects will combine to produce a radial colour gradient in the same sense as that seen in the data. After accounting for the varying morphological mix with environment, it appears that galaxies on the outskirts of these clusters have luminosity-weighted ages which are ~ 3 Gyrs younger than those in the core. It would be interesting to quantitatively compare this observation with theoretical predictions to test models for the infall history and transformation of galaxies in high density environments (Diaferio et al. 2001).

4.5.3 Caveats

This analysis and interpretation is based upon a number of assumptions that require consideration. Perhaps the largest source of uncertainty is the background subtraction method employed. It is apparent from Figure 4.1 that there are a number of galaxies, rejected by the background subtraction algorithm, which lie nearly directly upon the CMR (e.g. Abell 1650). Conversely there are also a number of galaxies which are defined to be cluster members but are in all likelihood interlopers. The background subtraction correction is re-emphasized to be purely a statistical method. There are two clear ways in which this method could be improved. Firstly, a larger sample of dedicated field observations could be used to improve the statistics. Secondly, spectroscopic observations of the clusters could be used to provide a more robust method to determine cluster membership (see Chapter 6).

During the analysis, the clusters are combined into a single artifical cluster to examine the radial dependance of the CMR. The richer clusters (i.e. Abell 550, 1285 and 3888) have a greater weight in the combined artifical cluster than the poorer ones (i.e. Abell 1079, 1084 and 1664). Although cluster-to-cluster variations are present within our sample, it is important emphasize that LARCS comprises a homogeneously X-ray selected sample of clusters (perhaps only missing about 10 per cent of clusters in the LARCS redshift and L_X range; Edge, priv. comm.; Ebeling et al. 1998) and therefore such cluster-to-cluster variations will be compensated for by the creation of the composite cluster. Using more clusters to create the combined cluster would be beneficial.

In the discussion the data is compared to that of Dressler (1980) to remove the $T - \Sigma$ relation from the LARCS clusters. Note that the LARCS dataset does not contain the sufficiently detailed imaging that is required to differentiate between morphological galaxy types (Chapter 2). Hence one is unable to derive a $T - \Sigma$ relation for the LARCS clusters and it is necessary to rely upon the morphology-density analysis performed by Dressler (1980) for other clusters. In using these data, it is also important to note that the Dressler (1980) sample is constructed with a local ($z < 0.06$) inhomogeneous sample of clusters and may, therefore, not be directly comparable to this study (although limiting Dressler's sample only to high

L_X clusters gives the same results). To remedy this situation would require *HST* snapshot imaging of the LARCS clusters to provide the necessary morphological information.

4.6 Summary

Eleven clusters with precise photometric observations have been analysed from the LARCS survey to trace the variation in the colours of evolved galaxies into the environmental transition region between clusters and the field.

- All of the clusters show colour-magnitude relations; many of these are strong and can be traced well beyond the central 1 Mpc, out to unprecedented clustocentric radii coverage of ~ 8 Mpc.

- The characteristic colour and slope of the CMR of galaxies in the cluster cores is found to change with cluster redshift across the range $z = 0.07$–0.16 covered by the sample. The variations in the CMRs are in agreement with those expected from galaxy populations which formed the bulk of their stars at high redshifts, $z \gg 2$.

- The majority of clusters in the survey exhibit a variation with radius in the colour of the CMR at a fixed luminosity. When combined into a single composite cluster, a radial colour gradient of $d(B-R)/dr_p = -0.022 \pm 0.004$ is observed from the cluster centre to ~ 6 Mpc.

- The composite cluster formed from the sample also shows a colour-local-density relation for the galaxies on the CMR. A colour gradient is identified in the modal colours of galaxies on the CMR amounting to $d(B-R)/d\log_{10}(\Sigma) = -0.076 \pm 0.009$ across three orders of magnitude in local galaxy density from the high-density core of the cluster to the outskirts.

- The expected change in the colour of the CMR with environment has been calculated due to the changing morphological mix. It is estimated that approximately 50 to 70 per cent of the radial and density colour gradient is

due to an increase in contamination by quiescent, early-type spiral galaxies falling close to the CMR. The CMR is suggested to consist of a passively evolving population (elliptical and evolved S0 galaxies) plus recent additions (morphologically young S0 and recently star-forming spiral galaxies).

- The analysis of these eleven clusters supports the previous claims of radial colour variations in individual rich clusters at $z = 0$ and $z = 0.23$. It is also shown that similar trends are visible when using local galaxy density as a more general measure of galaxy environment. Taken together with previous studies, it is suggested that these environmental trends in the colours of galaxies at a fixed luminosity most likely reflect differences in the luminosity-weighted ages of the galaxies in different environments. If interpreted purely as a difference in ages and accounting for differences in the morphological mix, then the gradient observed in the sample suggests that the luminosity-weighted ages of the dominant galaxy population within the CMR at 6 Mpc from the cluster core are ~3 Gyrs younger than those residing in the core.

- The results of the photometric analysis can provide a readily testable, quantitative prediction: if the observed colour gradient simply reflects age differences in passive stellar populations then we would expect that the typical $H\delta_A + H\gamma_A$ line strength of galaxies lying on the CMR should increase by $\sim$ 4Å when moving from the cluster core to the outskirts of these systems (Terlevich et al. 1999).

- Further studies are urgently needed to investigate the properties of galaxies in the lower density environments which connect rich clusters to the surrounding field, particularly at higher redshifts. This region is essential for investigating the impact of environment upon the star formation and morphologies of galaxies.

Chapter 5

2dF Spectroscopy and Data Reduction

5.1 Abstract

Spectroscopy is a vital ingredient of the LARCS project. Not only is it important in assignment of cluster membership, it can also yield information on the star formation histories of galaxies through measurement of spectral line indices.

In this chapter the spectroscopic followup observations using the two degree field (2dF) multi-fibre spectrograph on the 3.9 metre Anglo-Australian Telescope (AAT) are discussed. The survey design is explored in detail and the method for choosing spectroscopic candidate targets is examined with reference to the hardware limitations of the 2dF spectrograph. The 2dF observations undertaken are described and their completeness analyzed. The use of the automated data reduction pipeline, 2dFdr, is described and the method to determine the redshifts and line indices from the observations is discussed.

5.2 2dF Spectroscopy

The spectroscopy used in the LARCS project comes from the 2dF spectrograph (Lewis et al. 2002) * mounted upon the AAT, NSW, Australia. Within certain hardware constraints (detailed below), the 2dF spectrograph is capable of observing up to 400 sources simultaneously within a two degree diameter field on the sky. As can be seen from Figure 2.2, the size of the optical mosaic imaging on the sky has been chosen to correspond to the field of view of the 2dF spectrograph.

*The 2dF spectrograph is described in detail on part of the AAT website (http://www.aao.gov.au/2df/index.html).

Here the main aspects of the spectrograph and it's usage are discussed and briefly summarized below.

The 2dF spectrograph is mounted onto the top-end ring of the AAT. The major constituent parts of 2dF are the wide-field corrective optics (which includes an atmospheric dispersion compensator), a robotic fibre positioner, two spectrographs (each taking 200 of the fibre spectra) and the fibres themselves. A schematic diagram of the system is shown in Figure 5.1.

The four-component corrective lens system is located below the focal plane of the system. It focuses the light into the prisms of the fibres, yielding 1″ images across a two degree planar field of view at the AAT's prime focus. The system introduces a radial distortion in the image scale which varies from $15.5''\text{mm}^{-1}$ at the centre to $14.2''\text{mm}^{-1}$ at the edge.

The pair of identical spectrographs sit on the top-end ring of the AAT and each receive 200 fibres. The detectors are 1024 × 1024 pixels thinned Tektronix CCDs with $24\mu\text{m}pixels$. Each spectra lies roughly 5 pixels centre-centre from its neighbour on the CCDs and has a typical width of 3 pixels.

The robotic fibre positioner sits at the apex of the 2dF instrument. It has a robotic gripper on an X–Y gantry. The positioner is capable of placing one fibre about every 7 seconds which, taken together with overheads, means that the 400 fibres can be positioned within one hour. Since this is a non-negligible time loss during a night of observation, 2dF is fitted with two field plates. The field plates interchange positions using a tumbler mechanism. When in use, the field plate sits just above the focal plane, ensuring that the magnetically attached fibres are at the focal plane. When observing with one plate, the second field plate can be simultaneously configured with the robotic positioner thus preventing any time-wastage. The sub-mm accuracy of the robotic fibre positioner corresponds to $\sim 0.16''$ on the sky. The care taken in finding the astrometric solution in Chapter 2 is fully justified when using 2dF: an error in position of over 0.3″ means that a substantial fraction of the light from an object will miss the fibre.

On each of the two field plates, light is fed to the spectrographs through 400 fibres. A further 4 guide fibre bundles are used for field acquisition and guiding. At the ends of each fibre there is a magnetic button which is handled by the robotic

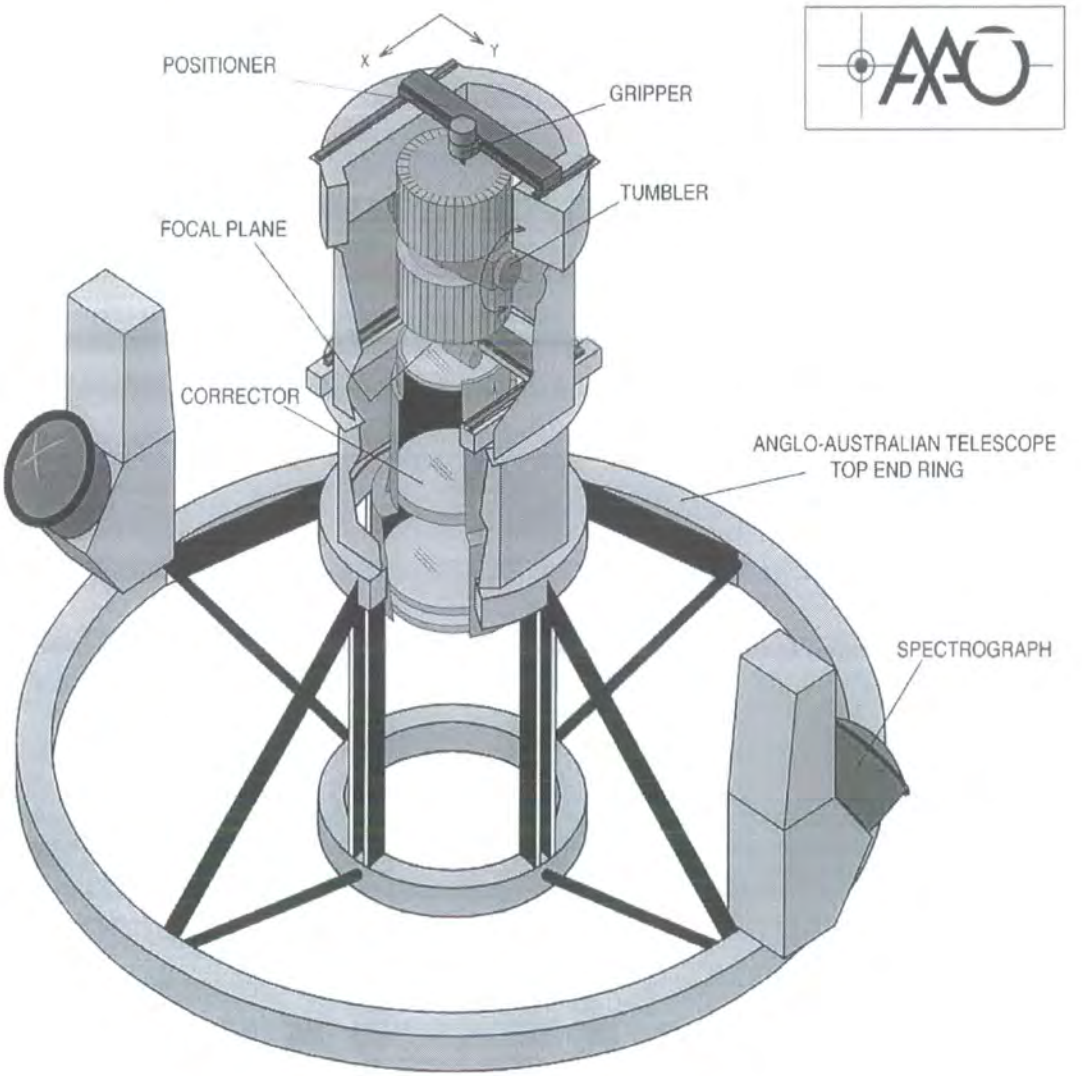

Figure 5.1: Schematic outline of the major components of the 2dF spectrograph sitting on the top end ring of the AAT, taken from the 2dF website.

gripper during the configuration of a field plate (see Figure 5.2). During observations, a prism at the terminus of the button reflects light from the source down the fibre. Each object fibre has a 140μm diameter core which corresponds to 2.16″ at the centre of the plate and 1.99″ at the edges.

5.3 Survey Design

In designing the observations to be undertaken with 2dF, it is necessary to bear in mind the goals of the survey: (i) to characterise the spectral properties of the members (star forming, post-starburst, passive, etc) and (ii) to correlate these star-formation histories with their dynamics, membership of substructure and local environment.

Therefore the aim is for high-quality, moderate resolution spectroscopy. The 600V gratings are selected as they provide the necessary resolution to measure key line indices (4Å) and precise velocity measurement ($\sim 120\,\mathrm{km\,s^{-1}}$). The restframe wavelength range with this grating is approximately 3700–5600Å for the clusters, providing coverage of the major line indices of interest ([OII]λ3727, D4000, Hδ, Hβ, Mgb, Feλ5270).

A signal to noise ratio (S/N) of 7–10 per resolution element on the faintest galaxies ($M^* + 3$) is desired, comparable to that obtained for spectroscopy in more distant Butcher-Oemler clusters (e.g. Couch & Sharples 1987; Dressler et al. 1999) and more than sufficient for redshift identification, as well as line index measurement.

The strategy, therefore, is to obtain spectroscopy complete down to an absolute magnitude limit of $M \sim M^* + 3$ in all of the clusters. This corresponds to $R \sim 20.5$ at the mean redshift of the LARCS sample, $z = 0.12$. At this limit, the CCD imaging catalogues contain a total of ~ 2000 galaxies over the full fields. The goal is to identify ~ 400 members in each cluster – a limit dictated by the need to statistically distinguish between the properties of independent subsamples of cluster galaxies, e.g. the dynamics of star–forming and quiescent galaxies, or the higher–order kinematics of galaxies in the core and infall regions of the cluster. To investigate the properties of rarer classes of galaxy (e.g. AGN/radio galaxies) advantage will be

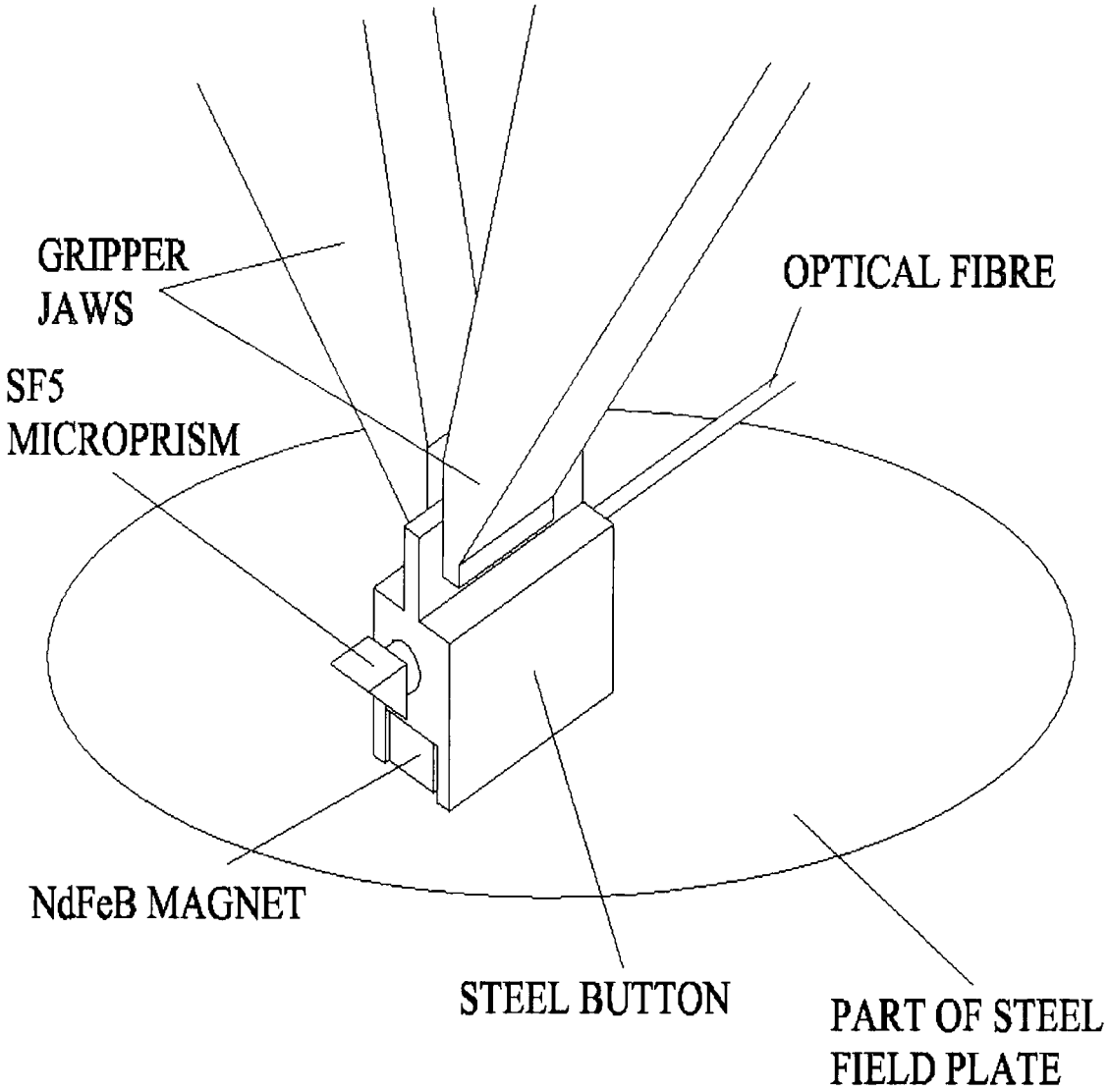

Figure 5.2: Schematic outline of a 2dF button in the jaws of the gripper, taken from the 2dF website.

taken of the homogeneous sample to combine catalogues across clusters. Taking into account field contamination (determined locally to each cluster), a subsample of 800 galaxies needs to be observed to guarantee $\sim$ 400 cluster members.

Hence, spectra are acquired via 2 configurations of 2dF in each cluster to provide a total of $\sim$ 760 galaxies (allocating $\sim$ 20 fibres per configuration to sky positions).

5.3.1 Spectroscopic Selection

The objects used as targets for the 2dF observations are chosen from the optical photometric catalogues derived from SExtractor (see Chapter 2). Following on from the star-galaxy separation described in Chapter 2, the 2dF target galaxies are selected to have CLASS_STAR < 0.1 and FWHM > 2. Finally, because of the accuracy required by the 2dF fibre positioner, only galaxies whose FLAG[†] is less than 4 are used; a higher value of the FLAG parameter would be a concern for the accuracy of the astrometric solution for that galaxy.

This sample is split into four parts based upon radial distance from the cluster core and magnitude. The spatial division creates an 'inner' and 'outer' sample of the prospective candidate targets: the division between the core and the halo being defined as a clustocentric radius of $30'$ on the sky (equivalent to $\sim$ 5 Mpc at $z = 0.12$). The division in brightness creates a 'bright' and a 'faint' sample. The precise magnitude cut is different for each individual cluster because of the varying redshifts of the clusters. In terms of absolute magnitudes, bright galaxies are defined to have $R_{bright} < R(M^* + 1)$ and faint galaxies in the interval $R(M^* + 1) < R_{faint} < R(M^* + 3)$. These divisions are made to ensure that the same absolute magnitude limit is probed to in the different clusters and will also be used to contrast the properties of the higher redshift clusters to the lower ones when looking for evolutionary trends (e.g. see Chapter 4). Similarly to Chapter 3, M^* is assumed to be $M_V = -21.8$. This value is converted into $R-$band magnitudes using

[†]The FLAG parameter is calculated for every object and coded in decimal as a sum of powers of 2. Thus by selecting galaxies whose FLAG is less than 4, objects that are originally blended with another one and objects whose neighbours may slightly bias the resulting photometry ("more than 10% of the integrated area overlaps the isophotal area of a detected neighbour", Bertin 1996) are included but objects with one saturated pixel or more are rejected.

the relations presented in Chapter 3 and then applied to each cluster to generate the target lists. For example, Abell 2204 at $z \sim 0.15$ has magnitude cuts thus: $R_{bright} < 19.5$ and $19.5 < R_{faint} < 21.5$.

The final galaxy sample in any cluster will thus consist of: a bright core of galaxies (Radius $< 30'$, $R < R(M^* + 1)$); faint core galaxies (Radius $< 30'$, $R(M^* + 1) < R < R(M^* + 3)$); bright halo galaxies (Radius $> 30'$, $R < R(M^* + 1)$). A fourth possible set (faint halo galaxies) is not used because at these large radii the faint sample will be heavily contaminated with field galaxies.

In addition to the target galaxies to be observed, 2dF requires four stars to be used for the guidance system. The four corresponding fibre bundles used for guidance have pivots located at the cardinal points of the two degree field. The fibre pivot angle constrains each of these fibre bundles to only be able to access about 0.25deg^2 of sky. Therefore a large sky density of fiducial stars is required ($\sim 20 - 30$ stars) per 2dF configuration to ensure that all of the four fibre bundles are allocated. In typical seeing of $1.0'' - 1.5''$ one can detect stars down to $V \sim 15$; a limit which has been established empirically using Landolt (1992) standards (see http://www.aao.gov.au/2df/manual.html). Equally, bright ($V < 12$) fiducial stars are of little use for guidance because they typically have diffraction spikes and faint haloes on the source material which results in poor centroiding and may have high proper motions resulting in a systematic shift in their present day position.

The fiducial stars are selected from the LARCS catalogues. To generate a list of suitable fiducial stars the following selection criteria is used: CLASS_STAR> 0.9, FWHM < 2.0 and $13 < R < 15$. This generates a list of in excess of 30 bright stars. Each of these stars are visually inspected to ensure they have no diffraction spikes which may cause poor centroiding and their astrometric solutions are compared with the USNO A1.0 astrometric catalogue (Monet et al. 1996) to ensure that any stars with large proper motions are removed.

5.3.2 "Configure" and Fibre Allocation

The selection of spectroscopic targets presented in the previous section results in ~ 1200 target galaxies and ~ 30 fiducial stars. Although at maximum, only ~ 760

of these $\sim$ 1200 target galaxies will be observed. The need for this high level of redundancy arises from the intrinsic restrictions of the 2dF positioner. The galaxies in the LARCS clusters are strongly concentrated towards the cluster centre; the local galaxy density at the centre of some clusters can be over 300 galaxies Mpc^{-2} (see Chapter 4). Further, the robotic fibre positioner itself can only place fibres within 11.4″ of a neighbour, although the exact minimum separation distance is a function of the geometry at which the fibres are placed due to the non-regular shape of their magnetic buttons. If only $\sim$ 800 galaxies are targeted over two configurations, many of the fibres would not be used as they could not be placed. With $\sim 40 - 50$ per cent more spectroscopic targets than 2dF fibres, the likelihood is that virtually all of the fibres will be used.

The allocation of fibres to spectroscopic targets is done using the CONFIGURE software package, supplied with the standard 2dF software (see http://www.aao.gov.au/2df/manual/). An input file for use with the package is derived from the LARCS photometric galaxy catalogues, consisting of the spectroscopic target's position (RA and Dec in J2000), an identifying string and an integer in the range 1–9 to denote the target's priority (9 being the highest priority). The spectroscopic targets are assigned their priority in accordance with the scheme set out in Table 5.1. An additional category, "targets of opportunity", is also included. This category contains objects in the field which ordinarily would not be included in the input galaxy catalogue. Examples of this class of object includes QSO candidates (which would be classified as stellar in the LARCS catalogues) and X-ray bright objects in the outer regions of the cluster that merited a higher priority.

Four configurations of the 2dF plates are created for each cluster to be observed for optimum flexibility. Since 2dF has two field plates (Plates 0 and 1) each with different numbers of operational fibres and different distortions, the plate configurations are non-interchangeable. Two fields are required per cluster, hence a total of four configurations have to be prepared per cluster. This means that when observing, it does not matter which field plate is the first to be used.

Firstly, one configuration is created from the whole input catalogue for each plate. The galaxies that become assigned from this first pass are then removed from the input list before the second set of plates are configured. In practice, there

Table 5.1: The integer priority given to the various groups of spectroscopic targets during usage of the CONFIGURE program.

Priority	Targets
9	Fiducial stars and cD (or BCG) galaxies
8	Bright core galaxies
6	Faint core galaxies
5	Targets of opportunity
4	Bright halo galaxies

is typically only 10-20 galaxies that are different between the two plates in the first pass. This ensures that there are no duplicate observations and maximum flexibility at the telescope is achieved. The process for creating these configurations is outlined below.

The fibres are assigned using the ALLOCATE command within CONFIGURE. About $\sim$ 10 fibres per spectrograph are not allocated at this time as they are to be allocated later to blank sky. The ALLOCATE command can be broken down into several distinct stages. In the first stage, an initial pass is made to allocate the highest priority (priority = 9) targets. A group of fibres that could be allocated to the target, given the hardware constraints (angle and length of fibre), are determined. Those targets which are the hardest to access, as defined by the difference between the number of all targets possible for the given group of fibres contained in a sector, bounded by the actual target and the fibres at the extrema, and the number of fibres, are given the highest priority (Colless et al. 2001). Once all of the priority 9 targets have been assigned, the lower priority targets are then assigned in turn in a similar manner. In the second stage, fibre swapping occurs. For each unallocated object, the program determines if a previously allocated fibre could be re-assigned to it and another, unallocated, fibre could be assigned to the target that had been just un-assigned. If no fibres can be assigned to this un-assigned target the process is recursively repeated. The process halts when a previously unallocated fibre is assigned to a target or the search reaches a depth of 10 iterations (Colless et al. 2001). If it does reach a depth of 10 iterations, but a gain has been made in

terms of object priority (see Table 5.1), then the new configuration is kept. In the third and final stage of the allocation process, checks are made for crossing fibres. For each pair of crossed fibres, an attempt is made to uncross them by swapping their target assignments. This process is repeated until no further uncrossing can take place.

The sky fibres are now assigned using the ALLOCATE SKY GRID command. The sky grid is effectively three concentric circles of target positions centred upon the field plate's centre (defined to be coincident with the core of the cluster in all cases save Abell 2204 whose optical mosaic is mis-observed) to which fibres can be automatically assigned. The program assigns the remaining fibres to these sky grid targets where it is able and checks for fibre crossings as above. After this allocation, there are typically $\sim$ 10 unallocated fibres left over. These fibres are assigned, if possible, manually either to spectroscopic targets which the ALLOCATE command missed or to random positions on the plate and then designated as sky fibres. It is essential that the sky allocations (both the sky grid and manual assignments) are checked to ensure that they are indeed blank sky and not accidentally placed upon an object (e.g. star). This is done by examination of the Digitized Sky Survey (DSS; see http://archive.stsci.edu/dss/). A catalogue and image of the sky within 3′ of a given sky position is obtained. If any other source is nearby (within 0.5″) or a very bright star is situated within the 3′ radius then the sky position is rejected. The fibre is de-allocated and reassigned, if possible, to another sky position. Typically, $\sim$ 5 sky positions have to be re-assigned in this way. The number of fibres that are left unallocated at the end of this procedure and cannot be manually allocated to any target object or blank sky is usually low (< 5).

Once all of the possible fibre allocations have been made, the configuration undergoes validity checking. Although the configuration may appear valid, it is only valid for at a single time and may readily be invalid if observed when the telescope is in a different position owing to translations in the target positions due to, for example, refraction, flexure and telescope misalignment. The configuration is therefore checked for validity over a range of dates and telescope hour angles. This check is performed with the CHECK OVER HA RANGE command. This highlights any fibres which are valid at zenith but would collide at larger hour angles (the checking is

done from minus four to plus fours hours). Typically there are ~ 5 such collisions discovered per configured plate. Fibres which would collide are re-allocated manually either to sky or other spectroscopic targets. In all cases, the aim is to preserve the number of allocations and priorities of assigned fibres. Unfortunately, this action sometimes necessitates the loss of some higher priority targets. Immediately prior to observing, the configurations are checked one final time to ensure that any problems (e.g. freshly broken or repaired fibres) can be dealt with. These 11^{th} hour alterations typically re-assign $\sim 5 - 10$ fibre allocations.

5.4 Observations

Two observing runs have been completed to date. The first run was observed by Edge, Couch and O'Hely in May 1998. A compromised star–galaxy separation was used for part of this and resulted in a plethora of stars being observed in Abell 2055. Many further difficulties were experienced during the 1998 run, e.g. poor weather and instrumentational failure, a full account of which is given in O'Hely (2000) and O'Hely et al. (in prep.). In this chapter, however, only the second observing run undertaken by Pimbblet and Couch (7–9 July 2000) and a subsequent service run (20 July 2001) will be discussed. Table 5.2 provides a summary of the latter LARCS 2dF observing runs made; Table 4.2 of O'Hely (2000) provides a similar summary for the former runs.

The first night (7 July 2000) was completely weathered off hence no observations took place. Parts of the next two nights were also adversely affected by high wind conditions which necessitated closure of the dome. Consequently, the only cluster to be fully observed was Abell 2204, with only one configuration observed for both Abell 22 and 3921.

A successful service run, however, has been made to recover the second configuration prepared for Abell 3921. This run was observed by Bridges and Cannon in good, clear weather conditions. Due to service time constraints, this observation was made with 300 B gratings instead of 600 V. The dispersion of 179Åmm^{-1} possessed by the 300 B gratings is approximately double that of the 600 V gratings, 91Åmm^{-1}. The wavelength coverage for the 300 B gratings is 4200Å, some 2000Å

larger than the 2200Å coverage of the 600 V gratings. However, the experience of the 2dFGRS team has shown that these gratings provide adequate resolution to determine redshifts and measure key spectral line indices (Couch, priv. comm.).

5.5 Data Reduction Pipeline

The fully automated 2dFdr reduction pipeline is used to reduce these data. A full description of the package is given in Bailey et al. (2001; see also http://www.aao.gov.au/2df/; Colless et al. 2001). An overview of the pipeline is given below:

There are several stages to the reduction pipeline, this first of which is to debais the CCD. The bias is calculated as the median of the CCD overscan regions and subtracted off. The images are then trimmed, removing the overscan region. Any bad pixels contained within the imaging are also flagged.

A fibre position file is then created by mapping the locations of the spectra on the CCD by using the FIND FIBRES command. A fibre flat field is used for this purpose as it possesses a high signal-to-noise ratio. A tram line map which traces the paths of the spectra across the CCD is generated by performing surface fits to the spectra. A visual check of the correspondence of the tram line map to the spectra is made to ensure the map is accurate. Additional lines can be added in or removed as necessary to ensure that the tram lines accurately trace each spectrum. This tram line map is then used as the starting location for the package to automatically identify and extract object flux in the fibres by translating and rotating to match each frame.

The fibres are extracted using the default TRAM command. Pixels are summed along each fibre (with a width of just less than the spacing of the tram lines) to generate an extracted 1024 spectral pixel x 200 fibre array.

A first pass of wavelength calibration is performed using the 2dF spectrograph's optical model and a knowledge of the central wavelength. The calibration is refined by using data from an arc lamp: lines in the argon/helium arc spectra are automatically identified and matched to a known list of lines. Anomalous and unmatched lines are discarded and the matching process is iterated up to four times. Typically, the final solution is determined from $\sim$ 21 lines (Colless et al. 2001) for

Table 5.2: Spectroscopic observations undertaken using 2dF. The total number of spectroscopic candidates in each plate configuration is given along with a breakdown of those objects that a reliable redshift has been obtained for.

Cluster	Configuration	Plate	Date	Grating	T_{Exp} (Hours)	Seeing (″)	Phot?	N(Fibres allocated)	N(Galaxies)	N(Stars)	N(Sky)
Abell 22	1	1	Jul 8 2000	600 V	5×0.5	1.4	yes	379	347	6	26
Abell 2204	1	0	Jul 8 2000	600 V	5×0.5	1.5	yes	379	280	65	34
Abell 2204	2	1	Jul 9 2000	600 V	5×0.5	1.7	yes	374	274	61	39
Abell 2204	3	0	Jul 9 2000	600 V	5×0.5	1.8	yes	369	236	97	35
Abell 3921	1	0	Jul 8 2000	600 V	5×0.5	1.6	yes	366	331	3	32
Abell 3921	2	0	Jul 20 2001	300 B	5×0.5	1.7	yes	374	338	0	36

the 300B gratings and $\sim$ 11 lines for the 600V gratings and possesses rms residuals of $\sim$ 3Å. Having accurately determined the dispersion solution, the spectrum is rebinned onto a linear wavelength scale.

Only at the end of the reduction pipeline is sky subtraction performed. One uses minimum of 10 sky fibres per spectrograph are used for this, though this number is often higher owing to the fibre assignment process (see Table 5.2). The sky fibres are renormalised using their mean flux and a median sky spectrum is then calculated. The median sky spectrum is then subtracted from each object spectrum. Although each sky fibre has been checked to ensure it is pointing at blank sky, occasionally it may accidentally be placed upon moving or variable sources, but because a median is used, is does not matter if a small number of the sky fibres are affected in this manner.

Since the spectroscopic targets are observed in multiple exposures (typically 5×1800 sec) it is essential to combine them together. This step uses the COMBINE REDUCED RUNS command and is the sole step where cosmic ray rejection (CRR) occurs; if CRR occurred earlier in the process, emission lines would be at risk of being rejected. The CRR process is similar to the CRREJECT package in IRAF. Those pixels which are significantly hotter ($> 5\sigma$) than the median value of the exposures when flux-weighted are defined to be cosmic ray events and are excluded from the final combined spectra. Several example spectra from the July 2000 run are displayed in Figure 5.3.

5.6 Redshift Determination

To determine the redshifts of the galaxies, two standard tasks within IRAF are used: the first task, XCSAO (Kurtz et al. 1992), uses the absorption features of the spectra whilst the second task, EMSAO (Mink & Wyatt 1995), uses strong emission lines. Here, the application of XCSAO to the spectra is described, whilst the usage of EMSAO is described in § 5.6.1.

The XCSAO task cross correlates every galaxy spectra with a number of template spectra to obtain the redshift. The template spectra comprises several stellar spectrum (including a synthetic G+K stellar spectrum, an A+K stellar spectrum

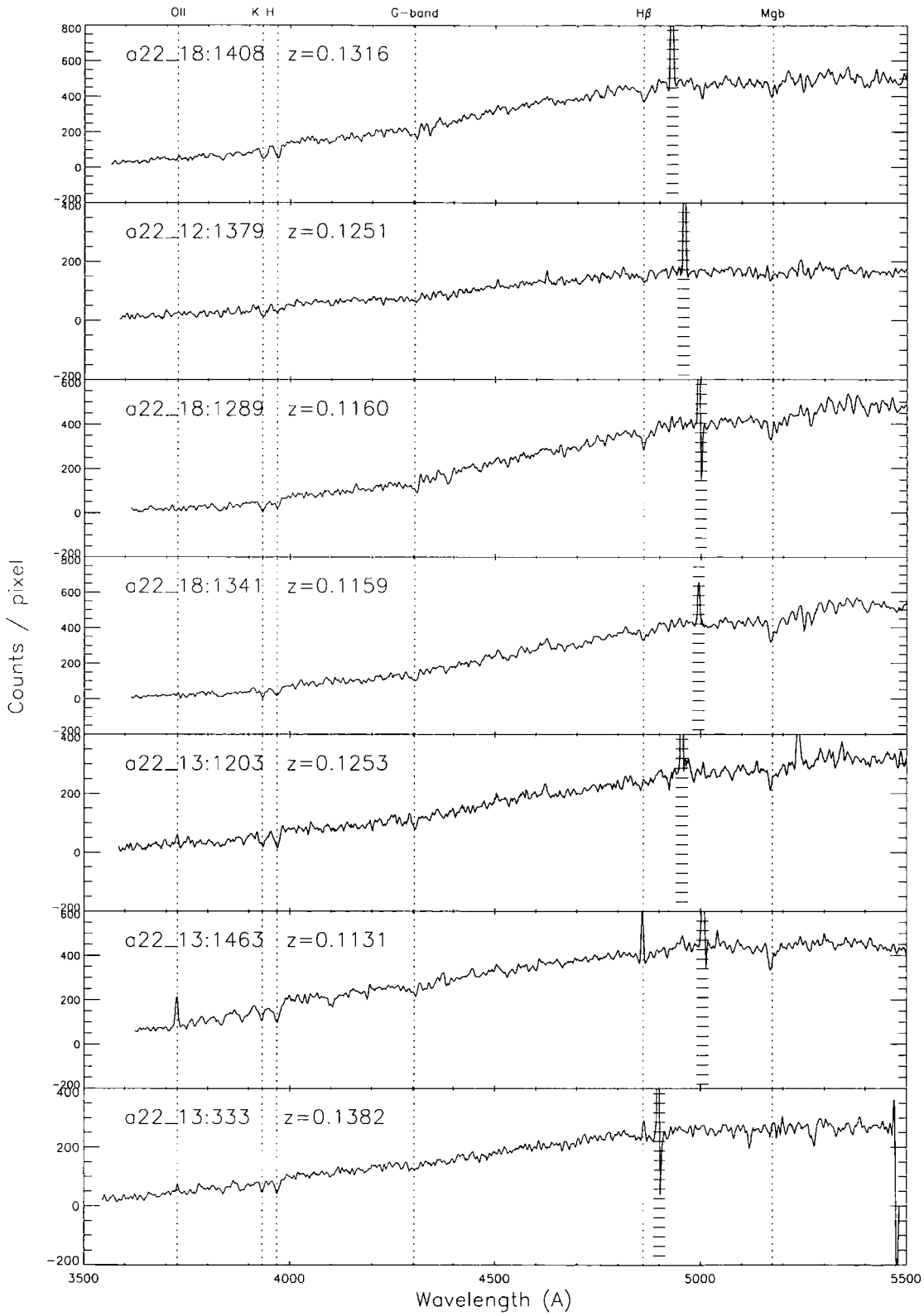

Figure 5.3: Example spectra, together with their determined redshifts, taken from the observation of Abell 22 in July 2000. The identification tag denotes the entry in the LARCS catalogues. The spectra have been de-redshifted to rest frame wavelengths and several key spectral lines (vertical dotted lines) are indicated. The short horizontal hatching denotes residual sky lines which are ignored for the redshift determination.

and a globular cluster spectrum) and several galactic spectrum (including M31 – a spiral galaxy, M32 –an elliptical galaxy). These template spectra are obtained from two sources, the first is the publicly available spectra published on the IRAF website (http://star-www.rl.ac.uk/iraf/web/iraf-homepage.html) for use with the RSVAO package and the second are kindly provided from Zabludoff's private collection.

The cross-correlation technique takes each galaxy spectrum / template pair and rebins them into log-wavelength space. The user specified wavelength range over which the spectra will be compared is set to 4000Å – 6000Å for the 600 V observations. The continuum is calculated via the ICFIT task and then subtracted from each spectrum. Emission lines in the spectra and obvious sky lines are suppressed by setting their values to that of the continuum. This suppression is vital in order to find absorption line redshifts for emission line galaxies. The ends of the galaxy spectra are windowed by a cosine bell to suppress any high frequency noise that may be present. Each galaxy spectra and template are then filtered in Fourier space to remove high frequency noise. The Fourier cross correlation, the Fourier transform of one spectrum multiplied by the conjugate of the transform of the second, is then calculated. The peak value of the cross correlation function is then obtained by fitting a parabola to it. The peak of the parabola provides the estimate of the redshift in cz (kms^{-1}) and the width shows the uncertainty, σ.

To determine the reliability of the measurements the method of Tonry and Davis (1979) is followed. They define a quality value, R_{TDR}, as the ratio of the height of the fitted peak to the average height of peaks in the anti-symmetrical part of the cross correlation function. The larger the value of R_{TDR}, the better the fit of the template spectrum to the galaxy spectrum. Figure 5.4 shows the distribution of R_{TDR} values as a function of redshift estimate, cz, in Abell 22. A value of $R_{TDR} > 3.0$ is found to indicate a good fit; more than 50 per cent of galaxy spectra with values less than this exhibited insecure redshift estimates. In Abell 22 (see Figure 5.4), $\sim$ 10 per cent of the galaxy spectra have insecure redshift estimates. This cluster is typical of those observed.

Since each 2dF fibre is cross-correlated with many templates, it is necessary to determine which of the redshift estimates are correct. The redshift is usually

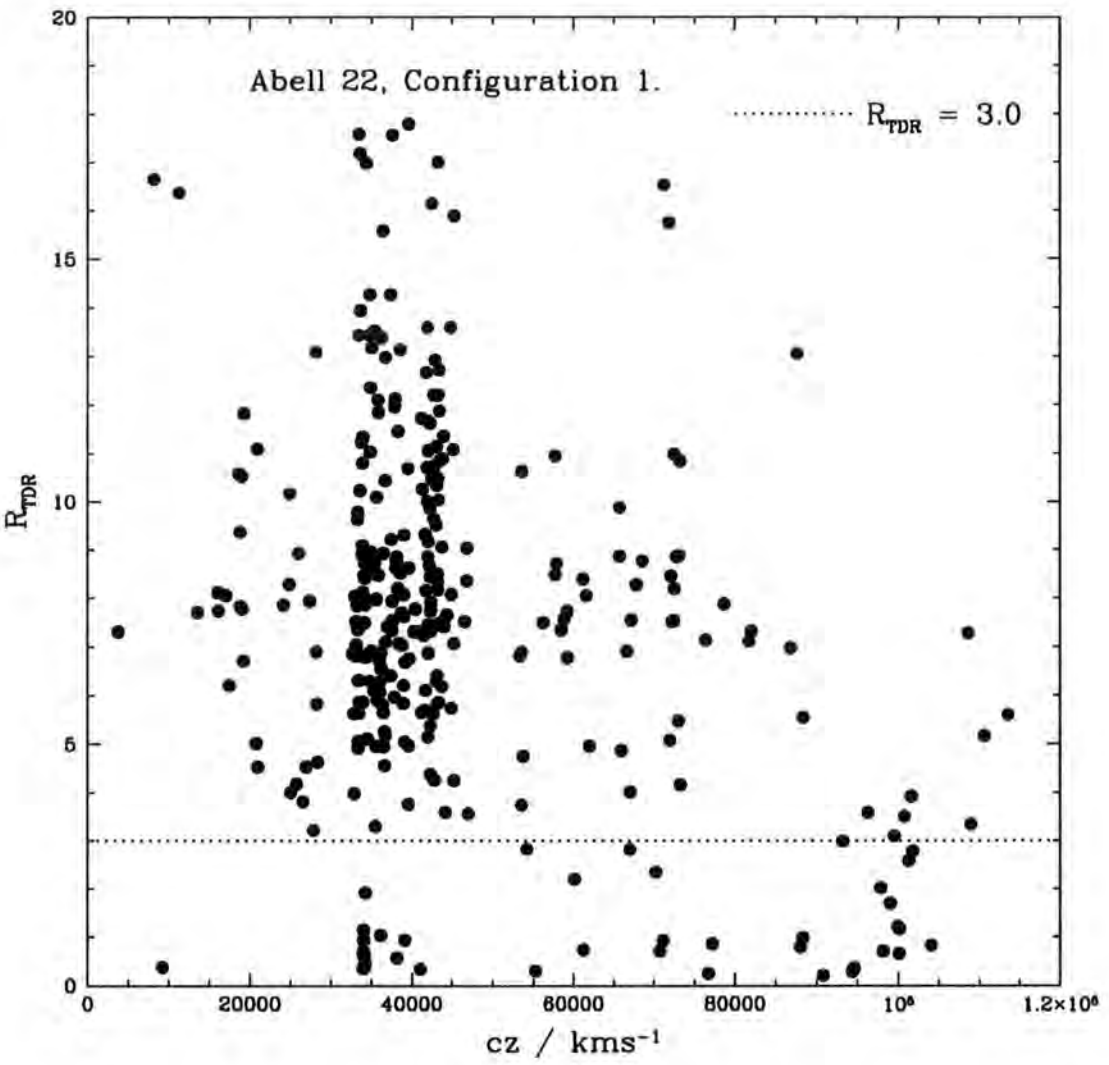

Figure 5.4: Distribution of R_{TDR} as a function of the estimated redshift, cz, using XCSAO for the first configuration of Abell 22. The dotted horizontal line denotes $R_{TDR} = 3.0$. Those galaxies with $R_{TDR} > 3.0$ are defined as having a secure redshift estimate.

taken to be the value with the highest R_{TDR}. To check this, each spectra is de-redshifted to rest frame wavelengths and inspected by eye to check that its emission and absorption features confirm the redshift determination (e.g. see Figure 5.3). It is found that $\sim$ 90 per cent of the redshifts found by the above method are verified as correct. The remaining fraction have their redshifts manually computed. These typically exhibited much noisier features and / or are high redshift galaxies, $z \geq 0.25$. Since XCSAO is configured to have an initial guess of $z \sim 0.1$ for all galaxies, these high redshift galaxies often suffer the worst determinations as XCSAO attempts to fit the templates to incorrect absorption features. Often, a higher initial guess ($z \sim 0.25$) readily solves this problem.

5.6.1 Accuracy of the Redshifts

Although it would appear from the manual checks that the redshift determinations for galaxies with $R_{TDR} > 3.0$ are accurate, it is still necessary to statistically ascertain their level of accuracy. Because 2dF observing time is at a premium, repeat observations of the same galaxies have not been undertaken. Hence, here two methods are employed to check the reliability of the redshift measurements.

The first method is to use the EMSAO task to generate an independent redshift estimate. EMSAO searches for the emission lines in the spectra by taking the XCSAO determined velocity as an initial guess. It then determines a redshift by the fitting of parabolic curves to any emission lines found. Since not all of the galaxies have emission lines, this check is only valid for about 20 per cent of the observations. Figure 5.5 shows the distribution of differences in redshift as obtained for the same galaxies using the two independent redshift determination methods and their dependance on redshift. The median rms of 65kms^{-1} is very similar to the value of 64kms^{-1} reported by the 2dFGRS team (Colless et al. 2001) in their repeat observations for their highest quality spectra. The pair-wise blunder rate, defined as those galaxies whose independent redshift determinations differed by more than 600kms^{-1}, is 2.7 per cent. This value is slightly less than the pair-wise blunder rate of 3.1 per cent reported by Colless et al. (2001).

Another method to check the redshifts is to examine previously published inde-

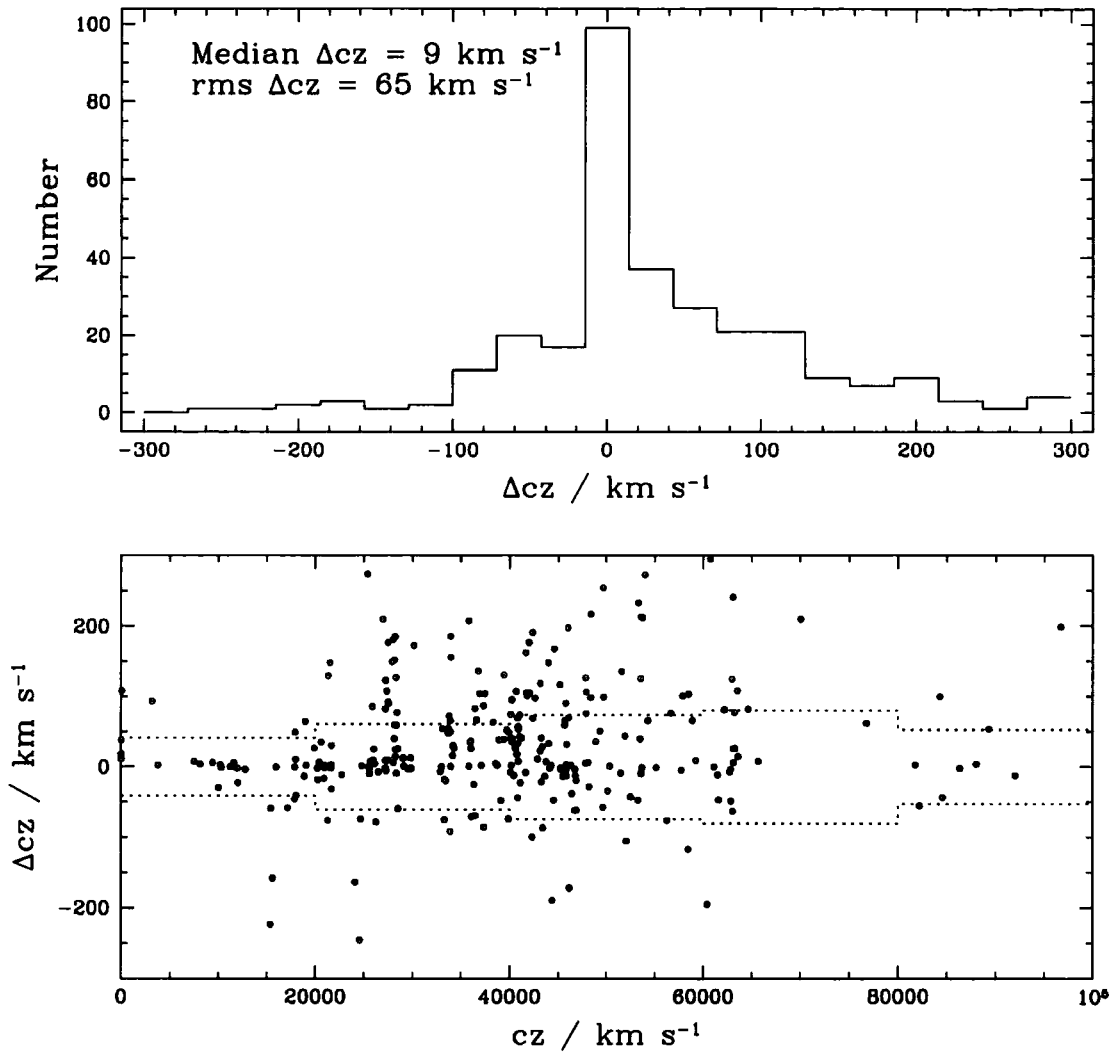

Figure 5.5: Distribution of differences in redshift between measurements made using the absorption lines (XCSAO) and using emission lines (EMSAO) is shown in the top panel. The dependance of redshift differences with redshift is shown in the lower panel together with a rolling rms (dotted lines).

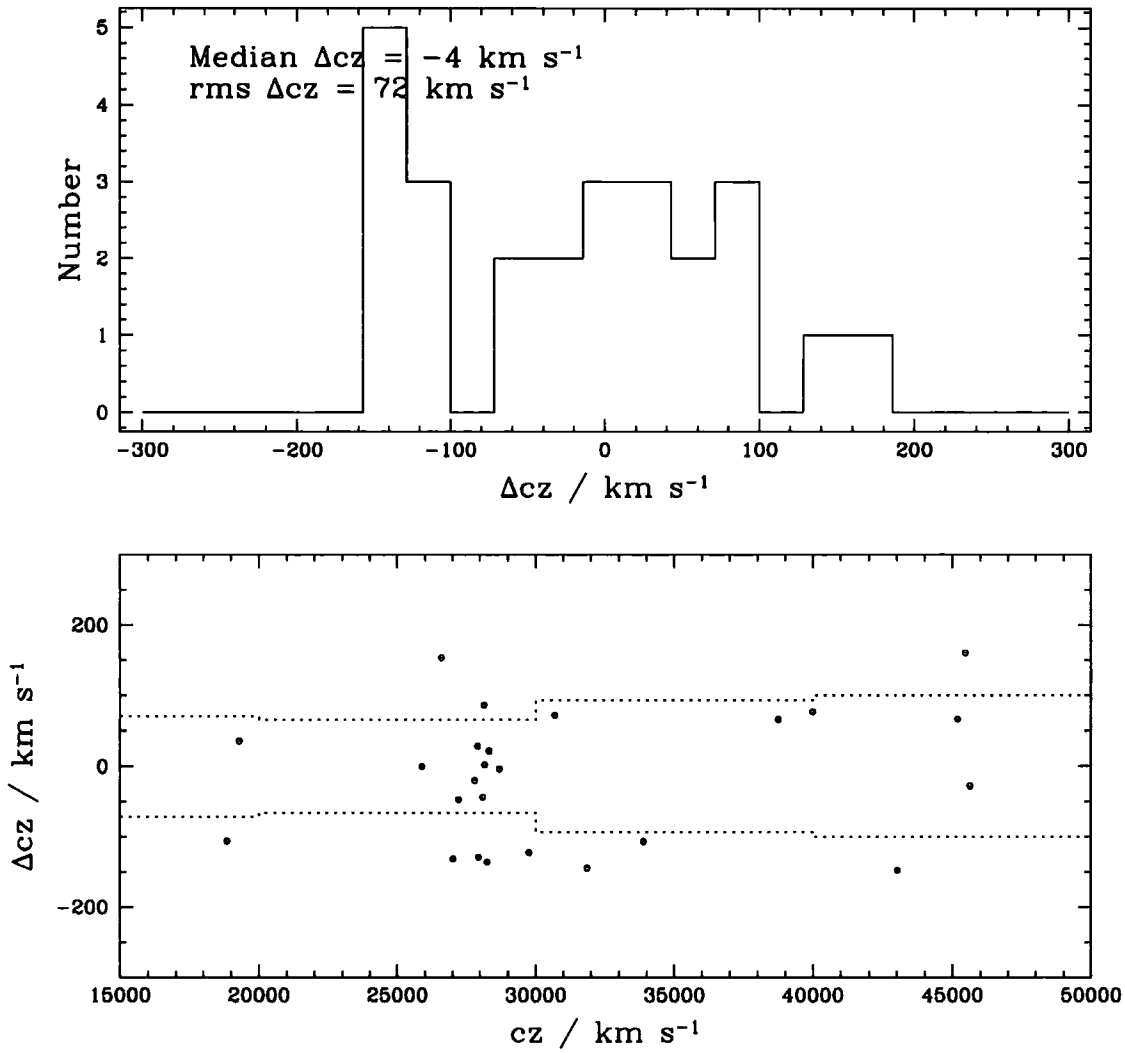

Figure 5.6: As for Figure 5.5 but for the comparison of LARCS galaxies to previously published *cz* determinations found using NED.

Table 5.3: Spectroscopic success rate of the star–galaxy separation method. Both Abell 22 and 3921 have an excellent success rate which is in line with the prediction made by photometric considerations. Abell 2204, however, exhibits a very poor rate of 75 percent.

Cluster	N(Stars) ($R_{TDR} > 3.$)	N(Galaxies) ($R_{TDR} > 3.$)	Success Rate
Abell 22	6	300	98 %
Abell 2204	166	488	75 %
Abell 3921	1	416	99 %

pendent measurements of the same galaxies. This is accomplished by searching the NASA/IPAC Extragalactic Database (NED) for any redshifts measured for galaxies in the field of the observations. In total, 25 galaxies with measured redshifts overlapped LARCS (including three in the field of Abell 22 from the 2dFGRS). The rms of the difference between the previously published redshifts and redshifts obtained using the techniques described above is 72 kms^{-1}. Again, this is similar to the estimate made above. Figure 5.6 shows the distribution of differences in redshift as a function of redshift as obtained from NED. There are no blunders in this comparison.

5.6.2 Success of Star–Galaxy Separation

From the redshifts determined above, it is possible to quantify how well the star–galaxy separation has performed. In Chapter 2, calculations showed that any galaxy catalogue generated from the criteria presented would have a stellar contamination rate not exceeding 3 percent.

Taking those spectra which have a secure redshift determination, $R_{TDR} > 3.0$, the stellar contamination rate from the spectroscopy is defined as the ratio of the number of stars ($cz < 500\mathrm{kms}^{-1}$) to the total number of secure redshifts obtained. Table 5.3 presents these numbers together with the spectroscopic success rate. Abell 22 and 3921 clearly have a success rate which is much higher than the predicted rate of 97 per cent. Abell 2204, however, has a very poor success rate.

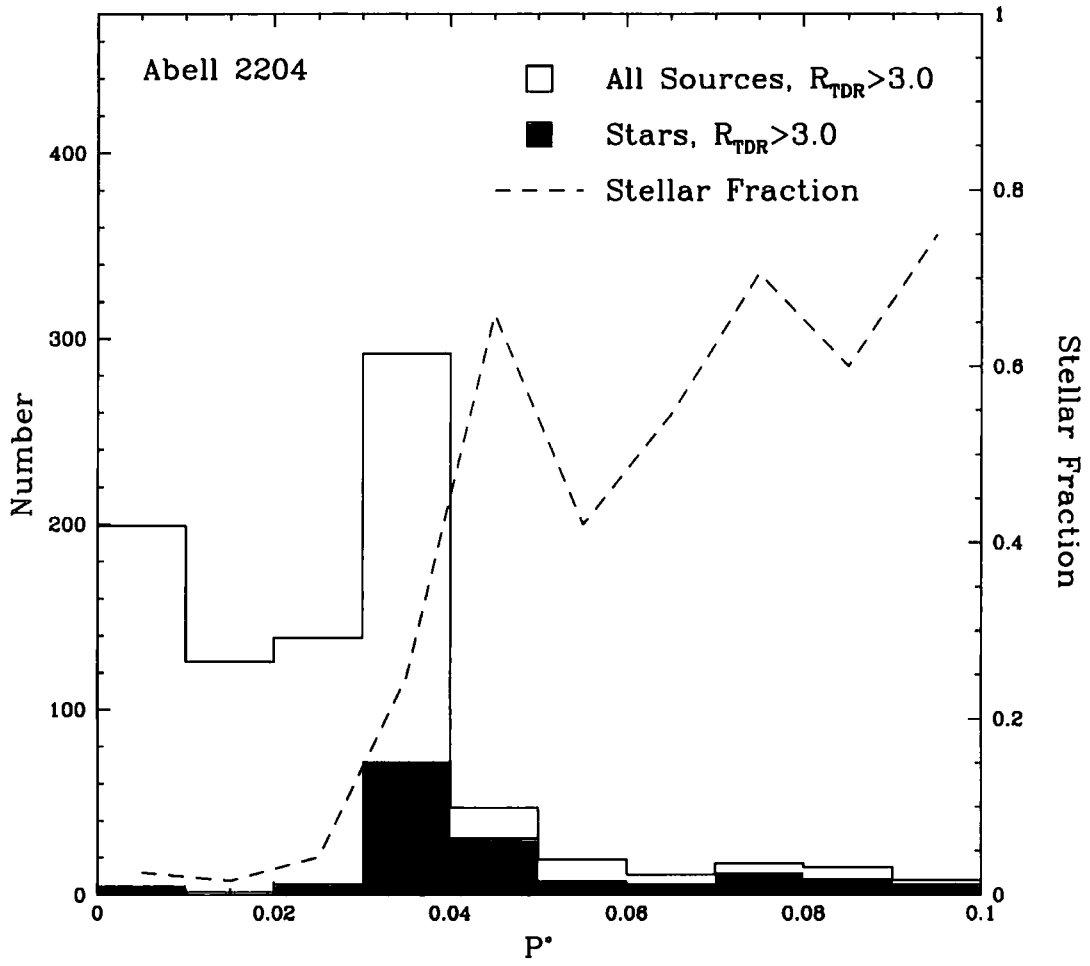

Figure 5.7: The distribution of P^* in Abell 2204 for spectroscopically confirmed stars is shown as the shaded histogram. The open histogram represents the distribution of all accurately ($R_{TDR} > 3.0$) determined redshifts. The fraction of stars (dashed line) rises sharply for $P^* > 0.04$.

What causes this range in stellar contamination rate given that these observations are selected using the same criteria? Firstly, an obvious area to investigate is the star–galaxy separation (see Chapter 2). The distribution of P^* for all spectroscopically confirmed stars with $R_{TDR} > 3.0$ in Abell 2204 are plotted as a fraction of all accurately determined ($R_{TDR} > 3.0$) redshifts in Figure 5.7. The fraction of stars clearly rises sharply for $P^* > 0.04$. It is suggested, therefore, that any future observations should be limited to galaxies with $P^* < 0.04$. Secondly, a cursory examination of the position of these clusters on the sky shows that the line of sight to Abell 2204 lies through the Galactic Bulge. This means that many more stars than would ordinarily be expected are present within the parent LARCS catalogue and hence in the potential spectroscopic target catalogue. Indeed, the photometric catalogue is about 150 per cent larger than a typical LARCS catalogue and $\sim$ 30 per cent of the total are bone-fide stars using the selection criteria generated in Chapter 2. By applying a simple cut of $P^* > 0.98$ to the parent LARCS catalogues, one is able to examine the starcounts. Figure 5.8 displays the starcounts for Abell 2204 against 22 and 3921. Clearly, the distribution of starcounts in Abell 2204 is not nearly as flat as for Abell 22 and 3921. At fainter magnitudes ($r > 19$), the number of stars in Abell 2204 is over eight times the number in the other catalogues. The colour-magnitude diagram for these objects displays no hint of a CMR: the majority of them possess a colour of $(B - R) \sim 1.0$. A visual inspection of the imaging for Abell 2204 also shows that there are more stars than in the other clusters. The final factor in this puzzle could be SExtractor itself. Abell 2204 is one of the highest redshift clusters in the LARCS sample, thus the observed magnitudes are generally fainter than for other clusters. At these fainter magnitudes, SExtrator's star–galaxy separation success rate becomes less reliable, dropping from 100 per cent to 90 per cent (Bertin & Arnouts 1996). With hindsight, therefore, it is perhaps unsurprising that many stars exist in the observations of Abell 2204.

5.7 Line Strength Measurement

The final stage in the data reduction pipeline is to measure various spectral line strengths for each of the galaxies observed. The measurement of spectral line

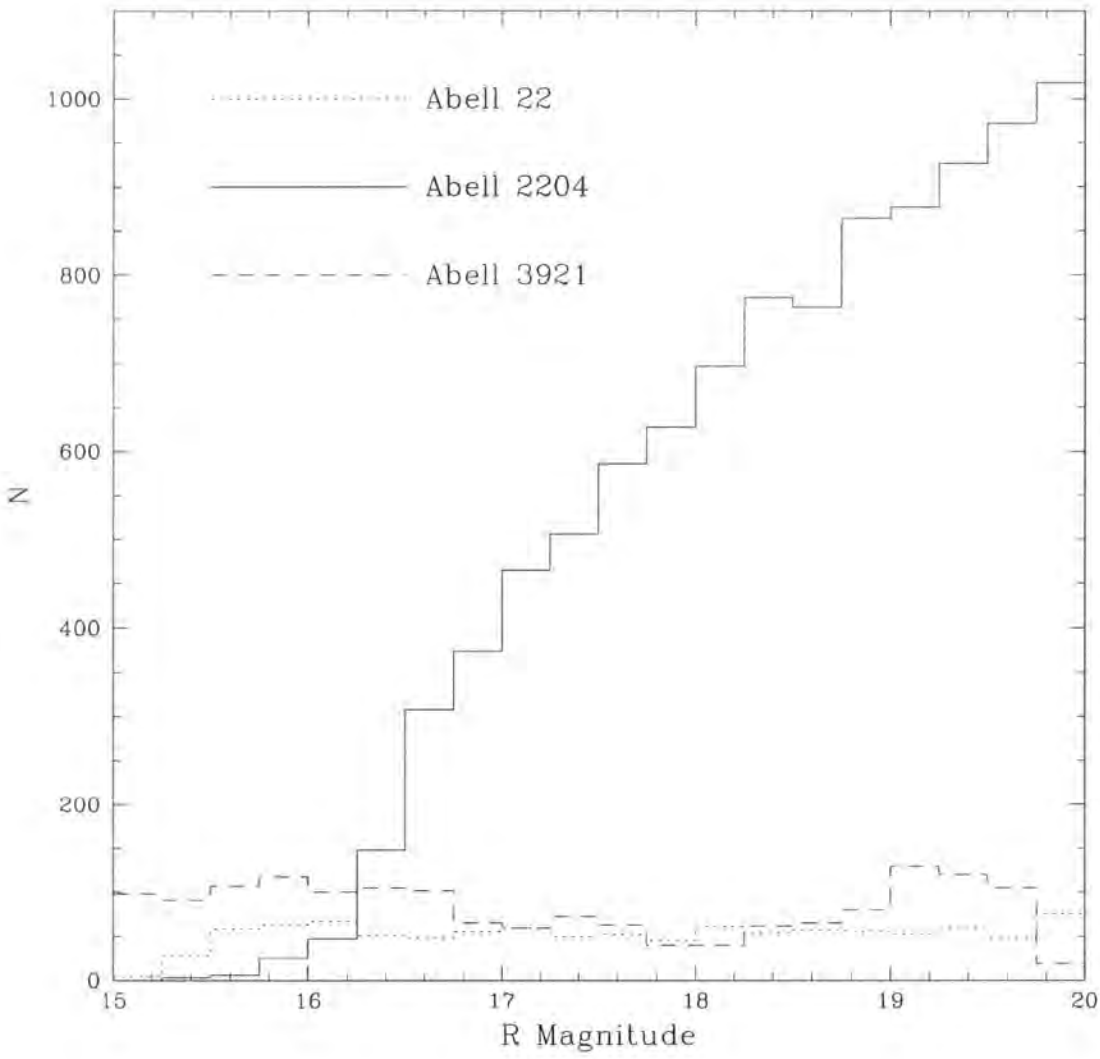

Figure 5.8: Starcounts for the parent LARCS catalogues of Abell 22, 2204 and 3921. Abell 2204 is very different from the other two clusters, possessing at least 8 times as many stars at $R \sim 19$.

strengths is accomplished using an automated program originally coded by Lewis Jones. The documentation for the algorithms that the program uses are presented in Worthey & Jones (1995) and Jones & Couch (1998) and are briefly summarized here.

The program calculates the equivalent widths (or equally, spectral indices) of up to 30 spectral features by finding the ratio of flux in a 30-40$\AA$ index passband to that of a continuum level. To calculate the continuum level, the program finds the mean flux in two 30-40$\AA$ sidebands blueward and redward of the index passband. The local continuum level is then defined the straight line connecting the mean of these two sidebands. The fixed values for the set of line indices and sidebands used to compute the equivalent widths are recorded in Table 5.4.

Following Jones and Couch (1998), the flux in each index band is then computed as:

$$F_\lambda = \frac{\sum F_{\lambda,k}/\sigma^2_{\lambda,k}}{\sum 1/\sigma^2_{\lambda,k}}$$

where F_λ is the summed flux for a given index, λ, $F_{\lambda,k}$ is the flux at point k for the index and $\sigma_{\lambda,k}$ is the Poisson error bar. The cumulative error bar for a given index, σ_λ, is then evaluated as:

$$\sigma^2_\lambda = \frac{1}{\sum 1/\sigma^2_{\lambda,k}}$$

The equivalent width, EW, for a given index is then:

$$EW = \int_{\lambda_B}^{\lambda_A} (1 - F_\lambda/F_C)$$

where F_C is the flux of the local continuum (see above for definition). Thus the resulting values for the measured EW will be negative for spectral features that are in emission whilst conversely, positive values are absorption feature. In this work, all EW values are presented as positive values and are specified as being in emission or absorption.

The detection limit of the measurements of [OII] is computed by finding the scatter of the EW of the spectral index about zero and assuming that the median of the negative tail of this distribution, 1.5Å , is then taken as the detection limit estimate. Any modulo value less than this is assumed to be noise.

Table 5.4: Spectral index, location of index passband and sidepassbands used to calculate equivalent widths. The F and A subscripts on some indices denote narrower and broader ranges respectively.

Index	Index	Sidebands ($\AA$)		Width
Name	Passband ($\AA$)	Blue	Red	($\AA$)
CN_1	4142.125–4177.125	4080.125–4117.625	4244.125–4284.125	35.00
CN_2	4142.125–4177.125	4083.875–4096.375	4244.125–4284.125	35.00
Ca4227	4222.250–4234.750	4211.000–4219.750	4241.000–4251.000	12.50
G4300	4281.375–4316.375	4266.375–4282.625	4318.875–4335.125	35.00
Fe4383	4369.125–4420.375	4359.125–4370.375	4442.875–4455.375	51.25
Ca4455	4452.125–4474.625	4445.875–4454.625	4477.125–4492.125	22.50
Fe4531	4514.250–4559.250	4504.250–4514.250	4560.500–4579.250	45.00
Fe4668	4634.000–4720.250	4611.500–4630.250	4742.750–4756.500	86.25
$H\beta$	4847.875–4876.625	4827.875–4847.875	4876.625–4891.625	28.75
Fe5015	4977.750–5054.000	4946.500–4977.750	5054.000–5065.250	76.25
Mg_1	5069.125–5134.125	4895.125–4957.625	5301.125–5366.125	65.00
Mg_2	5154.125–5196.625	4895.125–4957.625	5301.125–5366.125	42.50
Mg_B	5160.125–5192.625	5142.625–5161.375	5191.375–5206.375	32.50
Fe5270	5245.650–5285.650	5233.150–5248.150	5285.650–5318.150	40.00
Fe5335	5312.125–5352.125	5304.625–5315.875	5353.375–5363.375	40.00
Fe5406	5387.500–5415.000	5376.250–5387.500	5415.000–5425.000	27.50
Fe5709	5696.625–5720.375	5672.875–5696.625	5722.875–5736.625	23.75
Fe5782	5776.625–5796.625	5765.375–5775.375	5797.875–5811.625	20.00
Na_D	5876.875–5909.375	5860.625–5875.625	5922.125–5948.125	32.50
TiO_1	5936.625–5994.125	5816.625–5849.125	6038.625–6103.625	57.50
TiO_2	6189.625–6272.125	6066.625–6141.625	6372.625–6415.125	82.50
$H\delta_A$	4084.750–4123.500	4042.850–4081.000	4129.750–4162.250	38.75
$H\gamma_A$	4321.000–4364.750	4284.750–4321.000	4368.500–4421.000	43.75
$H\delta_F$	4092.250–4113.500	4058.500–4089.750	4116.000–4138.500	21.25
$H\gamma_F$	4332.500–4353.500	4284.750–4321.000	4356.000–4386.000	21.00
OII3727	3722.000–3735.000	3695.000–3715.000	3740.000–3760.000	13.00
CNviolet	3850.000–3870.000	3755.000–3810.000	3890.000–3920.000	20.00
OIII5007	4994.000–5022.000	4970.000–4990.000	5025.000–5056.000	28.00

5.7.1 Accuracy of the Measured Equivalent Widths

The method used to measure EWs is based upon finding the continuum level from two bands either side of the line of interest. To ensure that the measured EWs are comparable to previous studies (specifically, the MORPHS results; Dressler et al. 1999; Poggianti et al. 1999), these measurements are repeated using the purpose-written code[‡] of Dressler et al. (1999) for a sub-sample of the LARCS spectra consisting of $\sim$ 75 high quality ($R_{TDR} > 3.0$) spectra from Abell 3921. These spectra are representative of the observations made.

The code used by Dressler et al. (1999) is an interactive one which enables the user to simultaneously define the continuum level of each individual spectra and the central peak of each spectral feature desired. For each spectra, four important spectral features are measured where they are clearly discernable: H_β, H_δ, [OII] and [OIII]. Plotted in Figure 5.9 is the distribution of difference in the EW measurements when the method of Dressler et al. (1999) is employed. The rms difference in the measured EW remains constant at $\sim$ 0.5Å whilst the median offset between LARCS and MORPHS measurements is $\sim$ 0.1Å.

5.8 Completeness

From the results of the data reduction and redshift determinations, the spectroscopic completeness of the observations can now be investigated.

The spectroscopic completeness of the clusters, together with the number of secure ($R_{TDR} > 3.0$) redshift determinations, are illustrated in Figures 5.10, 5.11 and 5.12 for Abell 22, 2204 and 3921 respectively. Although the completenesses may appear poor at first glance, recall that there are intentionally many more potential targets than observations allow as outlined in §4.4 as it is impossible to fully observe the clusters owing to their high central concentrations.

In Abell 22, only one configuration was observed; the second was not undertaken due to inclement weather conditions. This cluster requires at least one more

[‡]The purpose-written code of Dressler et al. (1999) is based upon a Gaussian line fitting routine developed by Paul Schechter and is similar to using the SPLOT command within IRAF. This code was donated to Pimbblet in original form by Smail.

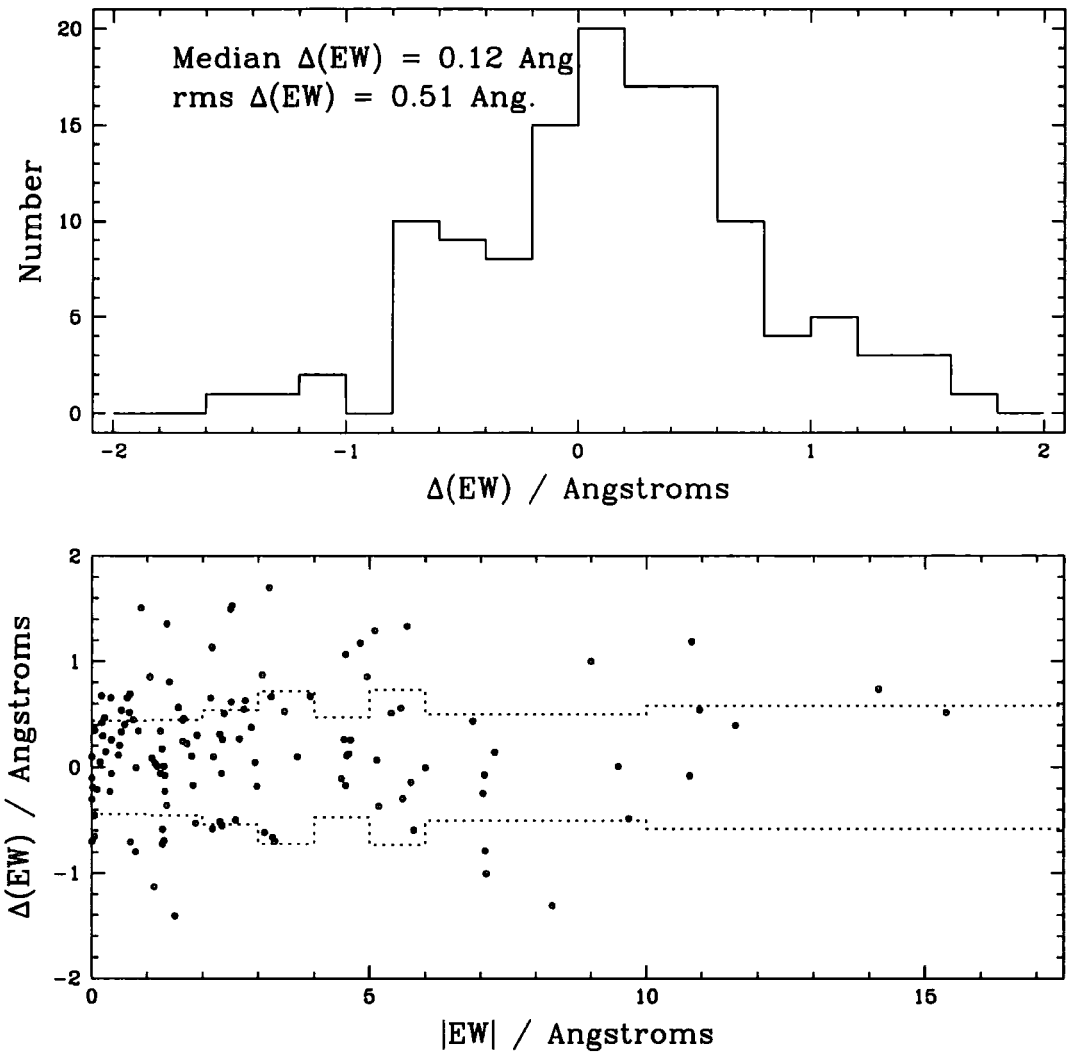

Figure 5.9: The distribution of the difference in measured EWs of a sample of high quality spectra from Abell 3921 when using the technique of the MORPHS collaboration (Dressler et al. 1999) is shown in the upper panel. The dependance of EW differences with EW is shown in the lower panel together with a rolling rms (dotted lines).

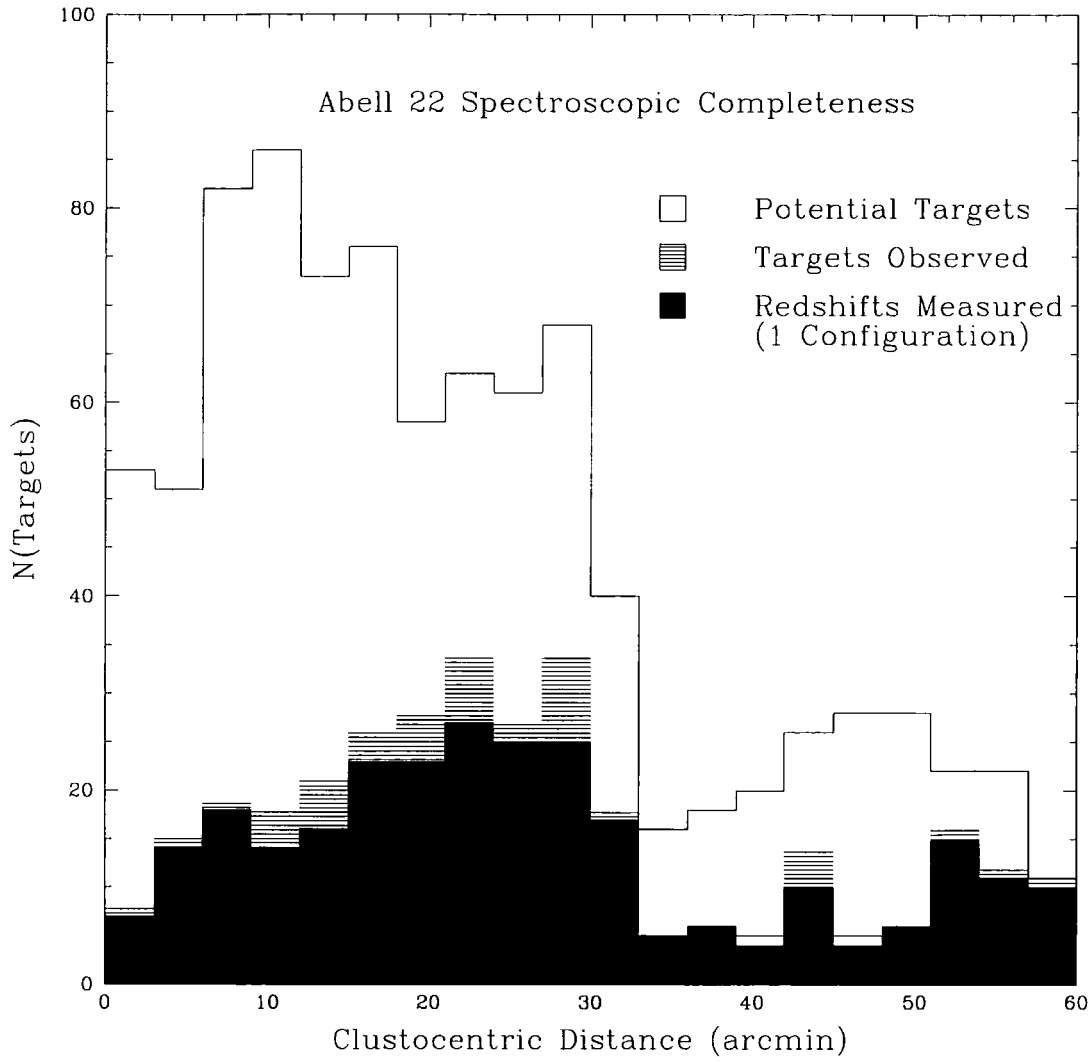

Figure 5.10: The number of potential spectroscopic targets for Abell 22 when the selection conditions detailed in §4.4.1 are applied (open histogram). The shaded histogram shows the actual spectroscopic targets observed in the July 2000 observing run using 2dF, whilst the solid histogram shows the number of secure redshifts measured.

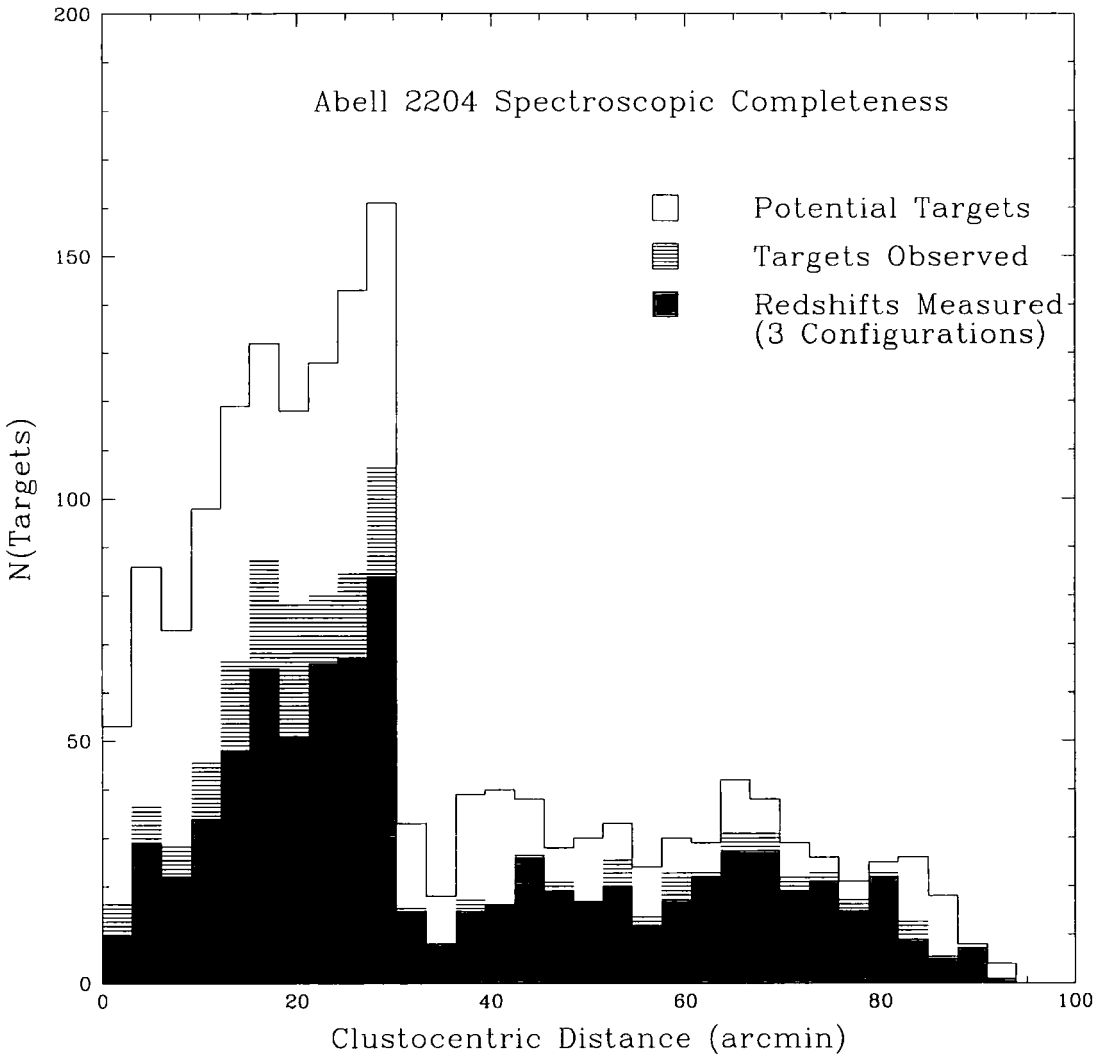

Figure 5.11: As Figure 5.10 for Abell 2204. The position of this cluster's centre is not located in the centre of the photometric mosaic, hence the clustocentric radius extends beyond 60′. This cluster is considered to be fully observed.

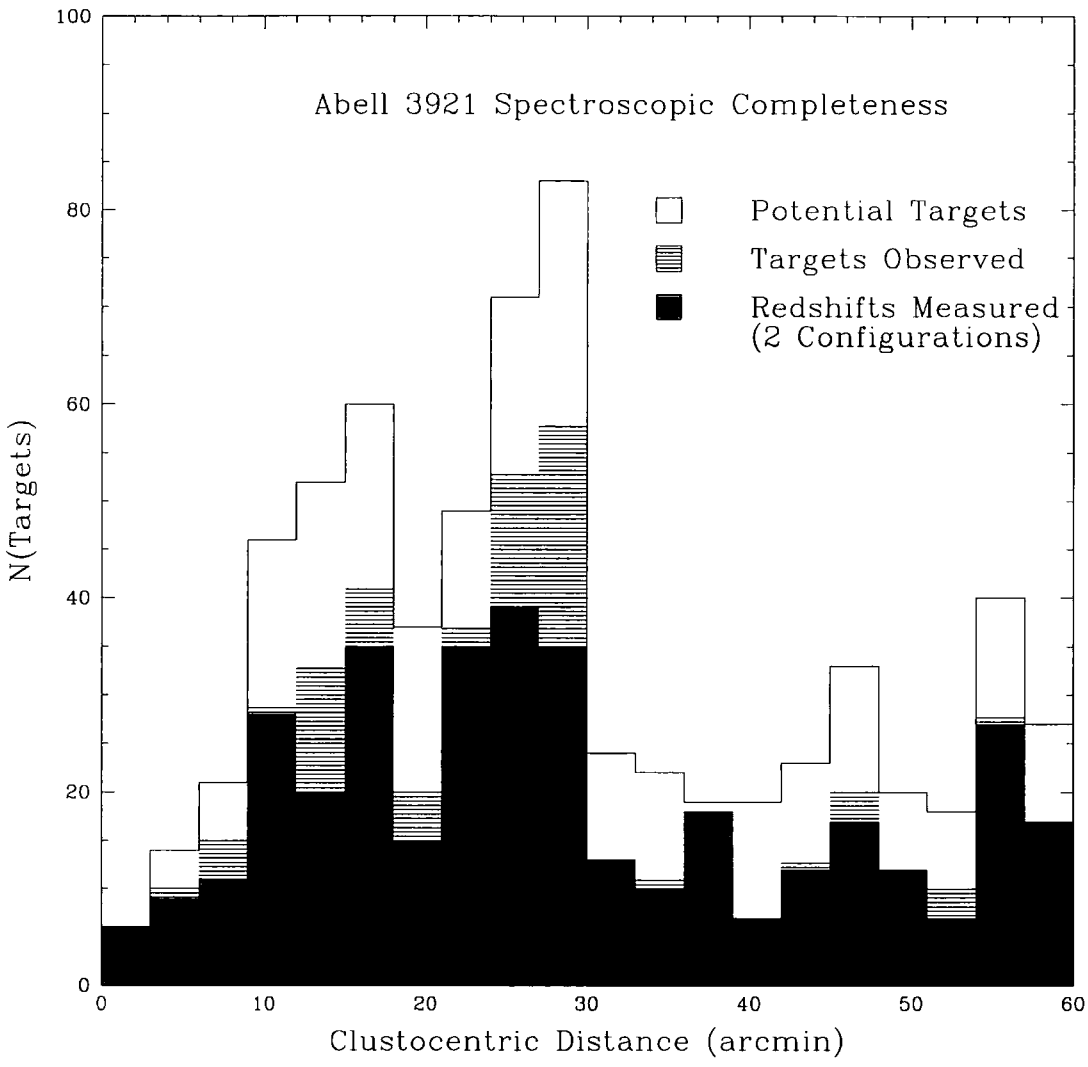

Figure 5.12: As Figure 5.10 for Abell 3921. Half of these data originated in the July 2000 run, half from the July 2001 service observations. This cluster is considered to be fully observed.

configuration to be considered to be fully observed, however, it is viewed that the results obtained with Abell 22 thus far can be considered to be representative.

Abell 2204 is completely observed, having had three configurations completed. Because the centre of A2204 is spatially offset from the centre of the photometric mosaic, the clustocentric distance in Figure 5.11 runs to a larger extent than the other clusters. Coverage in the outer regions (radius $> 30'$) is more complete than in the central, crowded region. Completeness in the inner regions is over 50 per cent.

Abell 3921 is also considered to be completely observed, having had two configurations completed. This cluster shows similar statistics to Abell 2204 with the outer regions appearing more complete than the inner ones.

The completeness levels are comparable to those obtained during the 1998 run and analyzed in O'Hely et al. (2001 in prep.) and O'Hely (2000).

5.9 Archival Data

There are two additional sets of archival data which are now added to the observations described above. These are the 2dF observations made by O'Hely, Couch and Edge in 1998 from the LARCS archive (see O'Hely 2000) and the 2dFGRS observations of the overlapping regions of the sky (see Chapter 3).

As noted above, Edge, Couch and O'Hely undertook a preliminary set of 2dF observations which suffered from many drawbacks. These observations are summarized in Table 5.5. Since they used the same selection, it is reasonable to include them in the spectroscopic analysis that follows.

5.9.1 2dFGRS Overlap

The overlap regions between the LARCS project and the 2dFGRS have also been investigated for additional spectroscopic data. Four LARCS clusters overlap with 2dFGRS: A22, A1084, A1650 and A1651 (see §3 for a detailed account of the photometric comparison).

At the time of writing only one of these clusters, Abell 1651, has had any obser-

Table 5.5: Summary of spectroscopic observations undertaken using 2dF by Edge, Couch and O'Hely in 1998. The total number of spectroscopic candidates in each plate configuration is given along with a breakdown of those objects that a reliable redshift has been obtained for. These observations all used the 600 V grating.

Cluster	Configuration	Plate	T_{Exp} (Hours)	N(Fibres allocated)	N(Galaxies)	N(Stars)	N(Sky)
Abell 2055	1	0	5×0.5	373	188	84	20
Abell 2055	2	1	7×0.5	367	99	231	20
Abell 2104	1	0	5×0.5	377	209	65	20
Abell 2104	2	1	8×0.5	368	197	78	22
Abell 3888	1	0	2×0.5	196	144	16	28
Abell 3888	2	1	2×0.5	364	242	78	23

vations made with 2dF (Colless et al. 2001; Cole at al. 2001). These observations source from two aspects of the 2dFGRS project. The first source is the '2dFGRS 100k Release' (see http://www.mso.anu.edu.au/2dFGRS/). This source has 120 observations (using the 300B grating) of objects overlapping with the Abell 1651 LARCS catalogue. These observations come with the actual spectra observed and the 2dFGRS's measurement of the redshift. The spectra are all high quality: they possess a median signal to noise ratio of $S/N \gtrsim 7.0$ and two or more spectral features are readily identified and can be used for redshift estimation. Redshift computation is similar to the method used by LARCS (see Colless et al. 2001); absorption and emission lines are fitted using a cross-correlation method. When a poor result is obtained from the automated redshift determination, the redshift is manually determined.

Of the spectra from the 2dFGRS 100k release, 9 are stellar, defining a spectroscopic stellar contamination of ~ 7 per cent. This is broadly in line with photometric considerations for the stellar contamination for the GRS/APM presented in §3. The redshifts obtained by the 2dFGRS team have been visually inspected to check their goodness of fit. None of them have been rejected on this basis.

Secondly, there is the 2MASS overlap (Cole et al. 2001) which provides an additional 83 observations. The spectral imaging is kindly provided by Colless (priv. comm.) since these data are not publicly made available at present. The 2MASS overlap has exactly the same data reduction pipeline as the 100k release, therefore it is safe to assume that the redshifts from this are just as accurate.

If the LARCS project would have observed the field of Abell 1651, all of the galaxies observed by the 2dFGRS team (both in the 100k release and the 2MASS overlap release) would have been included in the LARCS selection criteria. Therefore the inclusion of these data in this analysis is valid. It must be noted, however, that the selection of objects and magnitude limits for 2dFGRS (Colless et al. 2001) are different from the survey design for LARCS (e.g. the sample is not split into bright core, faint core and bright halo).

5.10 Summary

Targets from the LARCS photometric catalogue have been selected in a robust, reproducible manner for follow-up spectroscopic observations using the 2dF spectroscope at the AAT. Each target catalogue contains over 1000 potential targets to ensure that 2dF does not waste any fibres owing its need for a minimum separation between the buttons.

The July 2000 observing coupled with the July 2001 service run obtained over 2000 redshifts for targets in Abell 22, 2204 and 3921. The spectroscopic stellar contamination rate is confirmed as less than 3 per cent for Abell 22 and 3921, but due to its proximity to the Galactic plane, Abell 2204 suffered a rate of $\sim$ 25 per cent contamination.

The 2dFGRS overlap has provided an additional 203 spectra for Abell 1651. With the previous observations made by O'Hely (2000), the LARCS spectroscopic dataset presently consists of some 4489 spectra, boasting some 3086 confirmed galaxies over 7 clusters.

Chapter 6 | *Dynamical Analysis*

6.1 Abstract

Having described the spectroscopic observations in Chapter 5 the spectra are now analyzed to develop a view of the cluster dynamics. This analysis commences with a qualitative examination of the clusters using velocity histograms and wedge plots to compare previous redshift estimates with and search for signs of subclustering and other large-scale structure along the line of sight. A number of methods of spectroscopically determining cluster membership are then examined, including iterative clipping techniques and a mass model. The spectra are then typed using the MORPHs nomenclature and a selection function is developed to account for the observational strategy. Finally, cluster morphology and substructure are then examined using the Dressler-Shectman (1988) test.

6.2 Velocity and Spatial Structure

There are a number of ways to qualitatively and quantitatively examine the spectroscopic data in order to determine cluster membership. As the assignment of cluster membership can be controversial and fraught with difficultly, the 2dF spectroscopy is examined in a qualitative manner to start with.

Velocity histograms are used to make an initial estimate of a clusters redshift, indicate possible sub-structure and show any other structures appearing along the line of sight. Figure 6.1 shows the velocity histograms for the clusters. Similar diagrams for the 1998 observing run are presented and discussed in O'Hely (2000). The histograms are binned into 1000 kms^{-1} intervals. The inset panel is an enlargement of a 20000 kms^{-1} range around the cluster velocity, binned into intervals of 400 kms^{-1}.

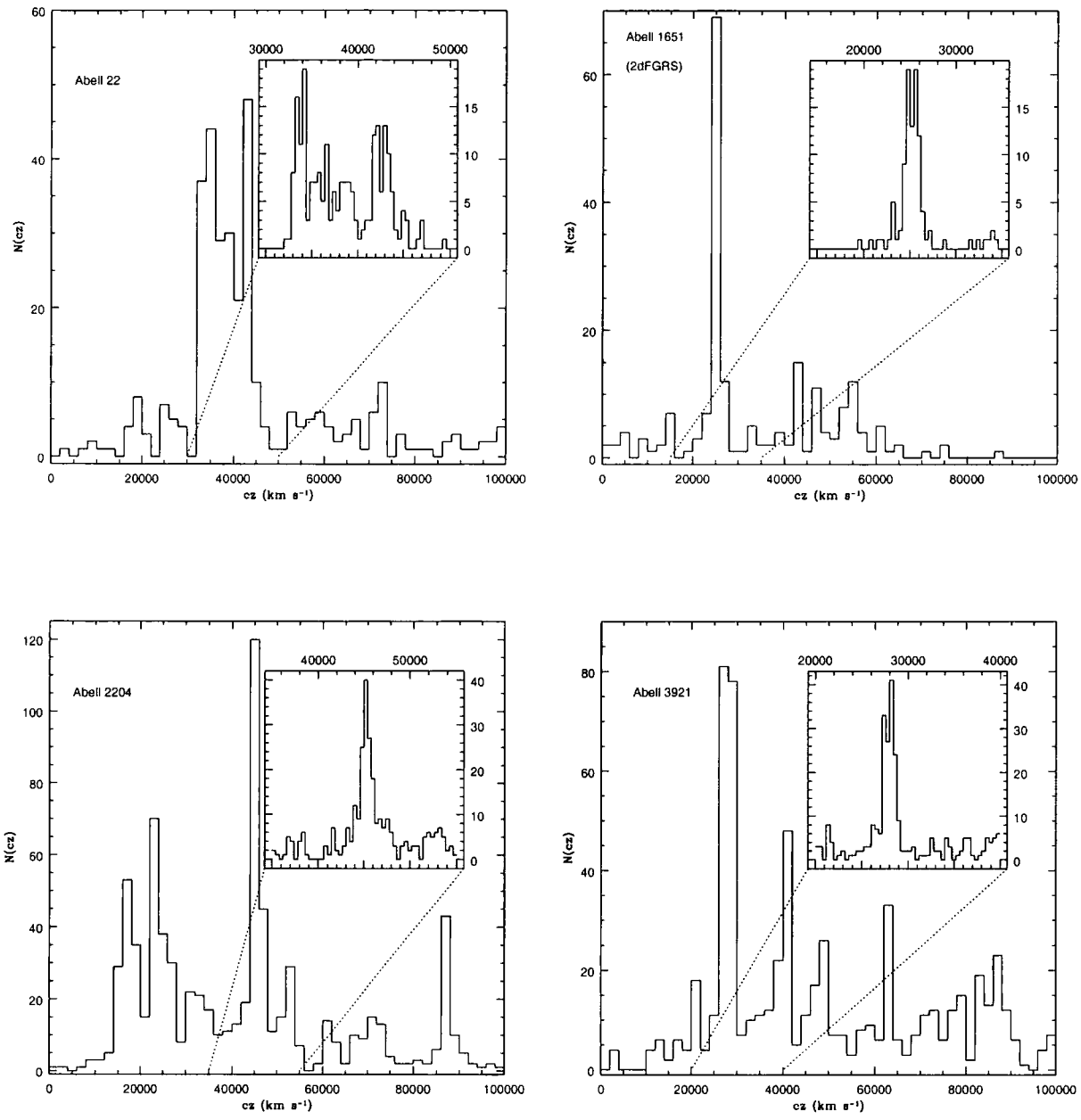

Figure 6.1: Velocity histograms for Abell 22, 1651, 2204 and 3921. The bins are 1000 kms^{-1} wide in the main plots and 400 kms^{-1} wide in the inset panels.

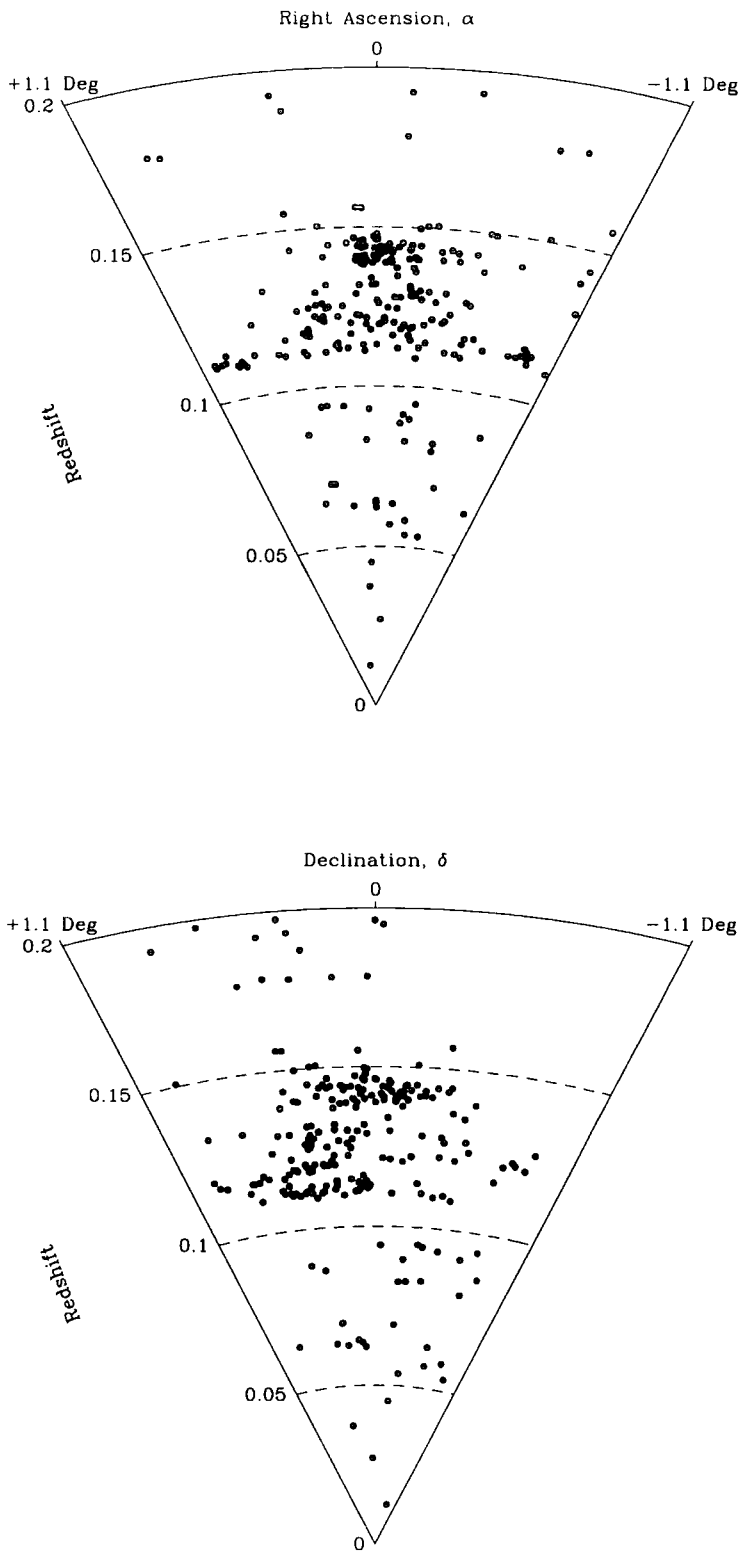

Figure 6.2: Wedge plots of RA and Dec versus redshift for Abell 22.

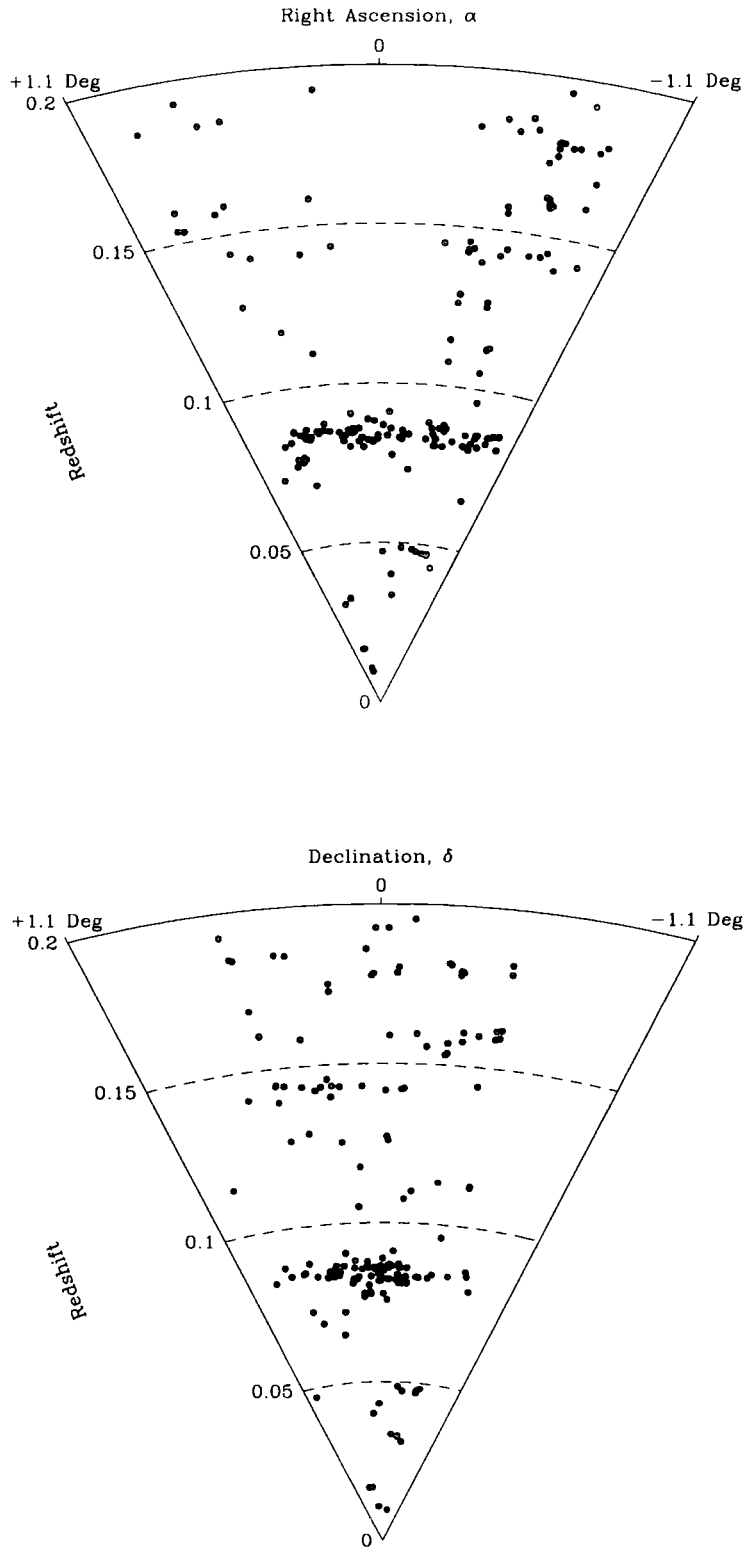

Figure 6.3: As for Figure 6.2 for Abell 1651.

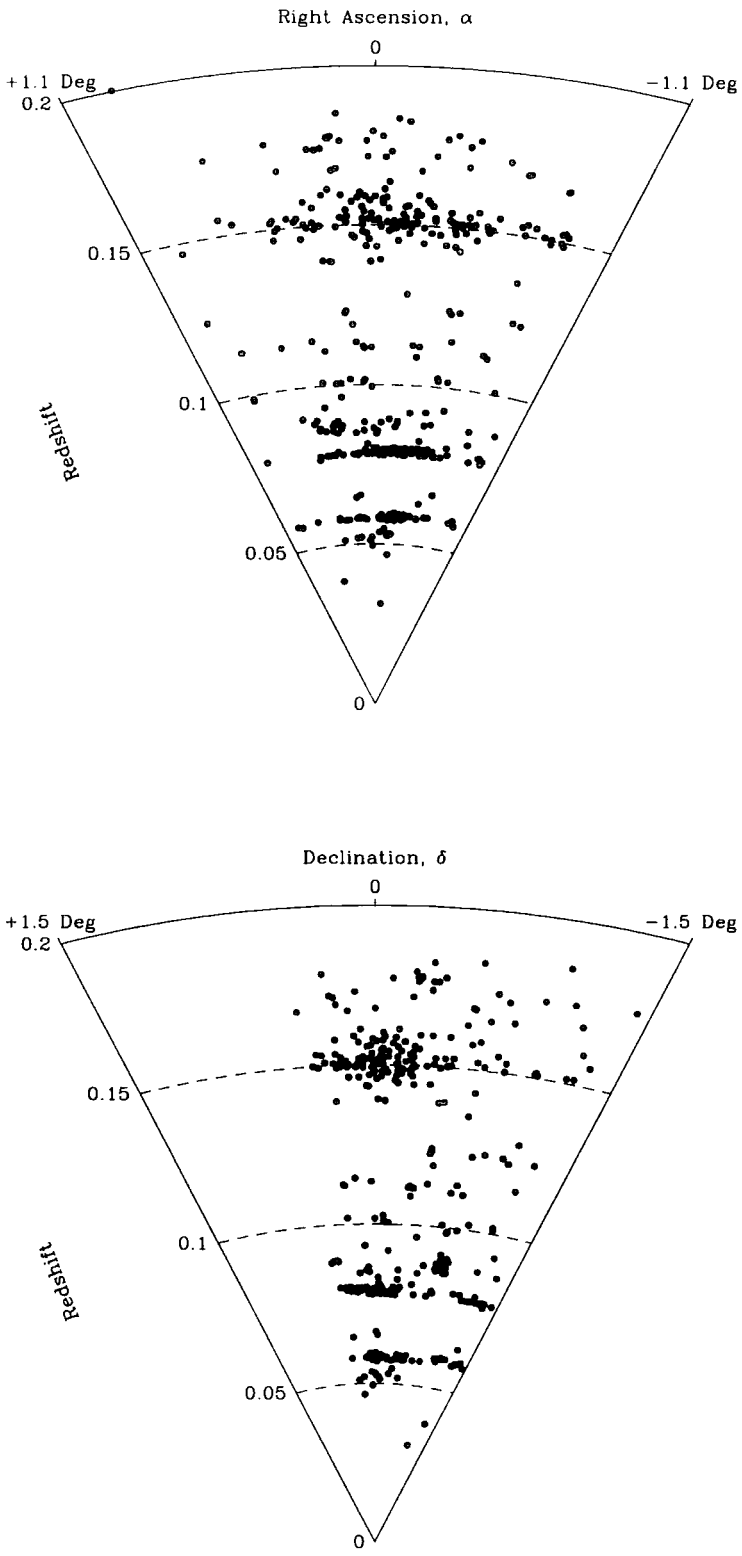

Figure 6.4: As for Figure 6.2 for Abell 2204. The declination has an unusual range owing to the incorrect pointing of the optical mosaic: the clusters centre is not located at the centre of the mosaic.

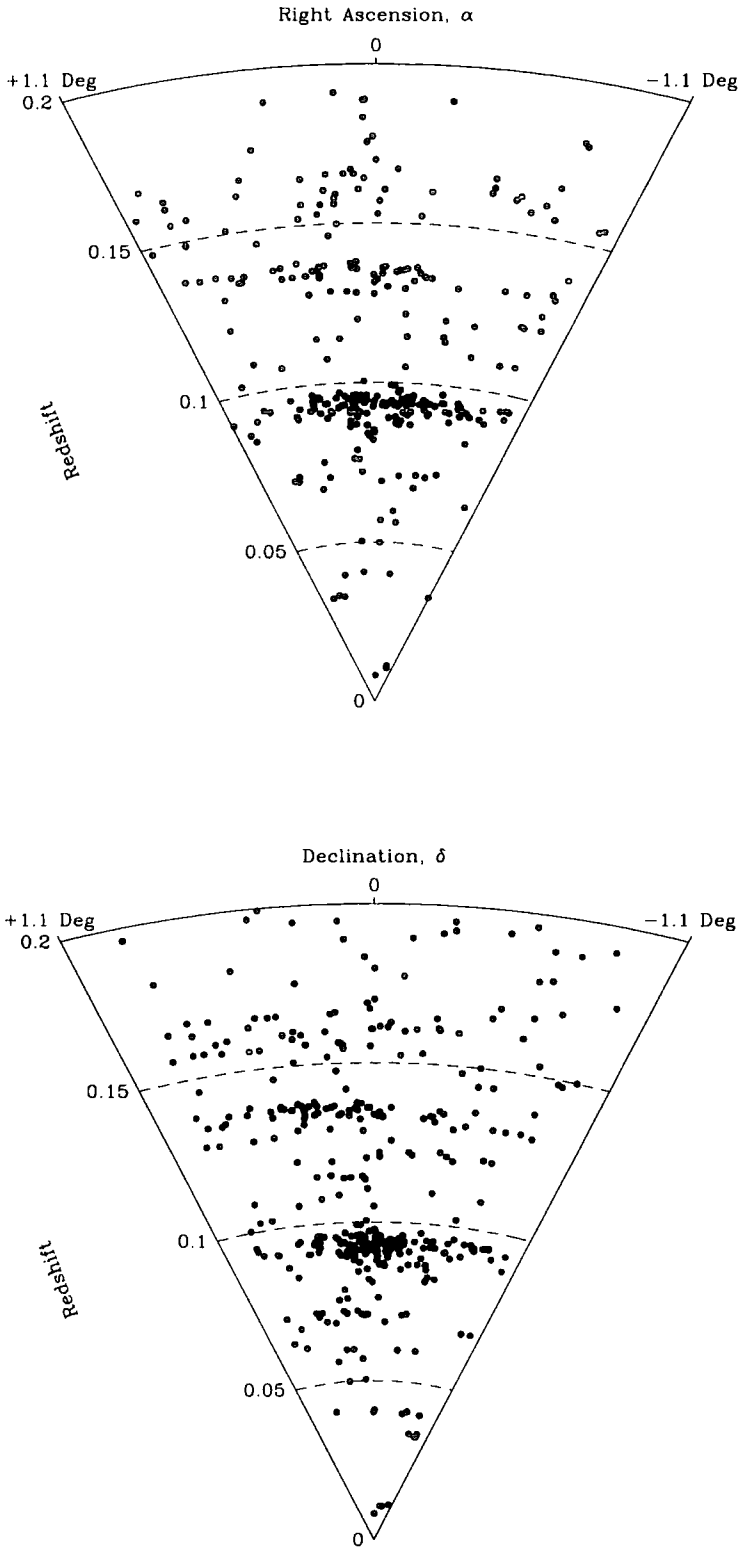

Figure 6.5: As for Figure 6.2 for Abell 3921.

Another way of looking at the cluster populations is to examine cone or wedge plots. Such plots show the position of the galaxies along the line of sight with respect to their angular position on the sky. They are widely employed in redshift surveys (e.g. 2dFGRS) to demonstrate the large scale structures of the Universe.

Note that although one may expect these plots to exhibit a 'finger of God' effect for the clusters, arising from the distorting effects in redshift space, this is not seen in the wedge plots for the LARCS clusters as the elongation in redshift space of the clusters is small in comparison to the angular extent of the plots.

Wedge plots for Abell 22, 1651, 2204 and 3921 are shown in Figures 6.2, 6.3, 6.4 and 6.5 respectively. Again, similar diagrams for Abell 2055, 2104 and 3888 are presented in O'Hely (2000).

6.2.1 Abell 22

Abell 22 has a central peak which coincides with previously published estimates of the clusters redshift, $cz \sim 39300\text{kms}^{-1}$ (Dalton et al. 1994). The peak of the distribution in the velocity histogram is unusually broad and appears to contain much substructure. The wedge plot (Figure 6.2) reveals that Abell 22 is a highly complex structure. The cluster itself is markedly ellipsoidal: compressed in Right Ascension but extended in Declination. Further, the cluster appears to extend in redshift space and merges with the foreground structure. These foreground galaxies are striking: a wall-like structure which appears to stretch across the entire RA range of the observations, but is more limited in scope in Dec(and offset from the cluster).

6.2.2 Abell 1651

The clean central peak located at $\sim 25000\text{kms}^{-1}$ is in good agreement with previously published redshifts for this cluster of 25220kms^{-1} (Struble & Rood 1991). Its distribution is very different to that of Abell 22's. The cluster sits alone in redshift space with no clear connection to other large scale structure. A possible sub-group is apparent in RA at a redshift just below that of the cluster.

Voids exist both in front and behind the cluster along the line of sight. There

are a small number of minor peaks in velocity space at $\sim$ 45000kms^{-1} and $\sim$ 55000kms^{-1}, indicative of large scale structure.

6.2.3 Abell 2204

This cluster possesses a distinct, singularly peaked dispersion at $\sim$ 45000kms^{-1}. Previously published redshifts of 45750kms^{-1} (Struble & Rood 1991) lie close to this value. The central peak is somewhat broader than Abell 1651's indicating that this cluster is comparatively more massive.

The walls and voids of large scale structure, dominate the line of sight to the cluster. Notable structures manifest themselves at $\sim$ 18000kms^{-1}, $\sim$ 22000kms^{-1} and $\sim$ 88000kms^{-1} with large, isolating voids devoid of galaxies dividing them up into distinct units.

6.2.4 Abell 3921

Abell 3921 demonstrates a clear over abundance of galaxies at a redshift of $\sim$ 29000kms^{-1}, agreeing well with previously published estimates of the redshift, 28780kms^{-1} (Dalton et al. 1994). The central peak of A3921 is not broad, spanning some $\sim$ 1500kms^{-1} in velocity space as presented in the inset panel of Figure 6.1. The cluster appears regular with no immediately obvious sub-structure.

Background to the cluster are a number of wall like structures ($\sim$ 40000kms^{-1}, $\sim$ 48000kms^{-1}, $\sim$ 62000kms^{-1} and $\sim$ 88000kms^{-1}) but unlike the other observations, the voids are not so noticeable along this line of sight: galaxies are spread throughout the regions between the major overdensities.

6.3 Spectroscopic Determination of Cluster Membership

Having examined the broad properties of the cluster velocity and spatial structure in the previous section, attention is now turned to defining the clusters in a more rigorous manner. In this section several statistical methods are employed to de-

termine cluster membership including an iterative clipping technique and a mass model.

6.3.1 Statistical Clipping

A traditional method to determine cluster membership is to use a statistical clipping technique. Two different statistical clipping techniques are investigated here: that of Colless (1987; C87) and Zabludoff, Huchra and Geller (1990; ZHG).

In their study of the uniformity of cluster velocity distributions Yahil and Vidal (1977; YV77) defined cluster membership using a 3σ clipping technique upon which C87 and ZHG also base their methods. YV77 assumes that the velocity distribution of the galaxies will follow an underlying Gaussian distribution. This is a valid assumption to make if the clusters are relaxed isothermal spheres and the galaxies are massless tracers.

The relaxed isothermal sphere assumption, however, would be invalidated if there is discovered to be substructure within the clusters (e.g. Zabludoff and Zaritsky, 1995). Such an effect adds a degree of uncertainty into the results produced by the method of YV77, but for ease of comparison to other results, YV77 provides a simple option.

Briefly, the method of YV77 is as follows. For a given sample of galaxies whose recession velocities are known, the mean radial velocity, $\overline{cz}$, and dispersion, σ_z are calculated. The most deviant galaxy in the sample is then identified. The values of $\overline{cz}$ and σ_z are then recalculated for the sample excluding this most deviant galaxy. If the deviant galaxy is found to be within $3\sigma_z$ of the new $\overline{cz}$, then the process is at an end. Otherwise, a new most deviant galaxy is identified and the process is iterated until no further galaxies are excluded from the sample. At the end of the iteration a cluster is defined as all those galaxies within $\pm 3\sigma_z$ of the mean. The $3\sigma_z$ limit chosen by YV77 was thought to be a reasonable compromise between excluding as much field as possible whilst retaining as many cluster members as possible. The method of C87 is identical to YV77 save that the initial removal of foreground and background groups is used to ensure that the velocity dispersion is not artificially enhanced.

Table 6.1: Initial clipping used and the results of applying the ZHG technique to the LARCS clusters. The errors are calculated from the method of DDD. These results are exactly the same when the technique of C87 is applied. Additionally, the results from O'Hely (2000) for Abell 2055, 2104 and 3888 are presented alongside for comparison. The final number of galaxies present within the cluster, N(gal), is given in the final column.

Cluster	Velocity Range	$\overline{cz}$	σ_z	N(gal)
	kms^{-1}	kms^{-1}	kms^{-1}	
Abell 22	41000-44500	42658 ± 96	783^{+79}_{-61}	65
Abell 1651	24000-28000	25348 ± 76	683^{+61}_{-48}	80
Abell 2204	43500-48000	45511 ± 76	975^{+59}_{-50}	162
Abell 3921	25000-30500	27822 ± 68	875^{+52}_{-44}	166
Abell 2055	27500-35000	30802 ± 92	698^{+69}_{-53}	105
Abell 2104	43000-49000	46548 ± 159	1193^{+112}_{-88}	172
Abell 3888	43000-49000	46063 ± 248	1678^{+178}_{-135}	163

The ZHG technique differs from the above in that any galaxies that are more than $2000\mathrm{kms}^{-1}$ away from the dominant cluster population are automatically removed from the sample. The mean velocity, $\overline{cz}$, and dispersion, σ_z, of this distribution is then calculated. The entire distribution is then looped over and those galaxies which are outside $1\sigma_z$ of their nearest neighbour are flagged for exclusion. This process is then iteratively repeated, excluding the flagged galaxies, until convergence of the galaxy population is achieved.

It is found that the results of the application of the C87 and ZHG techniques to the clusters give similar results in all cases. Table 6.1 presents the recession velocities of the clusters and their velocity dispersions. The values for the errors on the velocity dispersion and mean velocity are taken using the formula presented in Danese, De Zotti and di Tullio (1980; DDD). As with YV77, DDD is valid only for Gaussian distributions. The clusters analyzed by O'Hely (2000) are also presented for comparison.

Having established the results for the clusters and shown them to be the same for

either technique, the results from ZHG are adopted. This approach is now applied to the other overdensities observed along the line of sight to the clusters (see §6.2; O'Hely, 2000). An initial guess of the clipping to use is made by manual inspection of the velocity histograms and wedge plots for the fields (see Section 6.2). The results of this analysis are presented in Table 6.2. As suspected from the wedge plots, some of the other structures present along the line of sight can be thought of as clusters in their own right, e.g. Abell 2204-C, Abell 3921-A, Abell 3921-C and Abell 3921-D. Indeed, several of these clusters are readily identified from the literature: Abell 3921-A is identified as Abell 3921-2 (Katgert et al. 1996) whose previously determined redshift, $cz = 40172\text{kms}^{-1}$, agrees well the the value of 40208kms^{-1}. Abell 3921-C is identified as AM 2250-633 (de Grandi et al. 1999), previously determined to be at $cz = 63360\text{kms}^{-1}$. Abell 1651-A is suggested to be Abell 1658 seen in the CMR analysis (see Chapter 4). Abell 2055-A appears to be Abell 2052 ($cz = 10493\text{kms}^{-1}$; Struble & Rood 1999) whilst Abell 2104-A is suggested to be Abell 2103.

6.3.2 Mass Model

The techniques for defining cluster membership presented in the previous section only makes use of one parameter: the measured recession velocities. A mass model is capable of fully exploiting both spatial and redshift information to define the limits of a cluster. The mass model considered here is that of the Canadian Network for Observational Cosmology team (CNOC; e.g. Carlberg et al., 1996; Balogh et al., 1999).

The CNOC mass model derives from a theoretical model based upon the assumption that clusters are singular isothermal spheres. The technique is described in detail in Carlberg, Yee and Ellingson (1997; CYE) and briefly summarized here: Firstly, the difference in velocity, Δv, between each galaxy and the mean velocity of the cluster, $\overline{cz}$, is computed. The values of Δv are then normalized to the velocity

Table 6.2: As for Table 6.1 for other overdensities along the line of sight as determined from the velocity histograms and wedge plots.

Cluster	Clipping (cz/kms^{-1})	$\overline{cz}$ kms^{-1}	σ_z kms^{-1}	N(gal)	Comments
Abell 22-Wall	30000-35000	33811 ± 88	619^{+74}_{-54}	49	
Abell 1651-A	40000-45000	42843 ± 121	500^{+119}_{-69}	16	Abell 1658(?)
Abell 2204-A	16000-18500	17441 ± 50	360^{+42}_{-31}	51	
Abell 2204-B	22000-25000	23810 ± 41	393^{+32}_{-26}	91	
Abell 2204-C	86000-88000	87721 ± 36	235^{+31}_{-30}	38	
Abell 3921-A	37500-42200	40208 ± 112	945^{+91}_{-71}	70	Abell 3921-2
Abell 3921-B	47000-49000	48114 ± 99	476^{+92}_{-58}	22	
Abell 3921-C	60000-65000	62893 ± 145	948^{+123}_{-88}	42	AM 2250-633
Abell 3921-D	85000-90000	87505 ± 170	1050^{+147}_{-104}	37	
Abell 2055-A	8500-12000	10358 ± 71	485^{+60}_{-44}	46	Abell 2052
Abell 2055-B	22000-26000	22766 ± 152	861^{+135}_{-92}	31	
Abell 2055-C	51000-57000	53825 ± 174	955^{+155}_{-104}	29	
Abell 2104-A	16000-20000	17567 ± 184	902^{+170}_{-108}	23	Abell 2103(?)
Abell 3888-A	21000-24000	22691 ± 118	781^{+100}_{-72}	43	
Abell 3888-B	58000-65000	61232 ± 224	1449^{+191}_{-137}	41	

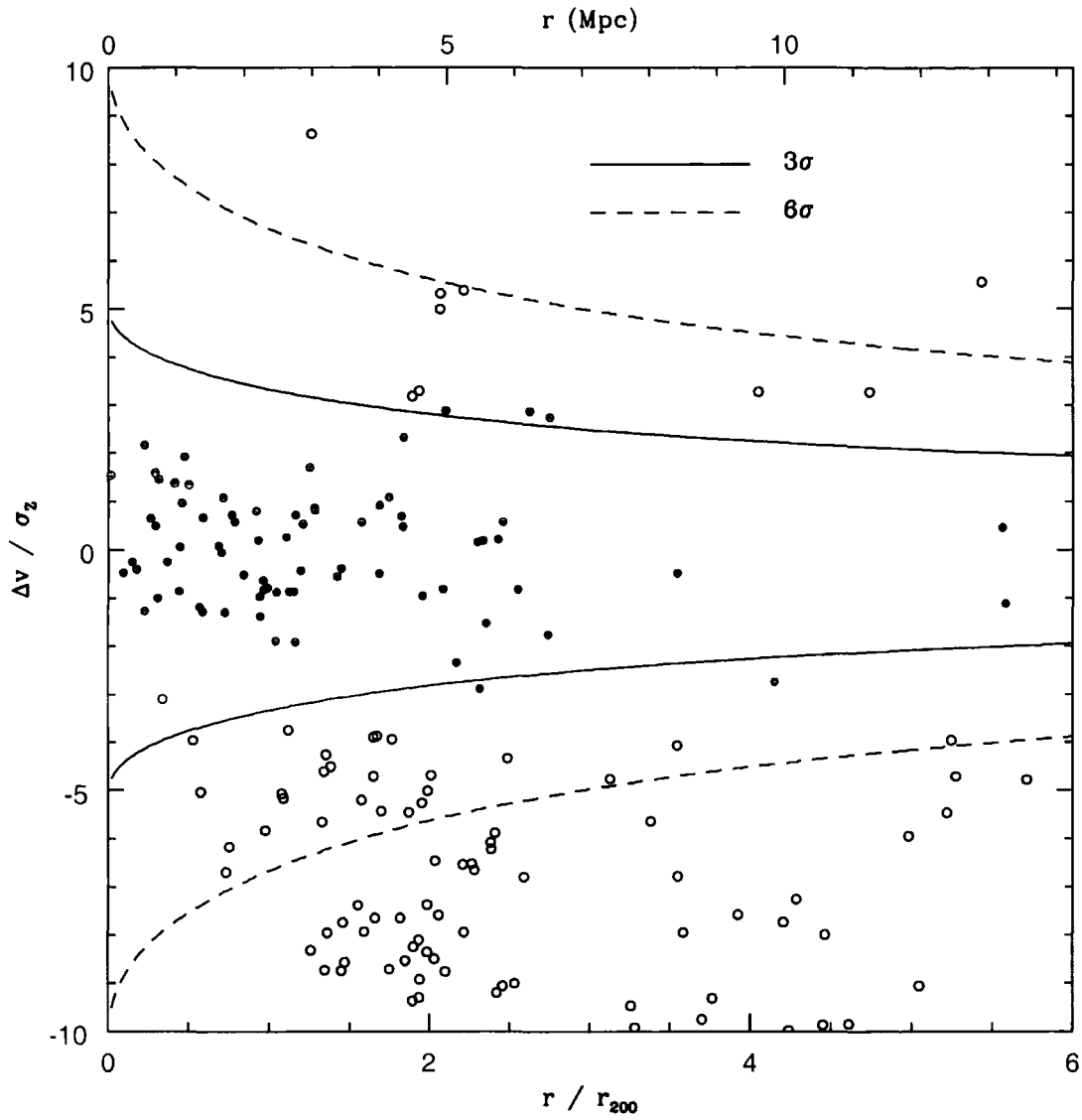

Figure 6.6: The cluster membership technique of CYE applied to Abell 22. The solid line denotes the 3σ contour of the CYE mass model; the dashed line is the 6σ contour. An equivalent scale to r/r_{200} is provided in Mpc along the upper axis. The filled points are those galaxies defined to be cluster members via the ZHG technique; non-members are open circles. r_0 is defined to be the X-ray centre of the cluster and v_0 is the mean recession velocity of the cluster.

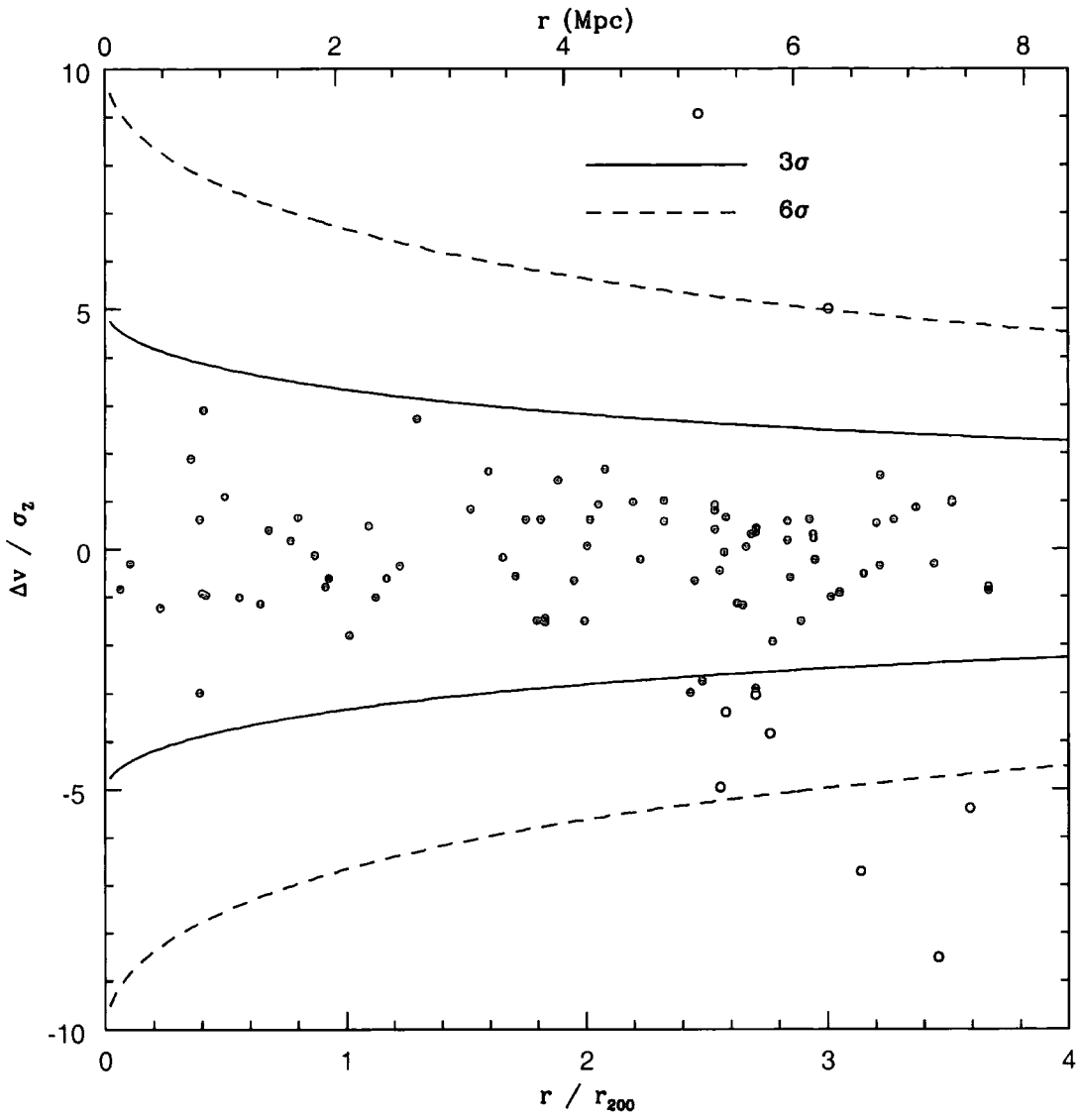

Figure 6.7: As for Figure 6.6 for Abell 1651.

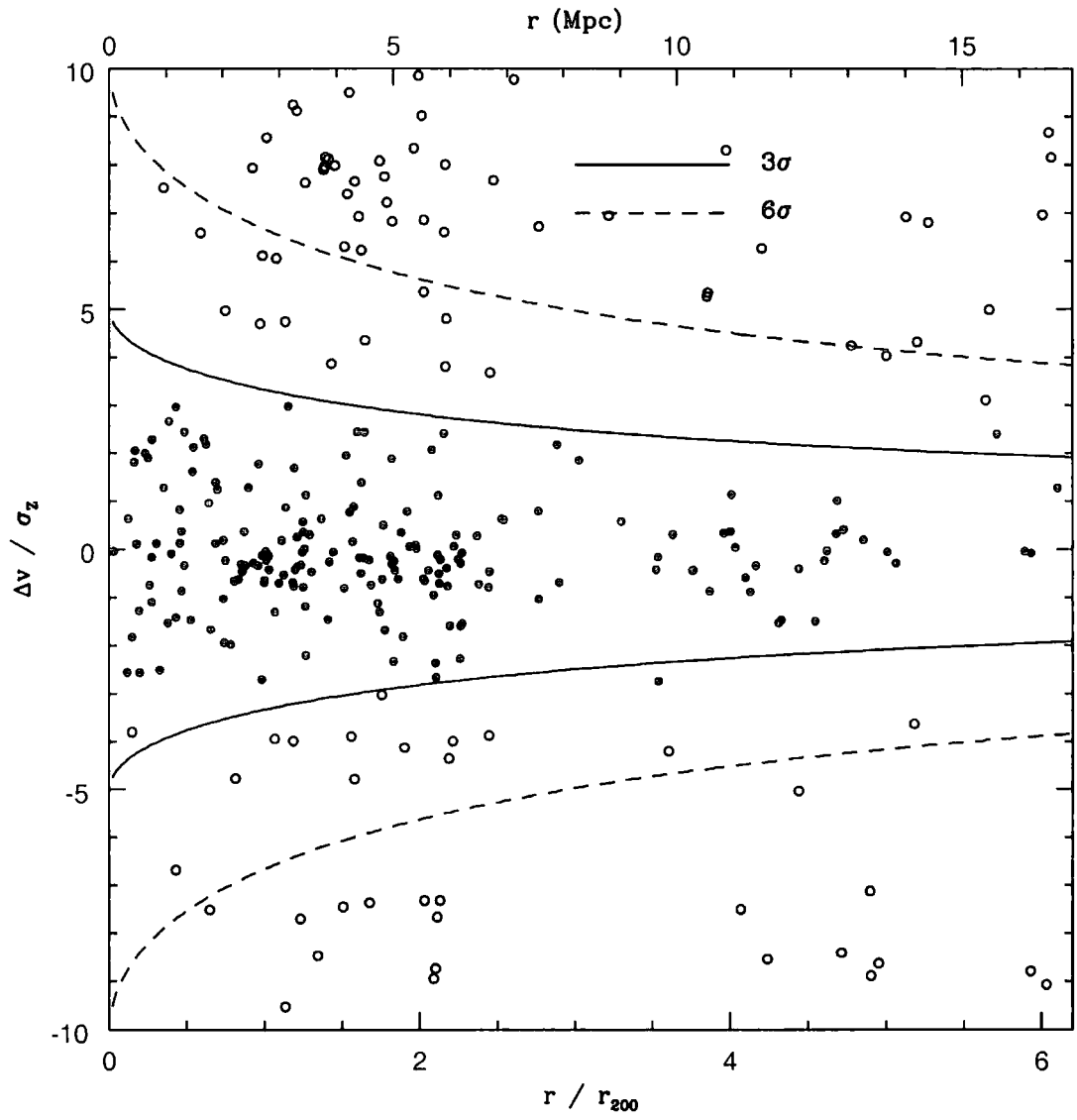

Figure 6.8: As for Figure 6.6 for Abell 2204.

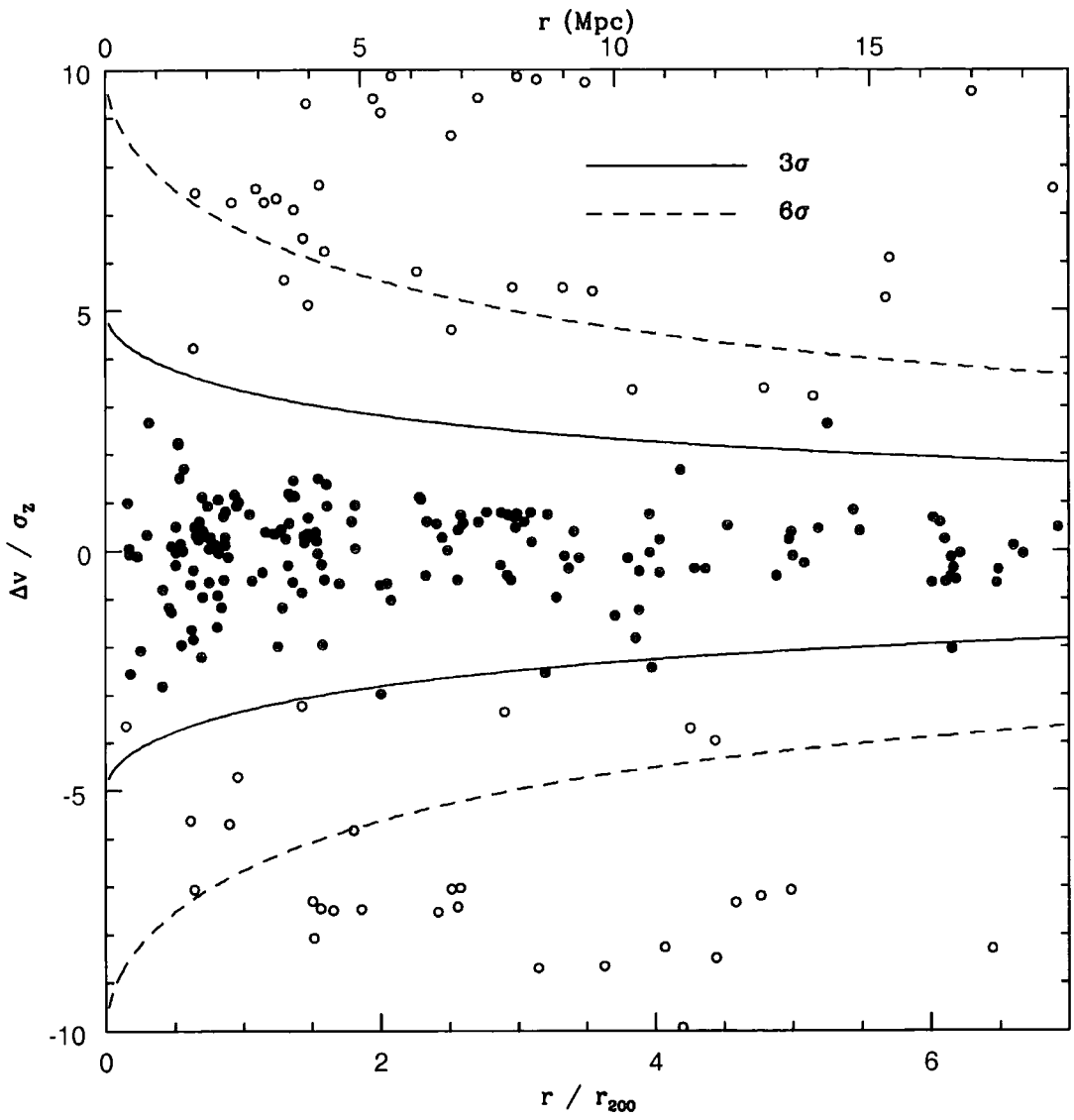

Figure 6.9: As for Figure 6.6 for Abell 3921.

dispersion of the cluster, σ_z, and plotted against the projected radius away from the centre of the cluster in units of r_{200}*. The mass model of CYE is then used to mark upon this plane the 3σ and 6σ contours which are to differentiate between cluster galaxies, near-field galaxies and field galaxies.

Using the assumption that a cluster is a singular isothermal sphere, Carlberg et al. (1997) derive the form of r_{200} as:

$$r_{200} = \left(\frac{\overline{\rho}(r_v)}{200\rho_{crit}(z)} \right)^{\frac{1}{2}}$$

where r_v is defined as the virial radius and $\overline{\rho}(r_v)$ is the mean density of the cluster interior to this radius. Arguments presented in CYE simplify this equation to:

$$r_{200} = \frac{(3)^{\frac{1}{2}}\sigma_z}{10H(z)}$$

where σ_z is the velocity dispersion of the cluster and

$$H(z)^2 = H_0^2(1+z)^2(1+\Omega_0 z)$$

The results of this analysis are presented in Figures 6.6, 6.7, 6.8 and 6.9 for Abell 22, 1651, 2204 and 3921 respectively.

The method of ZHG generally agrees well with the CYE mass model. Only a small number of galaxies in all of the clusters ($<$ 1 per cent) have had their membership reassigned. Those that had been assigned cluster membership under ZHG now find themselves moved into the category of 'near-field', between the 3σ and 6σ contours of the CYE mass model.

6.4 Spectroscopic Typing

Previous work on spectral evolution modelling has shown that there are features within a galaxies spectrum which can be readily correlated with their star formation histories (e.g. Bruzual & Charlot 1993; Poggianti et al. 1999). Measurement of spectral lines has led some authors (Couch & Sharples 1987; Dressler et al. 1999;

*The radius of r_{200} is defined to be the clustocentric radius at which the mean interior density is 200 times the critical density at the redshift of the cluster, $200\rho_{crit}(z)$

Poggianti et al. 1999) to adopt a spectroscopic classification scheme based upon the relative strengths of certain spectral features.

Here, the spectral nomenclature of the MORPHs collaboration is adopted (e.g. Dressler et al. 1999; Poggianti et al. 1999). This scheme evolved from the work of Couch & Sharples (1987) and Dressler & Gunn (1992). In this scheme, galaxies are typed into a particular spectroscopic class on the basis of equivalent widths of their Hδ ($\lambda = 4101$Å) absorption line against their [OII]($\lambda = 3727$Å) emission line. The strength of the Hδ absorption line is a good indicator of recent star formation, within the past 1-2 Gyr. The presence of [OII] in emission is an indicator of current ongoing star formation in galaxies. Taken in combination, therefore, these spectral line measures can reveal a galaxy's past star formation history. The [OII] line is chosen as it is readily available in the majority of the galaxies. In contrast, Hα (another potentially useful line to denote current star-forming activity; restframe wavelength of 6563Å) is generally unavailable due to the spectroscopic range covered.

There are six different spectral classes in the scheme proposed by Poggianti et al. (1999). The divisions between each class are illustrated by Figure 6.10. This spectroscopic typing scheme is described briefly below.

The first spectral class is simply labelled 'k'. The k class are passively evolving galaxies possessing metal absorption lines and an absence of (or very weak) emission lines. They have the same properties as the k-type galaxies described by Dressler & Gunn (1992): early-type galaxies exhibiting spectra typical of K giant stars (see top row of Figure 6.11). The k+a class also has metal lines and no (or very weak) emission features but possesses moderate Balmer absorption; the a+k class possesses stronger Balmer absorption still (see next two rows of Figure 6.11). Together, these two classes replace the mixed nomenclature "E+A" class (following the suggestion of Franx, 1993). The letter 'k' here again signifies the similarity to K type stars; the 'a' or 'A' correspondingly signifies similarity to A type stars (metal lines and Balmer absorption present). The k+a and a+k classes represent galaxies that have undergone recent star formation that has ceased. Galaxies typed as PSB or HDS by Couch & Sharples (1987) thus now fall into these two classes (Dressler et al. 1999).

The spectroscopic classes preceded by the letter 'e' are galaxies with emission

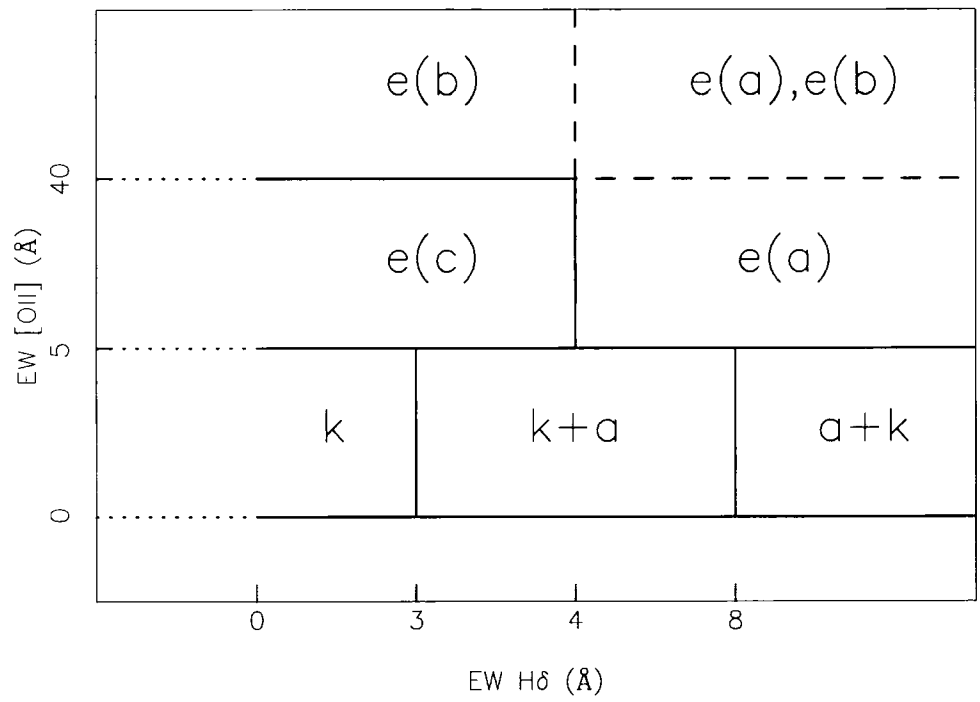

Figure 6.10: Schematic diagram of the spectroscopic typing used by the MORPHs collaboration (Dressler et al. 1999). Spectral types not based upon the relative EWs of Hδ and [OII] are not shown (e.g. AGN).

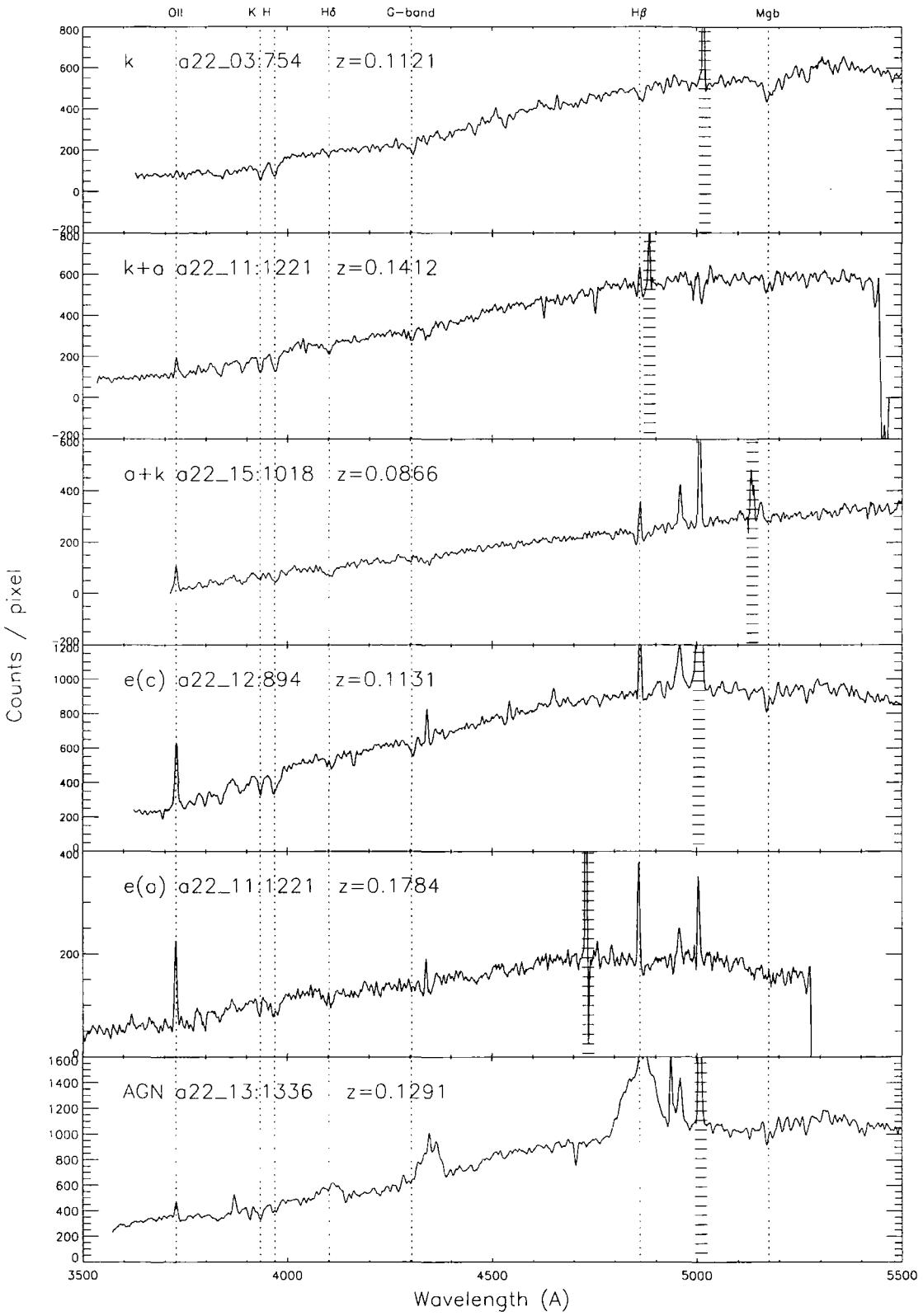

Figure 6.11: As for Figure 5.3 but with examples of the different spectroscopic types present within the observation of Abell 22 in July 2000.

lines present (following Dressler & Gunn 1992). Thus the e(c) class has a weak to moderate Hδ absorption line coupled with a moderate [OII] emission line. They possess an on-going, near constant star formation rate (Dressler et al. 1999). The e(b) class have strong [OII] emission (EW[OII]3727 > 40Å) which is indicative of a starbursting galaxy. The e(a) class have a similar strength of [OII] emission to the e(c) class but additionally possess strong Balmer absorption. They typically have a large population of A type stars. As can be seen from Figure 6.10 the e(a) and e(b) class can overlap for galaxies possessing strong EW[OII] and EW Hδ but this is not an issue for this study as no galaxy falls into this region. Figure 6.11 displays an example spectra of both the e(a) and e(c) types.

Additionally, however, there exists a small number of further spectroscopic types which cannot be assigned using the MORPHs typing. One such type are active galactic nuclei (AGN); these are defined by their broad lines. Within the 2dF spectroscopy, only one AGN cluster member is found (a22_13:1366; see bottom row of Figure 6.11); see also Chapter 8). To find one AGN out of 473 cluster galaxies (Table 6.1) is not unexpected; Dressler, Thompson, & Shectman (DTS; 1985) report that for a sample of 1268 galaxies over 14 clusters at $z \sim 0.04$, 1 per cent (i.e. 12) of all cluster galaxies possess active nuclei. Within the LARCS observations, therefore, one expects to find ~ 4 AGN. The absolute magnitude limit probed by DTS is brighter than LARCS, but the number of expected AGN should not increase by extension to the fainter LARCS absolute magnitude limit (Huchra & Burg 1992).

6.4.1 Spectral Misclassification Rate

It should be noted that in the previous chapter, it is found that there is an rms of ~ 0.5Å between the LARCS measurements of the EWs and those made using the method of Dressler et al. (1999) coupled with a median offset of ~ 0.1Å. This has the effect of blurring the boundaries between the various spectroscopic types. To investigate how much of an effect this is, a Monte-Carlo simulation is employed to perturb each $H\delta$ and [OII] spectral EW measurement 100 times. These new measurements of the two line strengths are then used to re-type the spectra in

Table 6.3: The median retyping rate resulting from a Monte Carlo simulation to perturb measurements of the EWs.

Spectral Type	Median Re-typing Rate (per cent)	Commonest New Typing
k	4.5	k+a
k+a	4.2	k
a+k	2.6	e(a)
e(c)	4.8	e(a)
e(a)	2.4	e(c)

the MORPHS scheme. The resulting percentage of re-classifications of the various spectral types is presented in Table 6.3. The re-classification rate is larger where the boundary levels are low (e.g. between k and k+a), although at no boundary is the misclassification rate larger that 5 per cent.

6.4.2 Resolution Effects

Although unintentional by design, two different spectral gratings have been used during the observations: 600V and 300B (see Table 5.2). The 600V grating has been used with the main scheduled telescope time for Abell 22, 2204 and 3921; the 300B grating has been used in the service run of Abell 3921 and the archival data for Abell 1651 from 2dFGRS. It is natural to enquire whether the observations made with the 300B gratings are directly comparable to the ones made with the 600V?

To assess the effect of the different gratings on subsequent measurements, the observations of Abell 22 made with the 600V gratings are convolved to the resolution of the 300B observations using the GAUSS task within IRAF. The equivalent widths of the Hδ and [OII] spectral line features in the convolved spectra are then re-measured. These new measurements are compared to the original measurements made on the 600V observations in Figure 6.12. To account for the effect that using the 300B gratings will have on the EW measurements (and hence spectroscopic

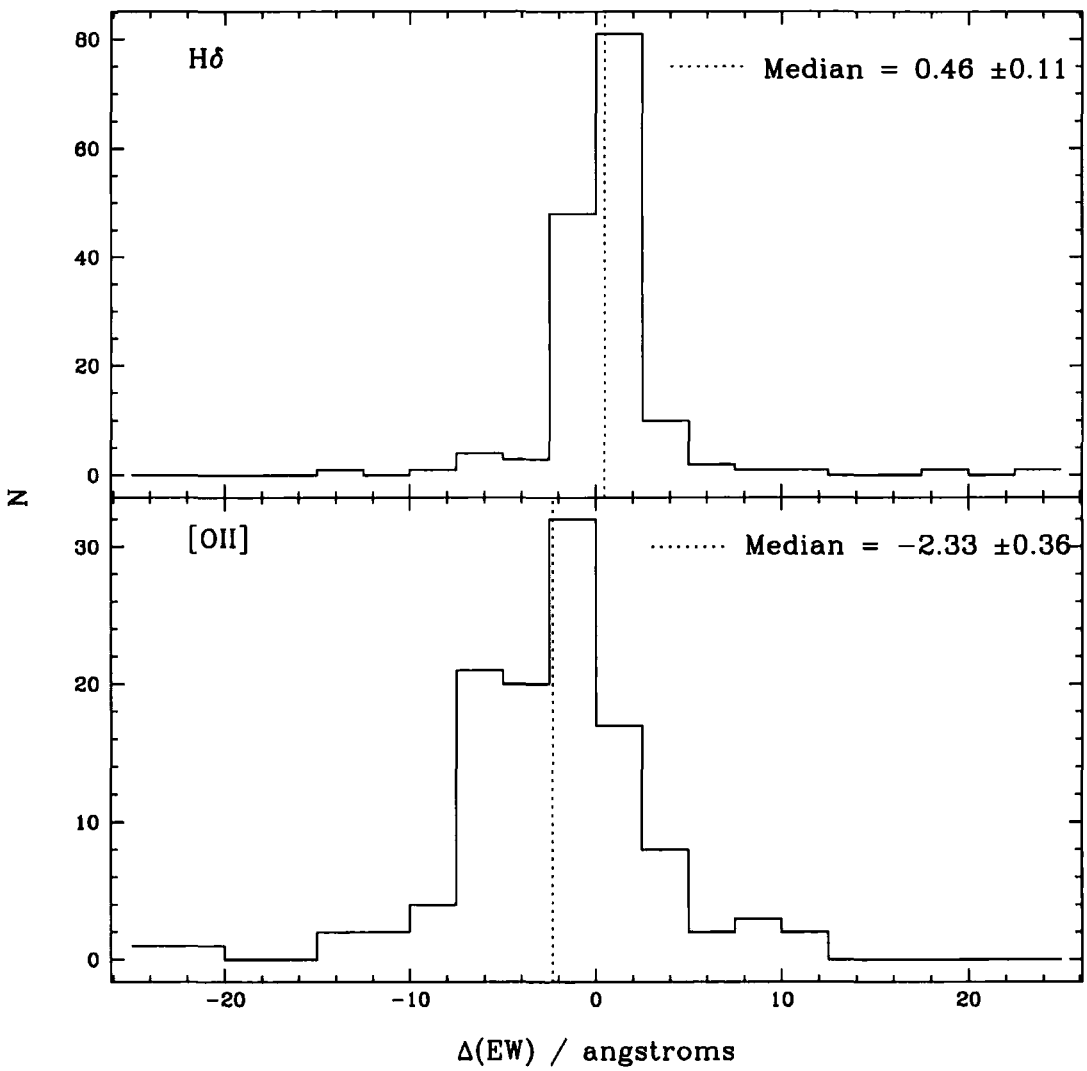

Figure 6.12: Histograms of the difference in measured EW of Hδ and [OII] between the 600V−300B gratings.

typing), the median EW translations established for Hδ and [OII] from Figure 6.12 are now applied to the 300B observations.

6.4.3 Selection Effects

Since each cluster has had a different number of observations made of it with varying degrees of success, it is necessary to define a selection function for the spectral sample and take this into account when comparing the various cluster populations to avoid any possible bias.

Two simple questions have to be answered in order to create the selection function: 1) out of the galaxy catalogues, how many galaxies were selected for 2dF observation? and 2) out of the galaxies that were actually observed, how many obtained reliable redshift estimates ($R_{TDR} > 3.0$)? The selection function is then simply the product of these two probabilities.

These questions are asked of each constituent part of the spectroscopic sample (the bright inner, the faint inner and the bright outer samples; see Chapter 5) of each cluster. Figure 6.13 displays the likelihood that a galaxy of a given magnitude will be selected for observation *and* have a good spectrum ($R_{TDR} > 3.0$) in each cluster observed. These values will now be applied to the observed sample to compensate for any selection bias.

Abell 2204 and 3921 are both relatively complete at bright magnitudes, having been observed to completion (see Chapter 5). Having had only one pointing owing to inclement weather, Abell 22 is much less complete. This is reflected by relatively lower likelihood values at all magnitudes (Figure 6.13).

Special Case: Abell 1651

Abell 1651 is a special case as it has not been observed by the LARCS project directly. Rather, data from the 2dFGRS team is used for this cluster. In creating the selection function for Abell 1651 the same questions asked of the other clusters are required of this. In order to proceed, therefore, it is necessary to create a catalogue of spectroscopic targets for this cluster from the LARCS parent photometric catalogue. Since there are no LARCS 2dF observations of this cluster, only the first question

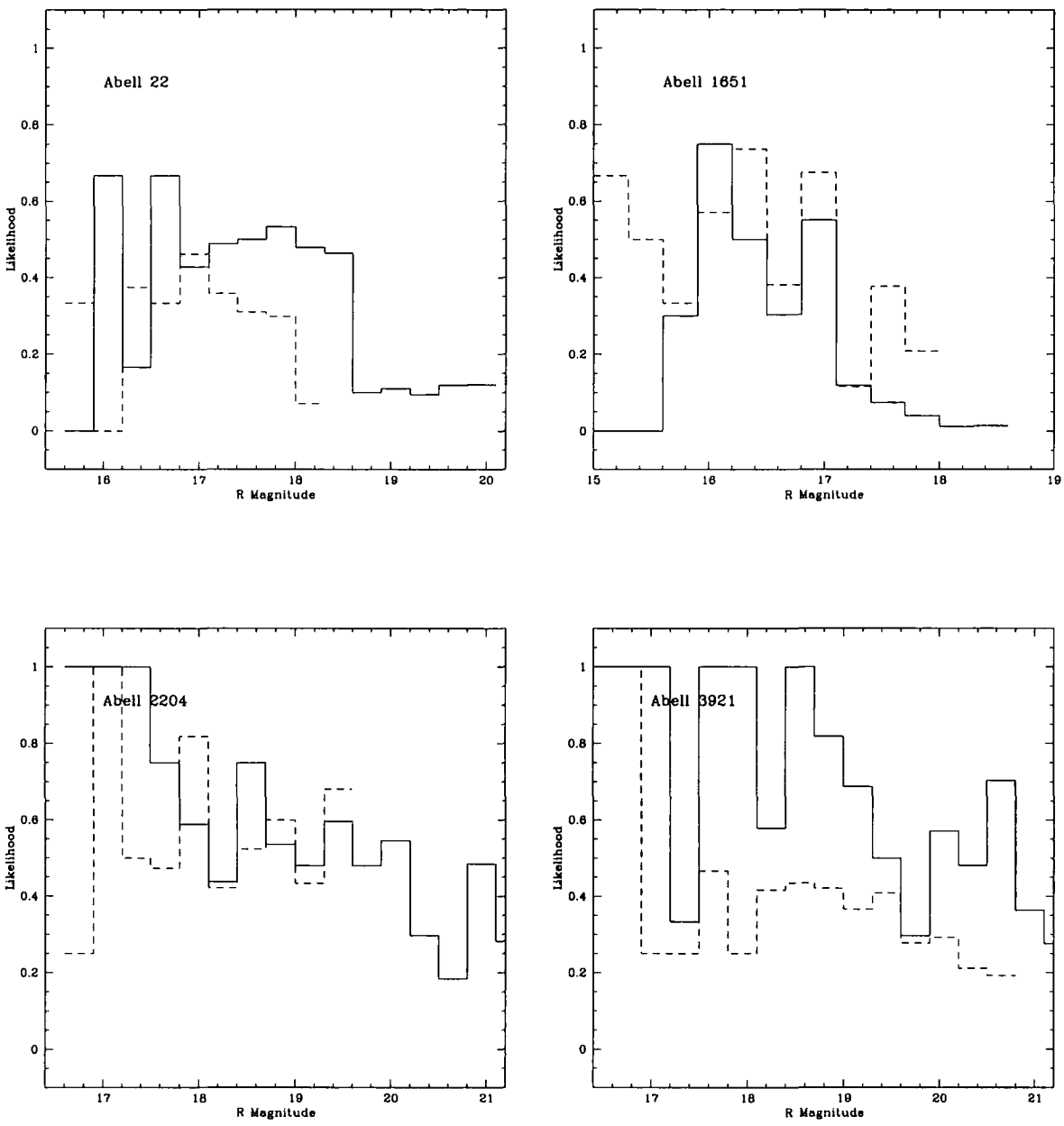

Figure 6.13: The likelihood that a galaxy of a given magnitude will both be observed and produce a quality redshift estimate ($R_{TDR} > 3.0$). The solid lines are represent the sample in the central 30 arcmin of the observation, the dashed lines represent the sample outside this distance. It is necessary to define these two likelihoods due to the observational strategy (see Chapter 5).

is pertinent here: out of the galaxy catalogues (appropriately cut at the 2dFGRS limiting magnitude of $b_J = 19.45$; see Chapter 3), how many galaxies have 2dfGRS spectra? This is then the only probability required.

6.4.4 Classifications

The results of using this classification scheme is presented in Tables 6.4 and 6.5. O'Hely (2000) presents a similar table for Abell 2055, 2104 and 3888 using the same code and definitions.

The observed fields are divided into four components based upon the mass model and the velocity histograms. The definitions of the cluster itself and the near field populations remain the same. However, because the field population is a very broad type, it is now sub-divided into two sub-samples. A clipping of $0.05 < z < 0.20$ is applied to the redshifts of the galaxies to exclude those field galaxies of very low luminosity close by and very high luminosity far away thus limiting the absolute magnitude range probed to be similar to that in the clusters. Using the velocity histograms, the remaining galaxies are divided up into high-density-field and low-density-field systems. The high-density-field category contains those galaxies which lie within $3\sigma_z$ of the overdensities presented in Table 6.2. The low-density-field category contains all of the remaining galaxies occupying the sparsely populated regions between the walls and clusters.

The numbers in Tables 6.4 and 6.5 refer to the actual raw number of galaxies of a given type that are observed. Since these numbers are raw, it is necessary to correct them for the actual observations undertaken. Firstly, a magnitude cut of $M_V = -20$ is imposed to ensure that the clusters can be directly compared to one another. Secondly, the weighting scheme (presented in Section 6.4.3) is applied to each galaxy. The percentage in brackets therefore denotes the weighted fraction of a given type within the cluster.

Clearly, Abell 1651 stands out as having a fraction of k+a galaxies which is much greater than the other clusters and no emission line galaxies. The reason for this is probably due to selection effects and the data source. As can be seen from Figure 6.13, bright galaxies in the centre of the cluster have not been observed

Table 6.4: Spectroscopic classification of galaxies observed by Pimbblet (2000; 2001). All galaxies have a value of $R_{TDR} > 3.0$. The † denotes the presence of one galaxy which falls into the cross-typing of e(a),e(b). N.B. No e(b) type galaxies are found. The numbers are the raw number of galaxies observed of a given type. The bracketed numbers are the selection function weighted percentages of a given classification within the population brighter than $M_V = -20$.

Field	N(Total)	N(k)	N(k+a)	N(a+k)	N(e(c))	N(e(a))
Cluster, Abell 22	74	41 (54% ± 5)	12 (18% ± 3)	0	15 (16% ± 3)	6 (12% ± 3)
Abell 1651	80	16 (16% ± 5)	55 (65% ± 5))	9 (19% ± 4)	0	0
Abell 2204	186	126 (71% ± 5)	21 (11% ± 2)	8 (5% ± 1)	23 (9% ± 2)	8 (5% ± 1)
Abell 3921	167	81 (55% ± 4)	40 (19% ± 3)	3 (1% ± 1)	22 (13% ± 2)	21 (12% ± 2)
Near Field, Abell 22	39	21 (39% ± 6)	7 (30% ± 5)	2 (6% ± 2)	6 (20% ± 4)	2† (3% ± 2)
Abell 2204	30	18 (62% ± 15)	7 (22% ± 9)	1 (0%)	4 (16% ± 7)	0
Abell 3921	21	14 (66% ± 16)	3 (0%)	0	2 (24% ± 10)	2 (10% ± 6)

Table 6.5: As for Table 6.4, but for the field samples.

Field	N(Total)	N(k)	N(k+a)	N(a+k)	N(e(c))	N(e(a))
High-Density-Field, Abell 22-Wall	61	26 (39% ± 4)	12 (17% ± 2)	2 (1% ± 1)	15 (30% ± 3)	6 (13% ± 2)
Abell 2204-A	53	38 (67% ± 8)	10 (23% ± 6)	5 (10% ± 4)	0	0
Abell 2204-B	94	78 (79% ± 9)	10 (15% ± 5)	6 (6% ± 3)	0	0
Abell 2204-C	45	39 (93% ± 11)	3 (7% ± 6)	2 (0%)	1 (0%)	0
Abell 3921-A	72	18 (49% ± 6)	11 (16% ± 4)	3 (0%)	21 (24% ± 4)	18† (11% ± 3)
Abell 3921-B	32	4 (21% ± 7)	10 (40% ± 11)	1 (0%)	8 (16% ± 7)	9 (23% ± 8)
Abell 3921-C	45	18 (55% ± 11)	9 (25% ± 8)	2 (0%)	5 (5% ± 3)	11 (15% ± 6)
Abell 3921-D	46	17 (38% ± 15)	9 (0%)	1 (0%)	8 (16% ± 10)	11 (46% ± 15)
Low-Density-Field, Abell 22	90	46 (45% ± 4)	19 (37% ± 4)	2 (2% ± 1)	11 (6% ± 2)	12† (9% ± 2)
Abell 2204	227	156 (65% ± 5)	36 (17% ± 3)	16 (7% ± 1)	13 (8% ± 1)	6 (4% ± 1)
Abell 3921	115	45 (27% ± 5)	25 (32% ± 5)	6 (4% ± 2)	17 (23% ± 4)	22 (13% ± 3)

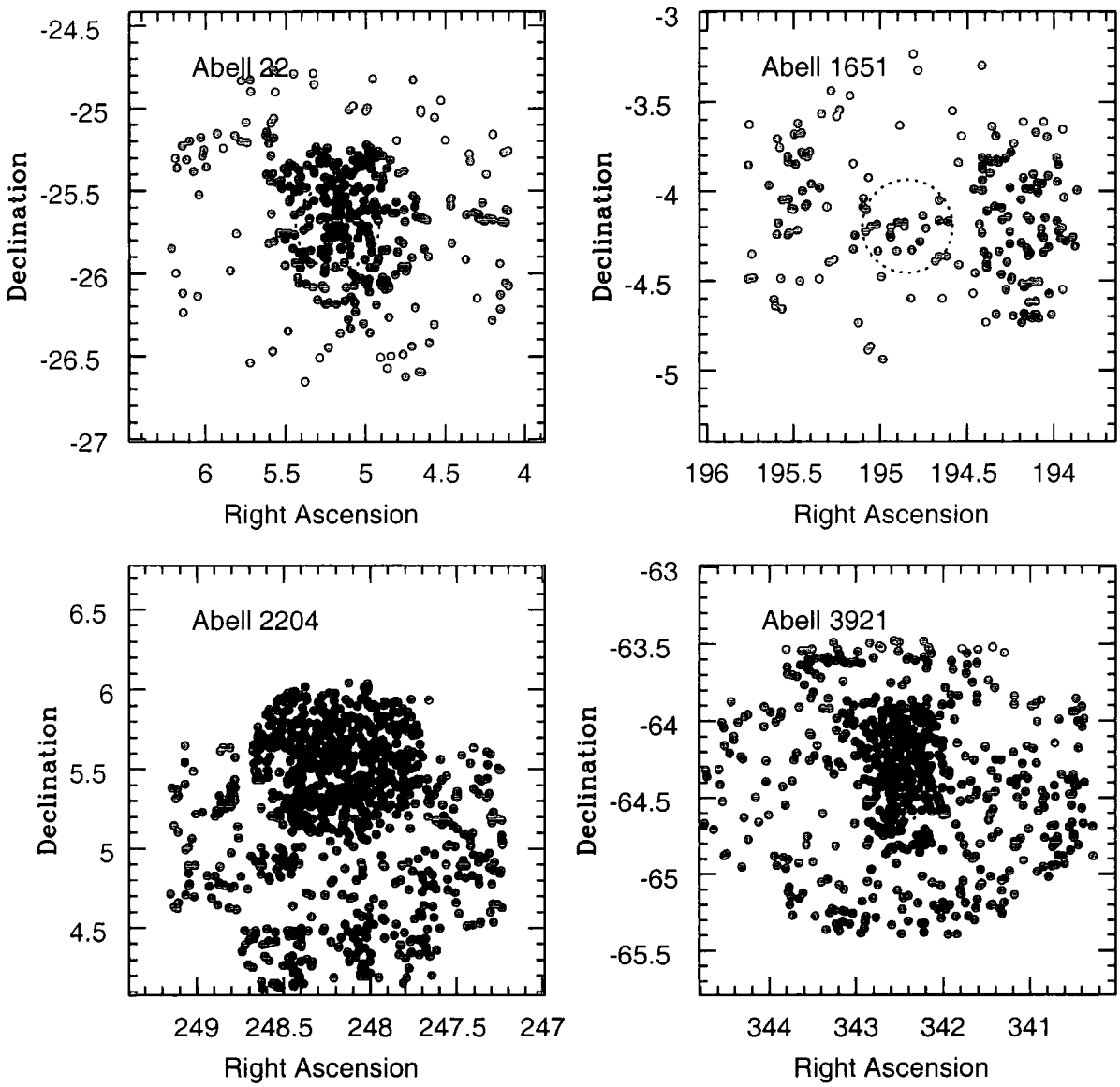

Figure 6.14: The spatial distribution of all the galaxies with 2dF spectra. The dashed circle represents 2 Mpc radius about the cluster centres. Abell 1651, from the 2dFGRS team, is clearly observed in a completely different manner to the others.

(compared to about 55% of galaxies of similar magnitude in the outer region). An inspection of the spatial distribution (Figure 6.14) of these galaxies reveals that whilst many galaxies in the outskirts of the cluster have been observed; observations in the central regions are very sparse. The 2dFGRS's observational technique and spectroscopic completeness are the reason for this (Colless et al. 2001). An observation of the tile (or tiles) covering the centre of the cluster clearly has not yet been made. This cluster is therefore viewed as not observed in a representative manner comparable to the other clusters.

6.5 Cluster Morphology and Substructure

With the 2dF spectroscopy, an investigation into the clusters morphology can readily be made and clues to the presence of substructure can be examined. A lack of consensus about what is the optimal tool to use for the detection of substructure led Pinkney et al. (1996) to investigate differences amongst a battery of statistical tools. They conclude by endorsing the Dressler-Shectman test as by far the most powerful and most sensitive (three-dimensional) substructure detection tool available in the general case.

The Dressler-Shectman test (Dressler & Shectman 1988; DS) has therefore been adopted to examine the LARCS clusters for any substructure. Their method is briefly outlined below. The spectroscopic catalogue is cut to only include spectroscopically confirmed cluster members. For each member, its ten nearest neighbours on the sky are found. For this group of 11 galaxies, the *local* mean velocity, $\overline{v}_{local}$, and velocity dispersion, σ_{local} is calculated and compared to the corresponding global values. Thus the deviation is:

$$\delta_i^2 = (11/\sigma^2)[(\overline{v}_{local} - \overline{v})^2 + (\sigma_{local} - \sigma)^2]$$

The parameter of merit, however, is the cumulative deviation, Δ:

$$\Delta = \sum_{i=1}^{N} \delta_i^2$$

which is the sum of all δ_i for the N cluster members. For a cluster velocity dispersion which is Gaussian in nature, the Δ statistic will be of order N. As the

Table 6.6: Results from the DS tests. The Δ statistic is shown for each cluster sample, the average result of the Monte-Carlo simulation and the most deviant result of the Monte-Carlo simulation. The probability of obtaining the result is given in the final column.

Cluster			Average	Most Deviant	
	N	$\Delta_{Observed}$	$\Delta_{Simulation}$	$\Delta_{Simulation}$	P(Δ)
Abell 22	74	111	108	154	0.436
Abell 1651	80	117	99	145	0.073
Abell 2204	186	352	271	359	0.001
Abell 3921	167	208	191	260	0.200

underlying distribution may not be Gaussian even for a cluster without substructure, 1000 Monte-Carlo simulation are run on the clusters, each time shuffling the galaxies' velocities but holding their positions constant. Caution must be exercised, however, as should the substructure be aligned along the line of sight to the cluster, the Δ statistic will not show this.

Table 6.6 shows the results of the DS test as applied to our clusters. The P(Δ) value gives the probability that $\Delta > \Delta_{observed}$, computed from the 1000 Monte-Carlo simulations. In the case of Abell 2204, the Δ statistic is very much larger than N; coupled with a low P(Δ), this cluster certainly has significant substructure. The other clusters have larger values of P(Δ), reducing the likelihood of them having substructure. The results from the DS tests are illustrated in Figures 6.15, 6.16, 6.17 and 6.18. Each galaxy is marked with a circle whose diameter is proportional to e^{δ}, therefore any subclustering will be seen as a localized group of overlapping circles.

The DS test results permit further investigation of the relationship between star formation history and dynamics within clusters. For each cluster galaxy its value of δ_i is taken and normalized by the peak DS statistic value, δ_{iPEAK}. The cluster galaxies are then combined and a search is performed for correlation with spectroscopic type. Figure 6.19 displays histograms of the normalised DS statistic for the clusters. Although one may expect that the more active (currently star forming) galaxies may possess a higher value of this statistic as they reside in dynamically hot

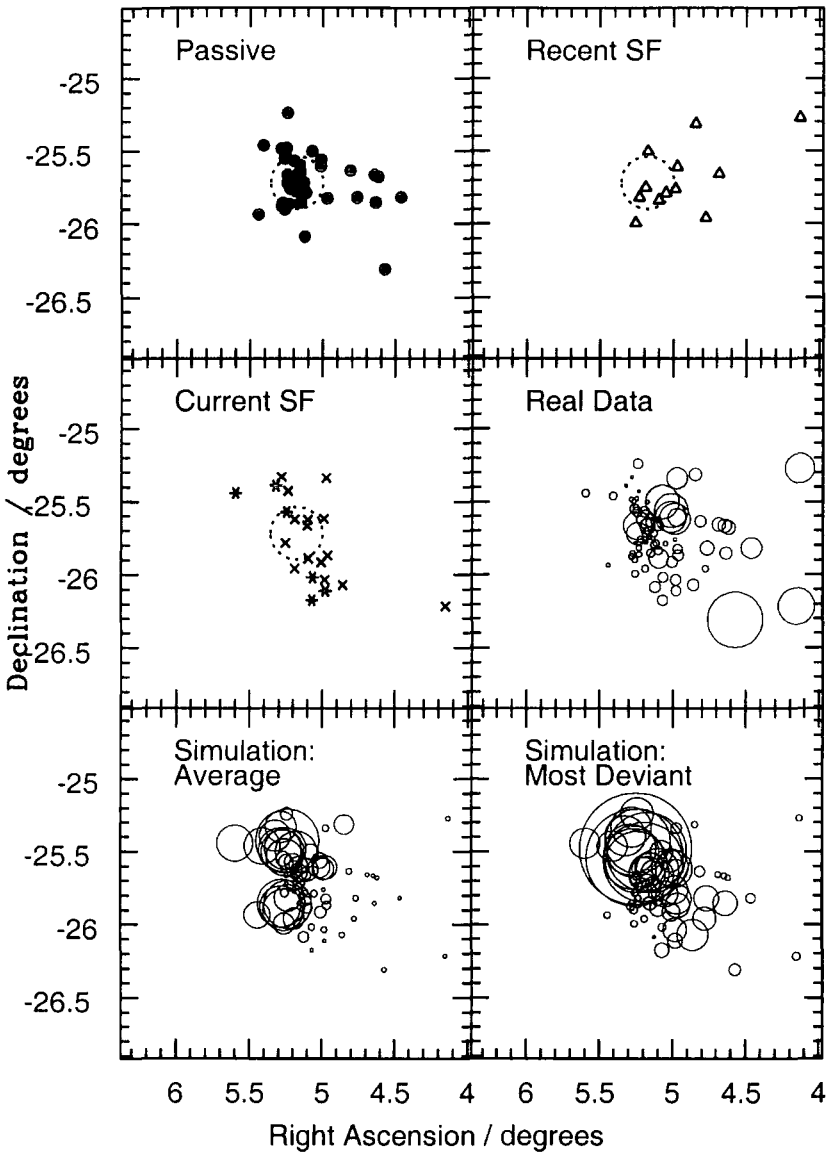

Figure 6.15: Spatial distribution of different spectral types and the results of the DS test for Abell 22. Top Left: the spatial distribution of k-class cluster members. The dashed circle represents a 2 Mpc radius on the cluster centre. Top Right: same, but for recent star-forming types: k+a (open triangles) and a+k (open circles). Middle Left: same, but for currently star-forming types: e(a) (stars) and e(c) (crosses). Middle Right: DS test of the actual data. Bottom Left: average of the 1000 Monte-Carlo simulations. Bottom Right: most deviant of the 1000 Monte-Carlo simulations.

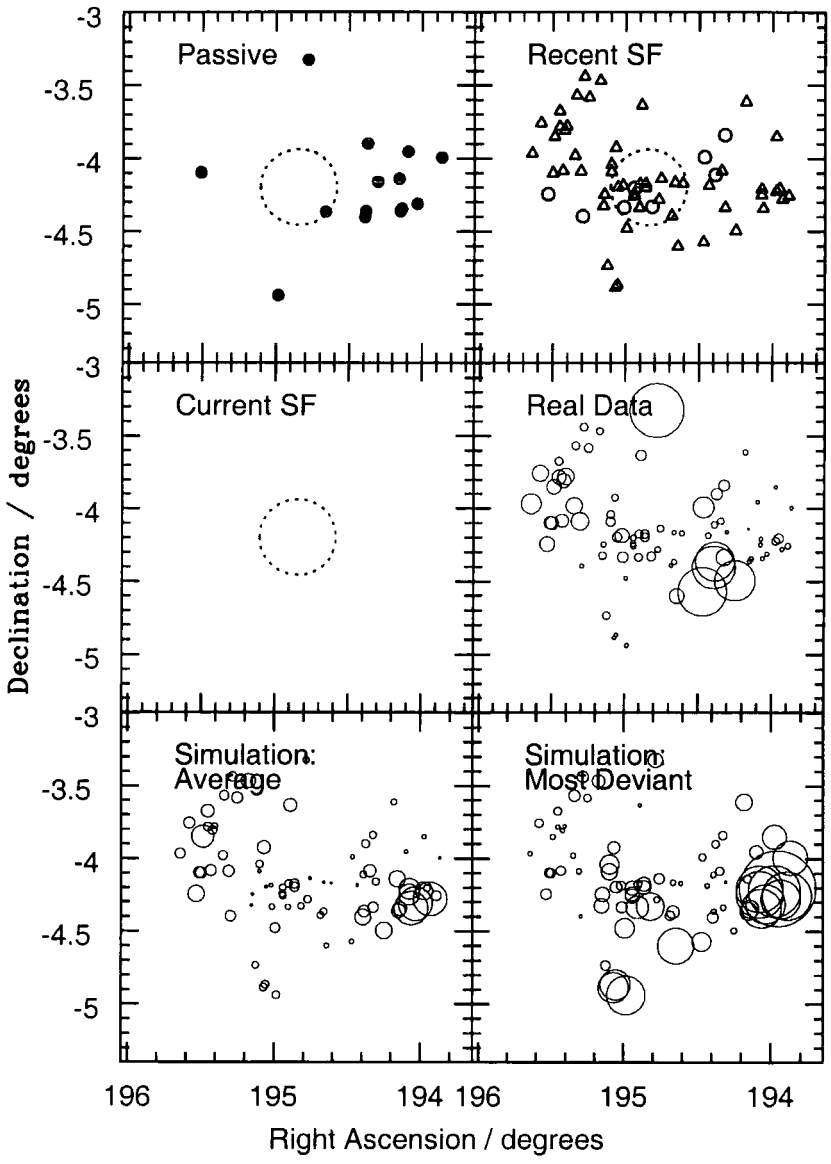

Figure 6.16: As for Figure 6.15 for Abell 1651.

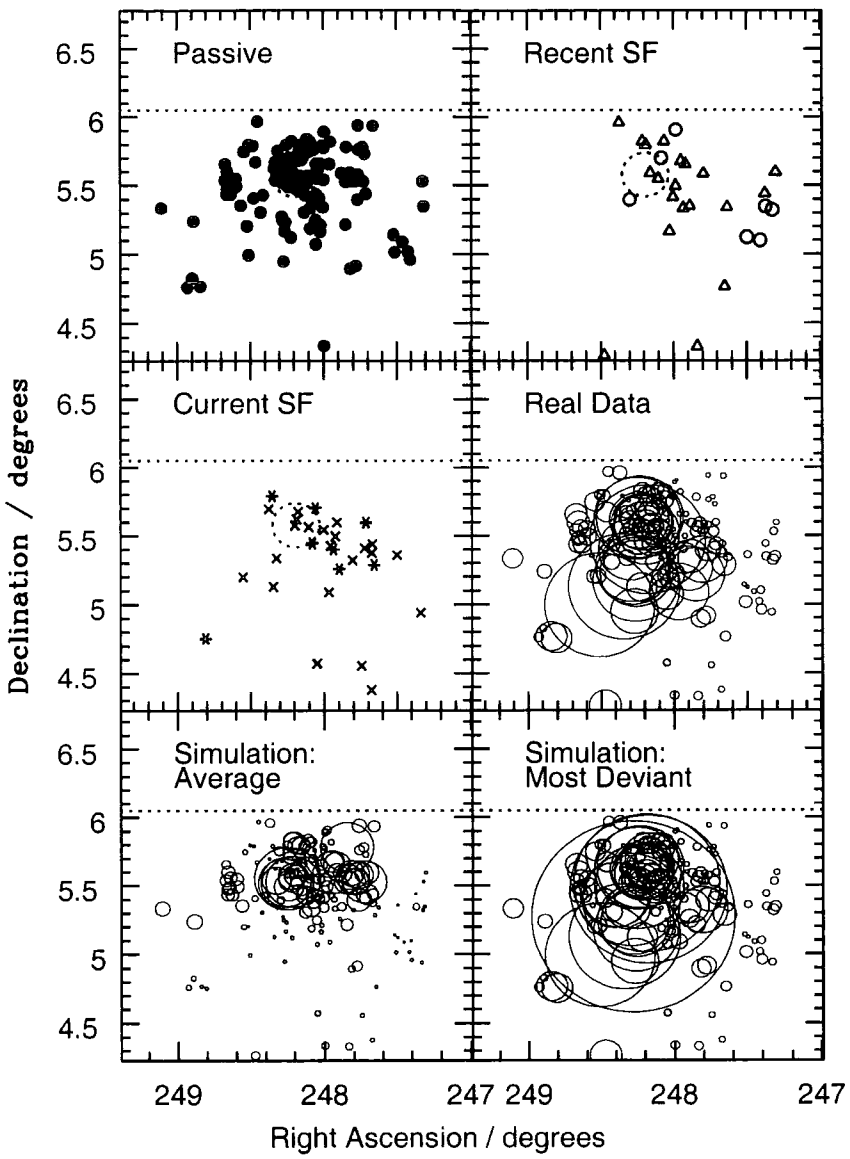

Figure 6.17: As for Figure 6.15 for Abell 2204. NB: this clusters' centre is not aligned with the centre of the optical imaging mosaic. To emphasize this, the dotted horizontal line denotes the extent of the optical mosaic in declination. Since the confirmed (Table 6.6) substructure is located centrally, this mis-observation is viewed to have not effected the result.

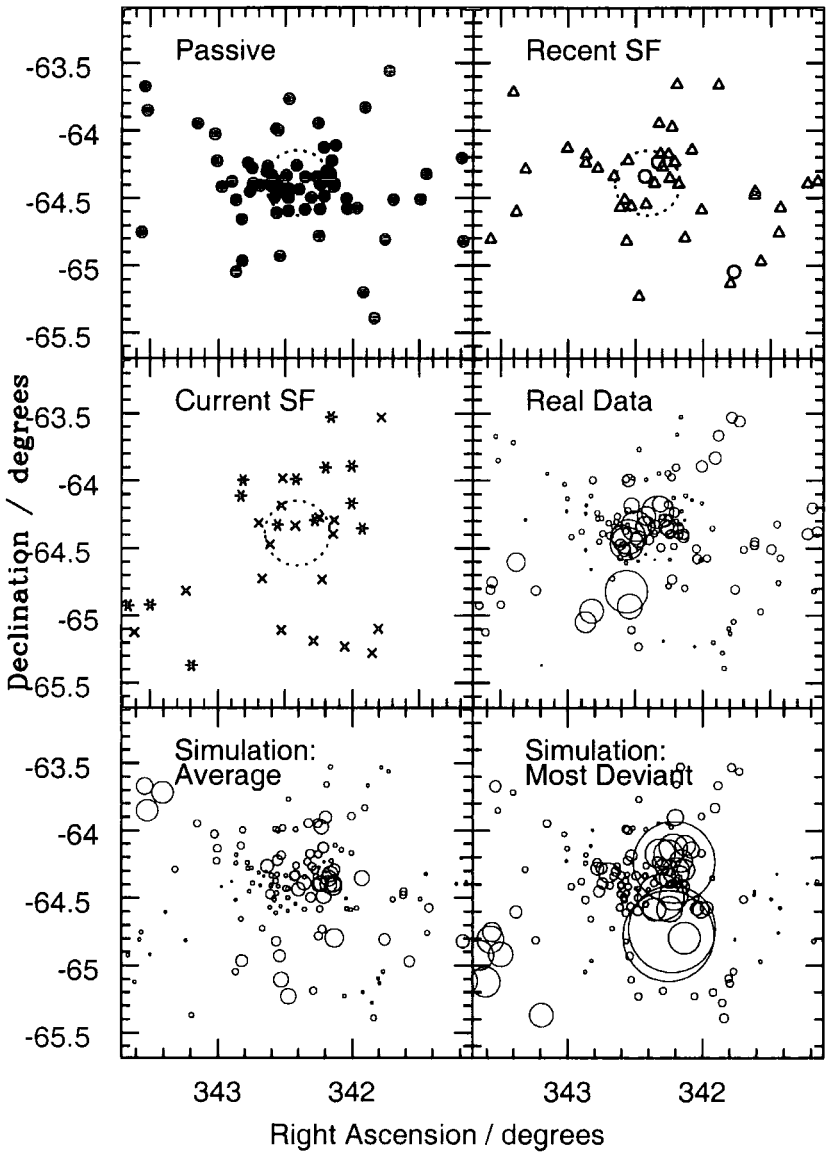

Figure 6.18: As for Figure 6.15 for Abell 3921.

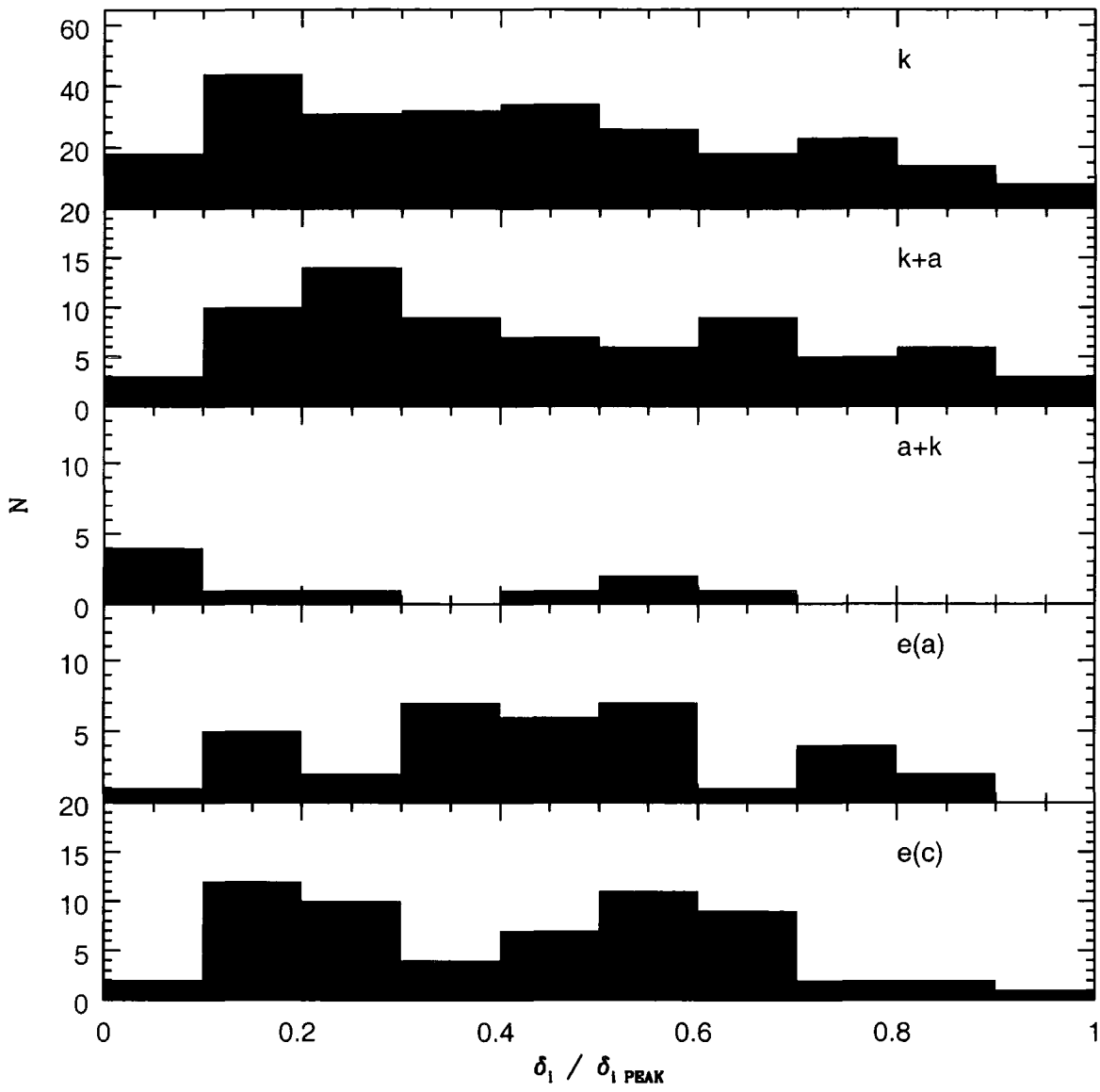

Figure 6.19: The normalized DS statistic, δ_i/δ_{iPEAK} as a function of spectroscopic type. The distribution of passive, recent star-forming and current star-forming galaxies are drawn from the same distribution at over 98 per cent confidence.

regions of the clusters, this is not immediately obvious. A K-S test is performed on these distributions (which are normalised as they have been throughout this work; see Figure 6.13) to test whether they are significantly different. This confirms the null hypothesis: the recently and currently star-forming galaxies are drawn from the same population as the passive galaxies at over 98 per cent confidence.

The DS test highlights a number of sub-groups within the clusters. Although Abell 22 and 3921 have no obvious subclustering; Abell 1651 and 2204 do. The properties of these groups, however, do not deviate in any significant way from the parent populations. There are approximately equal numbers of the spectral types, blue and red galaxies. There are individual galaxies within each cluster, however, that are highly deviant.

Using a two dimensional K-S test (Fasano & Franceschini 1987) it is also possible to ask whether the spatial distributions of the different spectroscopic types differs significantly. Each cluster is divided up into passives (k type), recently star-forming (k+a and a+k types) and currently star-forming (emission types). The two dimensional K-S test is performed between these samples for each cluster. In each case, the currently star-forming galaxies have a significantly different distribution to the other two groups (at over 99 per cent confidence).

6.6 Summary

The LARCS clusters that have been observed with the 2dF spectrograph demonstrate a range of properties: from the well defined peak of Abell 3921 to the spread of Abell 22 with its foreground wall-like structure. The velocity dispersions of the clusters have been calculated using the method of ZHG and C87; both methods produce the same results. The application of these techniques to a number of potential background clusters showed that many of them could be thought of as clusters in their own right. Using the technique of CYE, a mass model has been developed to better determine spectroscopic cluster membership.

The galaxies have been typed spectroscopically in line with the method of the MORPHS collaboration. A selection function has been developed to account for the way in which these observations were made to correctly weight the different

spectroscopic types. The clusters are found to possess a dominant fraction of passively evolving k-type galaxies in their core. This fraction falls off as one goes from the clusters, to their near-fields, high-density field regions through to low-density field regions.

Cluster morphology and substructure has been examined via the use of the DS statistic: only Abell 2204 demonstrates any significant evidence for substructure. Although it is found that the different spectroscopic types show no dependance on the DS statistic. The spatial distributions of the passive and recently star-forming galaxies are found to be significantly different to the currently star-forming galaxies.

Chapter 7 | *Spectroscopic Analysis*

7.1 Abstract

The colour-magnitude relation is revisited using the spectroscopically-determined cluster members found in Chapter 6. Using the biweight method, the CMR of the clusters is fitted to and the clusters are combined together to make a composite cluster. Signs of any environmental (radius and local galaxy density) variation of the CMR are then looked for. Spectroscopic trends within the composite cluster are also examined in detail and differences between the constituent spectroscopic types are discussed. Two composite field samples in high and low density regimes are then created to compare with the composite cluster sample.

7.2 The Colour-Magnitude Relation Revisited

Having determined the galaxies' redshifts and spectroscopic line strengths, the CMR is revisited in the light of the spectroscopic observations. To begin with, in this section colour-magnitude diagrams are constructed for spectroscopically confirmed cluster members (including the clusters observed by O'Hely, Edge and Couch in 1998). These diagrams are then evolved to a fiducial redshift and combined together in a manner similar to that employed in Chapter 4. A search for any radial blueing is then performed to confirm the result found in Chapter 4.

In Chapter 4 the CMR's variation with environment is investigated in the absence of spectroscopy by making a statistical correction to remove the contaminating field population. By employing spectroscopic membership, colour-magnitude diagrams are now constructed for spectroscopically-confirmed cluster members, as defined by the mass model of CYE. The colour-magnitude diagrams for the seven clusters with available 2dF spectroscopy are presented in Figure 7.1.

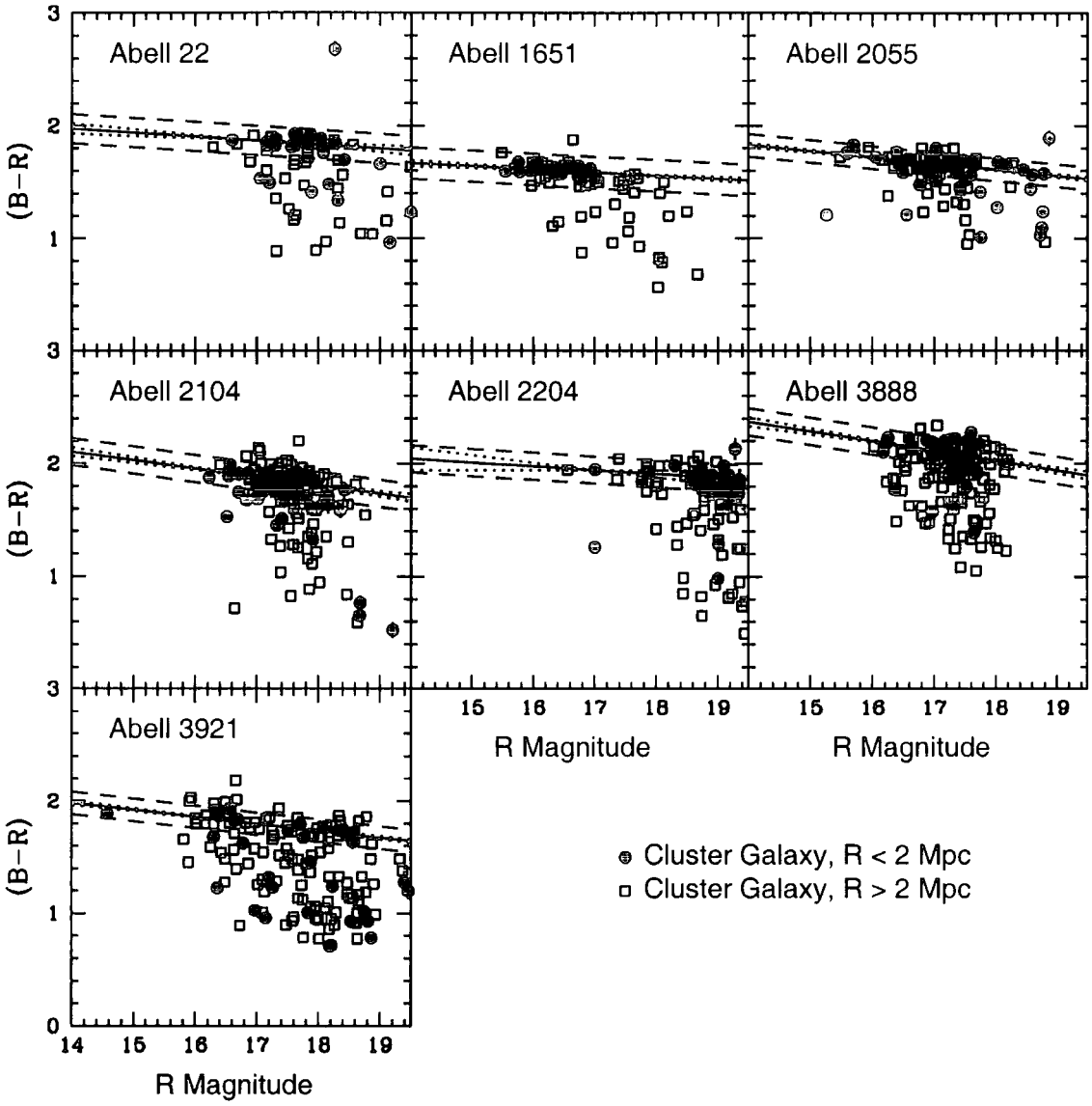

Figure 7.1: Colour-magnitude diagrams for spectroscopically-confirmed cluster members in all LARCS clusters with available 2dF spectroscopy. The solid circles are those galaxies within 2 Mpc of the cluster centre, the open squares are those galaxies beyond 2 Mpc from the cluster centre. The solid line is the biweighted fit to those galaxies within 2 Mpc of the cluster centre as presented in Table 7.1. The scatter of the fit is represented by the flanking parallel lines to this fit, whilst the uncertainty in the gradient is shown as the dotted line (centred at $R = 17$). The samples' selection effects results in a more scattered distribution on the colour-magnitude plane.

Table 7.1: Details of the clusters with spectroscopic observations. The given redshift is the spectroscopically derived one. The parameters of the biweight fit to the CMR within 2 Mpc of the centre of each of the clusters as plotted in Figure 7.1 are listed. The apparent R-band magnitude corresponding to the fiducial absolute magnitude of $M_V = -21.8$ is also given for each cluster.

Cluster	Redshift, z	Slope	$R_{M_V=-21.8}$	$(B-R)_{M_V=-21.8}$
A 22	0.1422	-0.036 ± 0.015	17.12	1.86 ± 0.13
A 1651	0.0845	-0.028 ± 0.009	16.06	1.61 ± 0.14
A 2055	0.1027	-0.054 ± 0.007	16.53	1.69 ± 0.10
A 2104	0.1552	-0.075 ± 0.013	18.41	1.78 ± 0.12
A 2204	0.1517	-0.033 ± 0.013	18.36	1.90 ± 0.12
A 3888	0.1534	-0.086 ± 0.014	18.47	2.00 ± 0.12
A 3921	0.0927	-0.062 ± 0.007	16.77	1.81 ± 0.10

The clusters again demonstrate their CMR but what is noticeable is that there are somewhat more bluer cluster members than resulted from the background correction method in Chapter 4. Such differences between the statistically- and the spectroscopically-determined cluster members will be examined later in this work. The biweight method is again employed to determine the slope and colour at the fiducial magnitude ($M_V = -21.8$) of the CMR for all spectroscopically-confirmed galaxies brighter than $M_V = -20$ within 2 Mpc of the cluster centre. The results of these biweight fits are presented in Table 7.1. The change seen in the slopes between those clusters analyzed in Chapter 4 and the spectroscopically determined slopes is negligible (within $\sim 1\sigma$), as is the change in colour at the adopted fiducial magnitude ($M_V = -21.8$).

7.2.1 Examination of Other Structures Along the Line of Sight

Attention is now turned to the other overdensities along the line of sight in order to ascertain their status. If the other overdensities noted in Table 6.2 are clusters, then they will exhibit CMRs similar to those of the LARCS clusters seen above.

For each of the overdensities noted in Table 6.2, a colour-magnitude diagram is constructed. The galaxies that are members of these overdensities are defined to lie within $3\sigma_z$ of the mean velocity, $\overline{cz}$. Whilst somewhat cruder than the CNOC mass model, this definition of membership is more than sufficient to search for the presence of a CMR. In Figure 7.2 the colour magnitude diagrams for these overdensities are presented. Since the number of galaxies in each of these structures is small, a fit to the CMR using the biweight method will not produce optimal results. The best that one is able to do is to plot the expected position of the CMR at the redshift of the structure. For this purpose, the spectroscopically determined CMR of Coma by de Propris et al. (1998) is used and k-corrected to the appropriate redshift.

Many of the overdensities exhibit a CMR. The most striking belong to the ones whose velocity dispersion, σ_z are large ($\sigma_z > 600 kms^{-1}$). Clearly many of these overdensities in the field of the observations should be thought of as clusters in their own right. It must also be noted here that these observations are incomplete. The potential clusters in the field of the LARCS 2dF observations were not directly targeted in the same way as the LARCS clusters; for instance, many of the galaxies belonging to Abell 2104-A lie (and concentrate) towards the edge of the LARCS mosaic observed using 2dF. Followup observations specifically targeted at the other overdensities would be able to provide more complete colour magnitude diagrams and improve understanding of stellar populations in the galaxies belonging to these structures.

7.2.2 Environmental Variation of the CMR

Attention is now returned to the main LARCS clusters. In Chapter 4, the photometric variation in peak CMR colour is investigated as a function of clustocentric

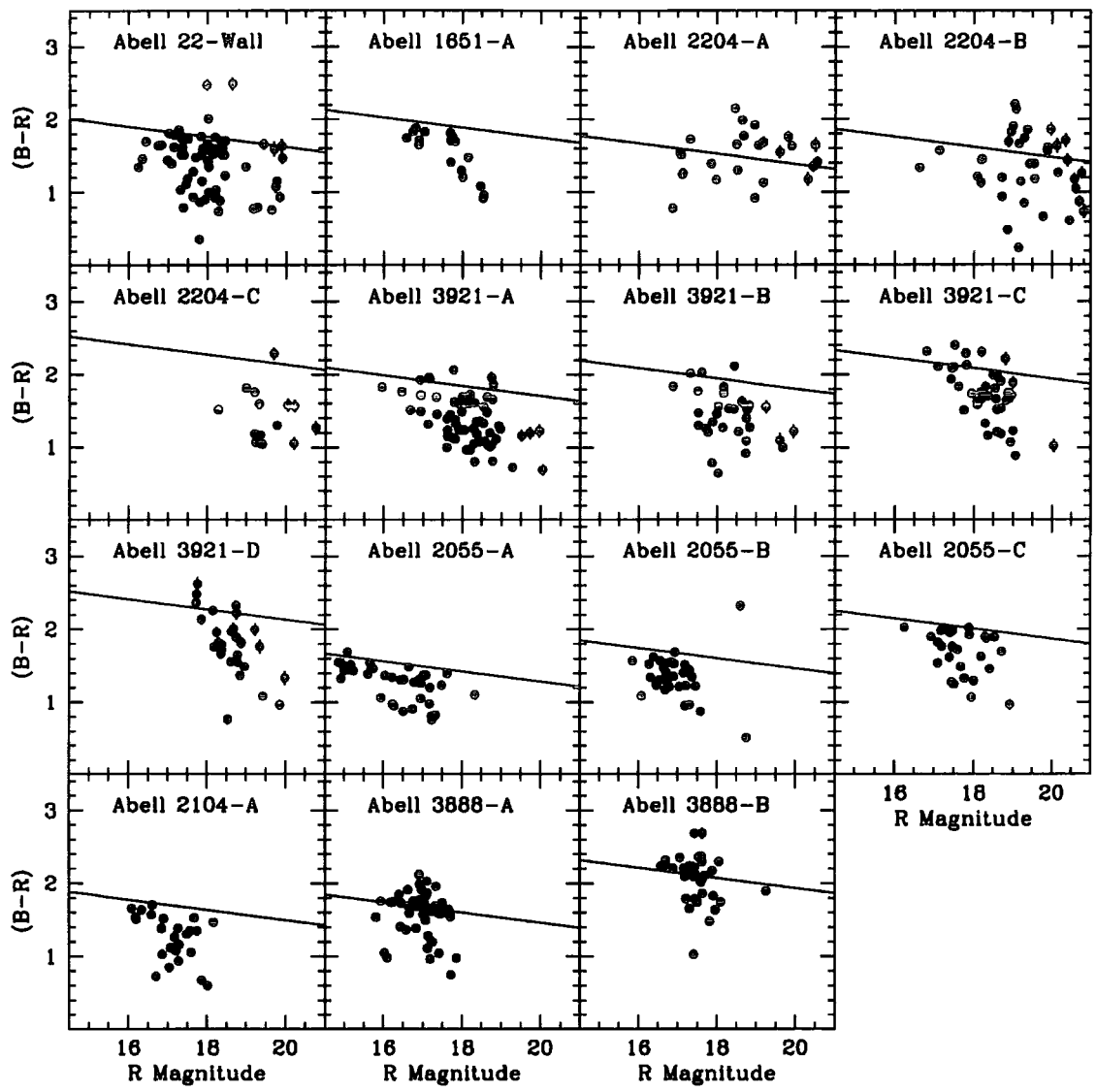

Figure 7.2: Colour-magnitude diagrams for other structures along the line of sight as noted in Table 6.2. A number of these diagrams exhibit noticeable CMRs providing further evidence for the existence of other evolved structures along the line of sight. The solid line is the CMR of Coma, k-corrected to the cluster redshifts.

radius. Having defined cluster membership, the issue of radial blueing is once again examined in the light of the 2dF spectroscopy.

In a similar manner to Chapter 4, the homogeneity of the clusters is again exploited by stacking them together to quantify any change with environment (clustocentric radius and local galaxy density). The production of such a composite cluster requires that the magnitudes, colours and positions of galaxies in the individual clusters are transformed onto a common scale. The apparent magnitudes of the galaxies are transformed to a redshift of $z = 0.12$. The slopes adopted to transform the colours of galaxies lying on the CMR are those found from the biweighted fit (Table 7.1). The clustocentric radius in each individual cluster is used as the common radial scale.

Since the number of galaxies in the composite cluster is much smaller than those present in the photometric analysis in Chapter 4, it is not possible to split the composite cluster up into 1 Mpc annulii. Therefore, using an arbitrary clustocentric radius of r_{200} (which corresponds to $r_p \simeq 2.5$ Mpc), the composite cluster is divided up into 'inner' and 'outer' samples. Considering all those galaxies brighter than $M_V = -20$ (which at $z = 0.12$ is equivalent to $R = 18.9$), a colour histogram of the radially divided composite cluster is constructed. There are 266 galaxies in the 'inner' sample and 352 in the 'outer' sample. Gaussians are then fitted to these histograms, in the same manner detailed in Chapter 4. The results of this analysis are presented in Figure 7.3. It is found that the peak colour of the CMR evolves bluewards with increasing clustocentric radius at a rate of $d(B-R)/dr_p = -0.016 \pm 0.005$ out to ~ 5 Mpc. This result is about 1σ less than the result obtained for the photometric sample (Chapter 4) and therefore is not viewed as significantly different.

The variation in the peak colour of the CMR with local-density is also investigated. For simplicity, the same values of local-density calculated in Chapter 4 are re-used here. Since our observations of the clusters are incomplete, an attempt at calculating three-dimensional local-densities would not result in a more accurate result. Again, due to small numbers, the composite cluster is split at $log_{10}(\Sigma) = 1.0$. Colour histograms of the split sample are then created from all those galaxies brighter than $M_V = -20$. These histograms are then fitted with

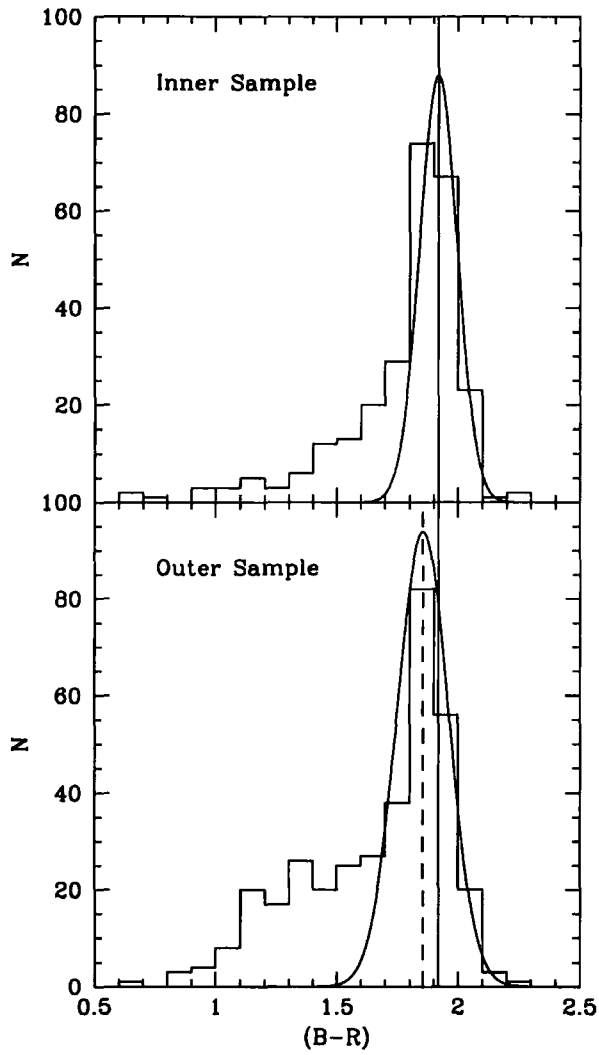

Figure 7.3: The composite cluster, radially split at $r_p = r_{200}$ is shown as a colour histogram. The CMR has had its slope removed in the construction of the composite cluster. The curve superimposed upon the histograms are the best fit Gaussian fits to them. The solid vertical line is the peak colour for the inner sample and the dashed vertical is the same for the outer sample. A blueward shift in the peak of the CMR of $d(B-R)/dr_p = -0.016 \pm 0.005$ is observed.

Gaussians (as above). The result of this analysis is presented in Figure 7.4. Again, the peak colour of the CMR evolves bluewards with decreasing local galaxy density at a rate of $d(B-R)/dlog_{10}(\Sigma) = -0.064 \pm 0.014$; about 1σ below the photometric result found in Chapter 4.

7.3 Further Spectroscopic Analysis of the Clusters

In the previous section the cluster galaxies are combined into a single composite cluster to examine the radial trend in $(B-R)$ colour in a similar manner explored in Chapter 4. It is found that there exists a modest, but significant, blueing of the colours of typical early-type galaxies from the core out to beyond the virial radius of $d(B-R)/dr_p = -0.016 \pm 0.005$; within 1σ of that found in Chapter 4. The $(B-R)$ colour is a good indicator of the recent star formation in a galaxies history (e.g. Searle et al. 1973), therefore one may expect that this radial trend in colour will translate into a radial trend with EW(Hδ) absorption line strength.

Terlevich et al. (1999) demonstrates the relationship between deviations in the $(U-V)$ colour of galaxies (from the CMR) and the equivalent deviations in the strength of Balmer absorption lines from observations of early-type galaxies in Coma. Based on the shift of $\Delta(B-R) \sim 0.1$ for typical galaxies out to 4 Mpc, it is estimated that this population should show enhanced Balmer absorption of $\sim$ 4Å equivalent width.

Taking the composite cluster, the trend in Balmer absorption is investigated as a function of clustocentric radius. Figure 7.5 shows the result of this analysis; the EW of the $H\delta$ line is plotted against the deviation in $(B-R)$ colour from the CMR in radial bins. The CMR can be clearly seen extending about $\Delta(B-R) \sim 0$. The mean values for the strength of the $H\delta$ line is given in Table 7.2 as well as the fraction of cluster galaxies with $H\delta$ strengths above EW= 3.0Å.

Using only the old population of galaxies (i.e. emission line galaxies with EW[OII]> 5.0 are excluded*; open circles in Figure 7.5), a detection of an increase in the mean

*Recall [OII] is a tracer of current, on-going star formation.

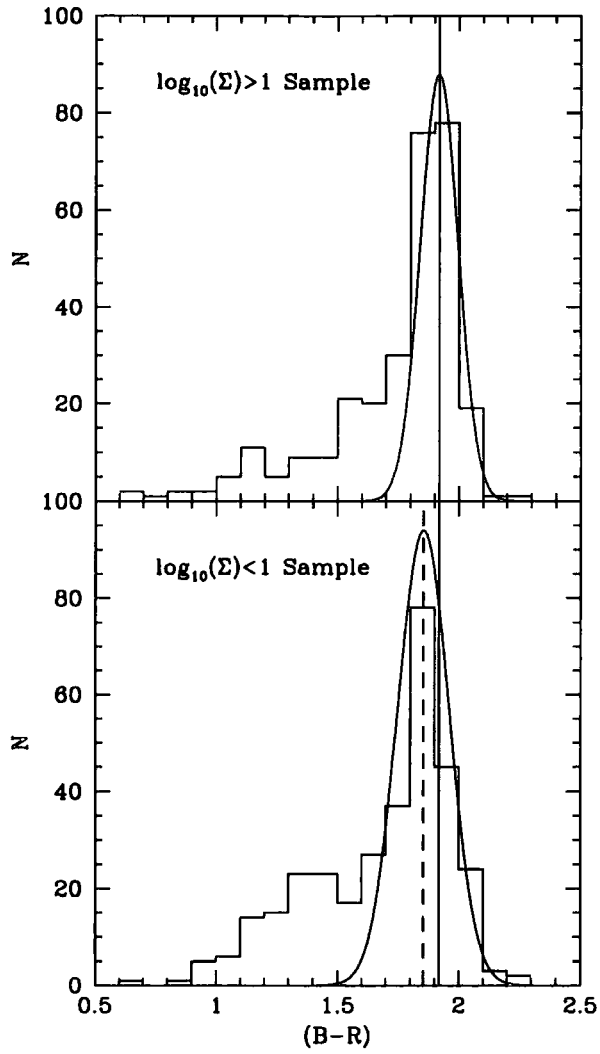

Figure 7.4: The composite cluster, split at $log_{10}(\Sigma) = 1.0$ is shown as a colour histogram. The CMR has had its slope removed in the construction of the composite cluster. The curve superimposed upon the histograms are the best Gaussian fits to them. The solid vertical line is the peak colour for the inner sample and the dashed vertical is the same for the outer sample. A blueward shift in the peak of the CMR of $d(B-R)/dlog_{10}(\Sigma) = -0.064 \pm 0.014$ is observed.

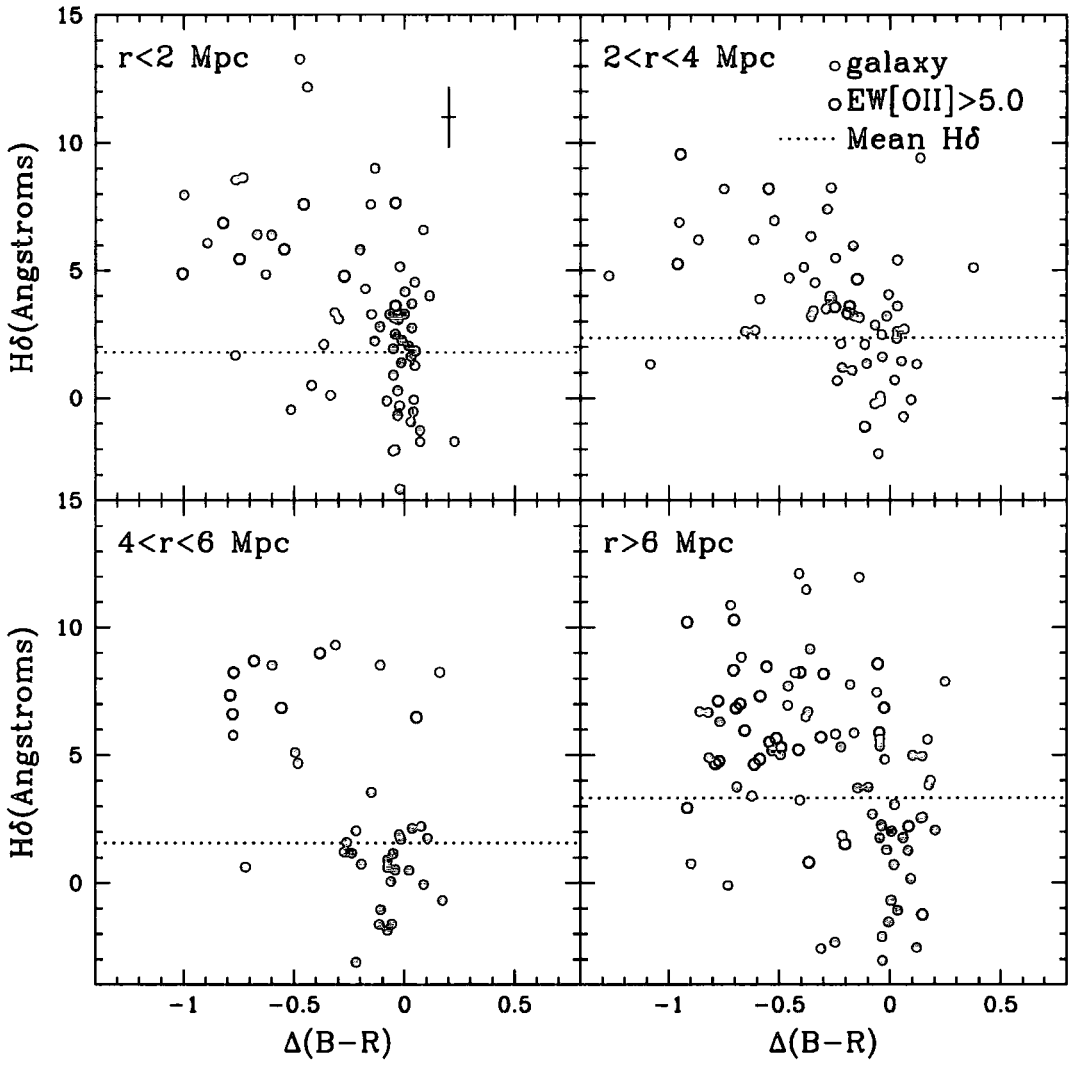

Figure 7.5: Plot of the strength of the $H\delta$ absorption line versus deviation in $(B-R)$ colour from the CMR of the composite cluster split into radial portions. The filled circles have EW[OII] > 5.0Å. The typical error on each galaxy is shown as a cross-hair. The mean value of the $EW(H\delta)$ absorption line is shown as the dotted line and is listed in Table 7.2.

Table 7.2: The mean strength of the $H\delta$ absorption line and the fraction of $H\delta$ strong galaxies, $f_{\mathrm{k+a/a+k}}$, (Hδ EW > 3.0Å) as a function of clustocentric radius in the artificial cluster (see Figure 7.5). The first half of the table presents figures for the whole composite cluster whilst the second half presents figures for a sample which excludes emission line galaxies (EW[OII]> 5.0).

Sample	Radius (Mpc)	$\overline{EW(H\delta)}$ / Å	$f_{\mathrm{k+a/a+k}}$
Full	0–2	1.59 ± 0.28	0.37 ± 0.08
	2–4	1.99 ± 0.35	0.35 ± 0.08
	4–6	2.37 ± 0.52	0.45 ± 0.09
	> 6	3.56 ± 0.29	0.56 ± 0.09
EW[OII]< 5.0	0–2	1.79 ± 0.44	0.32 ± 0.09
Only	2–4	2.35 ± 0.47	0.34 ± 0.09
	4–6	1.56 ± 0.66	0.29 ± 0.11
	> 6	3.32 ± 0.45	0.48 ± 0.10

strength of the $H\delta$ absorption line by $\sim$ 2Å from the cluster core region to the outskirts of the cluster is confirmed at $> 3.5\sigma$. The fraction of galaxies possessing a strong $H\delta$ absorption line also increases from 32 ± 9 per cent in the core region to 48 ± 10 per cent in the outskirts, but this detection is only at a $\sim 1.5\sigma$ level.

Attention is now turned to the colours of the galaxies. If the CMR is blueing with radius and $H\delta$ line strength is also a function of environment (i.e. radius), then this should be reflected in the mean colour of k-type galaxies. Figure 7.6 shows the colour distribution of the different spectroscopic types in the artificial cluster evolved to $z = 0.12$. Perhaps surprisingly, there appear to be more blue e(a) galaxies than e(c) galaxies (N(e(a),$(B-R) < 1.3$)=15; N(e(c),$(B-R) < 1.3$)=9). Closer inspection of the e(a) galaxies reveals that $\sim$ 85 per cent of them are within 3σ of the e(a) / e(c) borderline of EW(Hδ)=4.0 (Figure 6.10). Combined with the small numbers of galaxies in these populations, this excess (1.5σ) is not viewed as significant.

Figure 7.7 shows the colour-magnitude diagram for the composite cluster, split according to spectral type. Note how the passive k-type galaxies dominate the CMR whilst the recently and currently star forming galaxies have a large scatter. The currently star forming galaxies (e(a) and e(c)) appear to dominate the blueward half of the diagram ($(B-R) < 1.6$). Figure 7.8 shows the colour-magnitude diagram for the composite cluster, this time split at r_{200}. At $r_p < r_{200}$ the passive types dominate the CMR, with only small numbers of recently and currently star forming galaxies. At $r_p > r_{200}$ the scatter in colour increases with many more recently and currently star forming galaxies appearing in the bluer regions. The CMR itself also becomes more contaminated with these systems.

To investigate the change in stellar populations of galaxies with increasing clustocentric radius, the composite cluster is again used to trace the variation of EW(Hδ) with r_p. Instead of using individual EW measurements Hδ within each galaxy, multiple spectra are now combined using the IRAF task SCOMBINE[†] to improve the signal to noise ratio. The spectra are combined in 3 Mpc intervals based upon their clustocentric radius within the composite cluster. The EWs are

[†]The SCOMBINE task is analogous to the IMCOMBINE task (see Chapter 2) except that it works on one-dimensional spectra.

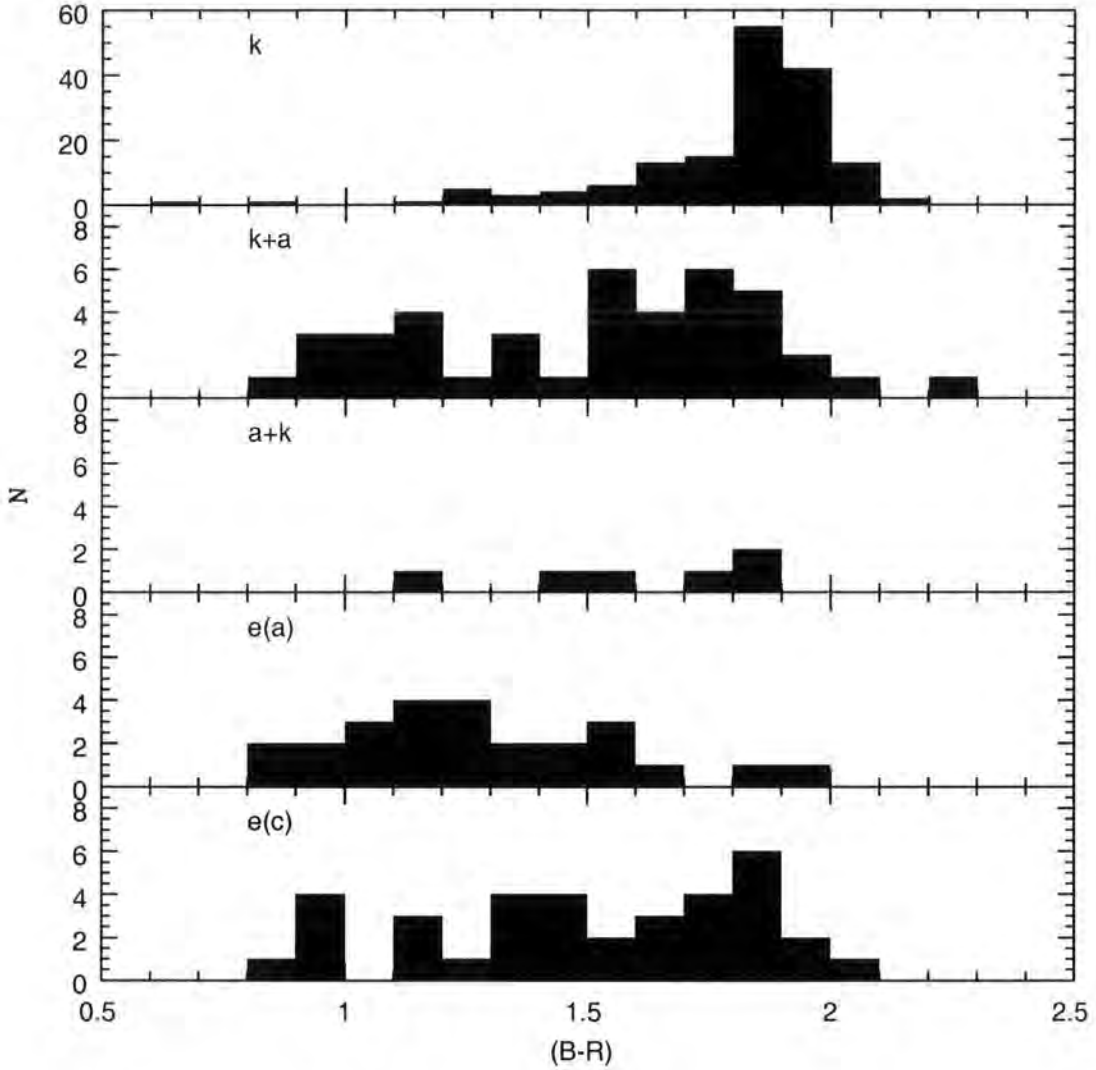

Figure 7.6: The colour distribution of the composite cluster (evolved to $z = 0.12$) split upon spectroscopic typing.

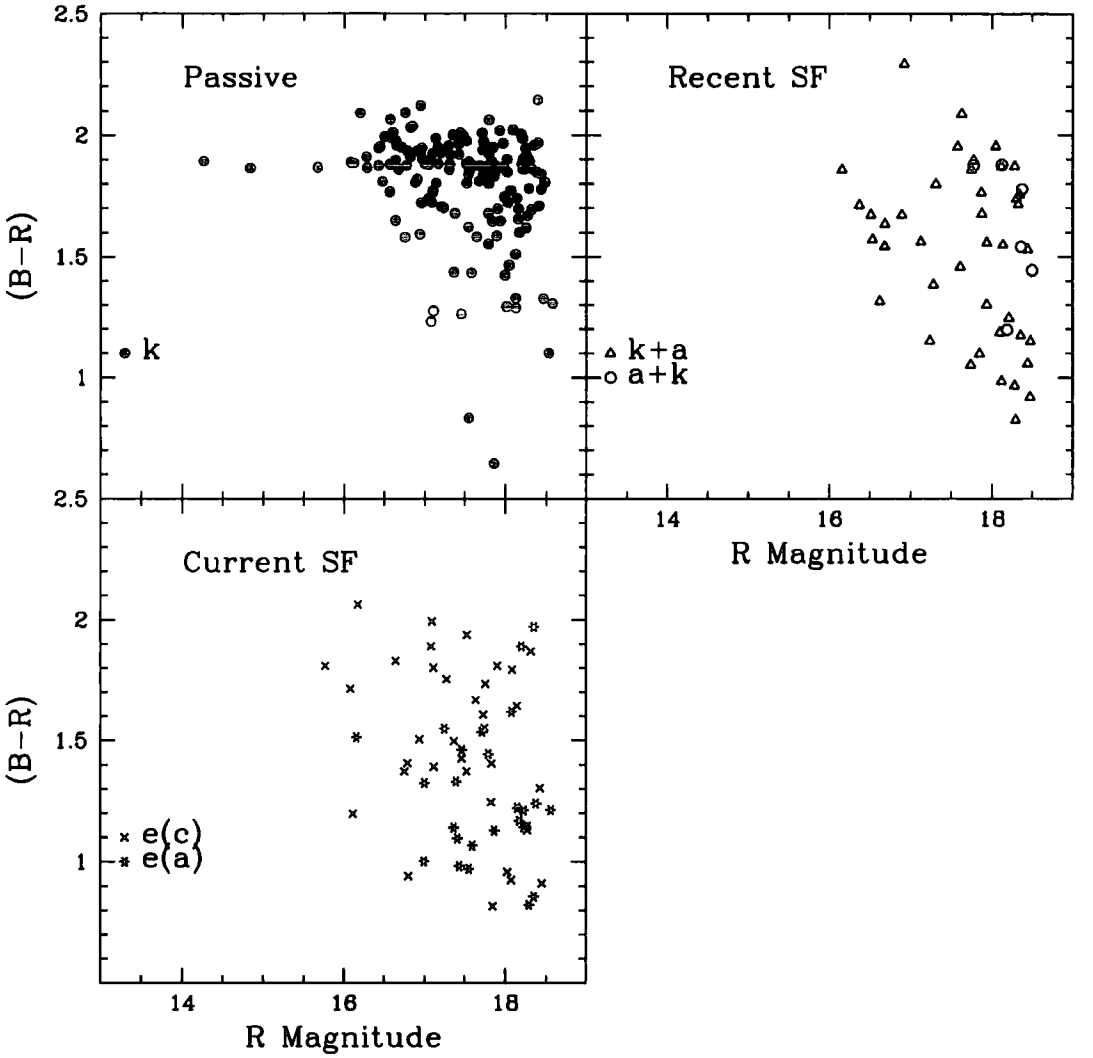

Figure 7.7: The colour-magnitude diagram for the composite cluster split according to spectral type. Symbols for the different spectroscopic types are the same as for Figure 6.15.

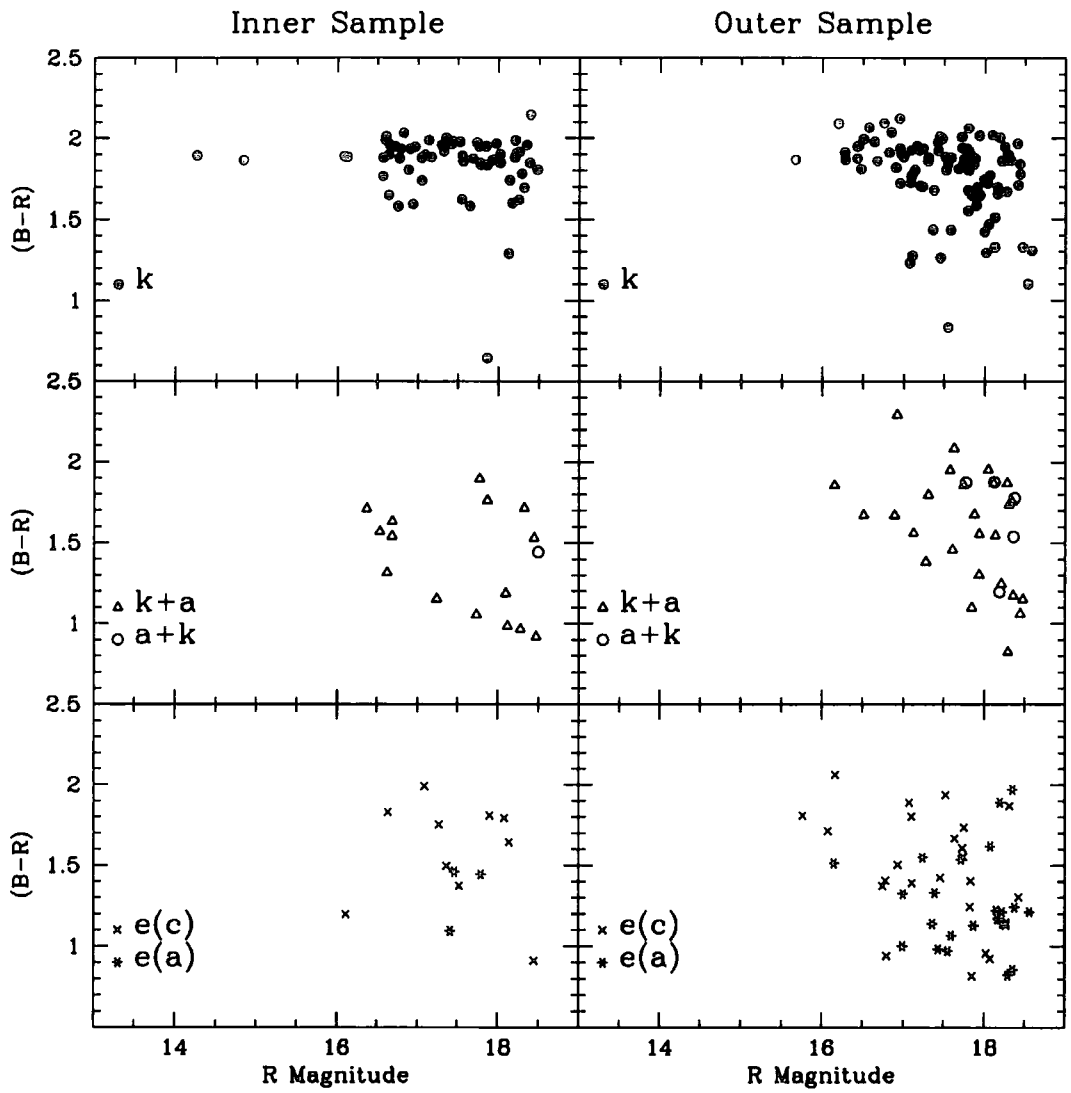

Figure 7.8: The colour-magnitude diagram for the composite cluster. The cluster is split radially at r_{200} into two samples as before. Symbols for the different spectroscopic types are the same as for Figure 6.15.

measured using the same procedure discussed in Chapter 5. The radial variation in EW(Hδ) for non-emission line galaxies (i.e. EW[OII]$<$ 5.0) is plotted in Figure 7.9. For this sample (i.e. passive and recently star forming types) the EW(Hδ) absorption line increases by $\sim$ 3Å from the cluster core region to the outskirts of the cluster by $> 5.5\sigma$. Also displayed in Figure 7.9 is the fraction of passive k-type galaxies, f_k, present within each point (with poissonian error bars). There is a trend for f_k to decrease with clustocentric radius, but it is not highly significant ($\sim 1.5\sigma$). Thus the increase in EW(Hδ) line strength is not entirely attributable to an increasing fraction of k+a/a+k type galaxies in the composite spectra.

To examine how the different spectroscopic types are distributed within the composite cluster, a cumulative radial distribution is derived for all galaxies brighter than $M_V = -20$. Figure 7.10 shows the distribution of spectroscopic types with clustocentric radius. The passive k-type galaxies dominate the core regions of the cluster ($r_p < 2$ Mpc). Figure 7.11 displays this cumulative radial distribution for the composite cluster, split into the three broad spectral types (passive, recently SF and currently SF). The passive k-type galaxies are seen to be the most centrally concentrated whilst the emission line galaxies (currently SF) avoid the cluster centre, possessing a more extended distribution. The magnitude breakdown of the composite cluster is displayed in Figure 7.12. The passive k-type galaxies are dominant at all magnitudes ($\sim$ 70 per cent). The currently star forming types increase at fainter magnitudes; from zero at bright ($M_V < -23$) magnitudes to just under 20 per cent at $M_V = -20$. Meanwhile, the recently star forming galaxies (k+a / a+k) fraction of the cluster population decreases from bright to faint magnitudes (from over 25 per cent at $M_V = -23$ to some 15 per cent at $M_V = -20$).

Velocity dispersion for the different spectral types are now computed using the same prescription as for the individual clusters. Table 7.3 gives the rest frame velocity dispersions and errors for the composite cluster, broken down into the different spectroscopic types. The distribution of these spectral types is displayed in Figure 7.13. Already it is possible to see differences between the populations; e.g. for the $r < r_{200}$ sample the ratio of the velocity dispersions of the currently star forming population to the passive is $\sigma_e/\sigma_k = 1.18 \pm 0.04$.

In order to ascertain how relaxed the different spectral populations are rel-

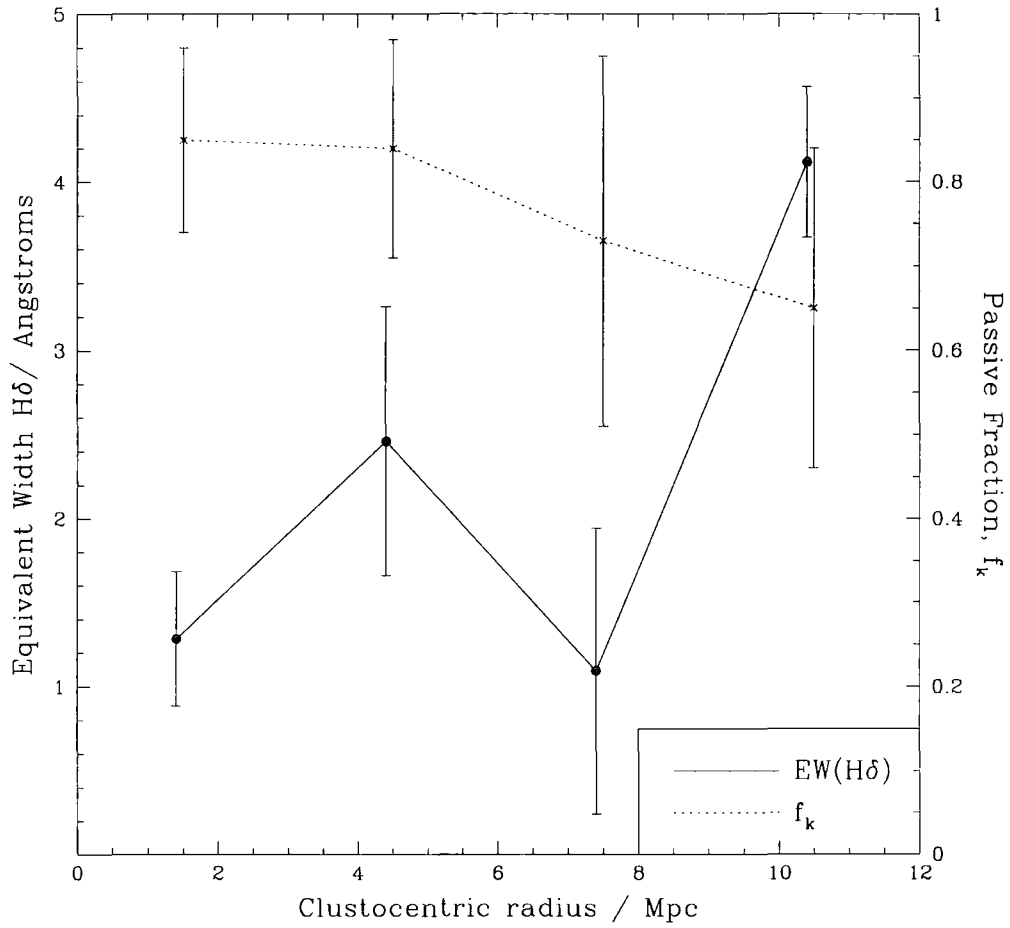

Figure 7.9: The trend of measured EW(Hδ) with radius for non-emission line galaxies within the composite cluster is shown as the solid line. The fraction of passive k-type galaxies, f_k, and associated poissonian errors contained in each point is also displayed as the dotted line.

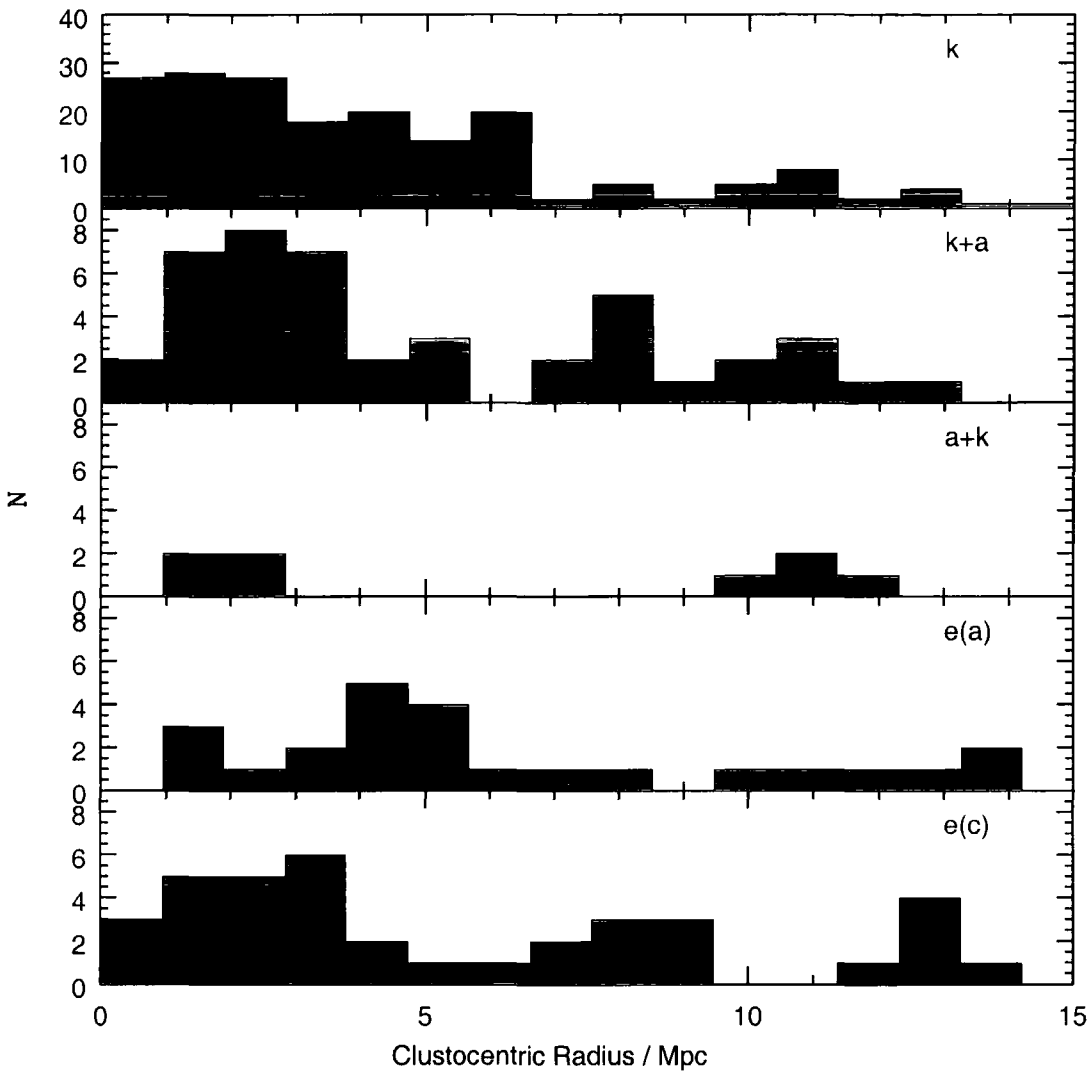

Figure 7.10: The radial distribution of the composite cluster population (evolved to $z = 0.12$) split upon spectroscopic type. Only galaxies brighter than $M_V = -20$ are presented.

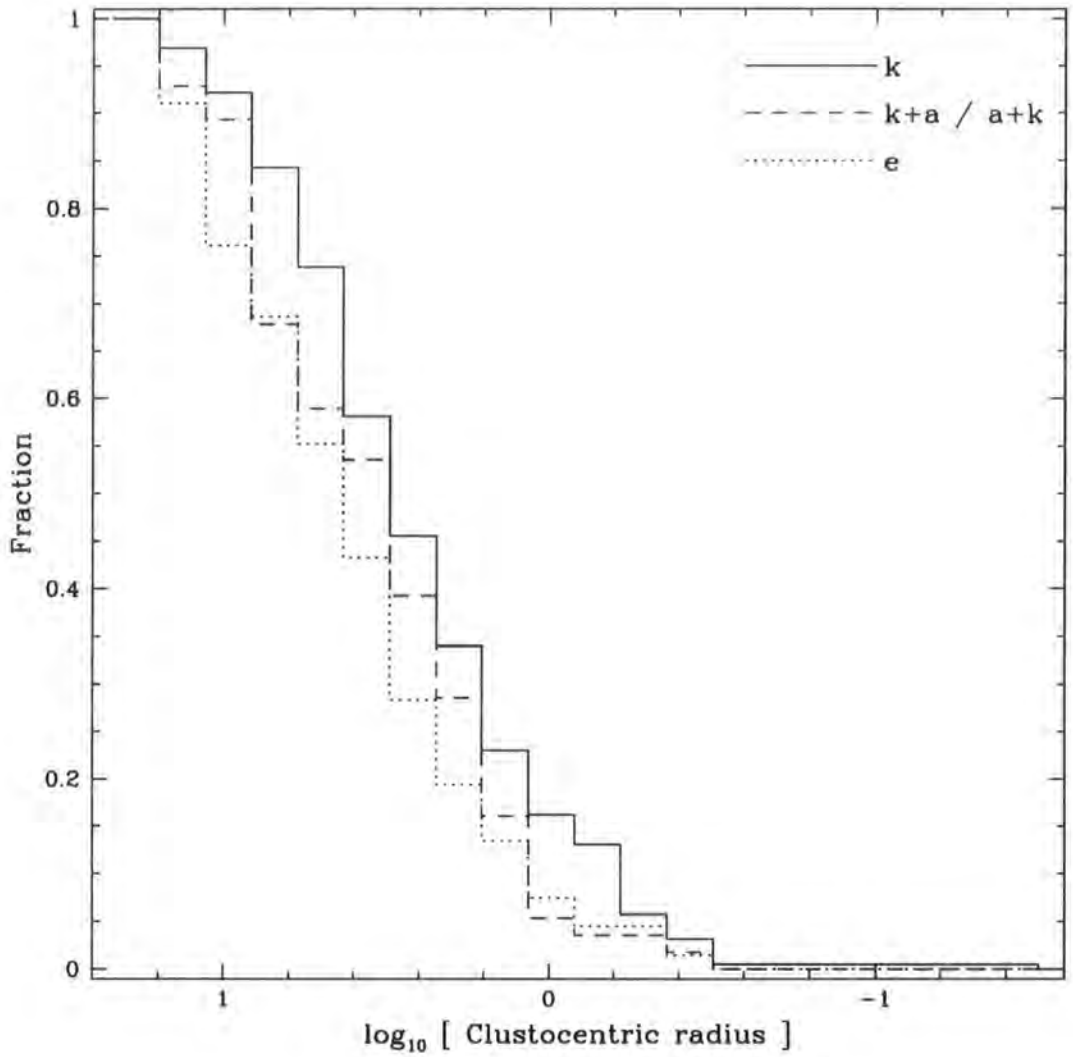

Figure 7.11: The cumulative radial distribution of the composite cluster (evolved to $z = 0.12$) split upon spectroscopic typing into passive (k), recently star-forming (k+a / a+k) and currently star-forming (e). There is a pronounced difference between these three groupings, with the passive k types being more centrally concentrated than the others.

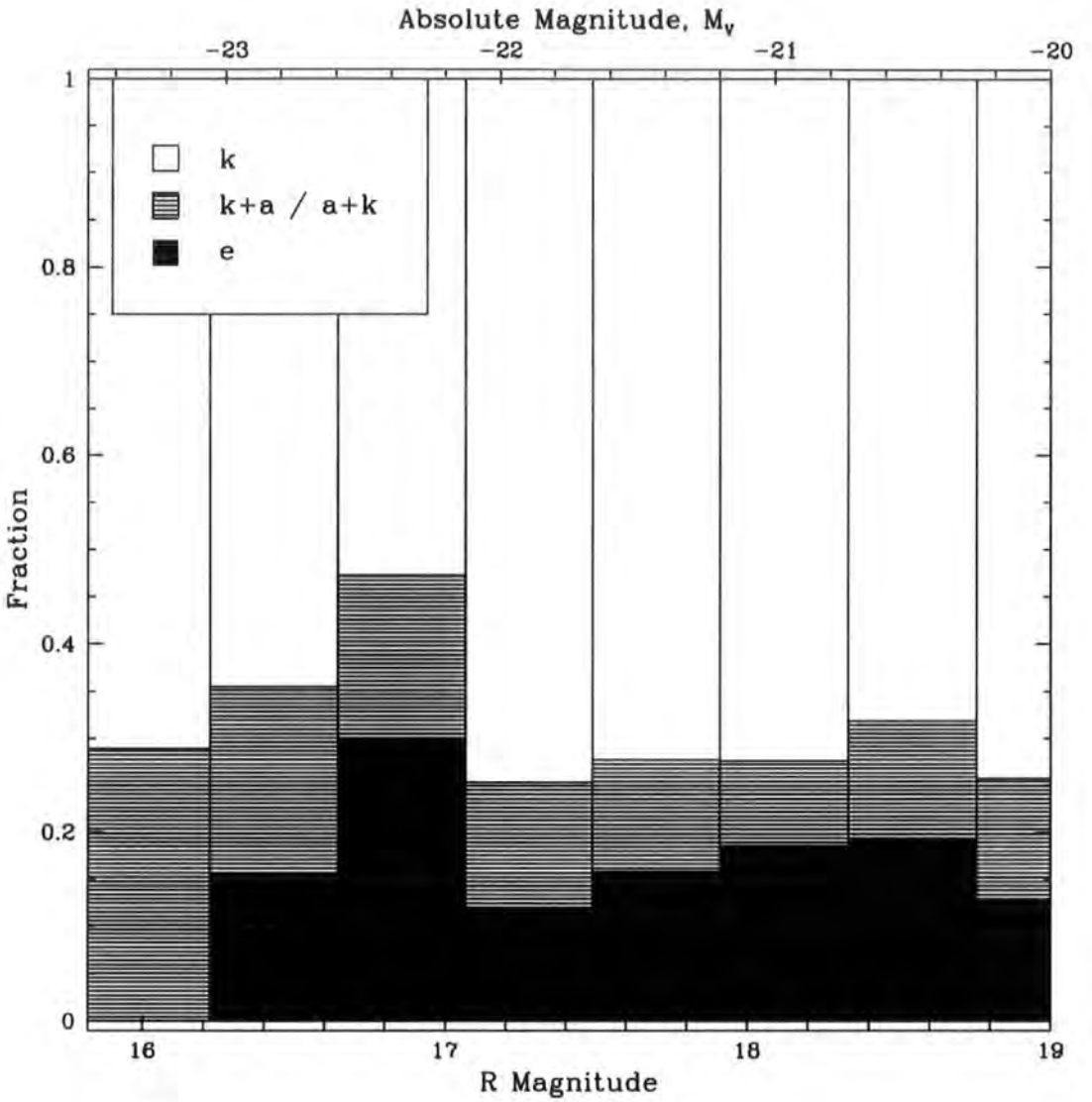

Figure 7.12: The magnitude breakdown of the spectroscopic types. Note how the passive k population (white) dominates the distribution at all magnitudes. It slowly falls from ~ 65 per cent of the population at $R = 16.3$ down to ~ 55 per cent at $R = 18.8$.

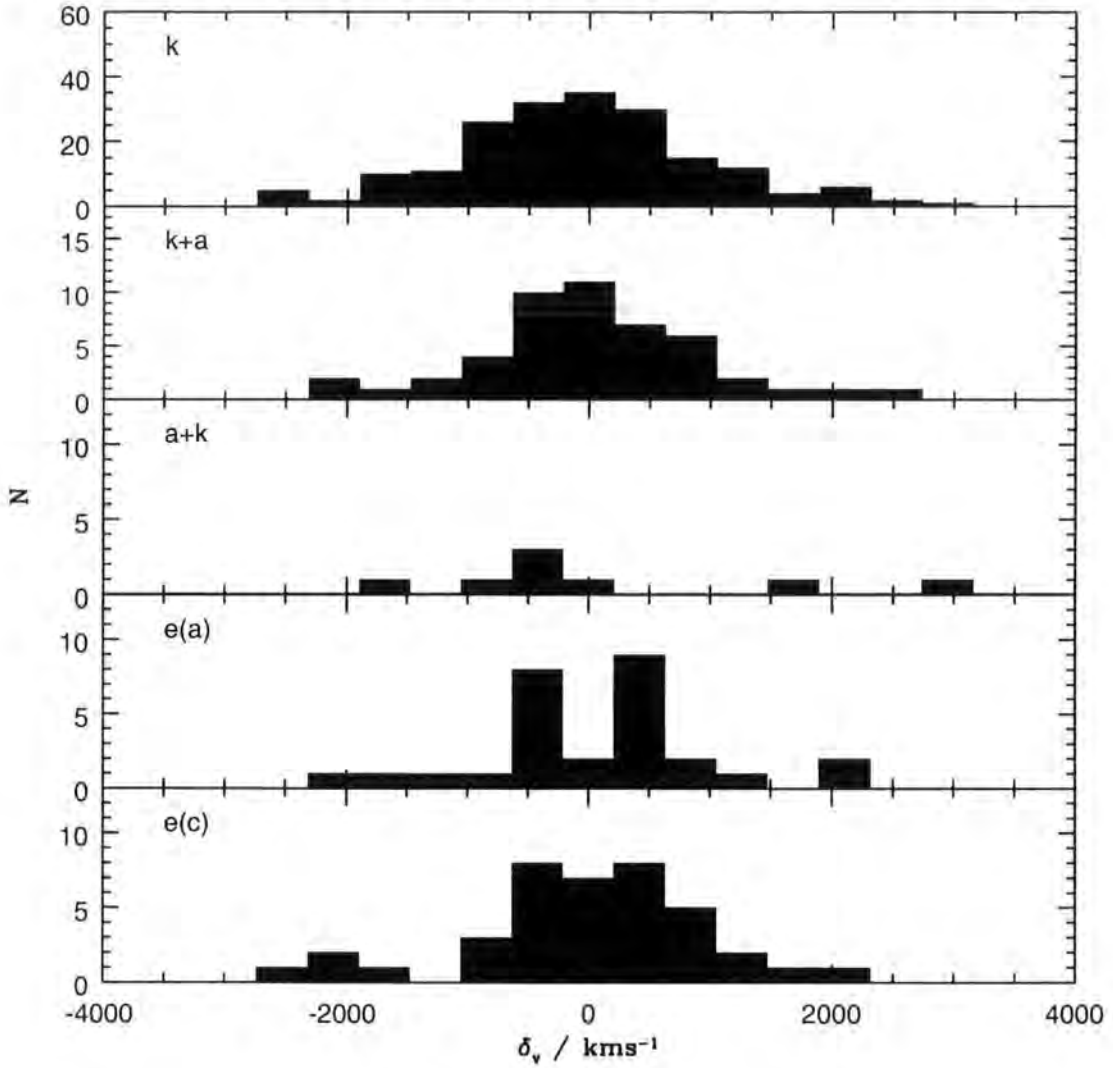

Figure 7.13: The restframe velocities of cluster members calculated relative to their respective cluster means and split on the basis of spectroscopic typing.

Table 7.3: Velocity dispersions of different spectroscopic populations within the composite cluster sample.

Sample	N	$< v >$ kms^{-1}	σ kms^{-1}	Error kms^{-1}
All				
k	191	-77	1027	96
k+a	48	21	925	227
a+k	8	69	1426	367
e(c)	39	-13	952	292
e(a)	28	35	982	302
$r < r_{200}$				
k	70	50	1097	101
k+a	15	234	1098	299
a+k	3	334	1995	395
e(c)	12	-521	1361	390
e(a)	4	381	1047	340

Table 7.4: Characteristic masses of the composite cluster using its different spectroscopic populations. (Note: $1M_{\odot} = 1.989 \times 10^{30} kg$).

Sample	M_{char}	r_{char}
	$M_{\odot} \times 10^{15}$	Mpc
k	1.48 ± 0.20	2.01
k+a	1.39 ± 0.48	2.33
a+k	2.41 ± 0.32	1.70
e(c)	1.45 ± 0.27	2.30
e(a)	2.63 ± 0.49	3.91

ative to one another one can proceed by combining information on the velocity dispersions with radial information. One technique to ascertain this is to derive the virial masses (M_{vir}) for the populations. Binney & Tremaine (1987) derive $M_{vir} = 3\sigma^2 r_{vir}/G$[‡]. Although the velocity dispersions (σ) are already known for these populations (Table 7.3), the virial radii (r_{vir}) are not. Further, the virial radii for these populations are not readily obtainable; even more inventive methods (e.g. Carlberg et al. 1996, 1997) possess a large degree of uncertainty. Given, however, that the parameters of interest are the *differences* between the masses of the different spectroscopic populations and not the absolute virial masses, one can readily proceed by finding a characteristic radius, r_{char}, instead of r_{vir}. In the spirit of Butcher & Oemler (1984), this characteristic radius is chosen to be R_{30}, the radius which contains 30 per cent of the given population. Table 7.4 shows the values obtained for R_{30} ($= r_{char}$) and M_{char}, the characteristic radii and masses for the different spectroscopic populations of the composite cluster. The determinations of M_{char} vary by up to $\sim 2\sigma$ depending upon which spectral type one chooses. The inference of this is that different members of the cluster have become accreted at different times.

[‡]The value of gravitational constant is chosen here to be $G = 6.67 \times 10^{-11} m^3 kg^{-1} s^{-2}$; further, note 1 Mpc $= 3.0856 \times 10^{22} m$.

7.4 Comparison to the Field Sample

A composite high-density and low-density field sample is now created in order to compare the cluster sample to. In creating these composite samples, the data are combined in the same way as the composite cluster was.

To start with, the corresponding regions of each field (excluding Abell 1651 for reasons given in Chapter 6) are cut to include only galaxies that are brighter than $M_V = -20$. Table 7.5 presents the makeup of these combined fields together with the makeup of the combined cluster sample. The fraction of passive k type galaxies falls off from 60 per cent in the core cluster regions to $\sim$ 40 per cent in the field. Whilst the numbers of recently star forming would appear to increase, the fraction of currently star forming only weakly increases.

7.4.1 Colour-Magnitude Analysis of the Field Populations

To create the colour-magnitude diagrams for the combined field samples, it is necessary to correct the individual components for their different slopes and redshifts. Since many of these components do not have well-defined CMRs (see Figure 7.2) these corrections are accomplished by using the relations presented in Figures 4.2 and 4.3.

The colour-magnitude diagrams for the high-density-field and low-density-field are presented in Figures 7.14 and 7.15 respectively. Whilst the high-density-field shows signs of a CMR for the passive types, this is non-existent for the low-density-field. Indeed the colours of the high-density-field do not exceed $(B - R) \sim 2.5$. In the low-density-field, the spread in colour is much greater. This can clearly be seen in Figure 7.16. To determine if these distributions are significantly different from each other and from the composite cluster (Figure 7.6), a K-S test is performed on each pairing. The result of these K-S tests shows that the null hypothesis is true: the colour distributions are all drawn from the same population.

Table 7.5: Spectroscopic classification of the combined sample (excluding Abell 1651). All galaxies have a value of $R_{TDR} > 3.0$ and are brighter than $M_V = -20$. As the field observations of Abell 2204 deviates from the other field samples by more than 3σ (see Table 6.4), the combined field presents fractions including and excluding measurements on Abell 2204.

Field	N(Total)	N(k)	N(k+a)	N(a+k)	N(e(c))	N(e(a))
Combined Clusters	314	60% ± 6	16% ± 5	2% ± 2	13% ± 4	10% ± 4
Combined High-Density-Field	332	55% ± 22	18% ± 17	2% ± 2	11% ± 13	13% ± 13
(As above, excluding A 2204	222	40% ± 20	20% ± 14	1% ± 1	18% ± 13	22 ± 12)
Combined Low-Density-Field	564	46% ± 6	29% ± 7	4% ± 2	12% ± 5	9% ± 4
(As above, excluding A 2204	359	36% ± 6	35% ± 6	3% ± 2	15% ± 4	11% ± 4)

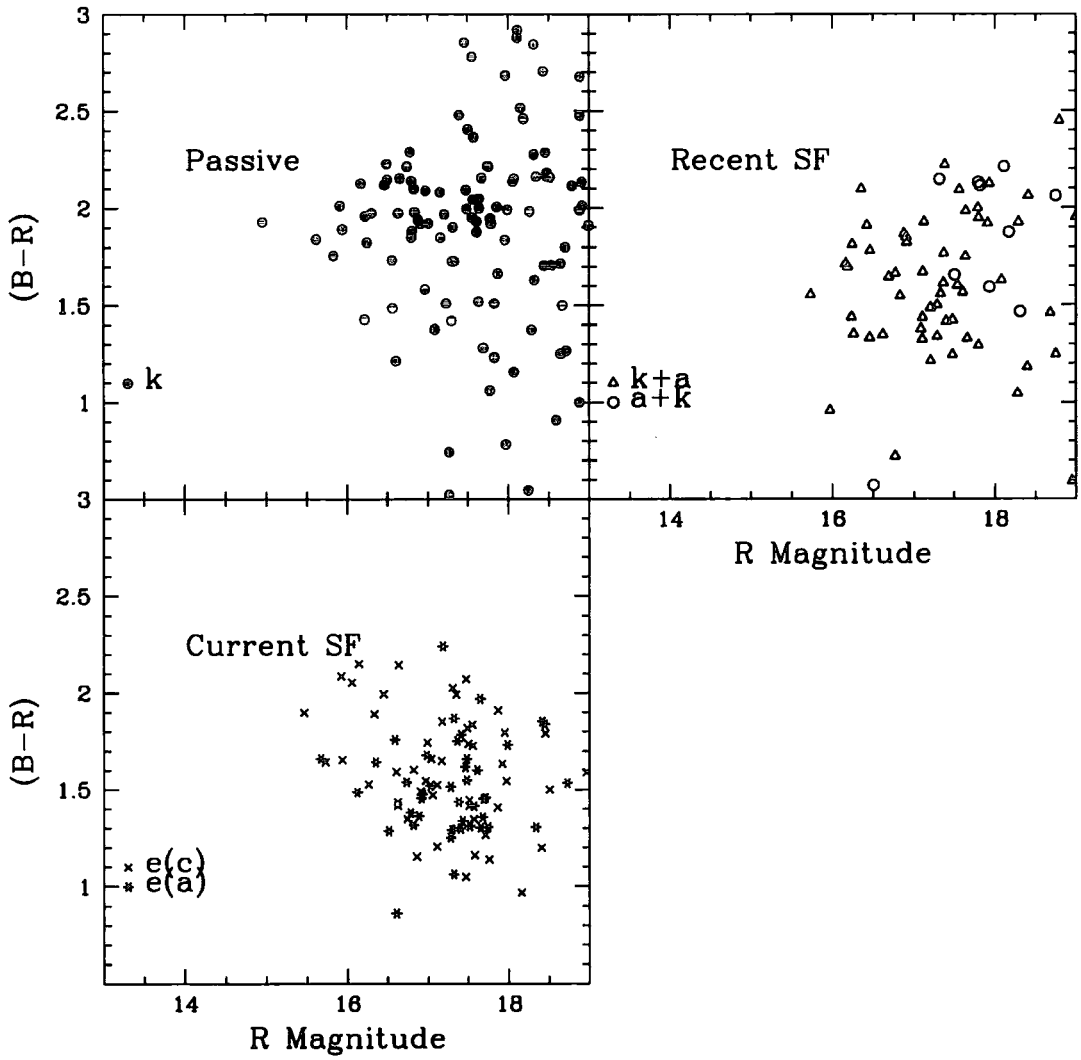

Figure 7.14: The colour-magnitude diagram for the composite high-density-field. Symbols for the different spectroscopic types are the same as for Figure 6.15.

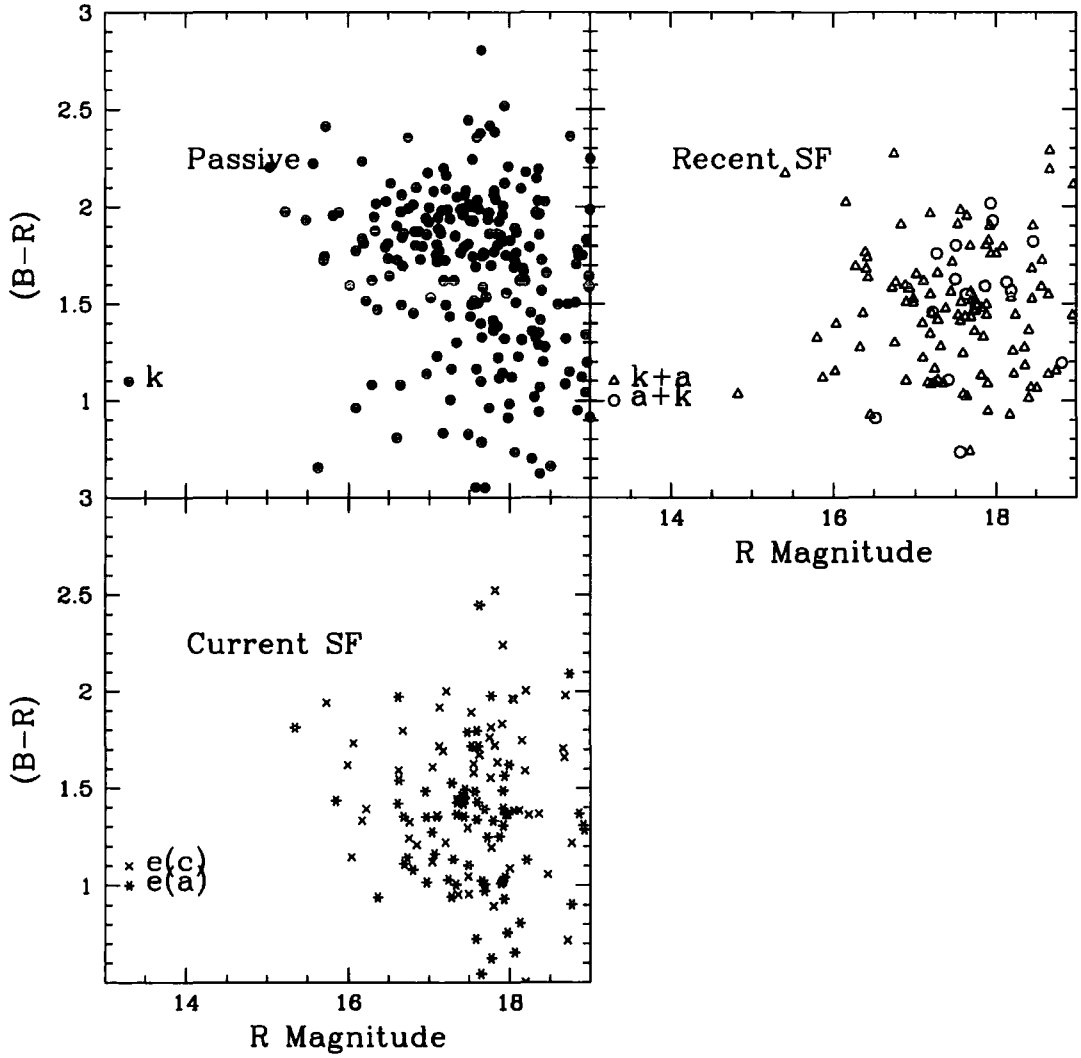

Figure 7.15: As for Figure 7.14 but for the composite low-density-field.

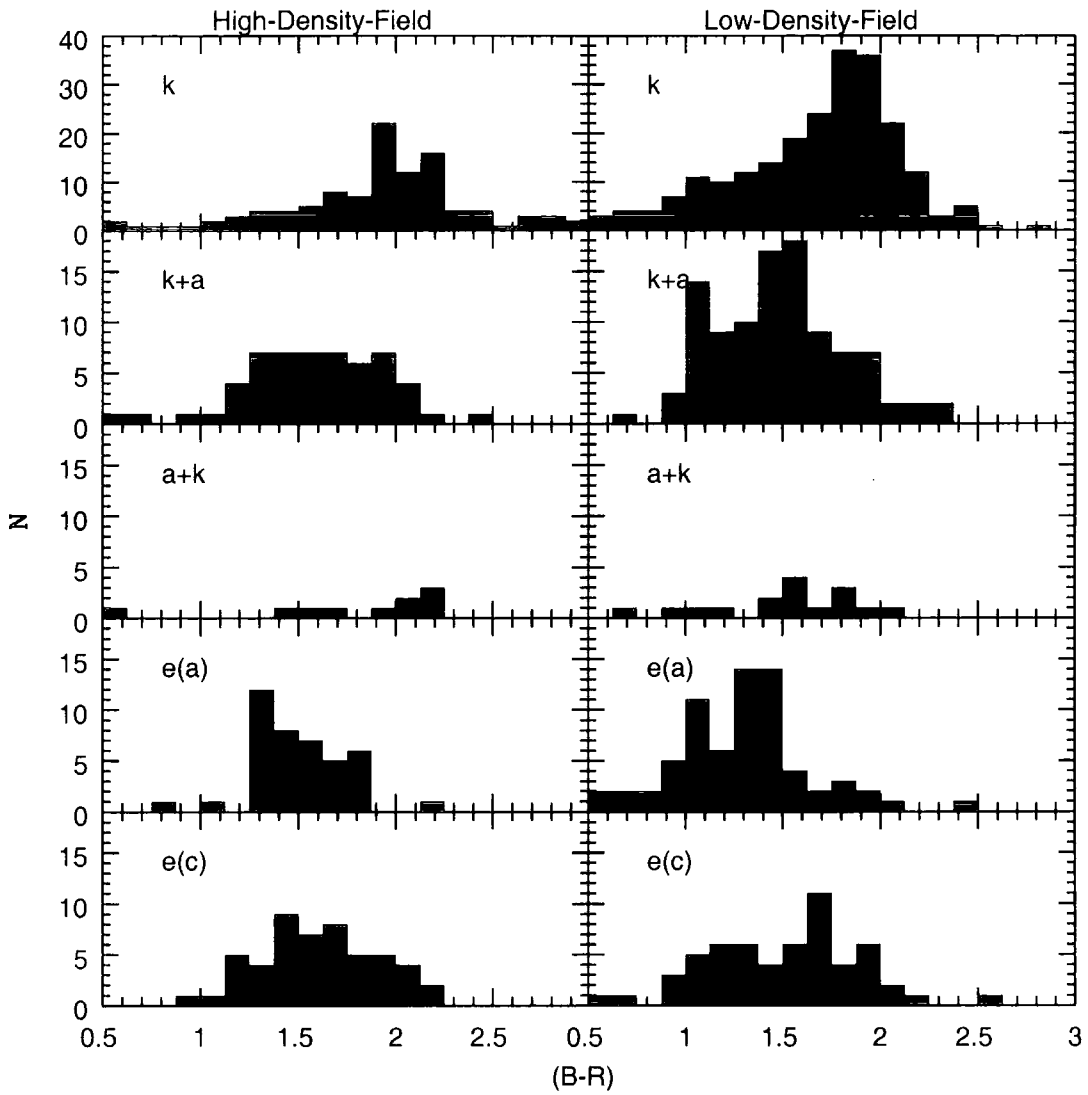

Figure 7.16: As for Figure 7.6, but for the two composite field samples. Note the excess of blue k-type galaxies over that of the cluster (Figure 7.6). These mainly come from poorer signal to noise galaxy spectra which results in probable spectral misclassification.

7.5 Summary

The colour-magnitude relation has been revisited and a spectroscopic blueward shift of $d(B-R)/dr_p = -0.016 \pm 0.005$ in the CMR with radius has been found; or $d(B-R)/dlog_{10}(\Sigma) = -0.064 \pm 0.014$ with local galaxy density. These results are not significantly different (only $\sim 1\sigma$ difference each) from the photometric blueing found in Chapter 4. A number of the potential background clusters also exhibit evidence for CMRs confirming their status as true clusters.

Further spectroscopic analysis has also suggested that there is a trend in the line strength of Hδ with radius. By exploiting the homogeneity of the clusters, a composite cluster is constructed at $z = 0.12$. An examination of how the colour-magnitude diagram evolves with radius is then made. The probability of the currently star forming galaxies being drawn from the same population (spatially and in colour) as the passive and recently star forming galaxies is found to be vanishingly small. The passive k-type galaxies are found to dominate the central core regions of the composite cluster whilst currently star forming galaxies preferentially lie nearer to the outskirts. The passive galaxies also dominate the composite cluster at all magnitudes.

Composite field samples have been created in the same manner as the composite cluster. These samples were then compared to the cluster sample. The fraction of passive k type galaxies falls off from 60 per cent in the cluster regions to $\sim$ 40 per cent in the field. Whilst the numbers of recently star forming would appear to increase, the fraction of currently star forming only weakly increases. The colour distributions of the field samples, however, show that they are not (95 per cent probability) drawn from the same population as the cluster sample.

Chapter 8 | *Further Analysis*

8.1 Abstract

During the course of this work, a number of further features of the LARCS dataset have been investigated. In this Chapter, these features (briefly comprising: quasi-stellar objects, a pathological galaxy, a local dwarf galaxy and background clusters) are discussed.

The use of the local galaxy density parameter, Σ, from Chapter 4, has highlighted its potential to detect background clusters. This parameter is tested to detect background clusters in the LCO observations of Abell 3888. The resultant detections are photometrically confirmed by the construction of colour-magnitude diagrams. Out of six potential background clusters detected by Σ, five are found to be bone-fide clusters.

8.2 Noteworthy Objects

A number of unusual objects worthy of note have been turned up in the course of this work. The imaging and spectroscopy have revealed a small number of quasi-stellar objects, some pathological galaxies and Tucana, a dwarf spheroidal galaxy.

8.2.1 Quasi-Stellar Objects (QSOs)

Several QSO candidates were intentionally entered into the spectroscopic selection process as 'Targets of Opportunity' (see Chapter 5). These objects were identified as point sources possessing a X-ray flux of $> 10^{-14}$ ergs^{-1}cm^{-2} by Edge and Pimbblet from ROSAT PSPC X-ray images of the clusters in a 0.5–2 keV passband. Being stellar in appearance (based upon the star-galaxy separation technique developed

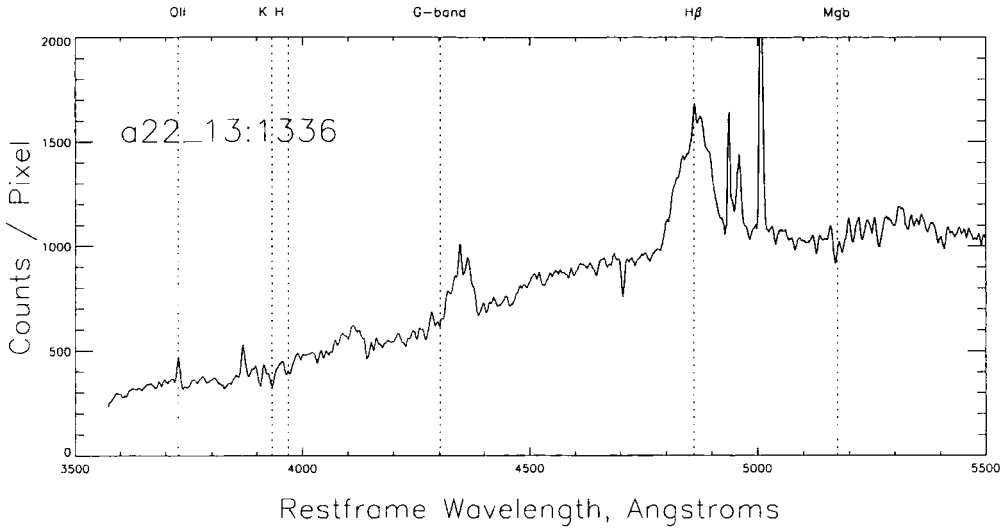

Figure 8.1: The spectrum of the AGN in Abell 22, de-redshifted to restframe wavelengths.

in Chapter 2) they would not ordinarily have been included in the spectroscopic target list. A more general analysis on the selection of QSO candidates can be found in Boyle et al. (2000) and references therein. Table 8.1 lists the intentional QSO candidates included in the July 2000 LARCS 2dF observations together with their current status and a further target that was serendipitously found to be a QSO.

The spectra of the QSOs are found to possess one or more broad emission lines characteristic of this class of object. The three confirmed QSO-like sources are logged with positions and approximate redshifts in Table 8.2.

The first of these sources (a22_13:1336) has been observed previously by Marshall, Fruscione, & Carone (1995) who found its velocity to be 38673 kms^{-1}, in good agreement with the measured velocity (Table 8.2). LARCS classify this source as an active galactic nuclei (AGN); a classification that Giommi et al. (1991) also gives. The spectra for this AGN is displayed in Figure 8.1.

The second (a3921_04:393), a QSO, has only one broad line in the covered spectral range. Presuming this line is [MgII] at 4581Å (Couch priv. comm.) the velocity can be estimated as 190930 kms^{-1}. The de-redshifted spectrum for this QSO is displayed in Figure 8.2.

The third (a3921_04:1707), also a QSO, exhibits a spectra that is very typical of a QSO, with broad Lyman α, [CIV] and [CIII] lines all present. The redshift of this QSO is approximately 2.204 making it the object with the highest confirmed

Table 8.1: List of QSO candidates included in the target lists for the July 2000 2dF observations and other galaxy targets serendipitously found to possess broad emission lines similar to QSOs. Intentional QSO candidates possess $P^* > 0.5$.

Candidate	P^*	R Magnitude	$(B-R)$	Observed?	QSO?
a22_03:632	0.89	17.74 ± 0.008	0.025 ± 0.010	No	Unknown
a22_13:1336	0.03	16.72 ± 0.007	1.358 ± 0.016	Yes	Yes
a3921_03:2117	0.78	19.10 ± 0.012	0.094 ± 0.025	No	Unknown
a3921_03:1018	0.99	18.51 ± 0.005	0.000 ± 0.047	Yes	No
a3921_04:393	0.98	20.16 ± 0.015	0.114 ± 0.022	Yes	Yes
a3921_04:1707	0.98	19.91 ± 0.012	-0.176 ± 0.017	Yes	Yes
a3921_04:1447	0.98	20.32 ± 0.018	-0.326 ± 0.022	Yes	No

redshift in the LARCS survey. The de-redshifted spectrum for this QSO is displayed in Figure 8.3.

8.2.2 A Dusty Cluster Galaxy in Abell 22

A cursory examination of the spectroscopically defined CMR for Abell 22 presented in Figure 7.1 reveals one apparently anomalous $R \sim 18.3$ cluster galaxy (a22_03:727) whose colour is much redder (by about 0.9 in $(B-R)$) than the cluster CMR.

Table 8.2: Positions of all of the observed objects together with their velocity estimate and designation.

Target	RA	Dec	cz / kms^{-1}	Designation
a22_13:1336	00 19 52.4	-25 22 30.0	38739 ± 19	AGN
a3921_03:1018	22 48 13.7	-64 22 58.1	296 ± 89	Star
a3921_04:393	22 48 13.0	-64 18 22.9	190930?	QSO?
a3921_04:1707	22 48 04.3	-64 29 49.7	661259 ± 242	QSO
a3921_04:1447	22 47 56.6	-64 27 18.2	-6.5 ± 16	Star

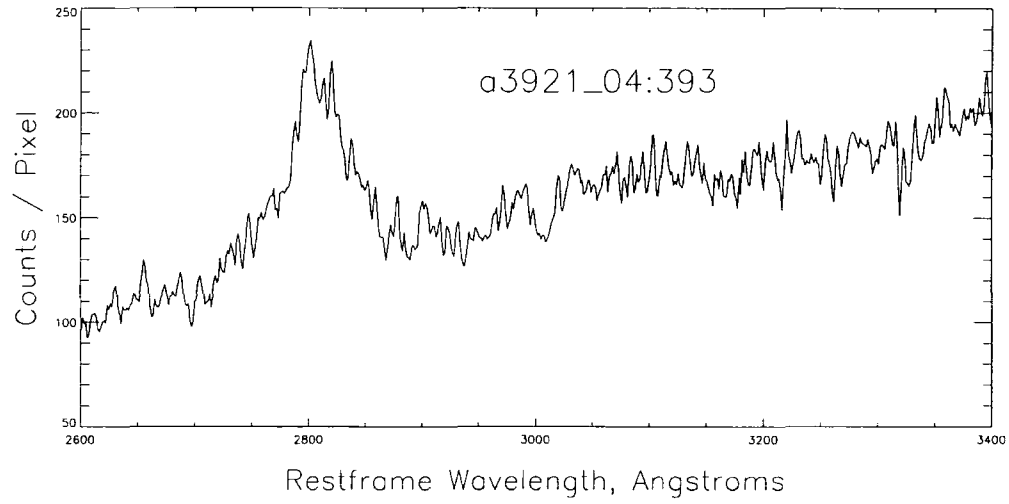

Figure 8.2: The spectrum of the QSO a3921_04:393, de-redshifted to restframe wavelengths.

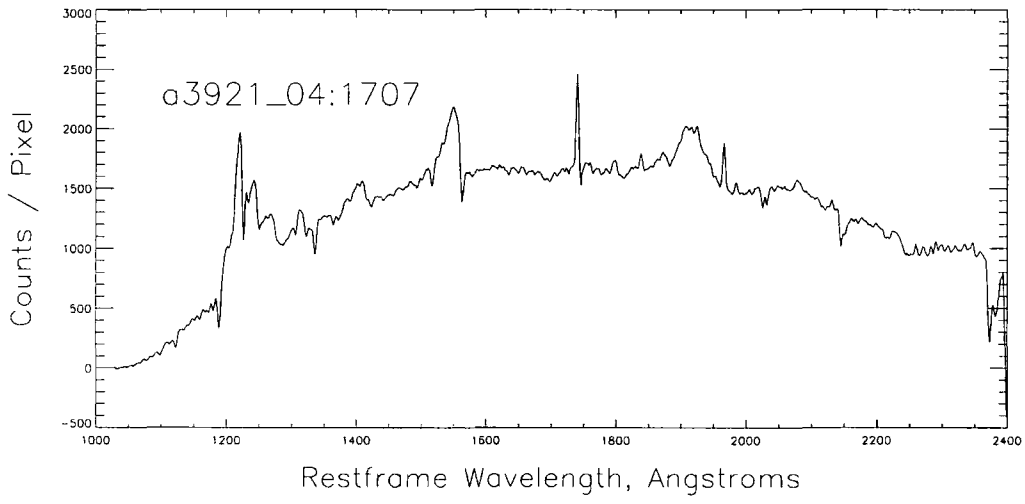

Figure 8.3: The spectrum of the QSO a3921_04:1707, de-redshifted to restframe wavelengths.

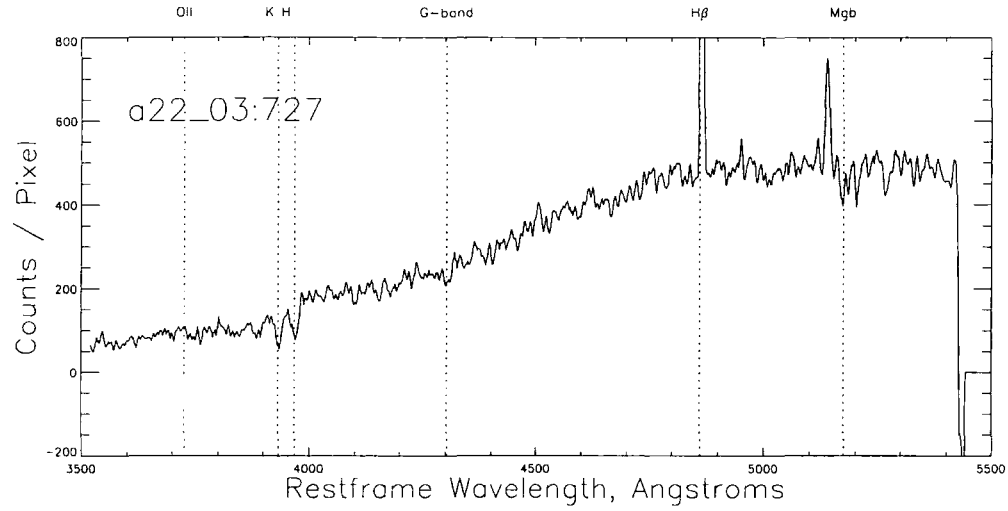

Figure 8.4: The spectrum of the dusty red galaxy in Abell 22, de-redshifted to restframe wavelengths.

The redshift estimation for this galaxy was checked by using the XCSAO and EMSAO tasks. This confirmed the redshift of this object (cz= 43907 $\pm$ 41kms^{-1}; $R_{TDR} > 11.0$) and therefore its status as a bone-fide cluster member. This velocity is 1249kms^{-1} ($1.6\sigma_Z$) greater than the cluster velocity (see Table 6.1). The de-redshifted spectrum for this galaxy is presented in Figure 8.4.

Why should a cluster galaxy exhibit such a red colour? One line of evidence to answer this question lies in the imaging of this galaxy. Figure 8.5 displays the R and B band imaging for this galaxy. Whilst the R-band imaging shows a classical elliptical galaxy with no obvious spiral arms, the B-band exhibits a dust lane across the centre of the galaxy. It is the presence of this dust lane which artificially causes its colour to be redder than the cluster CMR. The 2dF spectroscopy of this galaxy reveals that it is an ordinary, passive (k-type) galaxy with no emission lines.

8.2.3 Tucana

The LCO imaging of Abell 3921 has serendipitously encompassed the Tucana dwarf spheroidal galaxy first reported by Lavery (1990). Figure 8.6 displays the LCO R-band imaging of Tucana. Tucana is flattened and appears morphologically elliptical. Many of the brighter stars are readily resolved. The bright object near the centre of Tucana, however, is thought to be a foreground Galactic star (Lavery & Mighell

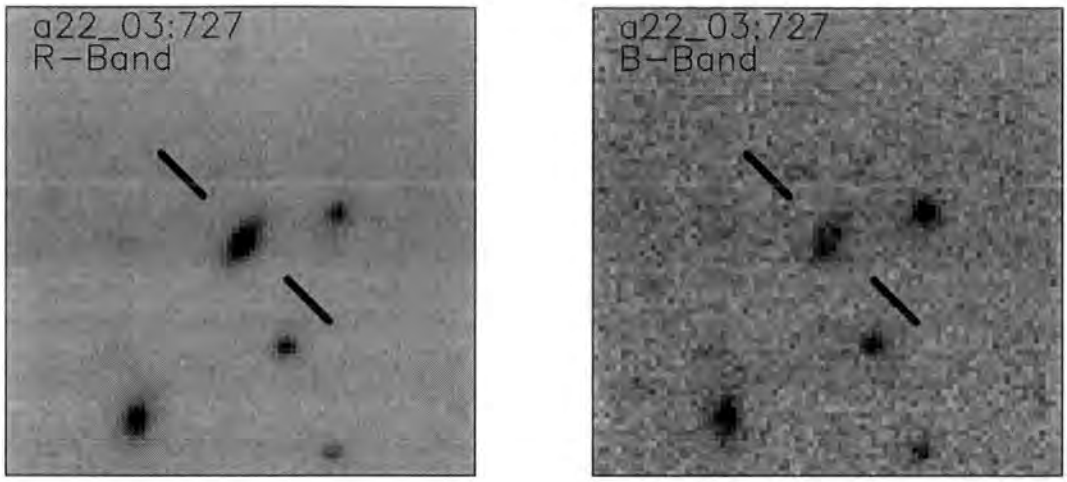

Figure 8.5: R and B-band imaging of the cluster galaxy a22_03:727 (indicated). The boxes are 30″ on the side. Note the dust lane crossing the centre of the galaxy in the B-Band imaging. This dust lane is causing the galaxies colour to be redder than its contemporaries.

1992)

Figure 8.7 shows colour-magnitude diagrams for stars (defined as having $P^* > 0.1$) in the Tucana galaxy and two adjoining sky regions (for comparison). These sky regions are chosen to be the same size on the sky as the Tucana sample and are sufficient for comparison purposes. Following Lavrey and Mighell (1992), these colour-magnitude diagrams are divided up into four smaller regions. For each region on the diagrams, the number of stars in excess of the sky regions is calculated for Tucana's colour-magnitude diagram (the lower right-hand number in Figure 8.7). For stars of $R < 20.5$, there are 10.5 more stars in the equivalent region of Tucana's colour-magnitude diagram than for the sky regions. Assuming poissonian errors, this corresponds to 2.1σ and is therefore not viewed as significant. For the three regions of stars with $R > 20.5$, the excess number of stars associated with Tucana is 2 (1.0σ), 28.5 (6.9σ) and 3 (1.5σ), respectively, for a total excess of 33.5 stars (6.7σ). The colour distribution is consistent with all the stars possessing a colour of $(B - R) = 1.84 \pm 0.12$.

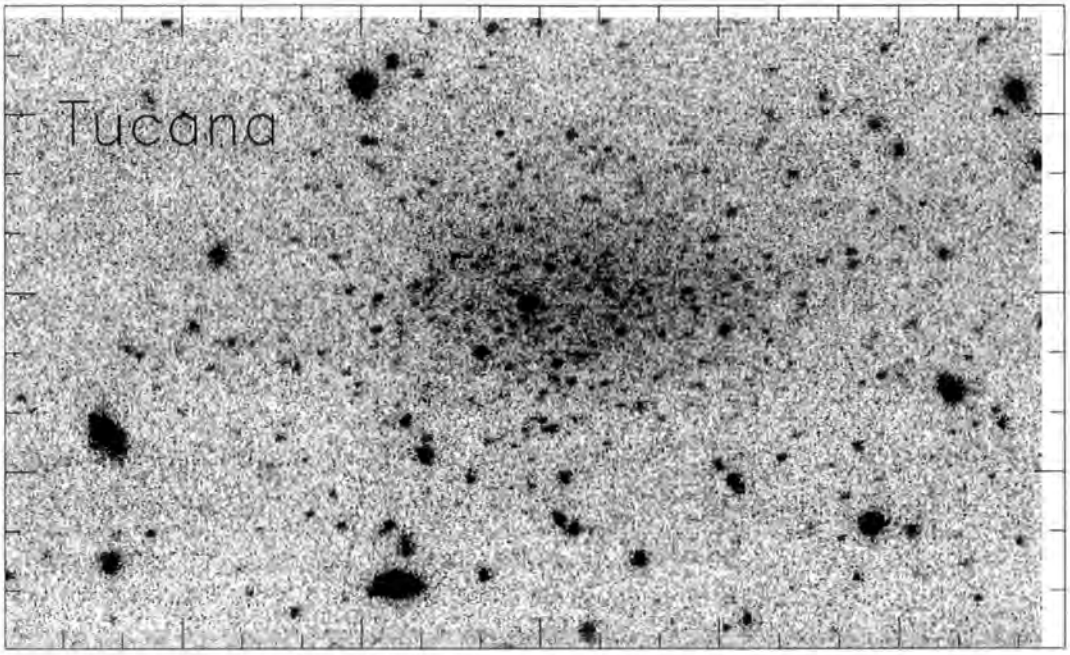

Figure 8.6: The LCO R-band image of the Tucana dwarf spheroidal galaxy. The tick-marks are placed at 20″ intervals. Many of the brighter constituent stars are clearly resolved, although the bright object near to the centre of Tucana may be a foreground Galactic star (Lavery & Mighell 1992).

8.3 Background Clusters

In Chapters 4 and 6 a number of background clusters are identified using colour-magnitude relationships and velocity / spatial distributions respectively.

The local galaxy density parameter presented in Chapter 4 also has potential to define other clusters along the line of sight by selecting galaxies that reside in highly overdense regions. To fully investigate its potential to find background clusters, its distribution across the mosaic observation of Abell 3888 is examined. Abell 3888 is chosen for this analysis as during its data reduction it was noted that the observations contained a number of likely background cluster candidates. Figure 8.8 displays the distribution of the local galaxy density parameter as a function of clustocentric radius in Abell 3888. From this distribution, galaxies over 2 Mpc from the cluster centre and possessing $\log_{10}(\Sigma) > 50$ are now selected to investigate if they constitute other background clusters. The 2 Mpc selection ensures that the selected galaxies are beyond the very cluster core whilst the $log_{10}(\Sigma) = 50$ limit thresholds only those galaxies in high density regimes. The spatial distribution of

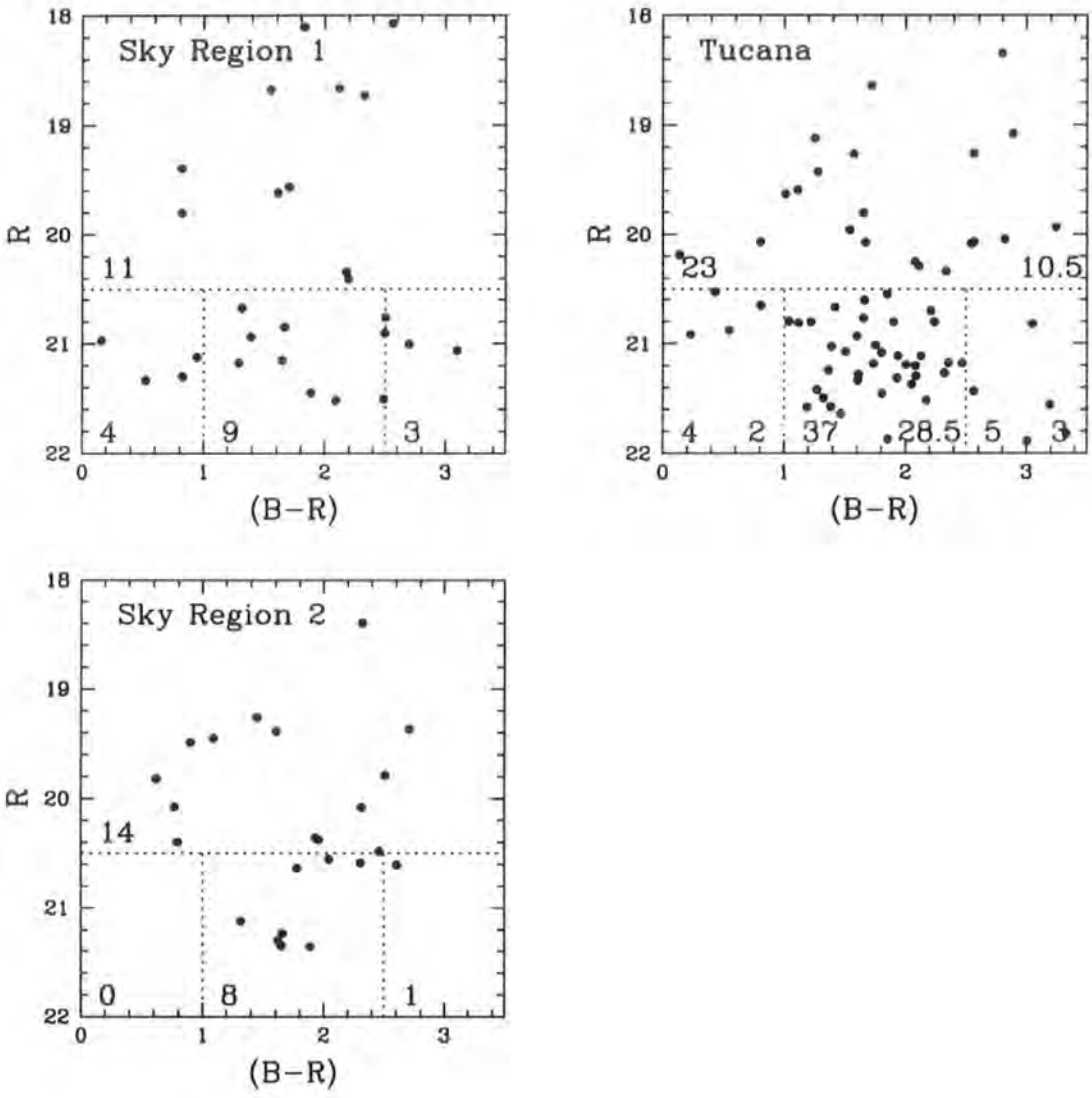

Figure 8.7: The colour magnitude for stars in the Tucana galaxy (Top Right) together with the two nearby sky regions (Top Left and Bottom Left). Each diagram is divided up into four regions. The number in the lower left-hand corner is the total number of stars for that region. For Tucana (Top Right), the number in the lower right-hand corner is the excess number of stars above the nearby sky regions.

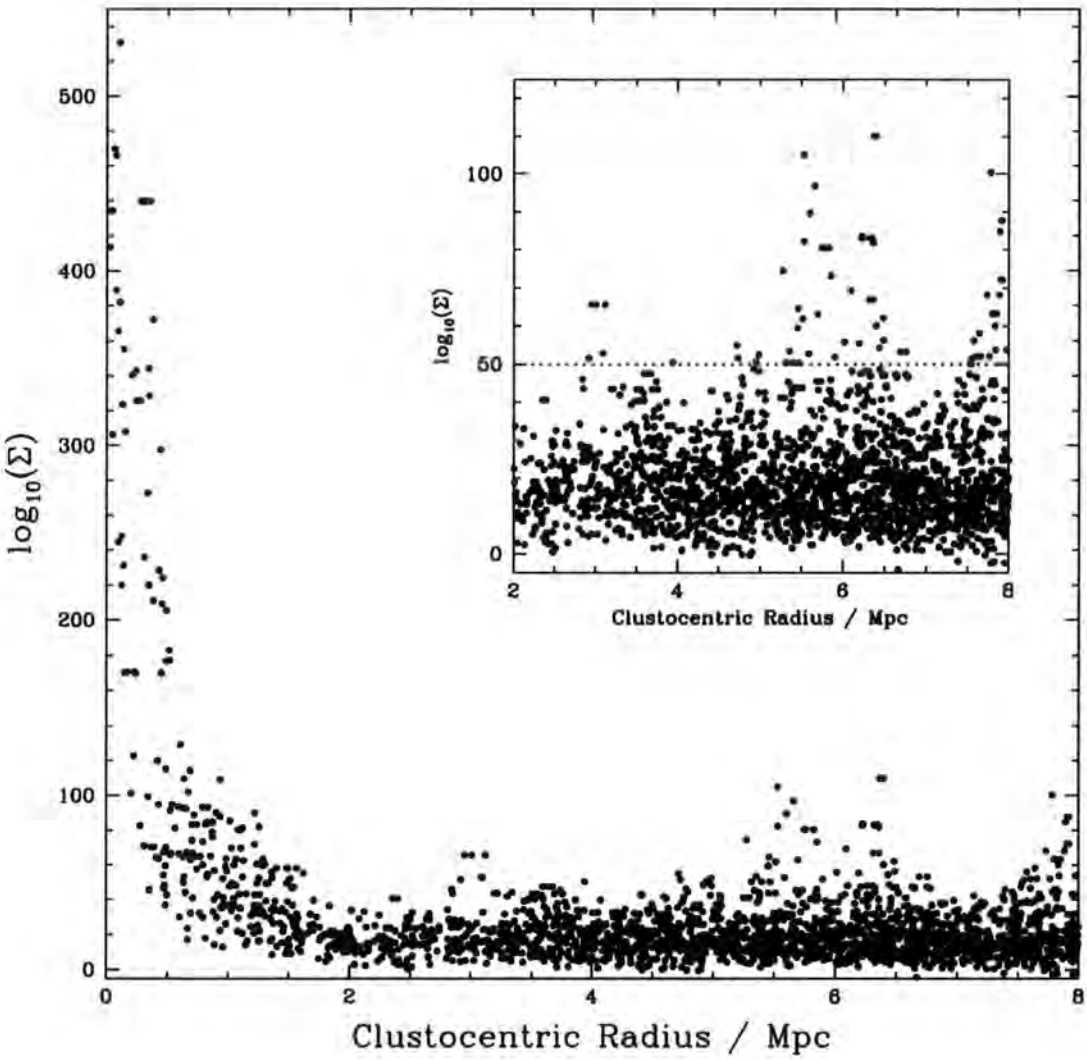

Figure 8.8: The distribution of the local galaxy density parameter, Σ, as a function of clustocentric radius in Abell 3888. The inset panel shows an enlargement of the region outside 2 Mpc. The horizontal dotted line represents the selection function for choosing other galaxy clusters.

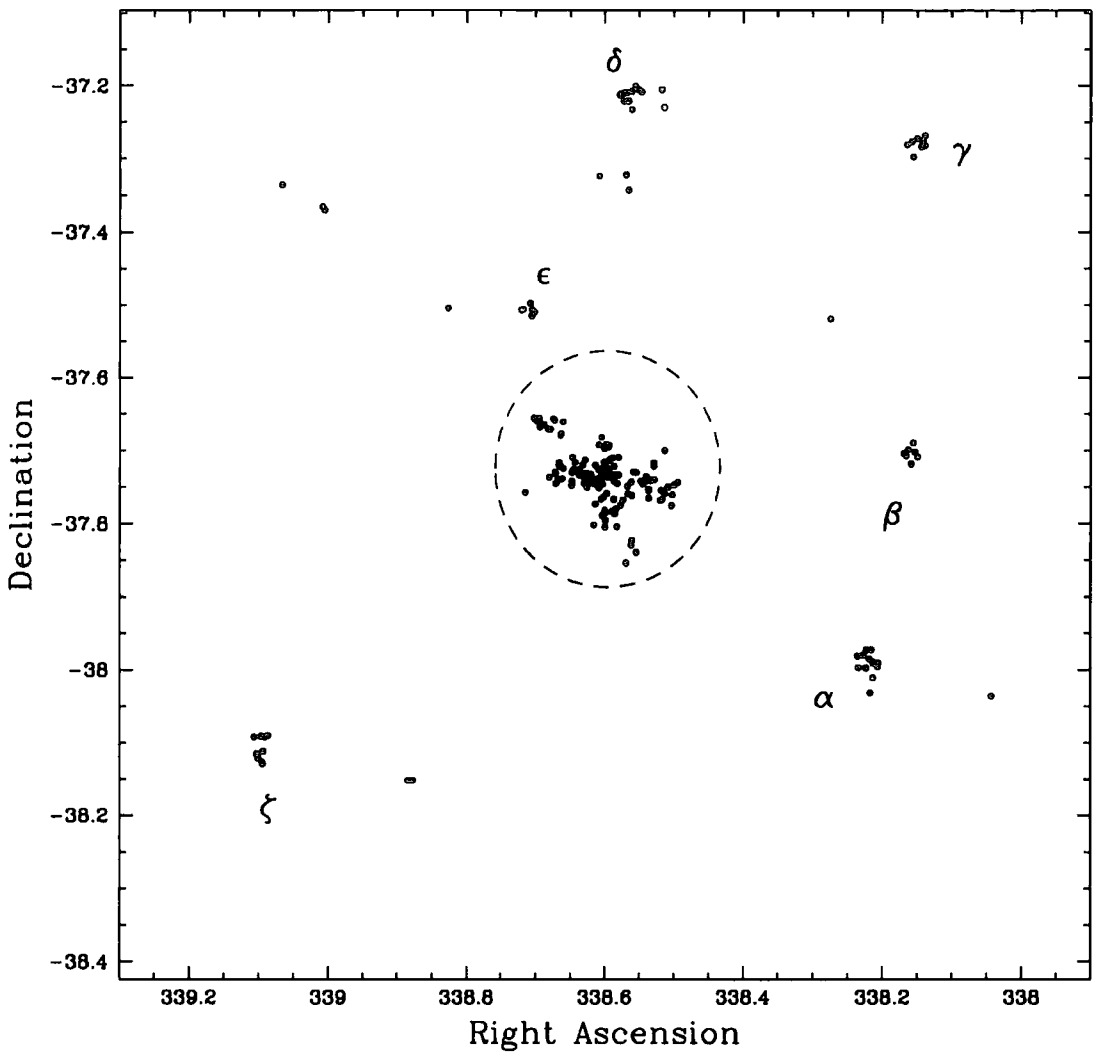

Figure 8.9: The spatial distribution of all galaxies selected in Abell 3888 having $\log_{10}(\Sigma) > 50$. These galaxies are clearly concentrated on the sky. The six obvious concentrations lying beyond 2 Mpc of the cluster core (dashed circle) have been labelled α through ζ.

these selected galaxies is presented in Figure 8.9. Clearly the galaxies selected in this manner are concentrated on the sky. Ignoring the central cluster itself, there are six main concentrations which are now labelled α through ζ (see Figure 8.9).

To examine if these six candidate clusters are bone-fide background clusters a cut of $\pm 1.5'$ is made in the parent catalogue around the central position of the candidates. The candidate clusters are presented in Figure 8.10 whilst the distribution on the colour-magnitude plane of the galaxies in these cuts is presented in Figure 8.11.

Five of the potential background clusters exhibit CMRs: α through ϵ. The presence of a CMR within ζ, however, is not obvious. Using the technique of Yee, Gladders & López-Cruz (1999)* the group CMRs provide a very rough manual estimate of the redshifts for the groups. These redshifts are approximately 21400, 22900, 61600, 33900 and 40100 kms^{-1} for groups α through ϵ. This technique cannot be used on group ζ as it does not exhibit a CMR.

The 2dF observations of Abell 3888 (see Chapter 5) provide a small number of redshifts for several galaxies (numbered in Figure 8.10). These redshifts are presented in Table 8.3. Groups β and ϵ, with multiple redshifts available, show a consistency between their constituent galaxies velocities. The other group candidates have less than 2 redshifts each, rendering any spectroscopic redshift determination insignificant. Note that the consistency between the 2dF observations and the technique of Yee, Gladders & López-Cruz (1999) is reasonable. Further, these estimated velocities correspond well to peaks in the velocity distribution reported by O'Hely (2000). Group α is confidently identified as Abell 3888-A and group γ as Abell 3888-B (see Chapter 6).

In summary therefore, groups α through ϵ are very probably clusters in their own rights (i.e. they exhibit a CMR and possess galaxies at similar redshifts). Group ζ is more than likely a simple projection effect as the distribution on the colour-magnitude plane at bright magnitudes is highly scattered.

*The technique of Yee, Gladders & López-Cruz (1999) involves measuring the $(B-R)$ colour of the CMR at $R = 17.0$, from which the redshift is predicted to be $z = 0.0786(B-R)^2 - 0.115(B-R) + 0.0287$. In this Chapter, the CMR has been fitted manually.

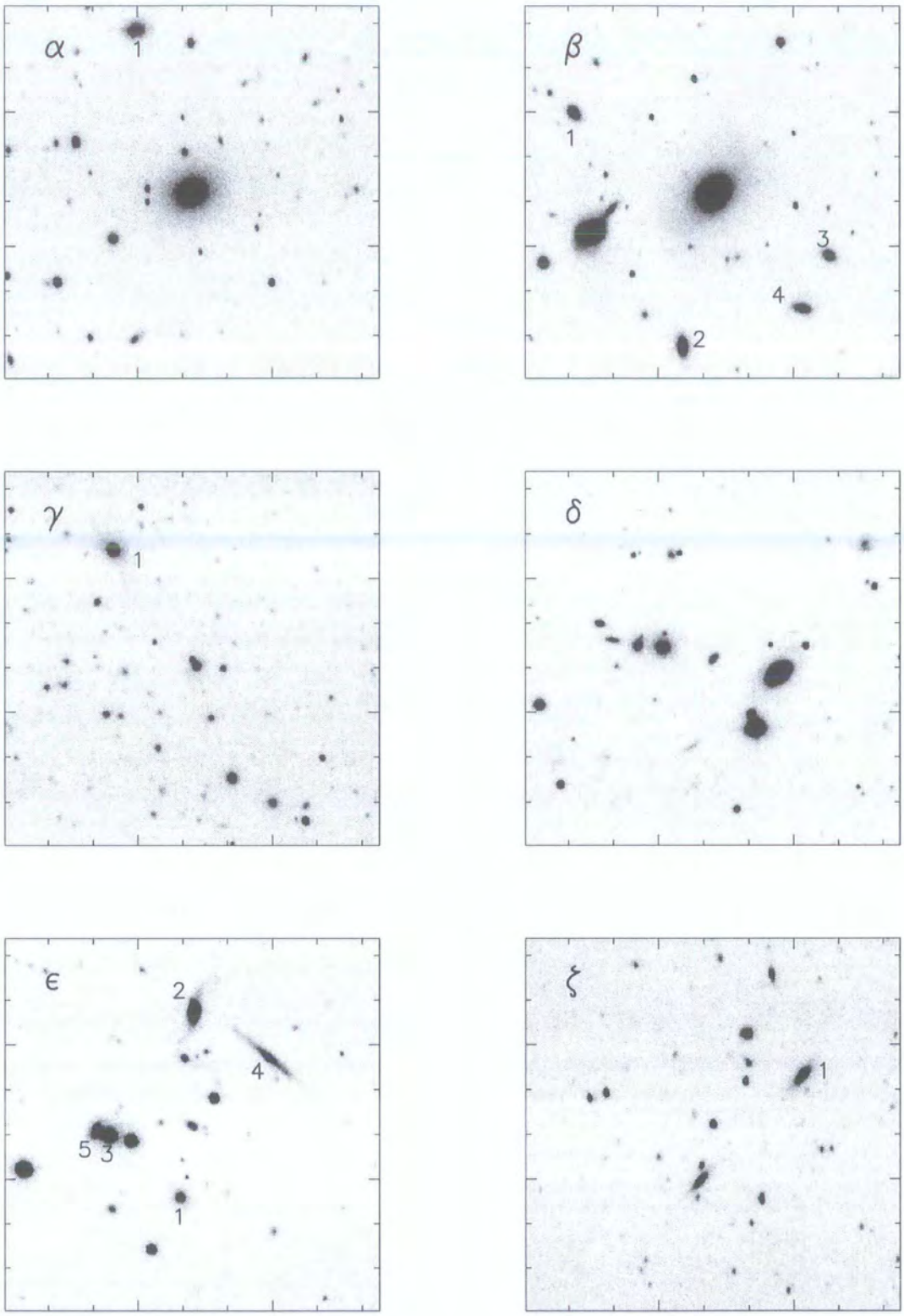

Figure 8.10: R band imaging of the six cluster candidates. Each box is $\sim 3'$ on the side with tickmarks every $20''$. The Greek lettering corresponds to the candidates positions presented in Figure 8.9, whilst the annotated numbering (where present) denotes galaxies which have had 2dF observations made of them (see Table 8.3). Already, some of these candidates appear as if they should be clusters (e.g. group β).

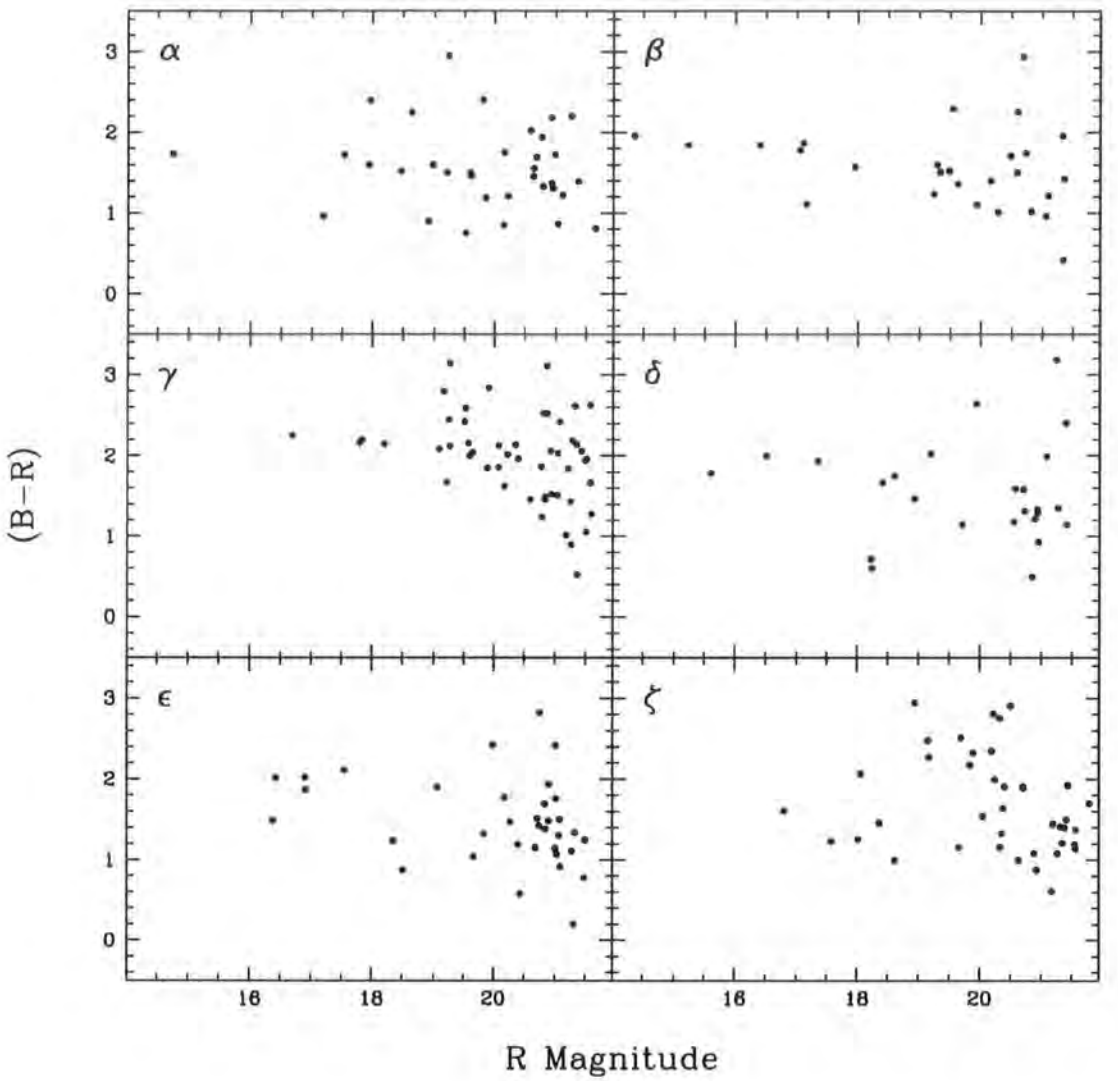

Figure 8.11: Colour-magnitude diagrams for all galaxies pictured in Figure 8.10. Some of the candidates (e.g. group β) present clear CMRs confirming that the overdense regions selected by the local galaxy density parameter are indeed background clusters.

Table 8.3: Redshifts of galaxies contained in the groups. The 'number' column corresponds to galaxies indicated in Figure 8.10.

Group	Number	Redshift (kms^{-1})	Photometric Estimate (kms^{-1})
α	1	22218 ± 34	21400
β	1	25346 ± 116	22900
	2	23370 ± 17	
	3	23978 ± 18	
	4	38478 ± 26	
γ	1	62265 ± 33	61600
ϵ	1	43486 ± 30	40100
	2	42557 ± 37	
	3	41779 ± 28	
	4	40667 ± 36	
	5	41511 ± 30	
ζ	1	17477 ± 17	

8.4 Summary

The LARCS dataset has serendipitously found a number of noteworthy objects briefly comprising three objects with broad emission lines (i.e. QSOs and AGN), a dusty cluster galaxy, the Tucana dwarf spheroidal galaxy and a number of background clusters.

The local galaxy density parameter, Σ, has been used to detect the presence of background clusters. This parameter makes at least a good first order pointer to the presence of background clusters. Further, the technique of Yee, Gladders & López-Cruz (1999) has proved to be able to provide a rough first approximation of the redshifts of these background clusters that is consistent with measured spectroscopic redshifts. Out of six possible background clusters highlighted by Σ in the LCO observations of Abell 3888, five of them are bone-fide clusters in their own right.

Chapter 9 | *Conclusions*

9.1 Summary

The major conclusions and achievements of this work have been highlighted at the end of each individual chapter. Here, these points are briefly summarized:

1. At the beginning of this thesis, a gap in the current observational dataset was highlighted. There was no low redshift survey of clusters of galaxies ($z \sim 0.1$) with which the findings of higher redshift studies (e.g. MORPHS, Dressler et al. 1999; CNOC Yee et al. 1996) could be compared. There was also no survey which fully traced the cluster population out from high density cluster core regions to low density regions where galaxies are infalling to the cluster potential.

   Both of these major niches have now been filled by the unique LARCS project, encompassing 21 clusters in the redshift range $0.07 < z < 0.16$. The radial extent of these observations covers some 10 Mpc at the mean redshift of the survey.

2. The LARCS catalogues are photometrically accurate to better than 0.03 mag and the astrometry to better than $0.3''$. The star-galaxy separation technique results in the low stellar contamination rate of ~ 2 per cent.

3. In comparing to the APM catalogue to assess the accuracy and reliability of the LARCS catalogues, shortcomings of the APM catalogue (and hence the 2dFGRS) have been highlighted. The primary shortcoming is the omission of several classes of galaxy from the APM (Blended, Resolved, Normal and LSB).

4. By developing a statistical method to select cluster members, the fiducial colour of the CMR is found to evolve bluewards with clustocentric radius and local galaxy density: $d(B-R)/dr_p = -0.022 \pm 0.004$ and $d(B-R)/d\log_{10}(\Sigma) = -0.076 \pm 0.009$ respectively. The $T - \Sigma$ relation cannot wholly explain this environmental effect but demonstrates that the CMR consists of a passively evolving population (elliptical and evolved S0 galaxies) plus recent additions (morphologically young S0 and recently star-forming spiral galaxies). Taken together with previous studies, these environmental trends in the colours of galaxies at a fixed luminosity are suggested to reflect differences in the luminosity-weighted ages of the galaxies in different environments. If interpreted purely as a difference in ages and accounting for differences in the morphological mix, then the gradient observed in the sample suggests that the luminosity-weighted ages of the dominant galaxy population within the CMR at 6 Mpc from the cluster core are $\sim$3 Gyrs younger than those residing in the core.

5. The 2dF spectroscopic follow-up observations have now provided redshift and equivalent width measurements for 7 of our clusters. Using these, a mass model has been pursued to provide cluster membership information and the galaxies spectroscopically typed in accordance with the MORPHS scheme. The environmental trends in the colour of the CMR were then confirmed as $d(B-R)/dr_p = -0.016 \pm 0.005$ and $d(B-R)/dlog_{10}(\Sigma) = -0.064 \pm 0.014$; only $\sim 1\sigma$ smaller than for the photometrically determined trends. A radial trend in EW(Hδ) has also been observed.

6. Composite cluster, high-density-field and low-density-field samples have been created and compared to one-another. The composite cluster is dominantly (60 per cent) composed of passive k-type galaxies whilst in the low-density-field this falls to 46 per cent. The fraction of recently star forming galaxies increases from cluster to field whilst the fraction of currently star forming galaxies only weakly increases.

7. A comparison of the two different cluster membership techniques has highlighted the need for spectroscopic observations of galaxies at any given red-

shift: statistically identified cluster galaxies will not necessarily mirror cluster galaxies identified spectroscopically.

8. Several serendipitously discovered objects exist in the LARCS dataset including QSOs, AGN, a dusty cluster galaxy, the Tucana dwarf spheroidal galaxy and several background clusters. The local galaxy density parameter, Σ, has been able to provide a good first order indicator to the presence of any large background cluster.

9.2 Further Directions

Although the LARCS project has obtained (incomplete) spectroscopy on seven of its clusters, the intention was always to obtain 2dF observations on all of the clusters. This aim has been frustrated by adverse weather conditions (Chapter 5; O'Hely 2000) and the allocation of larges amounts of telescope time to the 2dFGRS project. With the termination of the 2dFGRS project imminent*, the probability of the LARCS team gaining telescope time with the 2dF instrument should increase significantly. Further 2dF observations would yield a more complete picture of the LARCS clusters. Creating an artificial $z \sim 0.1$ cluster from even more clusters would increase the signal to noise ratio which would better constrain environmental effects within the clusters (e.g. radial blueing of the CMR).

The LARCS project has gained over 15 ks of time with the *XMM-Newton* X-ray space telescope to observe Abell 2055, 2104 and 3888 and the LARCS team is confident that more will be granted. When these data are delivered and combined the optical observations they will be able to investigate issues such as dynamical evolution within the clusters. Indeed, Zabludoff & Zaritsky (1995) used this approach to discover a subcluster collision had occurred within Abell 754 in the last ~ 1 Gyr. The analysis of their spectroscopic survey of the cluster gave evidence of a bimodal galaxy distribution which was significantly offset from the X-ray emission; consistent with previous cosmological simulations (Evrard, 1990). In addition the number of currently star forming galaxies in Abell 754 suggested that the collision

*Projected completion date of the 2dFGRS project is presently estimated as January 2002. The full public release date of all 250000 objects from this survey is estimated as June 2003.

of the subcluster's ICMs may contribute to the enhancement of star formation rate. Therefore with these XMM observations it will possible to place joint limits on the cluster-cluster merger rate at $z \sim 0.1$ and test the theoretical predictions of this rate made by Lacey & Cole (1993).

Further studies are urgently needed to investigate the properties of galaxies in the lower density environments which connect rich clusters to the surrounding field, particularly at higher redshifts. This region is essential for investigating the impact of environment upon the star formation and morphologies of galaxies. Kodama et al. (2001) have started to accomplish this in their examination of the patulous cluster Cl0939+4713 at $z = 0.41$ but more observations are needed.

9.3 The Future

In the immediate future, two major surveys of the sky are rapidly approaching completion: the 2dFGRS (e.g. Lewis et al. 2002) and the Sloan survey[†] (e.g. York et al. 2000). Both of these surveys will present an unprecedented view of the sky and likely supercede some aspects of the work presented here (e.g. analysis of clusters to large radii).

The LARCS overlap with 2dFGRS (see Chapter 3) should yield further redshifts and complete the LARCS project's planned observations of Abell 22, 1084, 1650 and 1651.

The LARCS catalogues (photometric and spectroscopic), meanwhile, will be made available online through both the University of Durham (UK) and the University of New South Wales (Australia). They will allow astronomers world-wide to make full use of this unique survey of X-ray luminous clusters at $z = 0.1$.

[†]Funding for the creation and distribution of the SDSS Archive has been provided by the Alfred P. Sloan Foundation, the Participating Institutions, the National Aeronautics and Space Administration, the National Science Foundation, the U.S. Department of Energy, the Japanese Monbukagakusho, and the Max Planck Society. The SDSS Web site is http://www.sdss.org/

9.4 Addendum

In January 2002, the 2dFGRS project reached termination. As predicted, the Las Campanas and Anglo-Australian Rich Cluster Survey team were awarded five nights of grey to dark time on the 2dF in May 2002.

Bibliography

Abell, G. O., 1958, ApJS, 3, 211

Abell, G. O., Corwin, H. G., & Olowin, R. P., 1989, ApJS, 70, 1

Abraham, R. G., Smecker-Hane, T. A., Hutchings, J. B., Carlberg, R. G., Yee, H. K. C., Ellingson, E., Morris, S. L., Oke, J. B., Rigler, M., 1996, ApJ, 471, 694.

Abraham R. G., Valdes F., Yee H. K. C., van den Bergh S., 1994, ApJ, 432, 75

Allen, S. W., 1998, MNRAS, 296, 392

Andreon, S., 1998, ApJ, 501, 533

Babul, A., Balogh, L. M., Lewis, G. F., & Poole,G. B., 2001, MNRAS, submitted

Bahcall, N. A., Fan, X., & Cen, R. 1997, ApJL, 485, L53

Bailey, J., Taylor, K., Robertson, G., & Barden, S. 2001, New Astronomy Review, 45, 41

Balogh, M. L., Morris, S. L., Yee, H. K. C., Carlberg, R. G., Ellingson, E., 1997, ApJL, 488, L75

Balogh, M. L., Schade, D., Morris, S. L., Yee, H. K. C., Carlberg, R. G., Ellingson, E., 1998, ApJL, 504, L75

Balogh, M. L., Morris, S. L., Yee, H. K. C., Carlberg, R. G., Ellingson, E., 1999, ApJ, 527, 54

Balogh, M. L. & Morris, S. L., 2000, MNRAS, 318, 703

Balogh, M. L., Navarro, J. F. & Morris, S. L., 2000, ApJ, 540, 113

Bardelli S., Zucca E., Zamorani G., Vettolani G., Scaramella R., 1998, MNRAS, 296, 599

Barnes, J. E. & Hernquist, L. E., 1991, ApJL, 370, L65

Bautz, L. P. & Morgan, W. W., 1970, ApJL, 162, L149

Beers, T. C., Flynn, K., & Gebhardt, K., 1990, AJ, 100, 32

Beers, T. C. & Tonry, J. L. 1986, ApJ, 300, 557

Bekki, K., Couch, W. J., & Shioya, Y., 2001, PASJ, 53, 395

Bertin E. & Arnouts S., 1996, A&AS, 117, 393

Binney, J. & Tremaine, S. 1987, Princeton, NJ, Princeton University Press, 1987

Blakeslee, J. P., Metzger, M. R., Kuntschner, H., & Côté, P., 2001, AJ, 121, 1

Bohringer, H. et al. 1998, The Messenger, 94, 21

Bower, R. G., Lucey, J. R. & Ellis, R. S., 1992, MNRAS, 254, 601

Bower, R. G., Kodama, T., & Terlevich, A., 1998, MNRAS, 299, 1193

Boyle, B. J., Shanks, T., Croom, S. M., Smith, R. J., Miller, L., Loaring, N., & Heymans, C., 2000, MNRAS, 317, 1014

Bruzual A., G. & Charlot, S., 1993, ApJ, 405, 538

Butcher, H. & Oemler, A., 1978, ApJ, 226, 559

Butcher, H. & Oemler, A., 1984, ApJ, 285, 426

Byrd, G. & Valtonen, M., 1990, ApJ, 350, 89

Caldwell, N. & Rose, J. A., 1997, AJ, 113, 492

Carlberg, R. G., Yee, H. K. C., Ellingson, E., Abraham, R., Gravel, P., Morris, S., & Pritchet, C. J., 1996, ApJ, 462, 32

Carlberg, R. G., Yee, H. K. C., & Ellingson, E., 1997, ApJ, 478, 462

Carlberg, R. G., Yee, H. K. C., Morris, S. L., Lin, H., Hall, P. B., Patton, D. R., Sawicki, M., & Shepherd, C. W., 2001, ApJ, 552, 427

Cole, S., et al., 2001, MNRAS, 326, 255

Cole, S., Lacey, C. G., Baugh, C. M., & Frenk, C. S., 2000, MNRAS, 319, 168

Colless, M. & Dunn, A., 1995, PASA, 12, 122

Colless, M. M. et al., 2001, MNRAS, in press.

Colless M., 1998, Wide Field Surveys in Cosmology, 14th IAP meeting held May 26-30, 1998, Paris. Publisher: Editions Frontieres. ISBN: 2-8 6332-241-9, p. 77

Colless M., 1989, MNRAS, 237, 799

Colless, M. M. (1987, Ph.D. Thesis, University of Cambridge)

Couch, W. J. & Newell, E. B., 1984, ApJS, 56, 143

Couch, W. J. & Sharples, R. M., 1987, MNRAS, 229, 423

Couch, W. J., Ellis, R. S., Sharples, R. M., Smail, I., 1994, ApJ, 430, 121

Couch, W. J., Barger, A. J., Smail, I., Ellis, R. S., Sharples, R. M., 1998, ApJ, 497, 188

Cross, N., et al., 2001, MNRAS, 324, 825

Dalton, G. B., Efstathiou, G., Maddox, S. J., & Sutherland, W. J., 1994, MNRAS, 269, 151

Danese, L., de Zotti, G., & di Tullio, G., 1980, A&A, 82, 322

Dekel, A. & Silk, J., 1986, ApJ, 303, 39

de Grandi, S., et al., 1999, ApJ, 514, 148

de Propris, R., Eisenhardt, P. R., Stanford, S. A., & Dickinson, M. 1998, ApJL, 503, L45

de Vaucouleurs, G., 1961a, AJ, 66, 629

de Vaucouleurs, G., 1961b, ApJS, 6, 213

de Vaucouleurs, G., de Vaucouleurs, A., Corwin, H. G., Buta, R. J., Paturel, G., & Fouque, P. 1991, Volume 1-3, XII, 2069 pp. 7 figs.. Springer-Verlag Berlin Heidelberg New York

Diaferio, A., Kauffmann, G., Balogh, M. L., White, S. D. M., Schade, D., & Ellingson, E., 2001, MNRAS, 323, 999

Dressler, A., 1980, ApJ, 236, 351

Dressler, A. & Gunn, J. E., 1983, ApJ, 270, 7

Dressler, A., 1984, ApJ, 281, 512

Dressler, A., Thompson, I. B., & Shectman, S. A., 1985, ApJ, 288, 481

Dressler, A. & Shectman, S. A., 1988, AJ, 95, 985

Dressler, A. & Gunn, J. E., 1992, ApJS, 78, 1

Dressler, A., Oemler, A. J., Butcher, H. R., Gunn, J. E., 1994, ApJ, 430, 107

Dressler, A., Oemler, A. J., Couch, W. J., Smail, I., Ellis, R. S., Barger, A., Butcher, H., Poggianti, B. M., Sharples, R. M., 1997, ApJ, 490, 577

Dressler, A., Smail, I., Poggianti, B. M., Butcher, H., Couch, W. J., Ellis, R. S., Oemler, A. J., 1999, ApJS, 122, 51

Drinkwater M. J., Phillipps S., Gregg M. D., Parker Q. A., Smith R. M., Davies J. I., Jones J. B., Sadler E. M., 1999, ApJL, 511, L97

Ebeling, H., Mendes de Oliveira, C., & White, D. A., 1995, MNRAS, 277, 1006

Ebeling H., Voges W., Bohringer H., Edge A. C., Huchra J. P., Briel U. G., 1996, MNRAS, 281, 799 (XBACs)

Ebeling, H., Edge, A. C., Bohringer, H., Allen, S. W., Crawford, C. S., Fabian, A. C., Voges, W., & Huchra, J. P. 1998, MNRAS, 301, 881

Edge, A. C. & Stewart, G. C. 1991, MNRAS, 252, 414

Ellingson, E., Lin, H., Yee, H. K. C., Carlberg, R. G., 2001, ApJ, 547, 609

Ellis, R. S., Smail, I., Dressler, A., Couch, W. J., Oemler, A. J., Butcher, H. & Sharples, R. M., 1997, ApJ, 483, 582

Evrard, A. E., 1990, ApJ, 363, 349

Fasano, G. & Franceschini, A., 1987, MNRAS, 225, 155

Folkes, S., et al., 1999, MNRAS, 308, 459. (also see http://www.mso.anu.edu.au/2dFGRS/)

Franx, M., 1993, PASP, 105, 1058

Fujita, Y., 1998, ApJ, 509, 587

Fukugita, M., Shimasaku, K., & Ichikawa, T., 1995, PASP, 107, 945

Ghigna, S., Moore, B., Governato, F., Lake, G., Quinn, T., Stadel, J., 1998, MNRAS, 300, 146

Giommi, P. et al. 1991, ApJ, 378, 77

Glazebrook K., Peacock J. A., Collins, C. A., Miller L., 1994, MNRAS, 266, 65 (G94)

Gott, J. R. & Thuan, T. X., 1976, ApJ, 204, 649

Gunn, J. E. & Gott, J. R. I., 1972, ApJ, 176, 1

Hubble, E. P., 1925, The Observatory, 48, 139

Hubble, E. P., 1936, "Realm of the Nebulae", Yale University Press

Hubble, E. & Humason, M. L., 1931, ApJ, 74, 43

Huchra, J. & Burg, R., 1992, ApJ, 393, 90

Jones, L. A. & Couch, W. J., 1998, PASA, 15, 309

Jones, C. & Forman, W., 1984, ApJ, 276, 38

Jones, C. & Forman, W., 1992, NATO ASIC Proc. 366, "Clusters and Superclusters of Galaxies", 49

Jones, L. A. & Worthey, G. 1995, ApJL, 446, L31

Kaiser, N., 1984, ApJL, 284, L9

Kant, I., 1755, "Allgemeine Naturgeschichte und Theorir des Himmels"

Katgert, P., et al., 1996, VizieR On-line Data Catalog: J/A+A/310/8. Originally published in: 1996, A&A, 310, 8

Kibblewhite E., Bridgeland M., Bunclark P., Cawson M., Irwin M., 1984, IAU Colloq. 78: Astronomy with Schmidt-Type Telescopes, 89

King, C. R. & Ellis, R. S., 1985, ApJ, 288, 456

Kodama, T. & Arimoto, N., 1997, A&A, 320, 41

Kodama, T., Bower, R. G., Bell, E.F., 1999, MNRAS, 306, 561

Kodama, T. & Bower, R. G., 2001, MNRAS, 321, 18

Kodama, T. & Smail, I., 2001, MNRAS, 326, 637

Kodama, T., Smail, I., Nakata, F., Okamura, S., & Bower, R. G., 2001, ApJL, in press

Kormendy, J. & Bender, R., 1996, ApJL, 464, L119

Kurtz, M. J., Mink, D. J., Wyatt, W. F., Fabricant, D. G., Torres, G., Kriss, G. A., & Tonry, J. L., 1992, ASP Conf. Ser. 25: Astronomical Data Analysis Software and Systems I, 1, 432

Lacey, C. & Cole, S., 1993, MNRAS, 262, 627

Lavery, R. J., 1990, IAU circ., 5139, 2

Lavery, R. J. & Mighell, K. J., 1992, AJ, 103, 81

Landolt A. U., 1992, AJ, 104, 372

Larson, R. B., Tinsley, B. M., & Caldwell, C. N., 1980, ApJ, 237, 692

Lewis, I. J., et al., 2002, MNRAS, in press

Lubin, L. M., Postman, M., Oke, J. B., Ratnatunga, K. U., Gunn, J. E., Hoessel, J. G., & Schneider, D. P., 1998, AJ, 116, 584

Lumsden, S. L., Nichol, R. C., Collins, C. A., & Guzzo, L. 1992, MNRAS, 258, 1

MacGillivray H.T. & Stobie R.S., 1984, Vistas in Astronomy, 27, 433

Maddox S., et al., 1998, Large Scale Structure: Tracks and Traces, 91

Maddox S. J., Efstathiou G., Sutherland W. J., Loveday J., 1990a, MNRAS, 243, 692. (also see http://www.ast.cam.ac.uk/~apmcat/)

Maddox S. J., Efstathiou G., Sutherland W. J., 1990b, MNRAS, 246, 433

Marshall, H. L., Fruscione, A., & Carone, T. E., 1995, ApJ, 439, 90

Metcalfe, N., Shanks, T., Fong, R., & Jones, L. R., 1991, MNRAS, 249, 498

Metcalfe N., Fong R., Shanks T., 1995, MNRAS, 274, 769

Mink, D. J. & Wyatt, W. F., 1995, ASP Conf. Ser. 77: Astronomical Data Analysis Software and Systems IV, 4, 496

Monet, D., 1996, American Astronomical Society Meeting, 188, 5404

Moore, B., Katz, N., Lake, G., Dressler, A., Oemler, A., 1996, Nature, 379, 613

Morris, S. L., Hutchings, J. B., Carlberg, R. G., Yee, H. K. C., Ellingson, E., Balogh, M. L., Abraham, R. G., Smecker-Hane, T. A., 1998, ApJ, 507, 84

Norberg, P., et al., 2001, MNRAS, 328, 64

Oemler, A., 1974, ApJ, 194, 1

Oemler, A., 1992, "Clusters and Superclusters of Galaxies", 29

O'Hely, E. (2000, Ph.D. Thesis "Bridging the gap", University of New South Wales)

O'Hely, E., Couch, W. J., Smail, I., Edge, A. C., Zabludoff, A. I., 1998, PASA, 15, 3, 273

Pimbblet, K. A., Smail, I., Edge, A. C., Couch, W. J., O'Hely, E., Zabludoff, A. I., 2001, MNRAS, 327, 588

Pimbblet, K. A., Smail, I., Kodama, T., Couch, W. J., Edge, A. C., Zabludoff, A. I., O'Hely, E., 2002, MNRAS, 331, 333

Pinkney, J., Roettiger, K., Burns, J. O., & Bird, C. M., 1996, ApJS, 104, 1

Poggianti, B. M., Smail, I., Dressler, A., Couch, W. J., Barger, A. J., Butcher, H., Ellis, R. S., & Oemler, A. J., 1999, ApJ, 518, 576

Quilis, V., Moore, B., & Bower, R., 2000, Science, 288, 1617

Rakos, K. D. & Schombert, J. M., 1995, ApJ, 439, 47

Reid I. N., Yan L., Majewski S., Thompson I., Smail I., 1996, AJ, 112, 1472

Roberts, M. S. & Haynes, M. P. 1994, ARA&A, 32, 115

Rood, H. J. (1965, Ph.D. Thesis, University of Michigan)

Rood, H. J. & Sastry, G. N., 1971, PASJ, 83, 313

Sandage, A., 1961, "The Hubble Atlas of Galaxies", Washington, D.C., Carnegie Institution of Washington

Sandage, A., Freeman, K. C., & Stokes, N. R., 1970, ApJ, 160, 831

Sarazin, C. L., 1988, "X-ray Emission from Clusters of Galaxies", Cambridge Astrophysics Series, CUP

Schlegel D. J., Finkbeiner D. P., Davis M., 1998, ApJ, 500, 525

Searle, L., Sargent, W. L. W., & Bagnuolo, W. G., 1973, ApJ, 179, 427

Shectman, S. A., Landy, S. D., Oemler, A., Tucker, D. L., Lin, H., Kirshner, R. P., Schechter, P. L., 1996, ApJ, 470, 172

Silk, J., 1985, ApJ, 297, 1

Smail, I. (1993, Ph.D. Thesis, University of Durham)

Smail, I., Dressler, A., Couch, W. J., Ellis, R. S., Oemler, A. J., Butcher, H., Sharples, R. M., 1997, ApJS, 110, 213

Smail, I., Edge, A. C., Ellis, R. S., Blandford, R. D., 1998, MNRAS, 293, 124-144

Smail, I., Kuntschner, H., Kodama, T., Smith, G. P., Packham, C., Fruchter, A. S. & Hook, R. N., 2001, MNRAS, 323, 839-849

Struble, M. F. & Rood, H. J., 1991, ApJS, 77, 363

Terlevich, A. (1998, Ph.D. Thesis, University of Durham)

Terlevich, A. I., Kuntschner, H., Bower, R. G., Caldwell, N., & Sharples, R. M., 1999, MNRAS, 310, 445

Terlevich, A. I., Caldwell, N., Bower, R. G., 2001, MNRAS, 326, 1547

Tonry, J. & Davis, M. 1979, AJ, 84, 1511

Toomre, A. & Toomre, J., 1972, ApJ, 178, 623

Toomre, A., 1978, IAU Symp. 79, "Large Scale Structures in the Universe", 79, 109

Treu, T., Stiavelli, M., Casertano, S., Møller, P., & Bertin, G. 1999, MNRAS, 308, 1037

van Dokkum, P. G., Franx, M., Fabricant, D., Illingworth, G. D., & Kelson, D. D., 2000, ApJ, 541, 95

van Dokkum, P. G., Franx, M., Illingworth, G. D., Kelson, D. D., Fisher, D., Fabricant, D., 1998, ApJ, 500, 714

Visvanathan, N., & Sandage, A., 1977, ApJ, 216, 214

Whitmore, B. C., Gilmore, D. M., & Jones, C., 1993, ApJ, 407, 489

Whitmore, B. C. & Gilmore, D. M., 1991, ApJ, 367, 64

Wolf, R., 1865, Astron. Nach., 65, 1

Wright, T., 1750, "An Original Theory of New Hypothesis of the Universe", London

Yahil, A. & Vidal, N. V., 1977, ApJ, 214, 347

Yee, H. K. C., Gladders, M. D., & López-Cruz, O. 1999, ASP Conf. Ser. 191: Photometric Redshifts and the Detection of High Redshift Galaxies, 166

Yee, H. K. C., Ellingson, E., Carlberg, R. G., 1996, ApJS, 102, 269

York, D. G., et al. 2000, AJ, 120, 1579

Zabludoff, A. I., Huchra, J. P., & Geller, M. J., 1990, ApJS, 74, 1

Zabludoff, A. I. & Zaritsky, D., 1995, ApJL, 447, L21

Zabludoff, A. I., Zaritsky, D., Lin, H., Tucker, D., Hashimoto, Y., Shectman, S. A., Oemler, A., Kirshner, R. P., 1996, ApJ, 466, 104

Zwicky, F., 1957, PASA, 69, 518

Appendix A | *The G94 Technique*

As some of the individual LARCS observations were made in non-photometric conditions it was necessary to independently calibrate such pointings. The technique of Glazebrook et al. (G94; 1994) has been applied to all of the clusters to optimally employ magnitude offset information across their entire mosaic. Here the G94 technique is described in detail.

A.1 Magnitude Offsets and the Overlap Function

For each LARCS cluster, there are 21 individual pointings which make up a cross-shaped mosaic as illustrated by Figure 2.2. The design of these mosaics is such that each pointing overlaps with its neighbours by 44 arcsec; making 32 overlap regions. The photometry of sources appearing in the inter-pointing overlap regions is used to determine the median magnitude offset between the non-photometric and photometric pointings in each passband. Only those sources which are unsaturated, not heavily blended or close to the chip's edge are used to obtain these values.

Therefore, for the n pointings*, of which $(1, \ldots m)$ are non-photometric and $(m+1, \ldots n)$ are photometric, the magnitude offset between pointings i and j is:

$$\Delta_{ij} =< Mag_i - Mag_j >_{pairs} \tag{A.1}$$

where $\Delta_{ij} \equiv -\Delta_{ji}$. Now, let a_i be the floating zeropoint of pointing i such that $a_i = 0$ if $i > m$.

*The variable n is used here as there are a small number of LARCS clusters where $n \neq 21$; e.g. Abell 3888 is missing two R-band mosaic tiles thus making $n = 19$; see Table 2.3 for the complete log of LARCS observations.

The overlap function, Θ_{ij}, is then defined as:

$$\Theta_{ij} = \begin{cases} = 1 & \text{if pointings } i \text{ and } j \text{ overlap} \\ = 0 & \text{if there is no overlap} \\ = 1 & \text{if } i = j \end{cases} \quad (A.2)$$

A.2 Minimization by Matrix Inversion

Since the non-photometric zeropoints are all defined to be variable parameters, the least squares solution for them can be found by minimizing the magnitude offsets residuals generated in Equation A.1 using a matrix inversion approach. The sum of the squares to be minimized is:

$$\Psi = \sum_{i=1}^{n} \sum_{j=1}^{n} w_{ij} \Theta_{ij} (\Delta_{ij} + a_i - a_j)^2 \quad (A.3)$$

where Θ_{ij} is the overlap function (Equation A.2) and w_{ij} are weightings used for each i, j pair. Potentially, w_{ij} could be set to the errors on each Δ_{ij} value, but this is found to make insignificant difference to the case that LARCS uses where all w_{ij} values are set to unity.

One proceeds by differentiating Ψ (Equation A.3) with respect to a_i to obtain the matrix equation:

$$\sum_{j=1}^{m} A_{ij} a_j = b_i \quad (A.4)$$

where:

$$A_{ij} = w_{ij} \Theta_{ij} - \delta_{ij} \sum_{k=1}^{n} w_{jk} \Theta_{jk}$$

and

$$b_i = \sum_{j=1}^{n} w_{ij} \Theta_{ij} \Delta_{ij}$$

thus giving the single step solution for a_i. Note: the δ_{ij} term is simply a classical delta function.

An inherent advantageous feature of this technique is that if some of the pointings are non-contiguous (owing to mis-observations) it does not matter. Indeed,

taken to the extreme case (only seen in Abell 644) where there are two discontinuous areas of the mosaic, the matrix becomes block diagonal and two independent solutions are generated. In Abell 644, luckily, there are photometric pointings in each discontinuous area. If there had not, the matrix would have become singular and inversion impossible.

A.3 Errors

For the solution found above, the overall rms residual, ε, is:

$$\varepsilon = \frac{\sum_{i=1}^{n}\sum_{j=1}^{n} w_{ij}\Theta_{ij}(\Delta_{ij} + a_j - a_i)^2}{\sum_{i=1}^{n}\sum_{j=1}^{n} w_{ij}\Theta_{ij}} \tag{A.5}$$

and the magnitude rms residual on each pointing from different overlaps is:

$$\mathrm{rms}_i = \frac{\sum_{j=1}^{n} w_{ij}\Theta_{ij}(\Delta_{ij} + a_j - a_i)^2}{\sum_{j=1}^{n} w_{ij}\Theta_{ij}} \tag{A.6}$$

Typically, the rms residuals are found to be low; < 0.01 mag (e.g. see Figures 2.5 and 2.6).

Appendix B | *Statistical Correction*

B.1 The Statistical Correction Technique

To examine the cluster galaxy population in the absence of spectroscopy, it is necessary to statistically subtract the field population from a given cluster plus field population. Typically, to obtain the cluster population one subtracts off an area and density-scaled portion of the defined field population, $F_{\rm pop}$, from the defined cluster plus field population, $C + F_{\rm pop}$. Both the $F_{\rm pop}$ and the $C + F_{\rm pop}$ are then binned onto a sensibly (say, steps of 0.5 in magnitude and 0.2 in $(B - R)$ colour) gridded colour-magnitude diagram. A straight forward subtraction is then performed to calculate the probability of a galaxy in a given colour-magnitude grid position of being a field galaxy. Thus:

$$P(\mathrm{Field})_{\rm col,mag} = \frac{\mathrm{N(Field)_{col,mag}} \times \mathrm{A}}{\mathrm{N(Cluster + Field)_{col,mag}}} \qquad \text{(B.1)}$$

where A is an area- and density-dependant scaling factor. For each galaxy in $C + F_{\rm pop}$, one proceeds by generating a random number between 0.0 and 1.0 and compare it to the galaxies' value of $P(\mathrm{Field})_{\rm col,mag}$ in order to determine if the given galaxy should be in the resultant cluster population. Problems in this method occur when directly subtracting the populations on the color-magnitude plane produces a negative number of galaxies in the cluster population, $C_{\rm popn}$, for a particular grid position. A resultant $P(\mathrm{Field})_{\rm col,mag}$ can thus be greater than 1.0. Therefore to utilize a background subtraction method to analyze a cluster population in the absence of spectroscopy, it is necessary to solve this "negative galaxy" problem. A typical method is to normalize all of the probabilities to the largest value of $P(\mathrm{Field})_{\rm col,mag}$. Clearly such a solution has drawbacks as the resultant $P(\mathrm{Field})_{\rm col,mag}$ distribution no longer reflects the appropriately scaled input data and has actually been scaled

away from it's true value in many locations on the color-magnitude plane for the sake of one (or a few) anomalously low counts in $C + F_{\rm pop}$ for a particular grid position.

The method adopted in this study is similar to that used by Smail et al. (1998) and Kodama & Bower (2001, KB01). If, when gridding up the colour-magnitude diagrams, one produces a negative galaxy in the computation of $P(\mathrm{Field})_{\rm col,mag}$, this is solved by increasing the grid size *for that particular grid position.* Thus the grid position (mag, col) is increased to include it nearest neighbours (col : col + 1, mag : mag + 1) and then $P(\mathrm{Field})_{\rm col,mag}$ is recalculated using this new 2×2 grid. If this is not enough to cure the negative galaxy problem, we increase the grid size for that particular grid position by one further step to (col − 1 : col + 1, mag − 1 : mag + 1) and so on until the field-corrected galaxy count exceeds zero.

B.2 Comparison to Other Works

In Figure B.1 the resultant $P(\mathrm{Field})_{\rm col,mag}$ distribution using this method and KB01 is compared. The grid position (3, 2) has a fluctuation in $C + F_{\rm pop}$ so that the number of galaxies in the corresponding grid position in $F_{\rm pop}$ makes the resultant $P(\mathrm{Field})_{3,2} > 1.0$. By normalizing to the anomalous value, *all* the rest of the probabilities are reduced from their original values and one is still left with a high probability at the original grid position. The KB01 method subtracts the excess probability (in this case 0.2) and distributes it evenly between its neighbours, making the original grid position $P(\mathrm{Field})_{3,2} = 1.0$. Using the new method, grid positions (3 : 4, 2 : 3) are resampled to make one new, larger grid position and calculate the new probability for this.

It is found that the negative galaxy problem exists in all clusters examined in this study. The number of grid-expansions required to cure the problem are typically around ten 2×2 expansions and a small number of larger order expansions. The expansions are typically situated away from the CMR, preferentially where the $C + F_{\rm pop}$ is sparse.

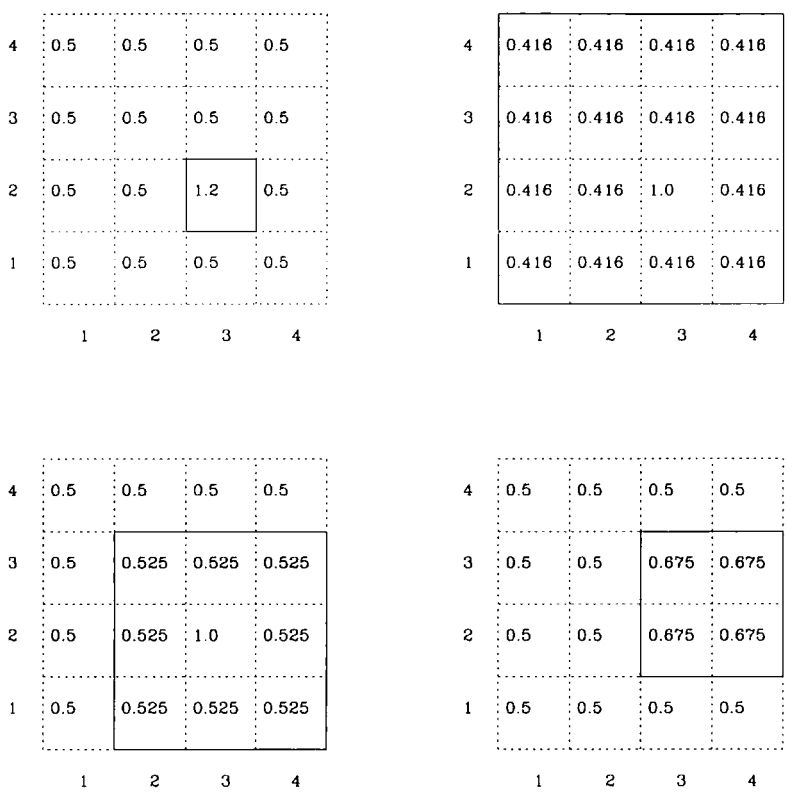

Figure B.1: A comparison of the statistical correction methods on the colour-magnitude plane. The galaxies have been binned into a colour-magnitude grid and the calculated P(Field) is shown for each grid position. [top left]: An example distribution of P(Field) containing a grid position with P(Field) > 1.0 – the negative galaxy problem. [top right]: Normalizing *all* the points to the anomalous grid position retains the original anomalous point and artificially decreases the probabilities in the remainder of the grid. [bottom left]: The approach used by KB01: the excess 0.2 probability is distributed equally into neighbouring grid cells. [bottom right]: Adaptive-mesh method used in this work – the lowest possible number of grid positions are used to recalculate the P(Field) distribution and no obvious fluctuation remains.

B.3 Advantages and Drawbacks

As with all background subtraction methods, this technique has advantages and drawbacks. Whilst it preserves the original probability distributions better than other methods, it also has a tendancy to "smear" the resultant distribution. To illustrate this one can imagine a situation where one grid position has a $P(\text{Field}) > 1$ whilst its neighbours have very small values of $P(\text{Field})$. Upon expansion of the grid, the probabilities of being a field galaxy significantly increase for those grid positions that initially had a very low $P(\text{Field})$. Therefore one effectively remove galaxies from adjoining grid positions to make up for the one grid position which had $P(\text{Field}) > 1$. It is because of this that one may expect that statistics on sparsely populated areas of a colour-magnitude diagram to be adversely affected (e.g. it is likely that the blue population, and hence f_B, would be underestimated). Unlike previous methods, this new technique, minimizes the number of grid positions affected in this manner.

B.4 Comparing the Cluster Membership Assignment Techniques

Two techniques have been used in this work to define cluster membership: the first method (presented in Chapter 4 and above) is a statistical background subtraction one that is used to remove the field population so that the cluster population can be defined and analyzed. The second method (presented in Chapter 6) is the spectroscopic determination of cluster membership. It is natural to enquire how these two methods compare.

This analysis commences with an illustration of some inherent differences between the two methods by comparing values for the Butcher-Oemler blue fraction, f_B. A brief review of the statistical background subtraction method and calculation of the P(field) statistic, a measure of the likelihood of a given galaxy being a cluster member, is then made. After calculating the P(field) statistics for the spectroscopically-determined cluster members the differences between the two techniques is directly analyzed. The overall success of the statistical background

correction presented in Chapter 4 is then evaluated.

B.5 The Butcher-Oemler Blue Fraction, f_B

As an illustration of the inherent differences between the two methods, the Butcher-Oemler blue fraction, f_B, is investigated. Following the prescription of Butcher & Oemler (1984; Chapter 4), values for f_B are calculated using the two different methods. The result of this analysis is presented in Table B.1. Whilst the blue fractions in Abells 22, 1651 and 3921 are equivalent under each method; other clusters (e.g. Abell 3888) show a difference ($> 3\sigma$).

An obvious implication of these results is that the distribution of spectroscopically-selected cluster members does not necessarily mirror those identified via a statistical background subtraction method. Although one cluster (Abell 2055) increases its blue fraction using the spectroscopically-selected sample, three others (Abells 2104, 2204 and 3888) significantly drop. This result reinforces a suggestion made by Diaferio et al. (2001) that there could be significant contamination from field galaxies in previous photometric studies (e.g. Butcher & Oemler 1984). One implication of this is that the tendency towards bluer galaxies at higher redshift may not be as strong as previously assumed (Diaferio et al. 2001).

B.6 Comparison of the membership definitions

B.6.1 Review

The statistical background correction employed to define cluster membership relies upon the creation of the P(field) statistic; lower values of this statistic indicate that a given galaxy is more likely to be a cluster member. The P(field) statistic is created by comparing the number of galaxies at a particular location on the colour-magnitude plane of the field observations to the cluster observations (Equation 12.1). As such P(field) is a method which effectively detects gross overdensities of galaxies along the line of sight.

In order to compare the two cluster membership definition methods it is nec-

Table B.1: The Butcher-Oemler blue fraction, f_B, for the two membership definition methods with poissonian errors. There is a significant difference of f_B in over half of these clusters.

Cluster	Photometric f_B	Spectroscopic f_B
Abell 22	0.02±0.02	0.06±0.06
Abell 1651	0.00±0.02	0.00±0.04
Abell 2055	0.06±0.03	0.15±0.05
Abell 2104	0.12±0.05	0.04±0.02
Abell 2204	0.28±0.07	0.13±0.06
Abell 3888	0.21±0.02	0.08±0.04
Abell 3921	0.20±0.08	0.25±0.10

essary to create the P(field) statistic for the spectroscopically determined cluster members. Using the field observations presented in Chapter 4, equation B.1 is re-written as

$$P(\mathrm{Field})_{\mathrm{col,mag}} = \frac{\mathrm{N(Field)_{col,mag}} \times \mathrm{A}}{\mathrm{N(Cluster)_{col,mag}} + \mathrm{N(Field)_{col,mag}}} \tag{B.2}$$

to create the P(field) statistic for the spectroscopically-confirmed cluster members.

B.6.2 A Comparison of P(field) Statistics

To investigate these differences more fully, the differences in the statistically and spectroscopically determined values of P(field) are examined. The P(field) statistic (see Chapter 4) is re-created for the spectroscopic observations of Abell 2055. Abell 2055 is chosen for this analysis as it exhibits a strong, well defined colour-magnitude sequence (see Chapter 4), has had spectroscopic observations made with the 2dF resulting in over 100 confirmed cluster galaxies (see Chapters 5 and 6) and has a notable difference in the value of f_B (Table B.1) between the two methods.

A map of the P(field) statistic on the colour-magnitude plane is presented in

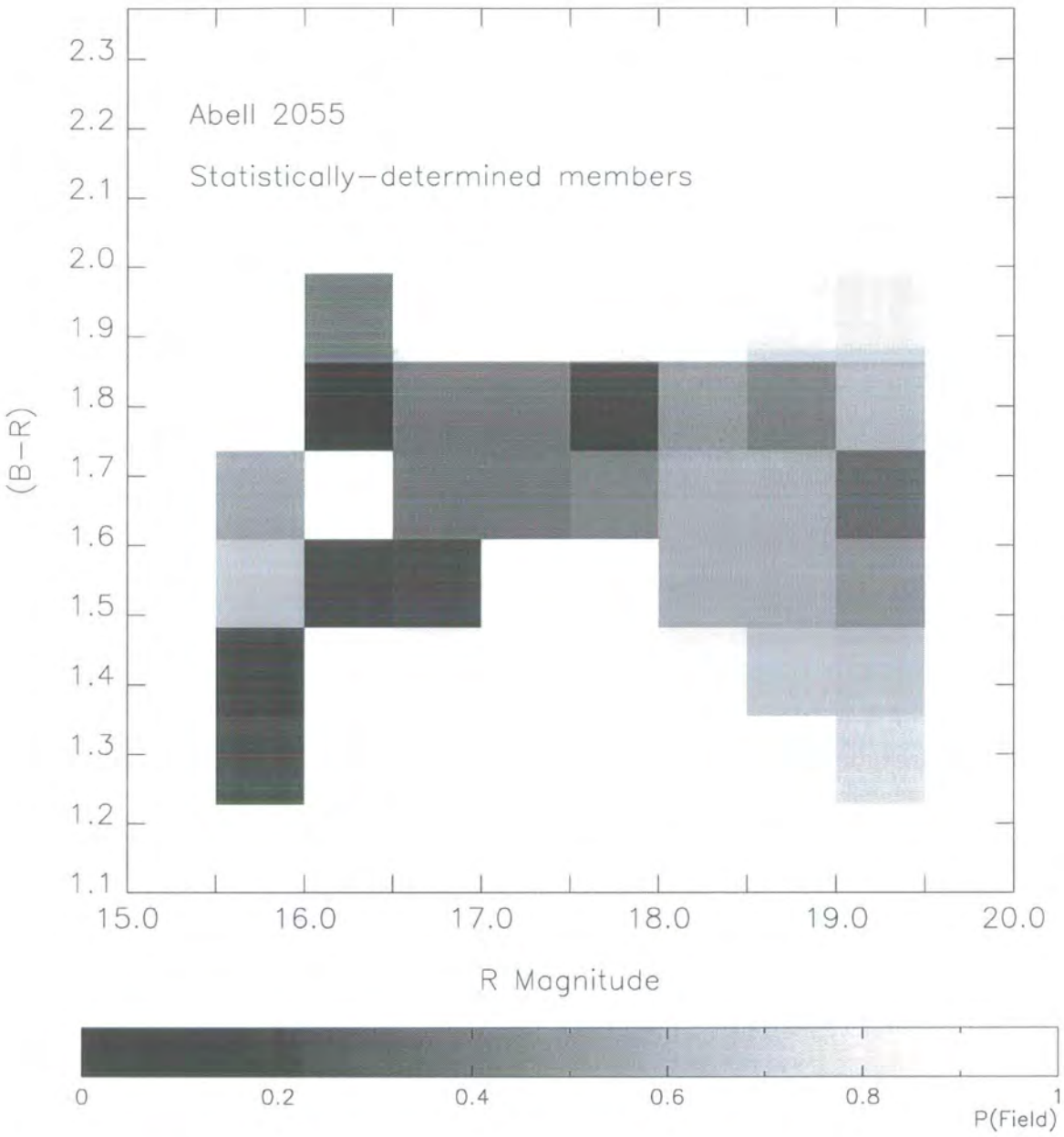

Figure B.2: The distribution of P(field) on the colour-magnitude plane that results from the statistical background correction method for Abell 2055.

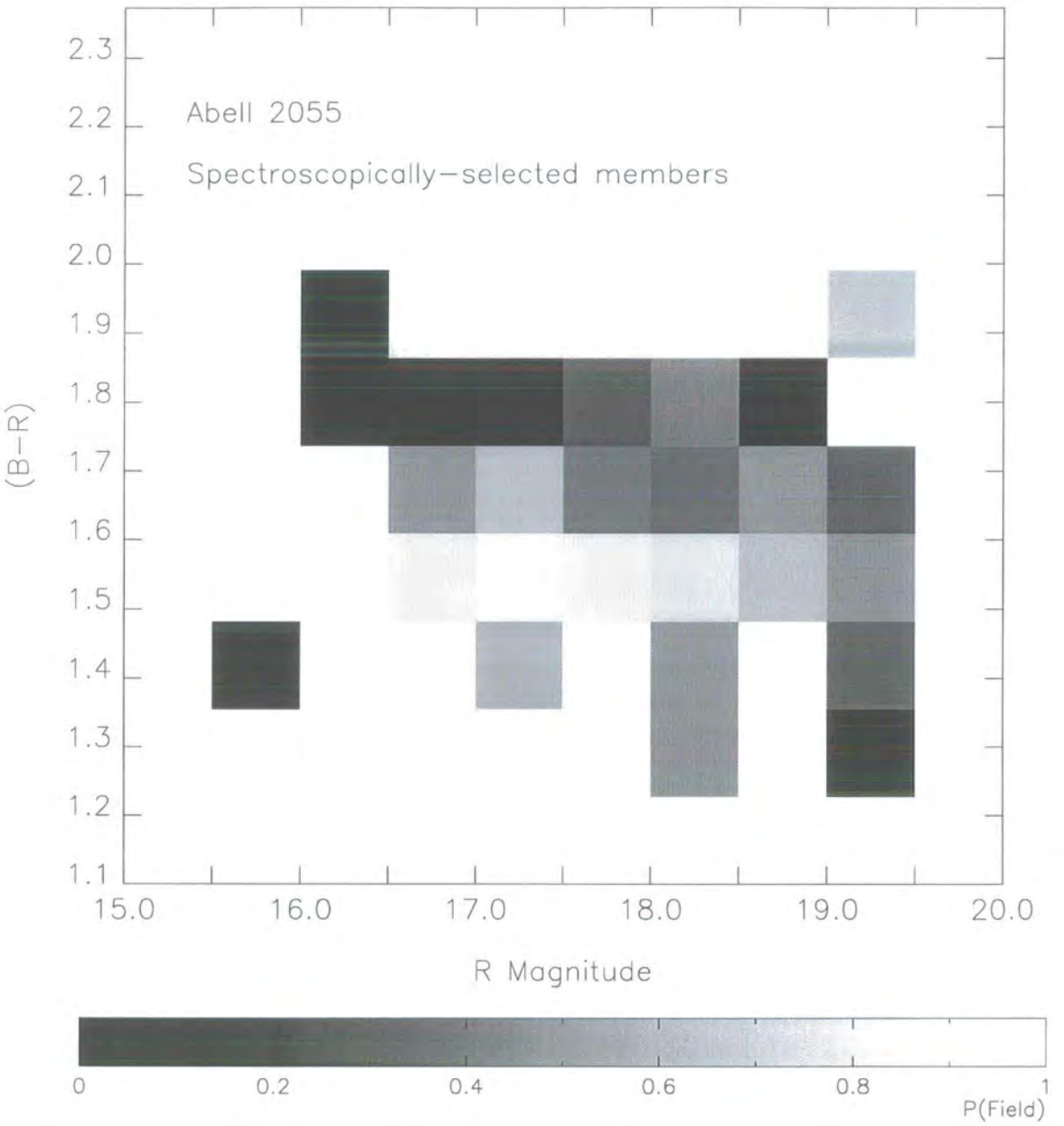

Figure B.3: The distribution of P(field) on the colour-magnitude plane that results from the spectroscopic method for Abell 2055.

Figures B.2 and B.3 for the statistically- and spectroscopically-determined cluster members respectively. The horizontal swathe of dark squares about $(B-R) \sim 1.7-1.8$ seen in these maps is the CMR. Although both methods clearly pick out the CMR, there are differences between them.

To more accurately analyze these differences, the ratio and the absolute difference between the two P(field) distributions are presented in Figures B.4 and B.5 respectively. The major difference between the two methods is the excess of blue galaxies in spectroscopic method which the statistical method simply does not have (the lighter patches in Figure B.4). Although, throughout the distribution on the colour-magnitude plane, there exist subtle differences (Figure B.5).

It is the presence of these galaxies in the spectroscopic method which creates the increase in f_B seen in Table B.1 for Abell 2055*.

B.7 Discussion

Clearly spectroscopically-selected cluster members are preferable to statistically determined ones. Even with 100 Monte-Carlo simulations, global cluster parameters such as f_B as resulting from the statistical method can be significantly different from those resulting from the spectroscopic method.

This brief analysis suggests that at least some of the original Butcher-Oemler (1984) signal may be due to contamination by field galaxies, supporting the analysis of Diaferio et al. (2001). The true values of f_B could potentially be significantly different to the ones quoted by Butcher & Oemler (1984); especially at higher redshifts. An implication of this is that the tendency toward bluer galaxies at higher redshifts may not be as strong as previously thought. Indeed some observations are now showing that there has been only a mild evolution in the abundances of massive clusters since $z \sim 0.5$ (Bahcall, Fan & Cen 1997).

*For the other clusters that show a sharp decline in f_B (e.g. Abell 3888), the reverse is true: an absence of these blue galaxies is seen in the spectroscopic method.

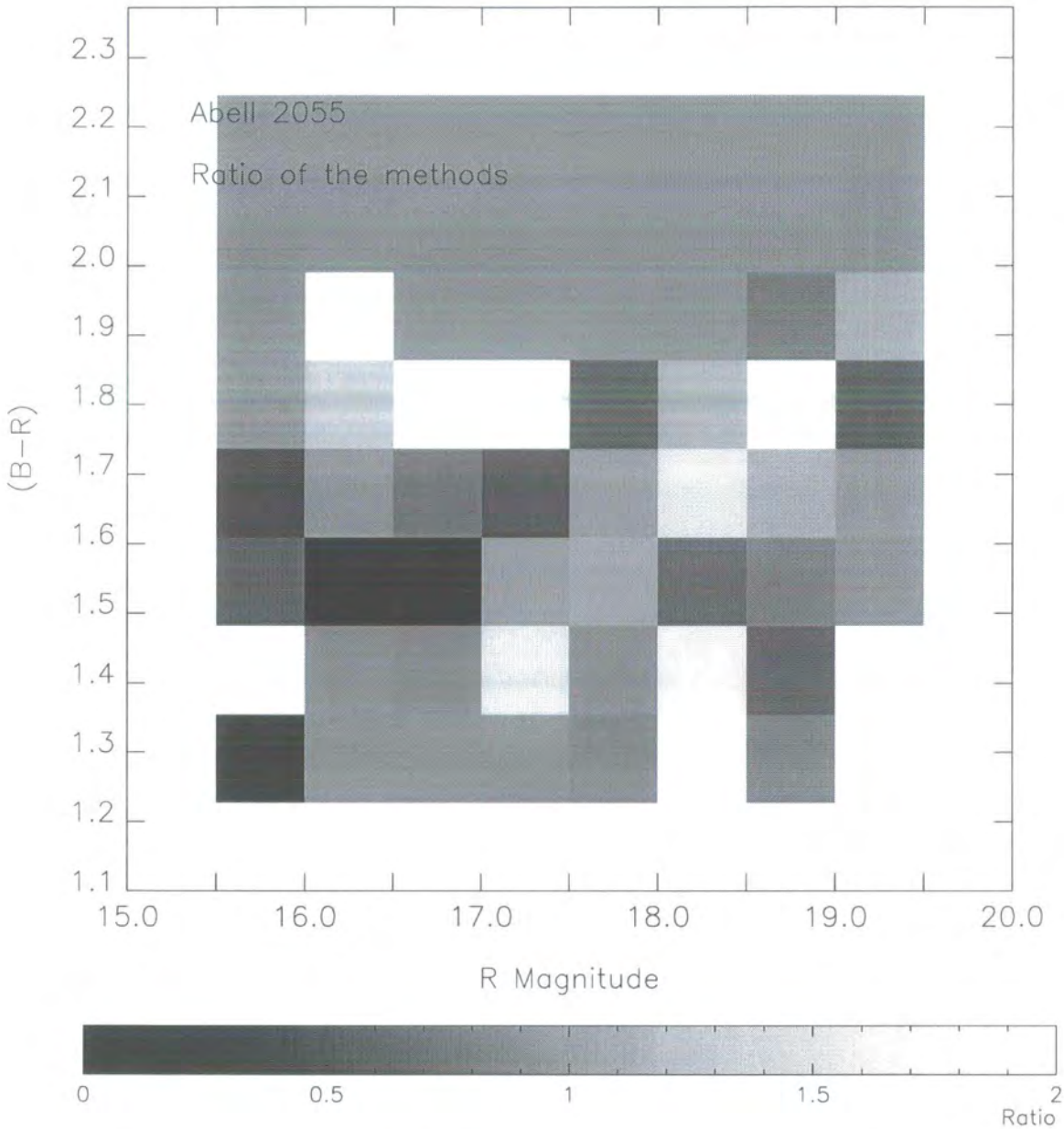

Figure B.4: Ratio of the P(Field) distribution on the colour-magnitude plane of the statistical background correction method (Figure B.2) to the spectroscopic method (Figure B.3). Note the excess of lighter (Ratio> 1.0) patches over darker (Ratio< 1.0) ones below $(B - R) \sim 1.5$.

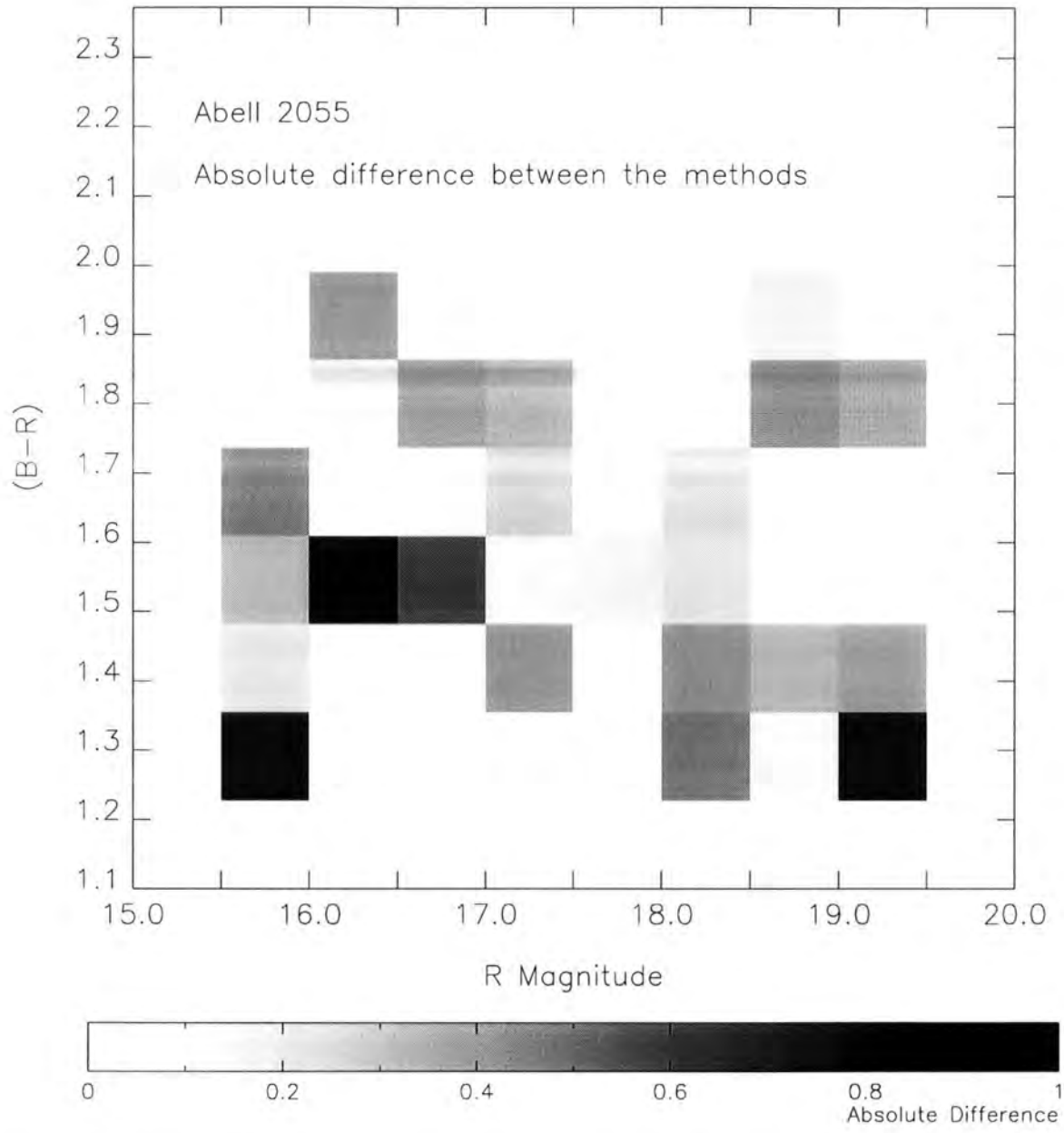

Figure B.5: Absolute difference of the P(Field) distribution on the colour-magnitude plane between the statistical background correction method (Figure B.2) and the spectroscopic method (Figure B.3).

B.8 Summary

The comparison of the statistical method of determining cluster membership to the spectroscopic method has shown that the methods can potentially yield significantly different results for global cluster parameters such as the Butcher-Oemler blue fraction, f_B. This result has potentially some serious implications for previous works that do not use spectroscopy (e.g. Butcher & Oemler 1984).

These findings emphasize the fact that spectroscopically-selected cluster members are essential to understand galaxy evolution and pursue cluster analysis at any given redshift.